Unsteady Aerodynamics of Rotorcraft at Low Advance Ratios in Ground Effect

A Thesis
Presented to
The Academic Faculty

by

Balakrishnan Ganesh

In Partial Fulfillment
of the Requirements for the Degree
Doctor of Philosophy in the
School of Aerospace Engineering

Georgia Institute of Technology
May 2006

Unsteady Aerodynamics of Rotorcraft at Low Advance Ratios in Ground Effect

Approved by:

Dr. Narayanan Komerath, Advisor
School of Aerospace Eng
Georgia Inst of Technology

Dr. Mark F. Costello
School of Aerospace Eng
Georgia Inst of Technology

Dr. LN Sankar
School of Aerospace Eng
Georgia Inst of Technology

Dr. A.T. Conlisk
School of Mechanical Eng
The Ohio State University

Dr. JVR Prasad
School of Aerospace Eng
Georgia Inst of Technology

Date Approved: Mar 24, 2006

Dedicated to my brother.

ACKNOWLEDGEMENTS

I wish to thank Prof. Narayanan Komerath for his guidance and support. I also express my appreciation to Prof. LN Sankar for his help and advice. I also acknowledge the members of my committee, Prof. JVR Prasad, Prof. M. Costello and Prof. A.T. Conlisk, for their assistance with the thesis.

I gratefully acknowledge my fellow students at the Wind Tunnel, who helped me without complaint. I also thank the Aerospace Shop Staff members for their help with machining jobs.

I thank Mr. Alan Egolf of Sikorsky Aircraft for sharing his experiences with ground effect operations. His practical insights are greatly appreciated.

This work was sponsored by the U.S Army Research Office under the Center of Rotorcraft Excellence Program. Their support is most appreciated. The reviewers from the Army Research Office provided valuable inputs that guided the progress of this study. I thank them for their guidance.

Finally, I thank my parents for their help and guidance.

TABLE OF CONTENTS

LIST OF TABLES

LIST OF FIGURES

Glossary

A	Area of Rotor disk
A_F	Cross-sectional area of circular cross-sectional fuselage
c	Empirical PIV Correction Coefficient
C_F	Coefficient of fuselage force
CFD	Computational Fluid Dynamics
C_P	Coefficient of Power $P/(\rho$ A $(\Omega$ R$)^3)$
C_T	Coefficient of Thrust $T/(\rho$ A $(\Omega$ R$)^2)$
D	Diameter of Rotor
d_p	Particle Image Diameter
F	Fuselage force
F_RF	Frequency of recirculation fluctuation
IGE	In Ground Effect
M	Magnification
OGE	Out of Ground Effect
PIV	Particle Image Velocimetry
R	Radius of Rotor
T	Thrust

T_i	Thrust in ground effect
T_o	Thrust out of ground effect
U_∞	Forward Velocity of helicopter/Freestream velocity
U_p	Maximum in-plane component of the flow velocity during PIV measurements
v_i	Induced Velocity
V_{Tip}	Rotor tip velocity
W_p	Maximum out-of-plane component of the flow velocity during PIV measurements
$\mathbf{Z}$	Light Sheet thickness during PIV measurements
$\mathbf{z}$	height above ground
Ω	Angular Velocity of Rotor
α	Rotor disk angle of attack
ϵ_m	Total relative PIV measurement error (Total PIV Measurement Error/Maximum Velocity measured)
κ	Induced Power Correction Factor
λ	Inflow Ratio $\frac{U_\infty \sin\alpha}{\Omega R} + \frac{v_i}{\Omega R}$
λ_h	Rotor hover inflow ratio
λ_i	Rotor induced inflow ratio $v_i/(\Omega R)$
μ **(Advance Ratio)**	Ratio of freestream velocity to rotor tip speed
μ^*	Dimensionless parameter that describes wake deflection angle
ρ	Density
σ	Random PIV error

σ_i	Random measurement error in the PIV image plane

SUMMARY

The aerodynamic characteristics of rotorcraft flying at low speed close to the ground are investigated. This will help better understand and quantify the flow field structures and unsteadiness associated with various in ground effect flight conditions. This study aims to separate out the various phenomena according to their causal factors.

Experimental investigations first involved flow visualization, which helped in identifying the various flight regimes and in getting an approximate estimate of the unsteadiness. It was found that there was considerably more unsteadiness in the flowfield while in ground effect. The problem was thereafter divided into its unsteady and quasi-steady aspects. Hotwire measurements were performed and the unsteadiness in the flow structure was quantified. It was found that there were long time scale fluctuations in the upwind side of the rotor disk, with significant changes in the inflow. These fluctuations were quantified and related to the flow parameters, which will help scale the results.

On the quasi-steady side, the fuselage loads for two fuselage cross-sectional shapes were investigated both in and out of ground effect. The fuselage cross-section shape had a significant effect on the loads felt by the fuselage in ground effect. It was found that the sideforce on a circular cross-section fuselage was considerably different when flying close to the ground.

The power required for the experimental configuration was measured to provide a basis for comparison. Finally, the flowfield around the ground vortex was quantified, and the structure of the ground vortex was investigated using Particle Image Velocimetry. It was found that tip vorticity was ingested by the ground vortex and that the strength of the ground vortex was considerably more than the tip vortex.

CHAPTER I

INTRODUCTION

The behavior of a rotor wake in the vicinity of the ground is challenging to predict. During flights in ground effect (IGE) conditions, the wake collides with the ground and causes a significant perturbation to the flow near the blade. Significant interactions between the main rotor wake and the ground have been associated with the formation and passage of the ground vortex . When a helicopter encounters a ground vortex, the main rotor may be forced to provide additional power and the stability of the aircraft may be degraded. This is because of the reduction in inflow due to the presence of the ground. This complexity is most apparent during the transition from hover to forward flight in ground effect. Flight time history for a helicopter in forward flight near the ground is shown in the report by Serr *et al* [68], and indicates that pitch-roll attitude, and power requirements are continually changing during the transition from hover to forward flight while close to the ground.

More importantly, such phenomena often carry a human cost [41] , and many incidents have been reported since the Vietnam War Era, which are directly ascribed to handling problems associated with rotorcraft flying close to the ground at low advance ratios. Harris *et al* carried out a comprehensive study of rotorcraft accidents over a 34 year period. The results for the accidents and the stages of flight in which they occur in, is shown in Fig. 1 [24]. It can be seen that most of the accidents occurred during take-off and hover. Out of these mishaps, 625 accidents were caused due to loss of control. It can be seen from Fig. 2 that more than 50% of the loss of control accidents occurred during flight close to the ground. It can be seen from Fig. 3 that most of the loss of control accidents occurred due to improper control inputs and winds. It is also to be noted that a significant number of the loss of control accidents are caused due to yaw controls, which can be seen in Fig. 4. These statistics are a motivation to study the unsteady phenomena in ground effect to help prevent such accidents in the future.

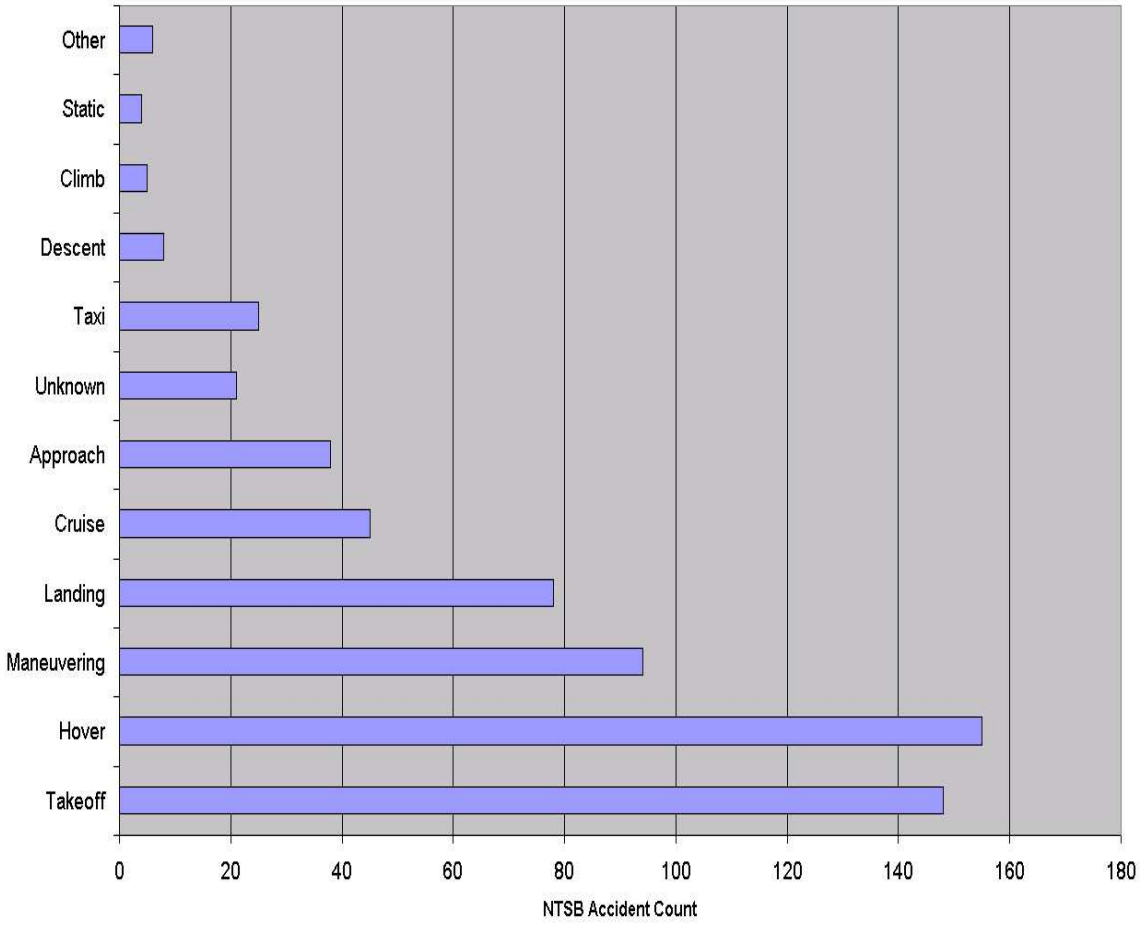

Figure 1: Accident Statistics from 1963 to 1997

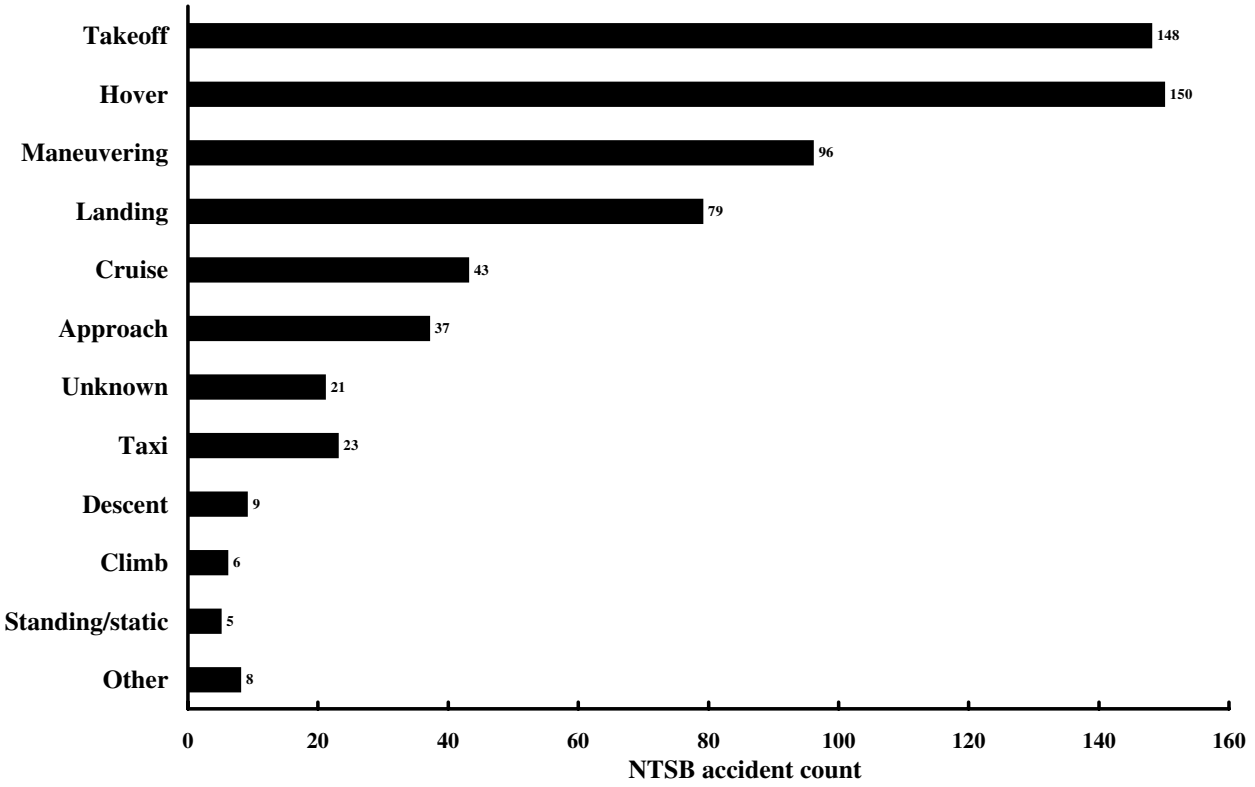

Figure 2: Loss of Control Accidents by Phase of Operation

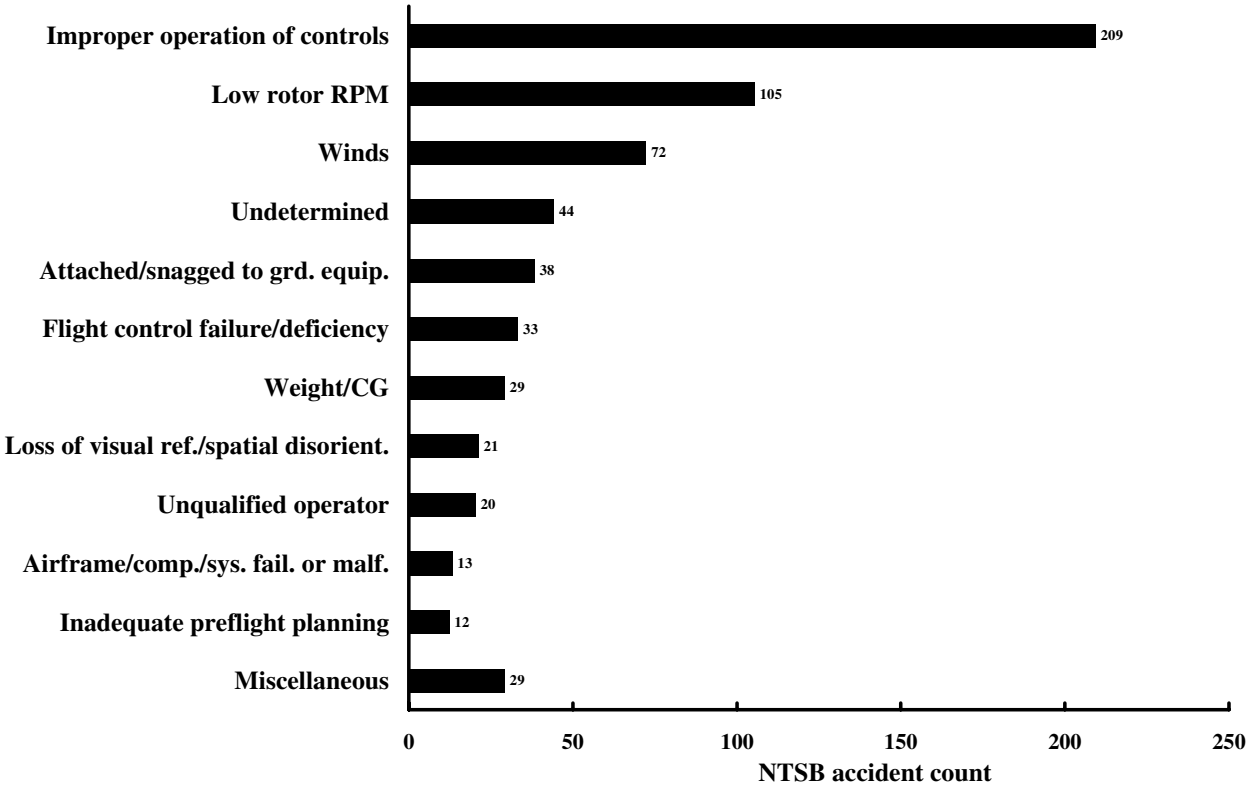

Figure 3: Loss of Control Accidents by Cause

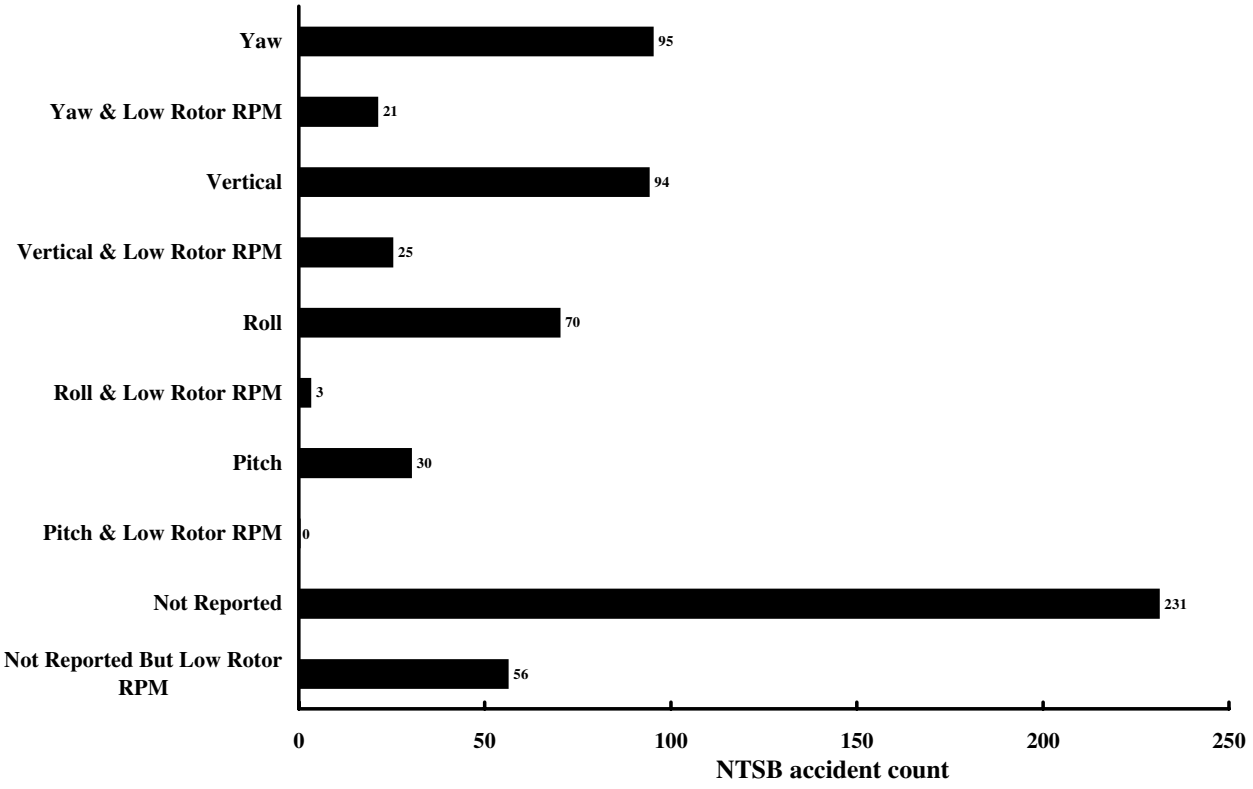

Figure 4: Loss of Control Accidents by Axis Lost

The issues associated with IGE flight include the following.

1. Effect of the ground on vortex strength
2. Effect of the ground on blade loads
3. Modification of rotor inflow due to wake distortion and the ground
4. Moments on rotor disk due to the ground
5. Forces on fuselage due to the ground
6. Deflection of wake due to fuselage and the ground
7. Influence of axial flow in vortex
8. Time lag effects on inflow and loads due to time scales of ground vortex unsteadiness and wake response

1.1 Summary of Flight Characteristics and Handling Qualities in Ground effect

The phenomena that are seen in forward flight near the ground are schematically shown in Fig. 5 taken from [61]. At low forward speeds, a small region of flow recirculation is formed upstream of the rotor near the ground. As forward speed increases, this recirculation develops into a vertical region between the tip of the rotor and the ground. This phenomenon increases the inflow through the forward part of the rotor disk. As a consequence the induced power requirement increases until the ground vortex is overrun. Fig. 6 from [61] shows the required power as a helicopter goes into forward flight. This figure indicates that the required power increases with speed between 5 and 20 knots. The change in inflow through the rotor not only affects the required power but the lateral trim as well (Fig. 7). Out of ground effect, at low speed the downflow through the front part of the rotor is lower than that through the rear part. This phenomenon causes the rotor to want to flap the left up (solid line in Fig. 7). The effect of the ground vortex is to increase the downward flow through the front part of the rotor disc, making the flow more uniform and reducing the

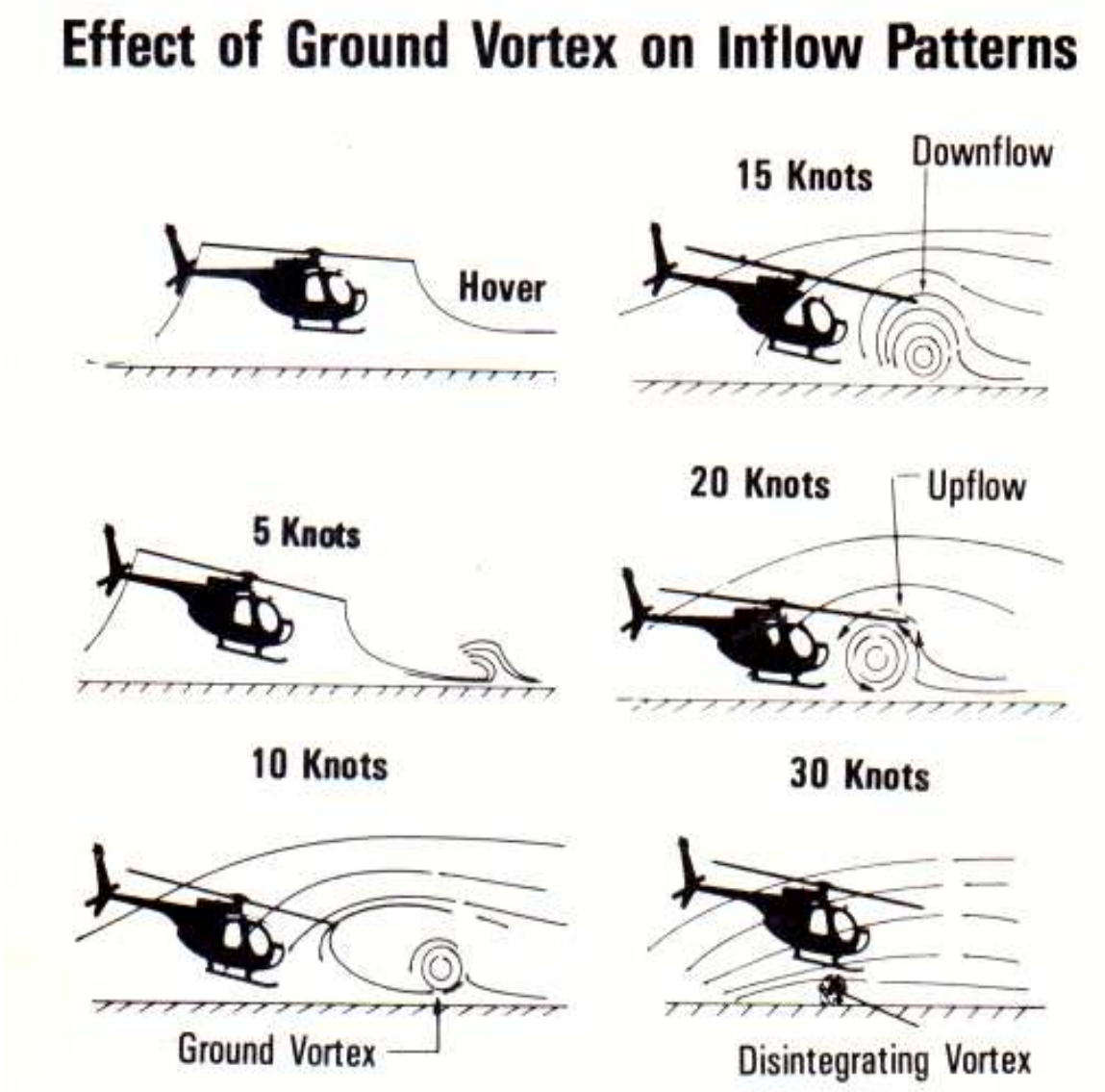

Figure 5: Schematic of Flow Regimes in Ground Effect. (Courtesy: NASA Civil Helicopter Safety Website)

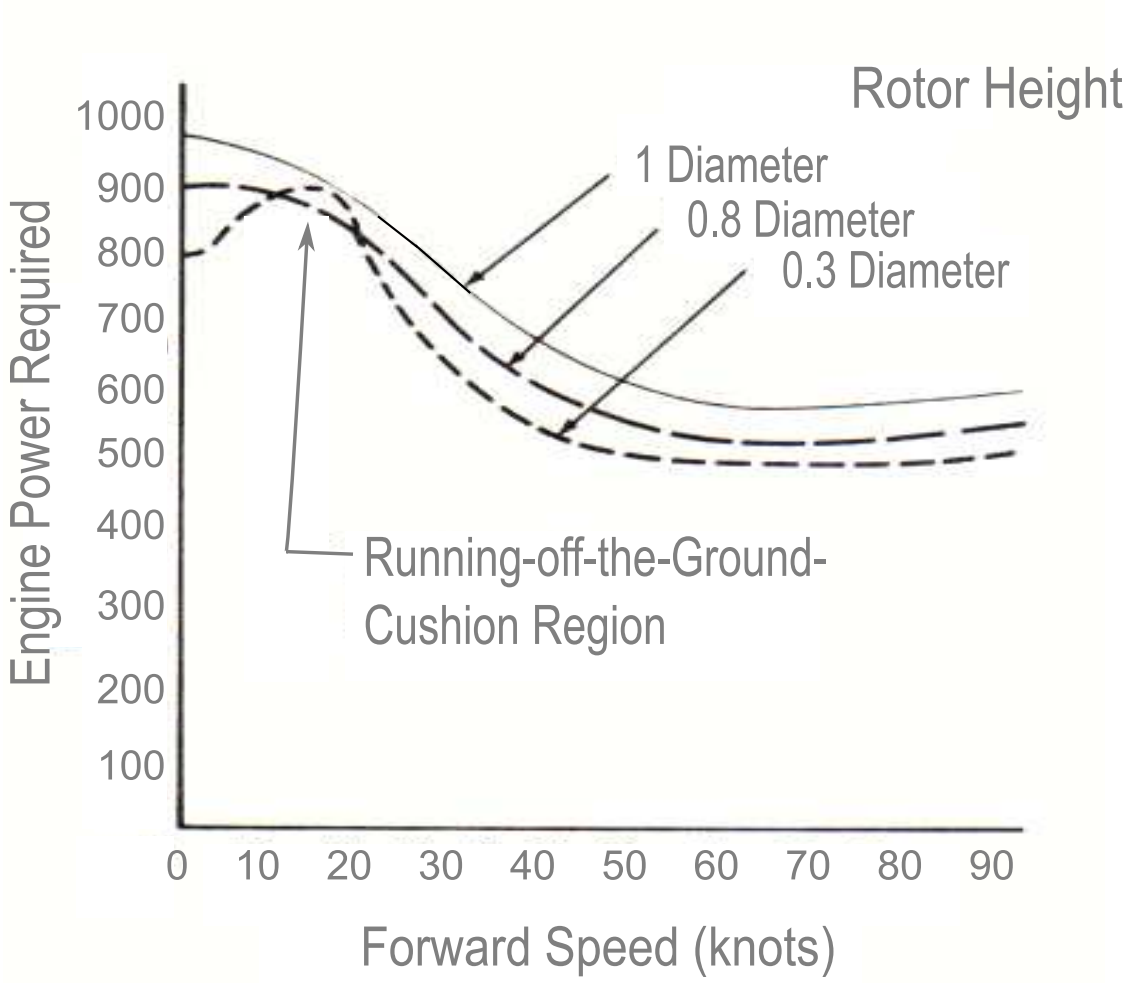

Figure 6: Power Requirements in Ground Effect. (Courtesy: NASA Civil Helicopter Safety Website)

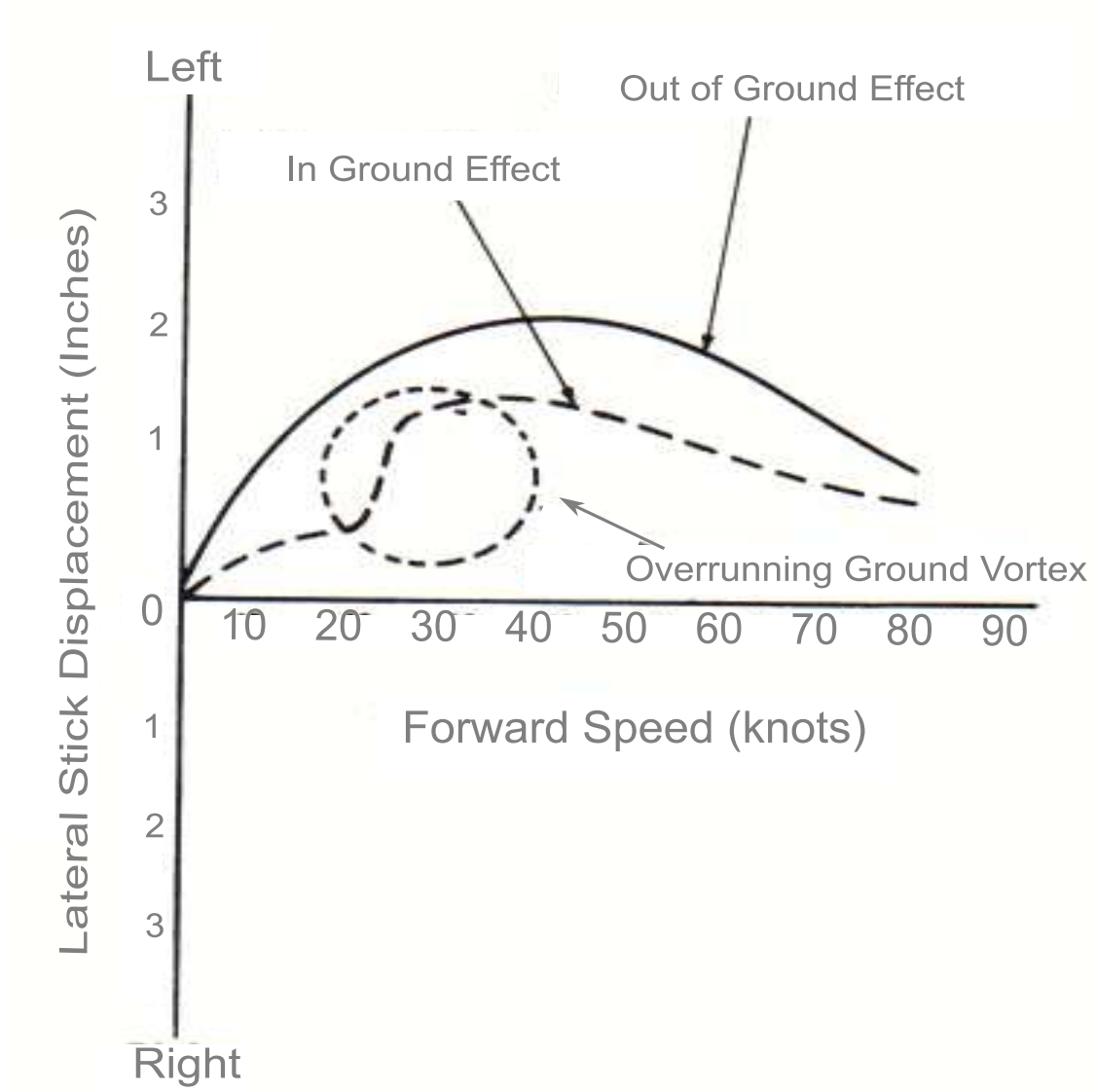

Figure 7: Lateral Stick Requirements in Ground Effect. (Courtesy: NASA Civil Helicopter Safety Website)

requirement for left stick. After the ground vortex is overrun, left stick is required suddenly (dotted line in Fig. 7). This sudden change in control input is just one example of the challenges of flight in ground effect.

1.2 Previous Work

Much of the early studies of ground effect concentrated on the variation of average thrust in hover when close to the ground. This was important to understand the hover capabilities of helicopters when flying close to the edge of their performance envelope, especially in "hot and high " operating conditions.

The earliest analytical studies were done by Kussner [45] and Betz [2]. They showed that the effect of the ground was minimal when the rotor was higher than 1 rotor radius above the ground. Analytical work in the 1940s studied the effect of ground proximity on a lifting airscrew [74], and developed a vortex cylinder model. Zbrozek modeled flight test data in terms of thrust increase as a function of rotor height in 1947. [42] Experimental work in this area was done at Georgia Tech in the 1950s, where the electromagnetic analogy was used to measure the normal component of the induced velocity in ground effect [21].

An experimental study performed by Lewis [51] showed that the effect of the ground on thrust was negligible when the rotor was more than one diameter above the ground. Ground effect has been examined by Cheeseman and Bennet [8] using the method of images, where a mirror-image of the rotor is placed below the ground plane. In their analysis the rotor thrust ratio in ground effect is expressed by Equation 1, where T_i is the thrust IGE, T_o is the thrust OGE, D is the diameter of the rotor, and z is the height above the ground.

$$\frac{T_i}{T_o} = \frac{1}{1 - (\frac{D}{2z})^2} \tag{1}$$

This equation compares well with experimental data in Fig. 8 [51]. Hayden [25] carried out performance measurements for several helicopters and developed an empirical equation for the thrust ratio similar to the above equation.

Frandenburg [18] recorded in-ground effects on the rotor and airframe. Interest in this area increased in the 1970s, spurred by the reports of unsteady forces and erratic handling

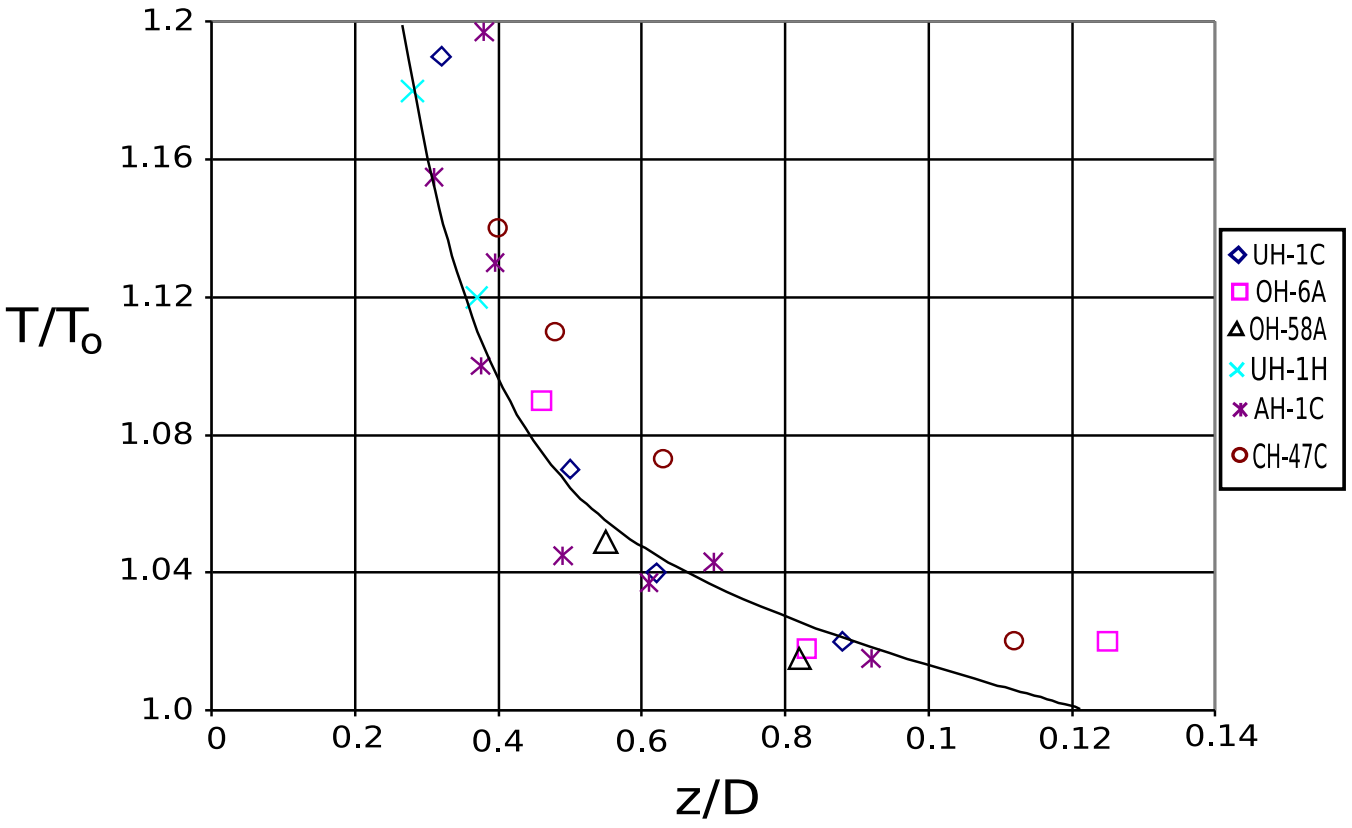

Figure 8: Thrust Ratio in Ground Effect

of rotorcraft flying close to the ground. Huston and Morris [33] were the first to report the recirculation vortex caused by a wind acting on the flowfield of a main rotor in ground effect. A more comprehensive experimental study of ground effect on tail rotor thrust was carried out by Empey and Ormiston in 1974 [17]. They found from helium bubble flow visualization that the ground vortex possessed a very small well-defined core, and they plotted variation of tail rotor thrust with wind velocity and azimuth. Koo and Oka [43] measured thrust, torque and induced velocity of a rotor in ground effect. They found that when a hovering rotor at high collective pitch angle flies close to the ground blade stall may occur causing thrust stagnation. They also found that there is a fluctuation of downwash and upwash causing unsteady flow recirculation. Wiesner [72] found that a ground vortex appears at low advance ratios under a rotor in ground effect. Sheridan and Weisner [69] experimentally examined low advance ratio forward flight IGE and noted the formation of a ground vortex. He found that the thrust at constant power reduced at low advance ratios in ground effect to a minimum value and thereafter increased once the ground vortex was overrun. In forward flight, where the wake is swept behind the rotor, the effect of the ground diminishes rapidly as forward speed increases. Ground effect is negligible for speeds above advance ratio of 0.15 . Sheridan et al [70] developed an empirical model in 1982 relating inflow components to height above the ground.

Landgrebe *et al* studied the wake characteristics of the helicopter in hover and low speed forward flight in ground effect [46]. They noted that while hovering, tip vortices in the wake boundary are transported downward, whereas in low speed forward flight the tip vortices travel inboard and slightly above the rotor and are then transported down through the rotor disk. They found that flow velocity at each flow field point varies with time, due to the rotation of the blades and the periodic passage of the tip vortices. They noted that the upward flow ahead of the wake boundary, changes over to downward flow as the wake boundary is approached. However, in ground effect, the downflow inside the rotor wake decreases as it approaches the ground. Kusmarwanto [44] showed that ground effect causes induced upwash at the rotor disk. Gao and He [19] derived an analytical expression on ground vortex position variation with advance ratio.

Curtiss *et al* were the first to categorize the two regimes of low advance ratio flight close to the ground [15] [14]. They found that when a lifting rotor operates close to the ground at low advance ratios two distinct flow regimes can be identified. In the recirculation regime, part of the rotor wake flows forward and upward and recirculates through the rotor and fluctuates at a low frequency. This flow regime is shown schematically in Fig. 9(a). As the advance ratio is increased the second flow regime appears, and a well-defined vortex forms under the upwind half of the rotor (Fig. 9(b)). They found that the flow field becomes more steady as the elliptically-shaped horseshoe vortex is formed on the ground under the rotor. They found that the vortex becomes smaller as the advance ratio is increased until it is convected downstream at high advance ratios. The existence of these flow regimes can be characterized by the dimensionless parameter μ^*, which can be derived from momentum theory.

$$\mu^* = \frac{\mu}{\sqrt{C_T/2}} \tag{2}$$

This parameter determines the gross characteristics of the wake, i.e., the wake deflection angle.

Curtiss *et al* contend that there is a difference in the flight condition at which the various flow phenomena exist depending upon whether a moving model test or a wind tunnel test is conducted. The recirculation regime is associated with a significant additional downward flow through the forward half of the rotor and the flow field is quite unsteady while the flow field associated with the ground vortex appears quite steady. It was also noted that low levels of translational acceleration influence the forces and moments acting on the rotor and that under accelerating conditions the ground vortex does not become fully established. In order to estimate the order of magnitude of the ground vortex strength, an elementary ground vortex was modeled as a line vortex, as per the method derived by Heyson [29]. Heyson [32] [28] [27] analyzed ground effect using a skewed cylindrical vortex sheet with an image vortex system. The linearized estimate of the ground vortex strength is at least an order of magnitude larger than that of the tip vortex. Heyson [31], [30] also showed that ground induced interference opposes the downwash through the rotor and could result in blade stall.

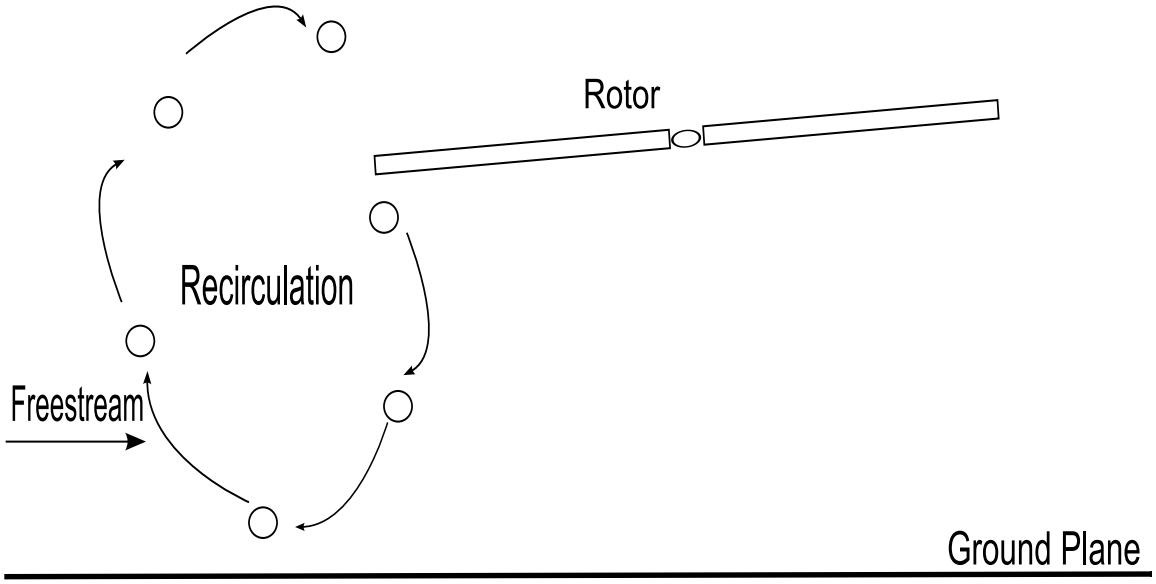

(a) Recirculating Regime

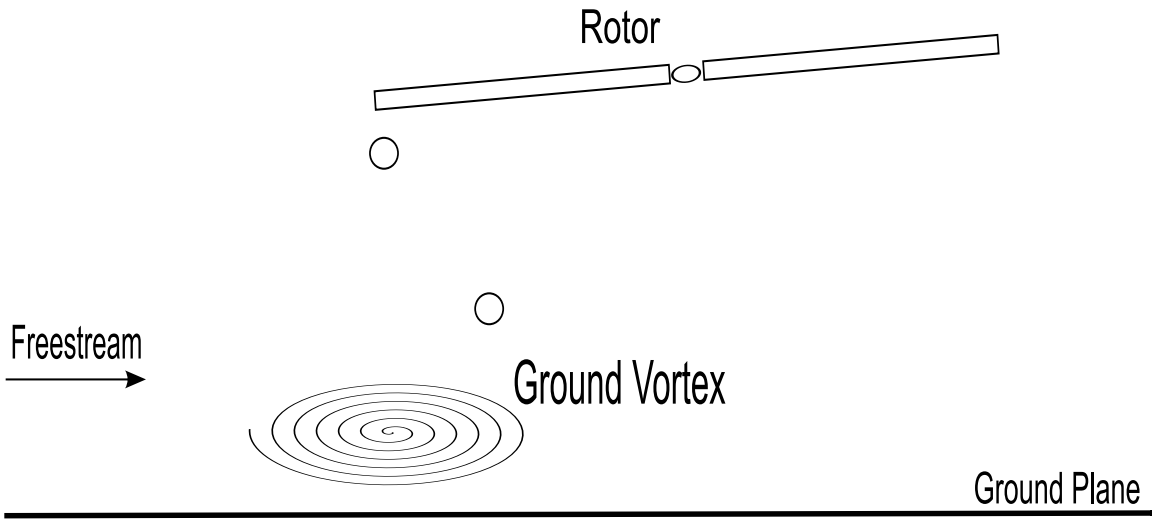

(b) Ground Vortex Regime

Figure 9: Two Regimes of Flight in Ground Effect at Low Advance Ratios

Curtiss *et al* also found that increasing collective pitch moves the ground vortex forward, and reducing height-to-diameter ratio moves the ground vortex forward [14]. They noted the change in hub moment that occurred due to increase in inflow in the upwind half of the rotor disk. They noted irregular variations in the thrust and hub moments with change in advance ratio. Lee [48], [49] conducted experimental studies that looked at helicopter performance in dynamic ground effect. Cerde et al [6] looked at take-of and landing performance of helicopters.

Hanker and Smith [23] conducted ground effect experiments at the Princeton Dynamic Model Track and found that the recirculation occurs until an advance ratio of 0.058, and that the ground vortex disappeared at an advance ratio of about 0.125. Cimbala *et al* [12] studied the unsteady behavior of the ground vortex, and noted that the ground vortex had a low frequency pulsing behavior. However, they were not able to find any preferred frequency of this behavior. Light [52] studied the trajectory of the tip vortex in ground effect and concluded that the tip vortex in ground effect contracted slightly and then expanded radially close to the ground.

Numerically, early studies did not correlate well with experimental results. DuWalt [16] modeled IGE using an axisymmetric, periodic wake, and a mirror image below the ground plane. Since the 80s, however, computational studies have been successful in predicting ground effect phenomena. Sun [71] used a free vortex wake model combined with prescribed position of ground vortex from experiments to compute the inflow. Quackenbush and Wachspress [62] , Graber *et al* [20] have also done image wake analysis to simulate ground effect. Chen [9] published a detailed survey of the various computational methods used in ground effect modeling in 1989. Saberi and Maisel [65], [66], [67] modeled vortex wake in ground effect for steady flight conditions using a free wake model. Lee and He [47] carried out a free wake analysis of a rotor in ground effect. They found that when the ground vortex approaches the leading edge of the main rotor, it induces large downwash on the rotor disk. Consequently the thrust is reduced and yaw control effectiveness in sideways and rearward flights is affected near the ground. They also found that the ground vortex is shaped like a half circle attached to two trailing vortices, similar to a horseshoe vortex

with a large core. The ground vortex strength is sensitive to the wake decay rate, an input parameter depending on both the rotor height above the ground and the wind speed. They also found that a nose-down pitching moment is produced with the formation of a ground vortex. Lowering the height above the ground increases this pitching moment.

Sun [37] used a pure Computational Fluid Dynamic (CFD) method to analyze the flowfield around a rotor near the ground. Kang and Sun carried out a computational study [38], which confirmed the formation of the ground vortex due to rolling up of the wake. More recently, Griffiths and Leishman have used a free wake model to model twin rotors in ground effect. They have compared two methods of modeling ground effect, the method of images and a surface singularity method [22].

Peters and He have used finite state dynamic inflow theory [58], [57], [55], [56], [26] to model helicopter performance where the induced inflow is represented as a system of first order differential equations in the time domain. Aerodynamic interference between a helicopter and ship deck [54], [60], [75] was modeled with a source panel representation and it was shown that considerable rotor trim changes occurred in ship ground effect. Itoga *et al*, [35], [36] have tried to model a sloping ground plane to simulate ship borne operations using vortex panels to simulate the ground plane. Helicopters are often required to land on a rolling ship deck. It has been thought that the rotor performance is affected by the non-uniform and rolling ground surface (in dynamic ground effect). Experimental research has been attempted by Iboshi *et al*, [34]. These results indicate that dynamic ground effect does affect the rotor performance to a considerable extent.

CHAPTER II

RESEARCH PLAN

2.1 Objectives

The objectives of the proposed work are to study the physics of the flow of a rotorcraft flying at low advance ratios in ground effect. It aims to explain the unsteady fluctuations in inflow and relate them to the seemingly random fluctuations observed by rotorcraft operators in ground effect.

2.2 Planned Approach

The investigation into the ground effect problem was to proceed on two fronts. On one hand the unsteady, seemingly random, fluctuations noticed in the past had to be investigated. On the other hand, the quasi-steady change in loads due to change in ground vortex shape had to be studied. The outline of the research plan is given in Fig. 10.

The study of this problem began with flow visualization. This was to understand the differences in the wake structure between the OGE and the IGE cases. The unsteadiness of the inflow fluctuation was to be quantified using hotwire measurements. This was to study the unsteady fluctuations in the flowfield around a rotor in ground effect. On the other hand, the quasi-steady effects of the wake structure on the fuselage loads were to be studied. Finally, the structure of the ground vortex was to be studied using Particle Image Velocimetry.

2.3 Experimental Facilities

The experimental investigation into the ground effect phenomena was conducted in the John Harper $7'$x$9'$ tunnel at Georgia Tech. This is a closed circuit tunnel powered by a 600hp electric motor. An eddy current clutch provides speed control. The turbulence level in the tunnel is 0.5 %. The rotor is an untwisted NACA 0015 two-bladed teetering rotor

with an 18" radius and a chord of 3.375". Rotor solidity is 0.12 and collective is fixed at 10° . The rotor was run at 2100 RPM by a 3hp electric motor mounted to a frame above the test section. The tip speed at this RPM is 100 m/s and the advance ratio can be varied upwards from 0.03. The rotor shaft is tilted forward by 6° to simulate forward flight.

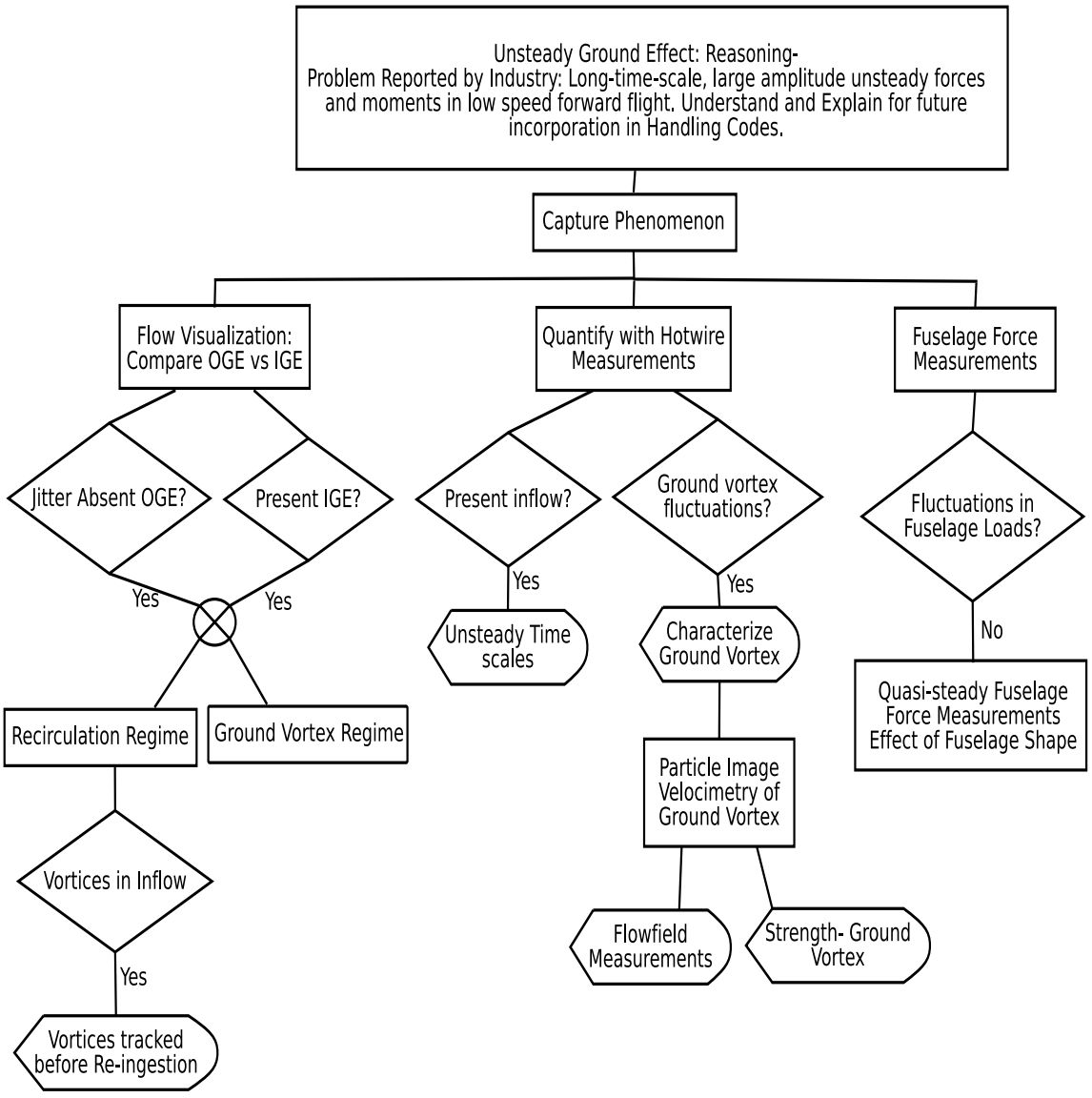

Figure 10: Planned Approach to Research

CHAPTER III

FLOW VISUALIZATION

3.1 Experimental Setup

The experiments were conducted in the John J. Harper Low Speed Wind Tunnel of Georgia Institute of Technology. This facility is a closed-circuit wind tunnel and was described in the earlier chapter. The rotor installation in the test section can be seen in Fig. 11 and the coordinate system is shown in Fig. 12. The rotor specifications and test conditions are shown in Table 1. These conditions in Table 1 are roughly equivalent to those of a UH1B helicopter hovering at a skid altitude of 4ft, with a headwind varying from 0 to 38 knots.

The laser sheet optics (New Wave Research Gemini 30Hz) was placed downstream of the rotor in the test section. To capture the flow visualization images, a Sony DV camera or a Sony CCD camera was placed perpendicular to the plane of the laser sheet. Flow seeding was done by fog machines placed upstream of the rotor. The setup for the flow visualization is shown in Fig. 14. The ground plane was a wooden board 8' x 8' in size and is shown in 13.

Table 1: Rotor Specifications and Test Conditions

Radius R (in)	18
Chord (in)	3.375
Airfoil	NACA 0015
Collective pitch	10°
Rotor Shaft Tilt Angle	6°
Solidity	0.1193
Advance Ratio (μ)	0.03 to 0.10
Rotor RPM	2100
Ground Clearance h/R (IGE)	0.72
Ground Clearance h/R (OGE)	2.77

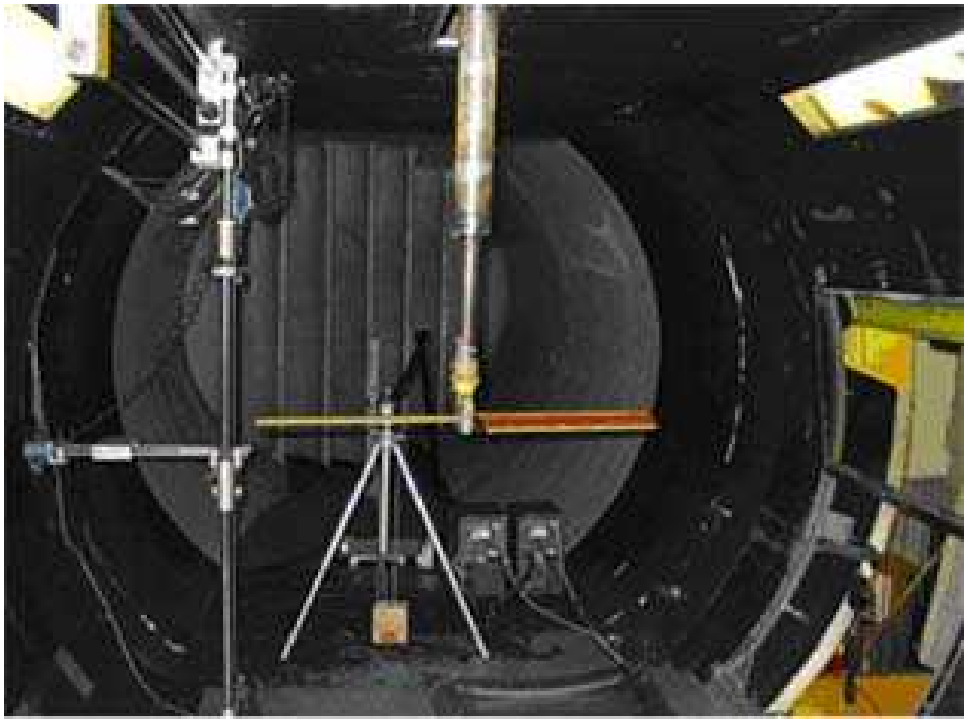

Figure 11: Rotor Setup in the Harper Wind Tunnel

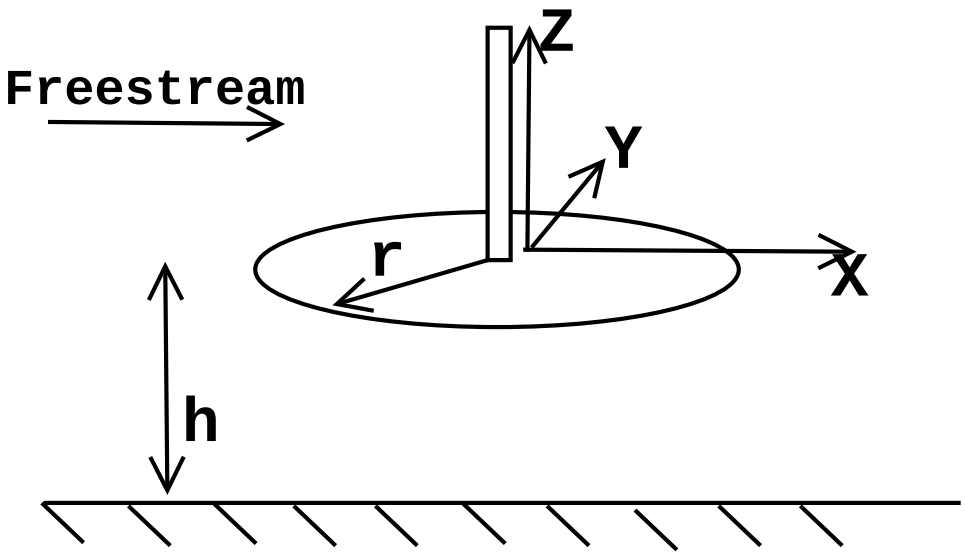

Figure 12: Co-ordinate System of the Rotor Setup

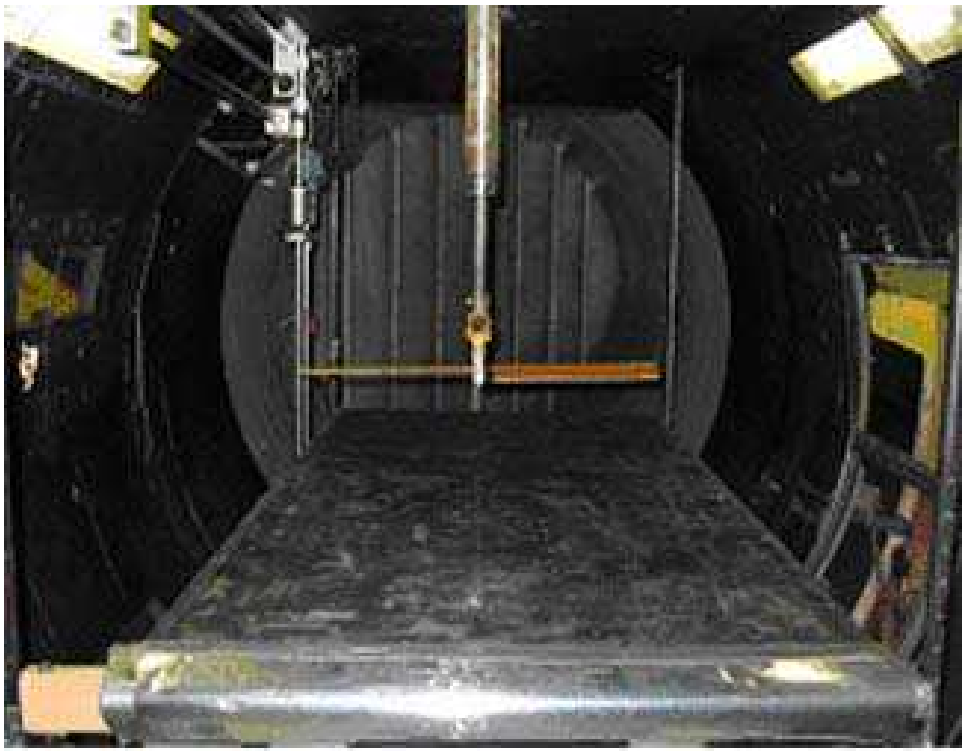

Figure 13: The Ground plane in the Tunnel

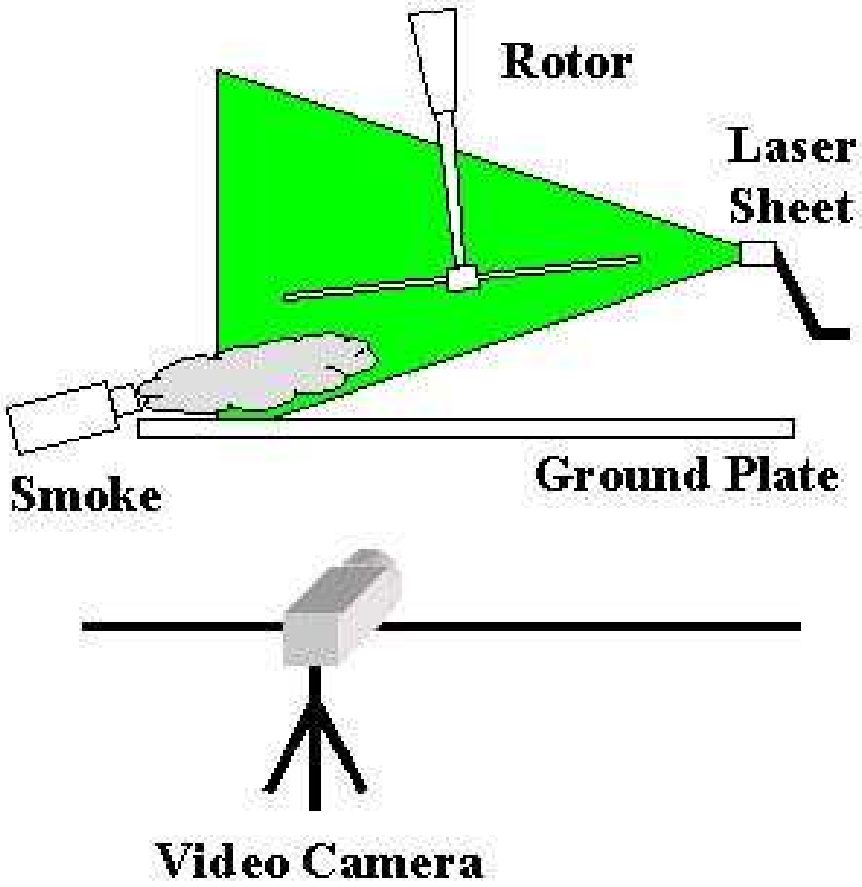

Figure 14: Co-ordinate System of the Rotor Setup

3.2 In Ground Effect

3.2.1 Recirculation Regime

At low advance ratio, the rotor wake is flowing forward and upward and recirculating through the rotor disk. This recirculation phenomenon is observed in the range $\mu \leq 0.06$. This phenomenon can be seen in Fig. 15, which shows the case of $\mu = 0.03$. It can be seen that the vortices are deflected upward and are re-ingested into the rotor disk.

A similar flow structure is seen at an advance ratio of 0.04 in Fig. 16, with some subtle differences. It can be seen that the recirculation occurs with a tighter trajectory, though the number of vortices that could be tracked before re-ingestion was the same as in advance ratio of 0.03. The flow is in a transition phase at $\mu = 0.05$ and a puffing tendency of the vortex close to the ground was noticed. In other words, it was seen that the ground vortex appeared to periodically grow and shrink in size. The flow is in the midst of changing over from the recirculation to the ground vortex stage. A large ground vortex is seen, but there is also some recirculation into the disk.

The vortices were tracked using a bitmap algorithm to mark vortex voids in the acquired images. Up to 8 vortices were tracked in the recirculation circle. This works out to a frequency of recirculation of approximately 9Hz in this case. The trajectory for the case of $\mu = 0.03$ is shown in Fig. 17.

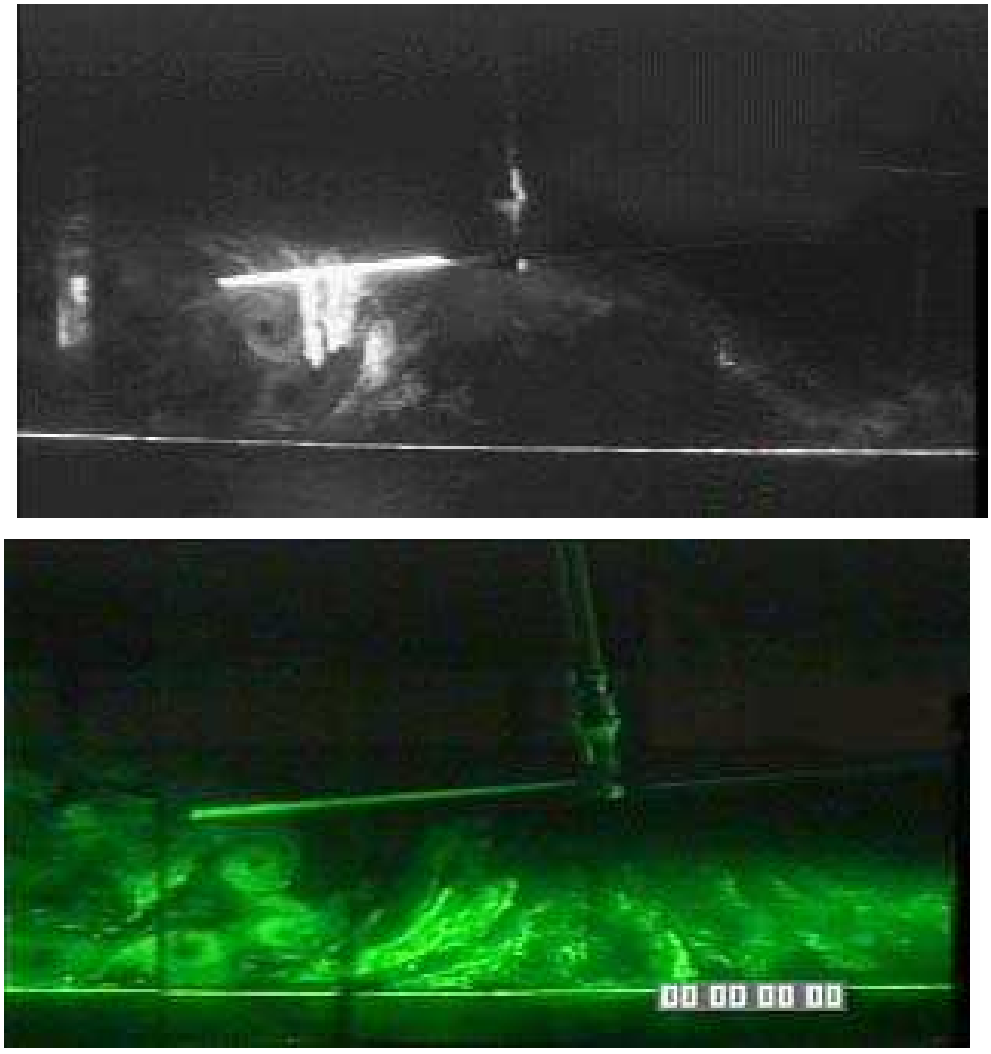

Figure 15: Recirculation of vortices at $\mu = 0.03$

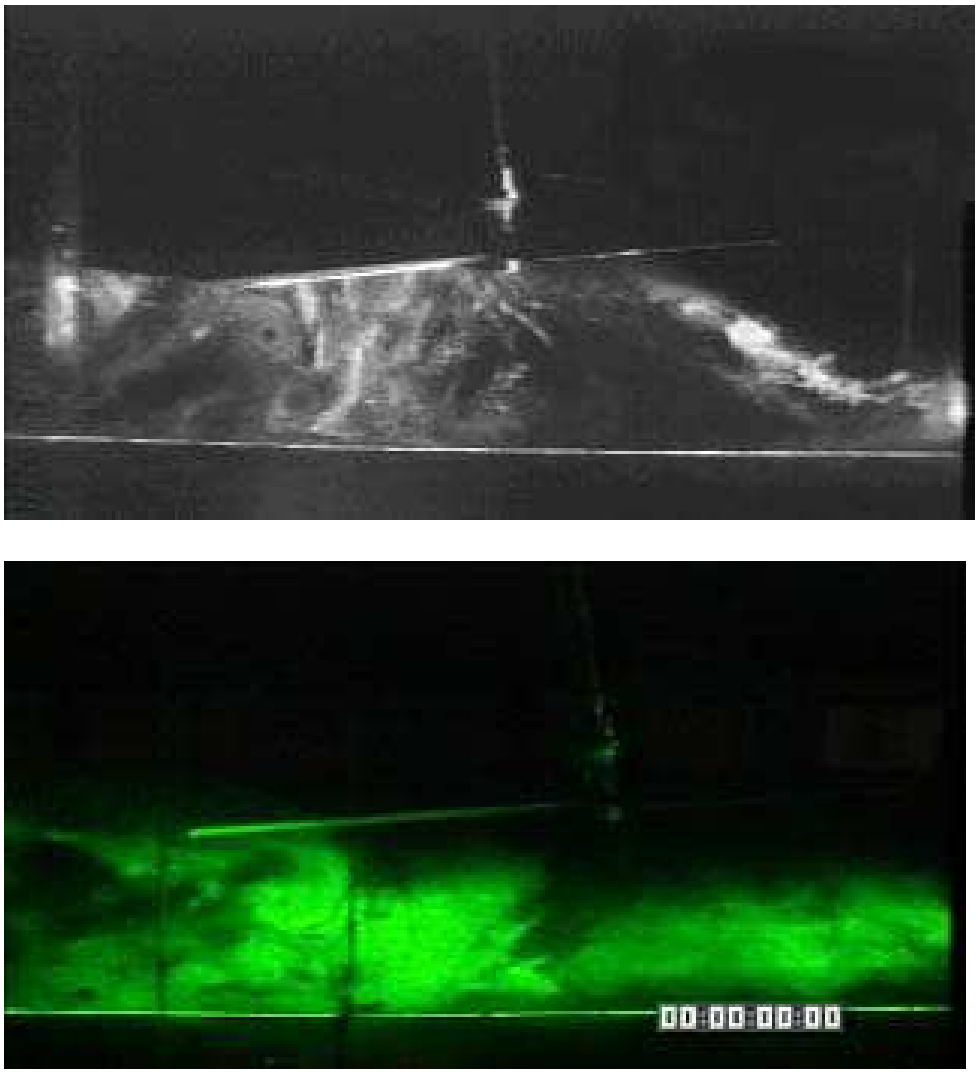

Figure 16: Flowfield at $\mu = 0.04$

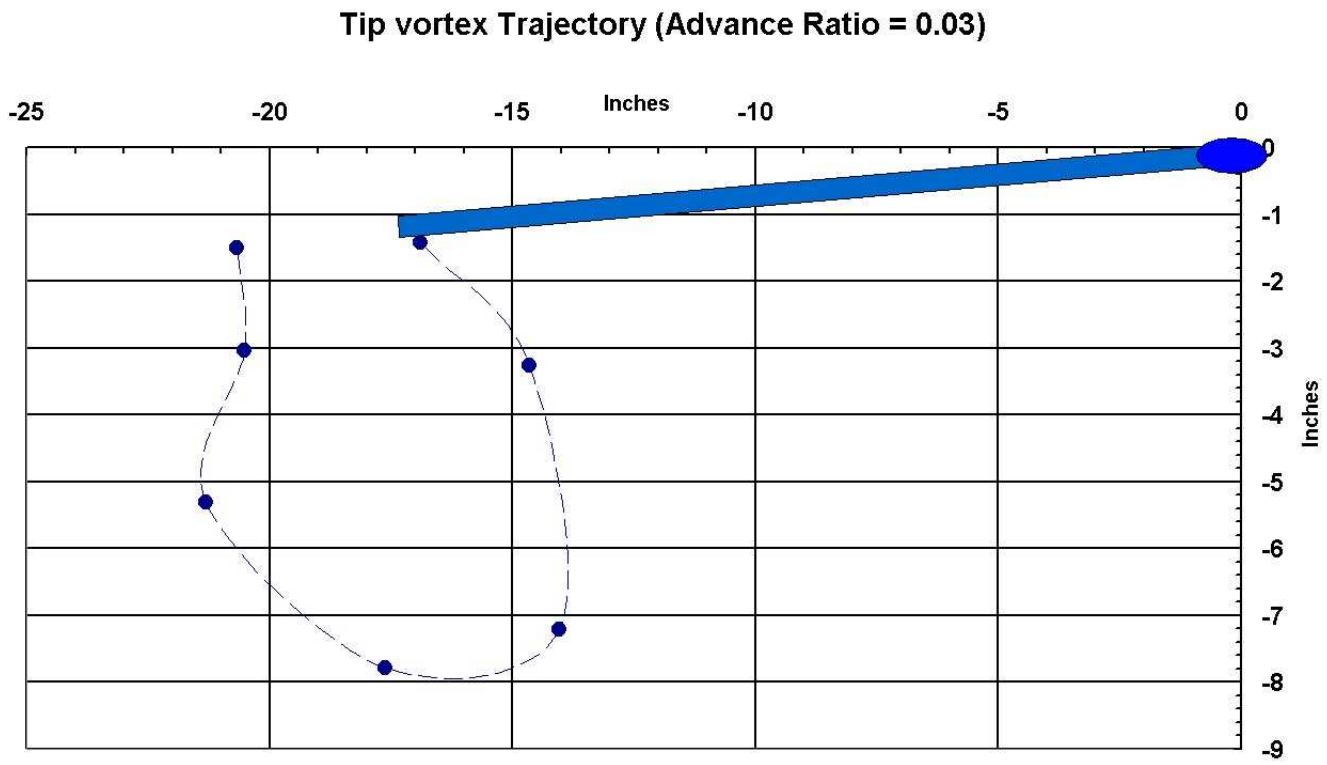

Figure 17: Trajectory of tip vortices at $\mu = 0.03$

3.2.2 Ground Vortex Regime

At $\mu = 0.06$ the ground vortex had clearly formed as can be seen from Fig. 18. The ground vortex appears as a large void that appears as a separated region under the rotor. At $\mu = 0.07$, the ground vortex become smaller (Fig. 19) and moves backward. This trend continues till the ground vortex is swept away from under the rotor at advance ratios greater than 1.25. This rearward movement of the ground vortex core is shown to scale in 20.

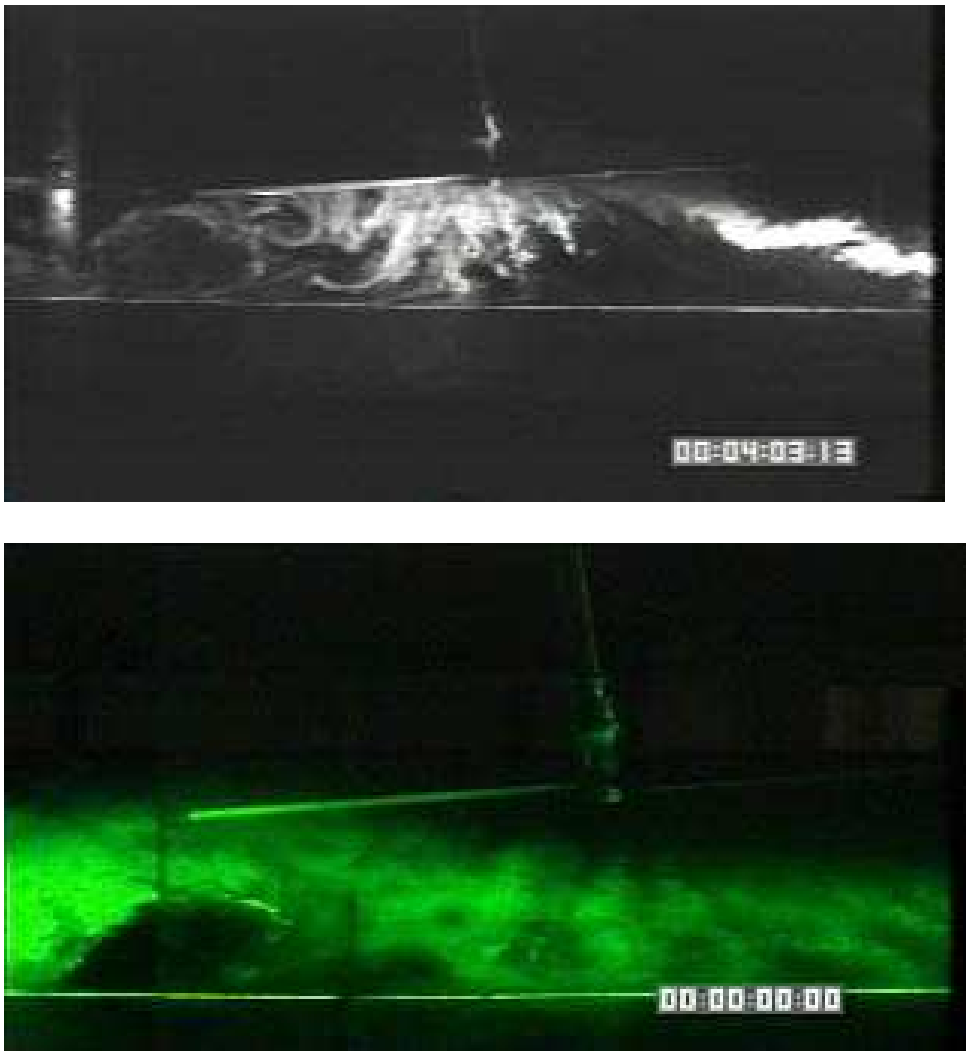

Figure 18: Ground Vortex at $\mu = 0.06$

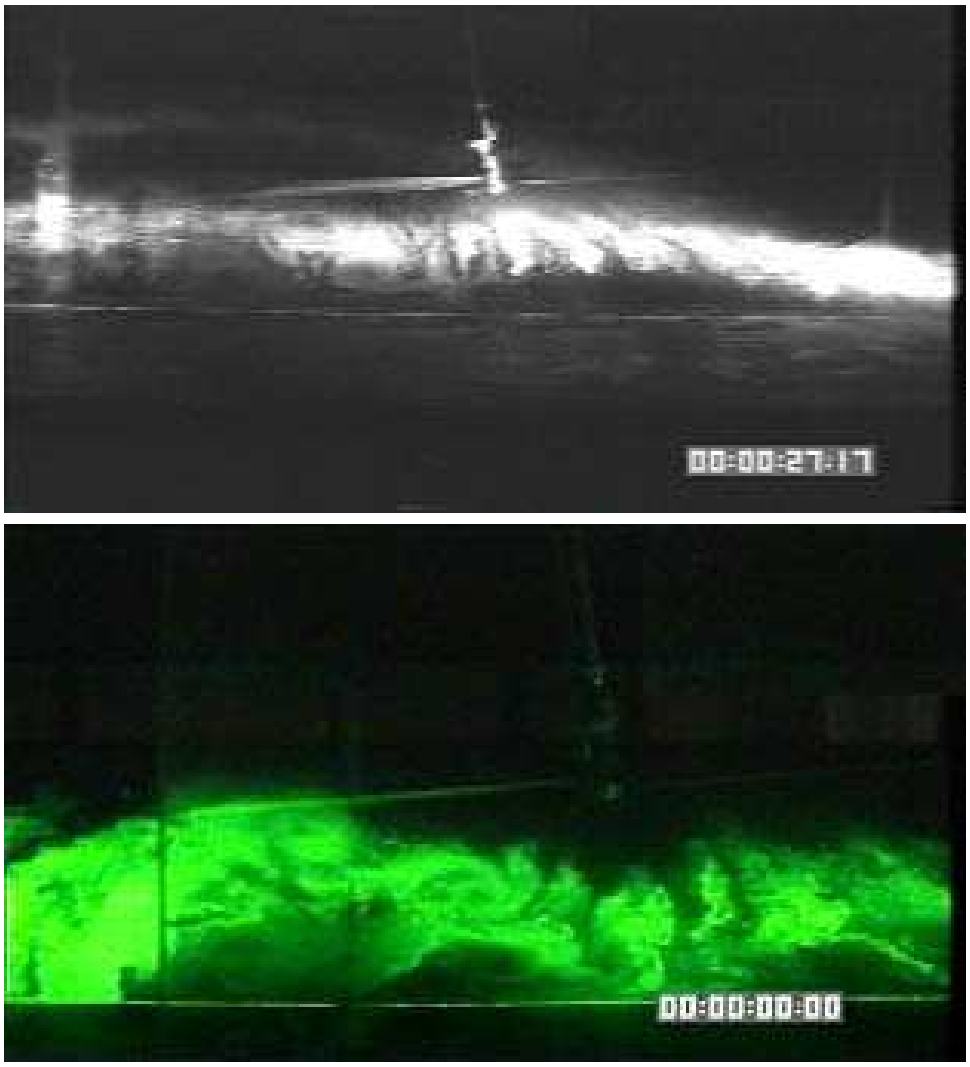

Figure 19: Ground Vortex at $\mu = 0.07$

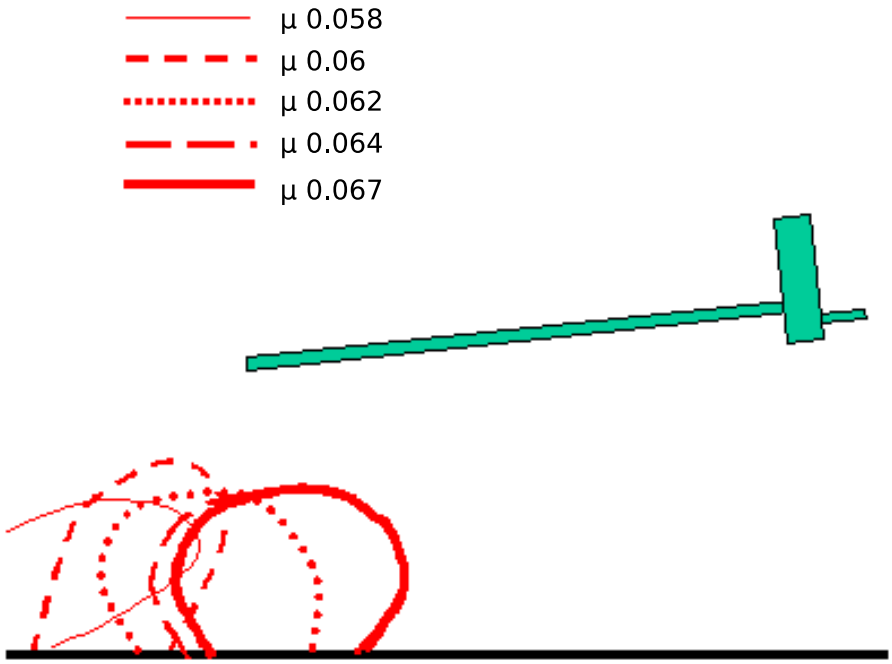

Figure 20: Position of Ground Vortex

3.3 Out of Ground Effect

The next step was to compare the flowfield out of ground effect to understand the differences between the two regimes of flight. The notable difference was the steadiness of the wake without the presence of the ground. The second difference was the trajectories of the tip vortices. The difference in the tip vortex trajectory at $\mu = 0.03$ can be seen in Fig. 21.

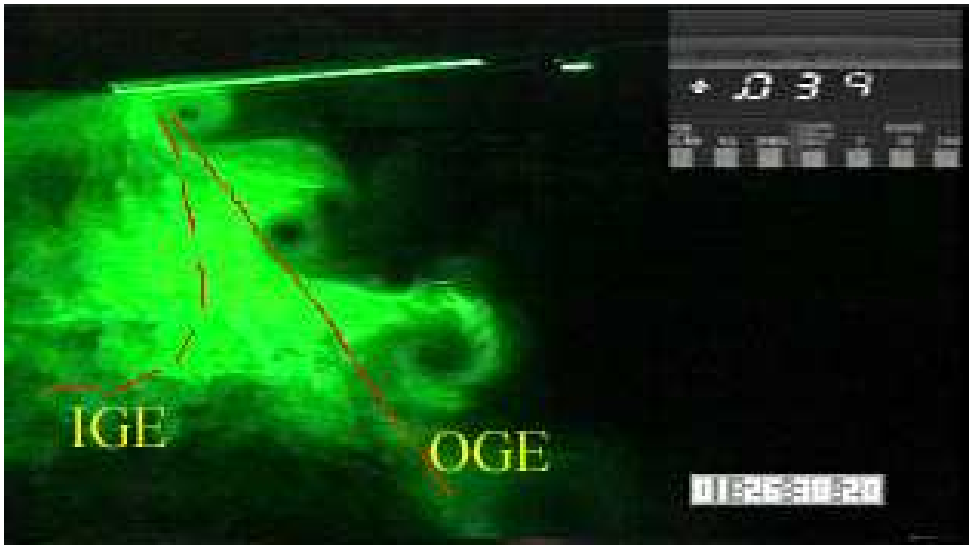

Figure 21: Difference in tip vortex trajectory- OGE vs IGE

Table 2: Tip Vortex Jitter OGE vs IGE

Jitter	IGE: X (in)	IGE: Z (in)	OGE: X (in)	OGE: Z (in)
Peak to peak	0.86	0.61	0.57	0.34
Standard Deviation	0.22	0.2	0.2	0.14
Measurement Uncertainty	0.18	0.18	0.11	0.11

3.3.1 Jitter of Tip Vortices

It can be seen that the presence of the ground induces the tip vortices to curve up, which causes their re-ingestion into the rotor disk. The flailing of the tip vortices that was noticed in the IGE case was not present in the OGE visualization. The steadiness of the flow at an advance ratio of $\mu = 0.04$ without the presence of the ground plane can be seen in Fig. 22. In order to quantify the extent of the steadiness, the vortices were tracked spatially from frame to frame, and the magnitude of the shift of the void center was measured and is shown in Table 2. The point to note is that though the standard deviation of jitter is almost the same in the OGE and IGE cases, there is a big difference in the peak to peak jitter between IGE and OGE. This implies that there is a long time scale jitter present in the IGE case. This can be linked to the recirculation of the vortices into the rotor disk.

3.3.2 Summary

Two distinct flow regimes were seen for a rotor flying at low advance ratios in ground effect. Recirculation of the rotor wake occurs at lower advance ratios and formation of a ground vortex occurred above an advance ratio ≈ 0.058. The ground vortex moves further downstream and decreases in size as the advance ratio increases. The trajectory of the tip vortices was tracked and indicates a re-ingestion frequency of 9 Hz for this test condition. The jitter of the tip vortices were quantified and it implied a disturbance of the order of every 0.2 secs of the vortex position in the IGE case.

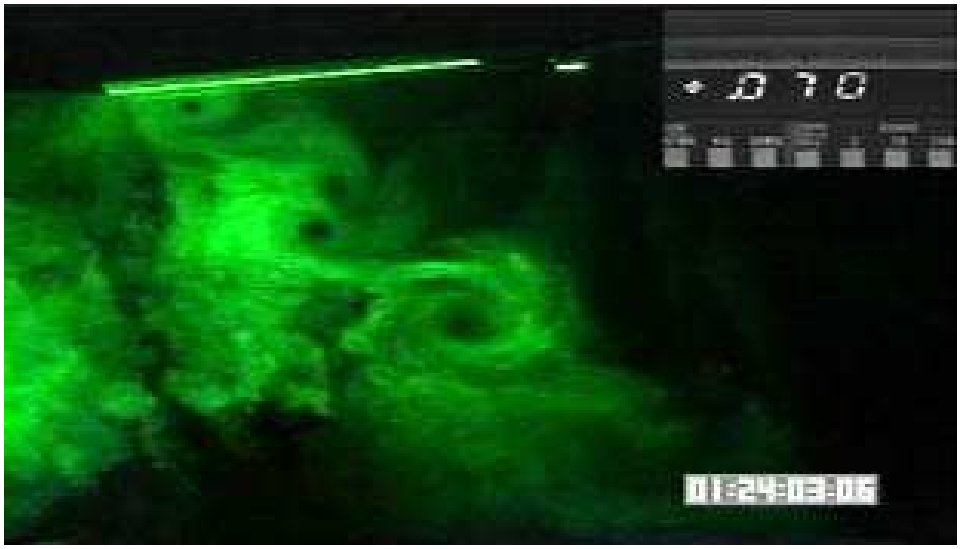

Figure 22: Steady tip vortex trajectory OGE $\mu = 0.04$

CHAPTER IV

HOTWIRE MEASUREMENTS

4.1 Objectives

After the flow visualization experiments, it was necessary to have a more quantitative measure of the unsteadiness in the flowfield around the rotor in ground effect. The Hotwire measurements would help in obtaining quantitative data concerned with flow unsteadiness with the ground plane, which would then be compared to the OGE case to understand the differences.

4.2 Experimental Setup

Time histories of velocity and frequency spectra were obtained using hot-wire probes (TSI 120120) in the flow field. The data were recorded on a personal computer through a Labview PCI board. The test cases were the same as was done for flow visualization. The hot-wire measurement setup with the ground plane is shown in Fig. 23. Hotwire measurements were done both at the ground plane at a height of 1" above the ground plane and also in the inflow region, and the expected recirculation region. The location of the hotwire measurements close to the ground is shown in Fig. 24. The barocel in the Wind Tunnel was first calibrated using air pressure balanced by precision weights. The hotwires were then calibrated in the Wind Tunnel with respect to the barocel readings. The errors measured in repeated steady validation runs was less than 1% of the measured value. Hotwire measurements only give an estimate of the magnitude of the velocity and not its components. However, hotwires are very useful for measuring fluctuations in velocity, which was the aim of the experiment.

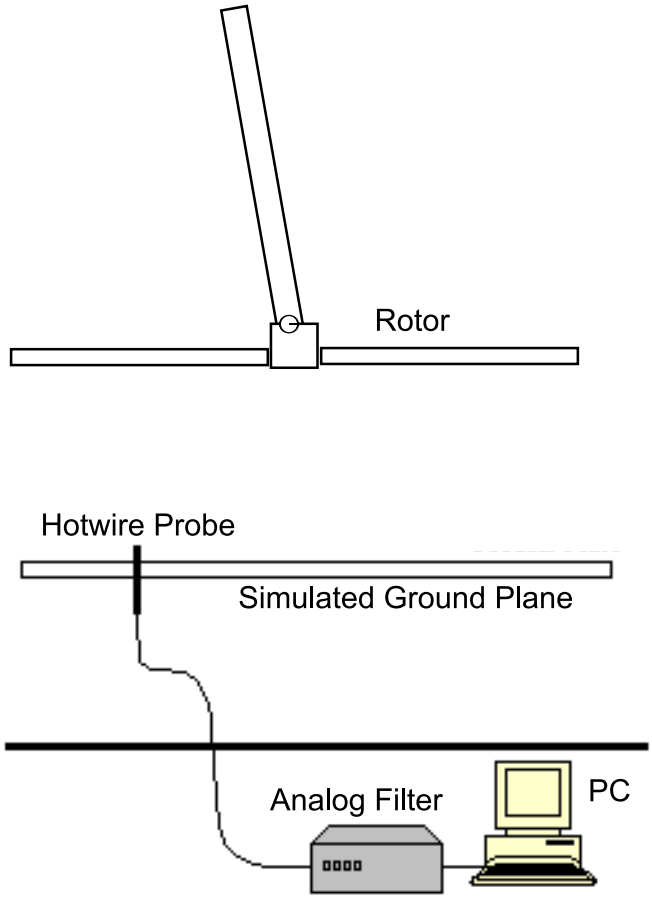

Figure 23: Hotwire Measurement Setup in the Harper Wind Tunnel

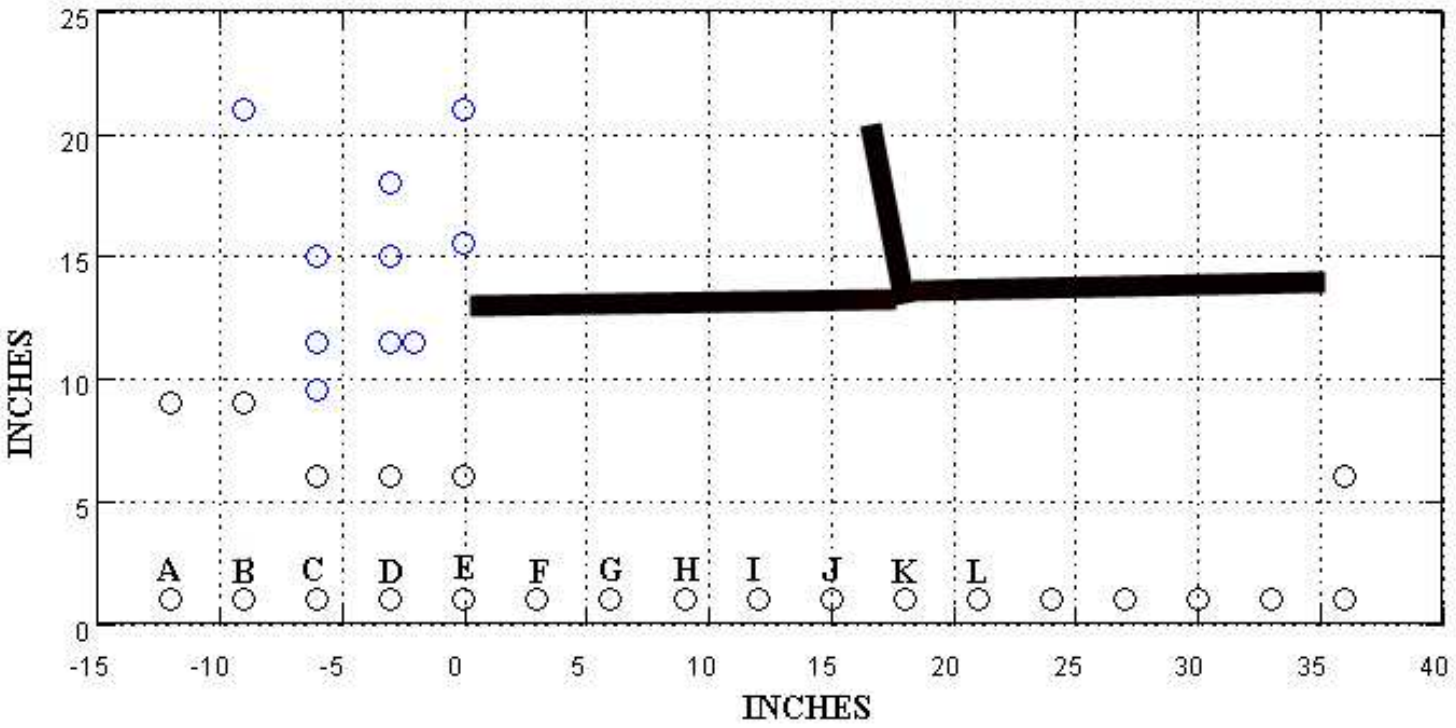

Figure 24: Hotwire Measurement Locations close to the ground

4.3 Results and Discussion

4.3.1 Inflow Velocities

The most notable result was the difference in the fluctuations in the inflow velocities obtained from the hotwire measurements. As was expected, the inflow magnitude was lower for the IGE case. However, the magnitude of fluctuations was negligible in the OGE case, while it was about 5 to 10% in the IGE case, and is shown in Fig. 25. The upper and lower bounds are marked in red and green respectively, and represent twice the standard deviation. Also it has to be noted that the IGE case appears to have spikes that seem to re-occur approximately at one second intervals. This is the effect of the recirculation of the tip vortices. To get a better idea of the frequency of these fluctuations, a Fourier analysis was done to the velocity time trace. The results and the measurement point are shown in Fig.26. It can be seen that the 2 per rev component dominates the flow, out of ground effect. However, with the ground plane, the spectrum is dominated by low frequency components. The peak frequency IGE at an advance ratio of 0.04 is 1.1 Hz and this indicates that there is a long time scale disturbance in the inflow velocity.

4.3.2 Velocities near the Ground Vortex

4.3.2.1 Advance Ratio 0.05

The results of the hotwire measurements close to the ground vortex are plotted in Fig. 27. It can be seen that at point A, a velocity fluctuation at low frequency (1 to 2 Hz) occurs and appears to be related to the movement of the flow separation point ahead of the nascent ground vortex. This correlates with the flow visualization results at $\mu = 0.05$ where the flow appeared to switch between recirculation and the preliminary stage of formation of a ground vortex. At both points C and E, the frequency of the velocity fluctuation became relatively broad-band (between 0 and 50Hz). The mean flow velocities at these points were higher than free stream speed, which is approximately 16.5fps at $\mu = 0.05$. At point G, a low frequency velocity fluctuation occurs. However, it is not similar to the large velocity separation-like change that occurs at point A, and appears to be induced by the passage of the tip vortex.

4.3.2.2 Advance Ratio 0.06

The hotwire measurements close to the ground vortex at advance ratio of 0.06 are plotted in Fig. 28. At point C, which was near the front edge of the ground vortex, the flow showed occasional large-amplitude fluctuations with a long time scale. This velocity fluctuation resembles the one seen at point (a) for $\mu = 0.05$ case, but is much less frequent. At point F, which was located in the ground vortex, the velocity fluctuates with broad band (between 0 and 50Hz) frequency. This velocity fluctuation resembles the one seen at point C and E for $\mu = 0.05$ case. The tip vortices directly impinge near point J, and the fluctuation is mainly high frequency, and is dominated by the 1 per rev and 2 per rev components.

4.3.2.3 Advance Ratio 0.07

The hotwire measurements close to the ground vortex at advance ratio of 0.07 are plotted in Fig. 29. At point E, a low frequency velocity fluctuation occurs, but the amplitude of the largest spikes is less than half of the corresponding values at C for the $\mu = 0.06$ case. The fluctuating flow separation that appears at lower advance ratios does not appear above an advance ratio of 0.07. The regions of high frequency fluctuations have moved downstream as was expected from the flow visualization analysis.

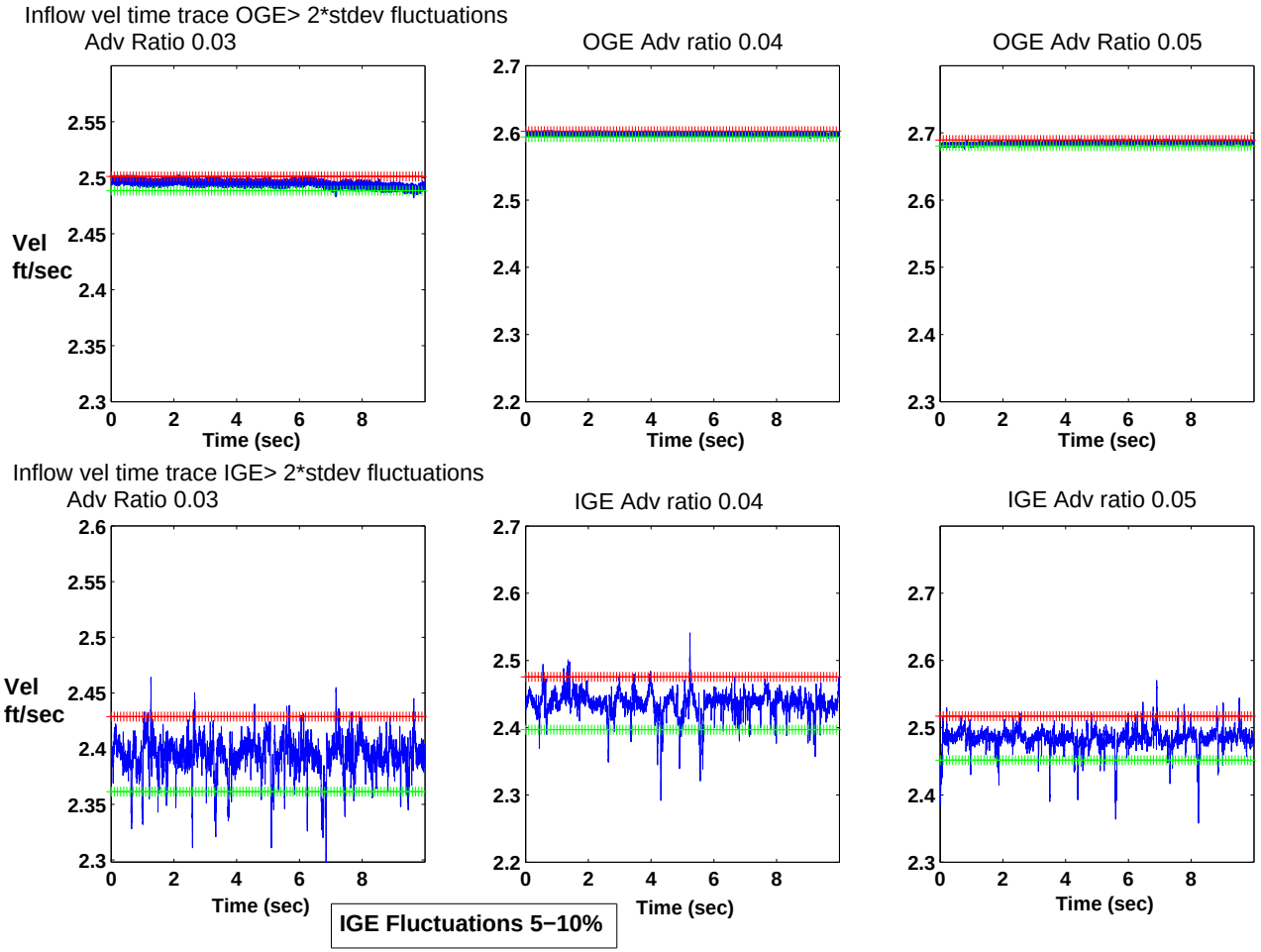

Figure 25: Comparison of Inflow Velocities: IGE vs OGE

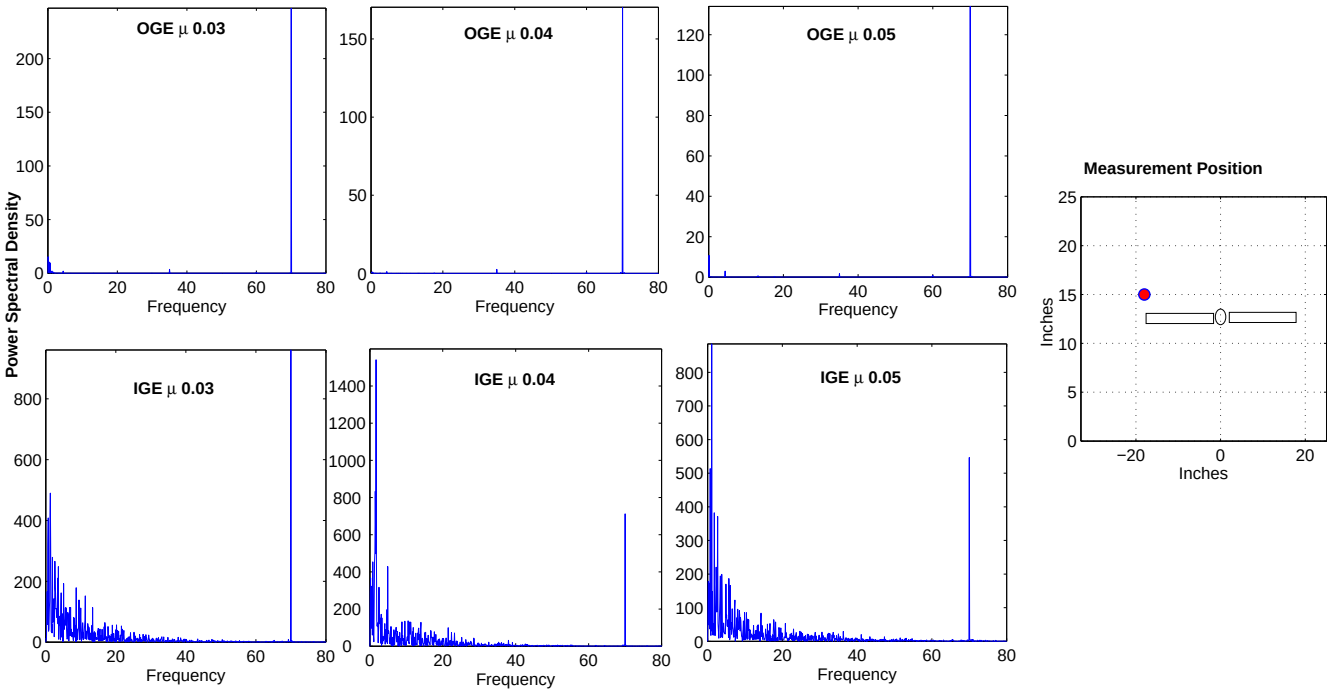

Figure 26: Measurement Position and Inflow spectra

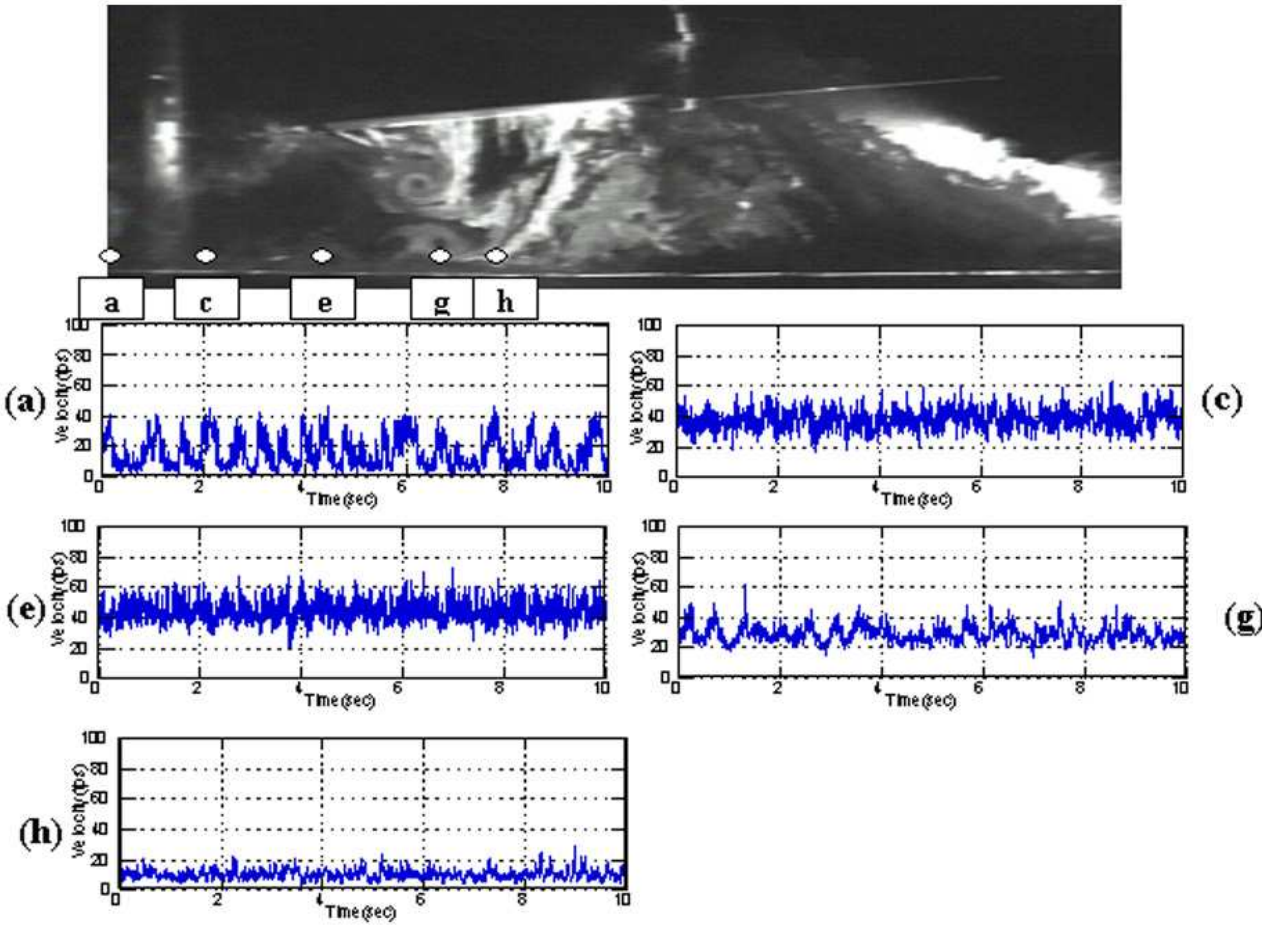

Figure 27: Hotwire Measurements $\mu = 0.05$

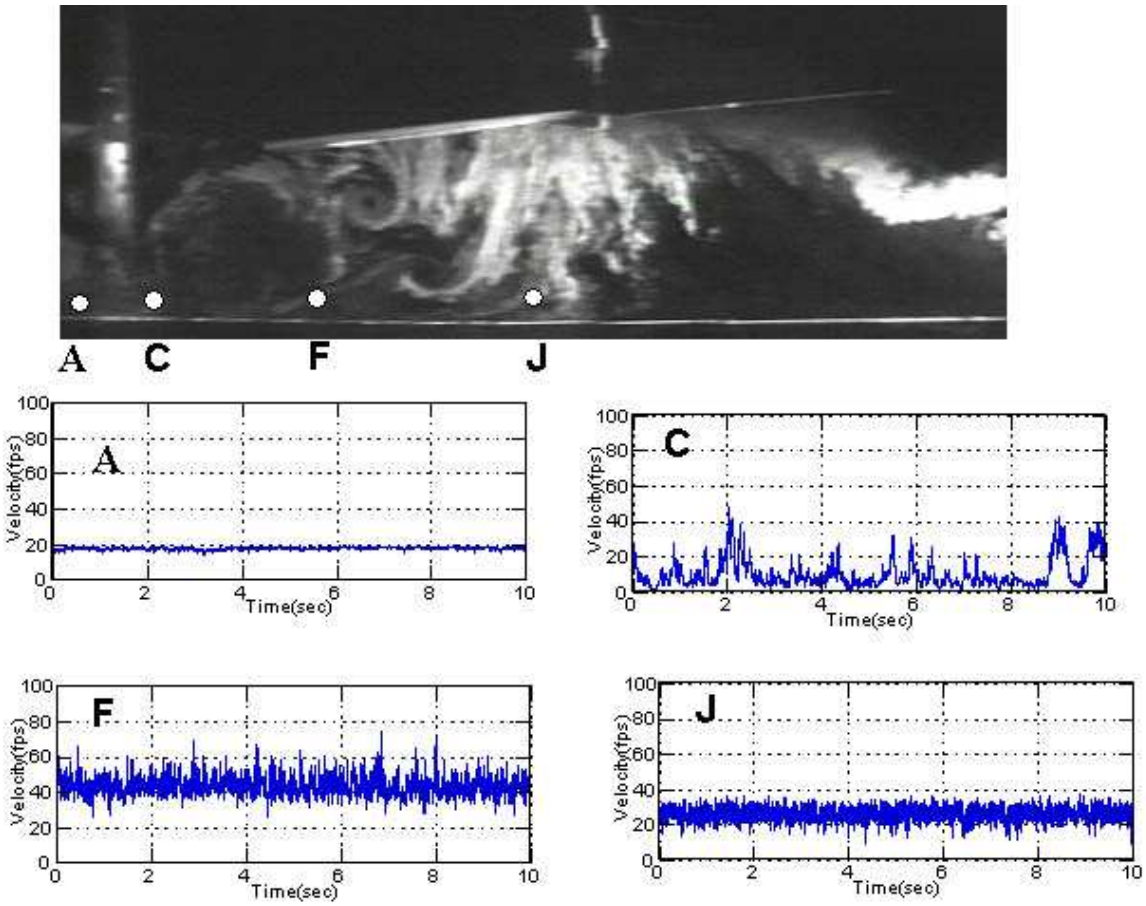

Figure 28: Hotwire Measurements $\mu = 0.06$

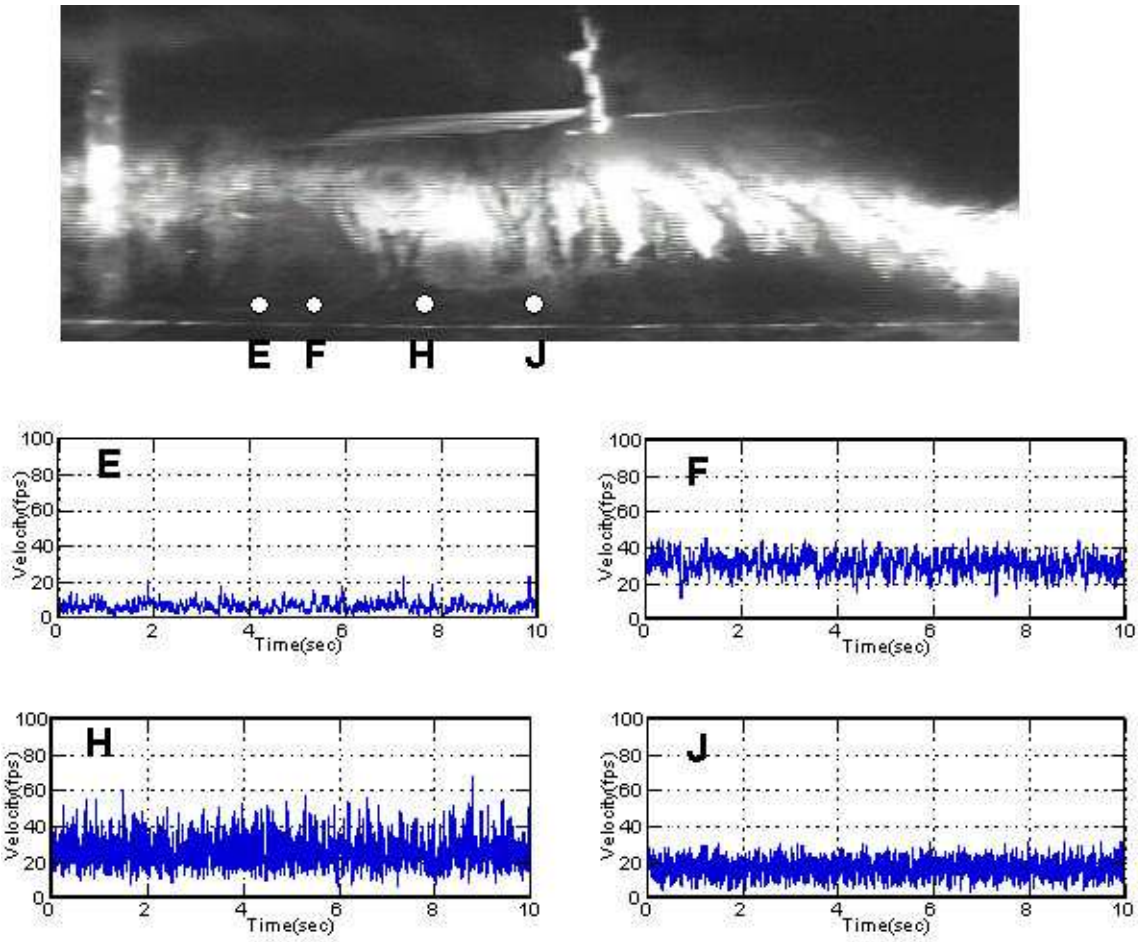

Figure 29: Hotwire Measurements $\mu = 0.07$

4.3.3 Frequency Analysis of the Wake Structure

Frequency analysis of the hotwire measurements provided interesting insights into the flow structure around a rotor in ground effect. The dominant frequencies in the hotwire measurements around the rotor at an advance ratio of 0.03 are shown in Fig. 30. The peak frequency at each location is displayed at various locations around the rotor. The X and Y axes are shown in inches, with the zero position of the X axis being the rotor hub center, and the zero position of the Y axis being the ground. This plot is juxtaposed with the flow visualization snapshot at that advance ratio to help correlate the frequency distribution with the flow structure.

It can be seen that this is the beginning of the recirculation regime and the path of the vortices is marked in the flow visualization picture. In the area where vortices impinge on the ground, the dominant frequency is the 2 per rev component. Behind this region is the dead zone in the middle of the wake being turned outward by the presence of the ground plane. The other interesting point is the presence of low frequency components above the inflow plane. It can be seen that the dominant frequency is of the order of 1 Hz, implying the presence of long time scale fluctuation in the recirculation regime. It should be noted that this low frequency component is stronger than even the blade passage frequency. It will be shown later that this low frequency component goes away once the advance ratio increases above 0.06 and the rotor transitions into the ground vortex regime.

The frequency distribution at an advance ratio of 0.04 is shown in Fig. 31. The wake structure is quite similar to that seen at an advance ratio of 0.03. The 2 per rev component can be seen at the path of the vortices and the low frequency component can be seen above the inflow plane. The frequency distribution at an advance ratio of 0.05 is shown in Fig. 32. It can be seen that this is the regime where features of both the recirculation and the ground vortex regimes are present. A nascent ground vortex can be seen in the flow visualization and its effect can be seen in peak frequency distribution. The low frequency peaks can be seen above the inflow plane. The ground vortex has formed at an advance ratio of 0.06 and can be seen in Fig. 33. By now the tip vortices are being convected downstream of the ground vortex and a strong 1 per rev component is seen behind the ground vortex. The

effect of recirculation above the inflow plane has now reduced, and a 2 per rev component starts dominating the inflow region. The ground vortex regime is fully established by an advance ratio of 0.07 and this can be seen in Fig. 34. It should be noted that now the inflow region is completely free of low frequency peak frequencies, and is dominated by the 2 per rev component. The ground vortex and the area behind it can be correlated with the peak frequency distribution.

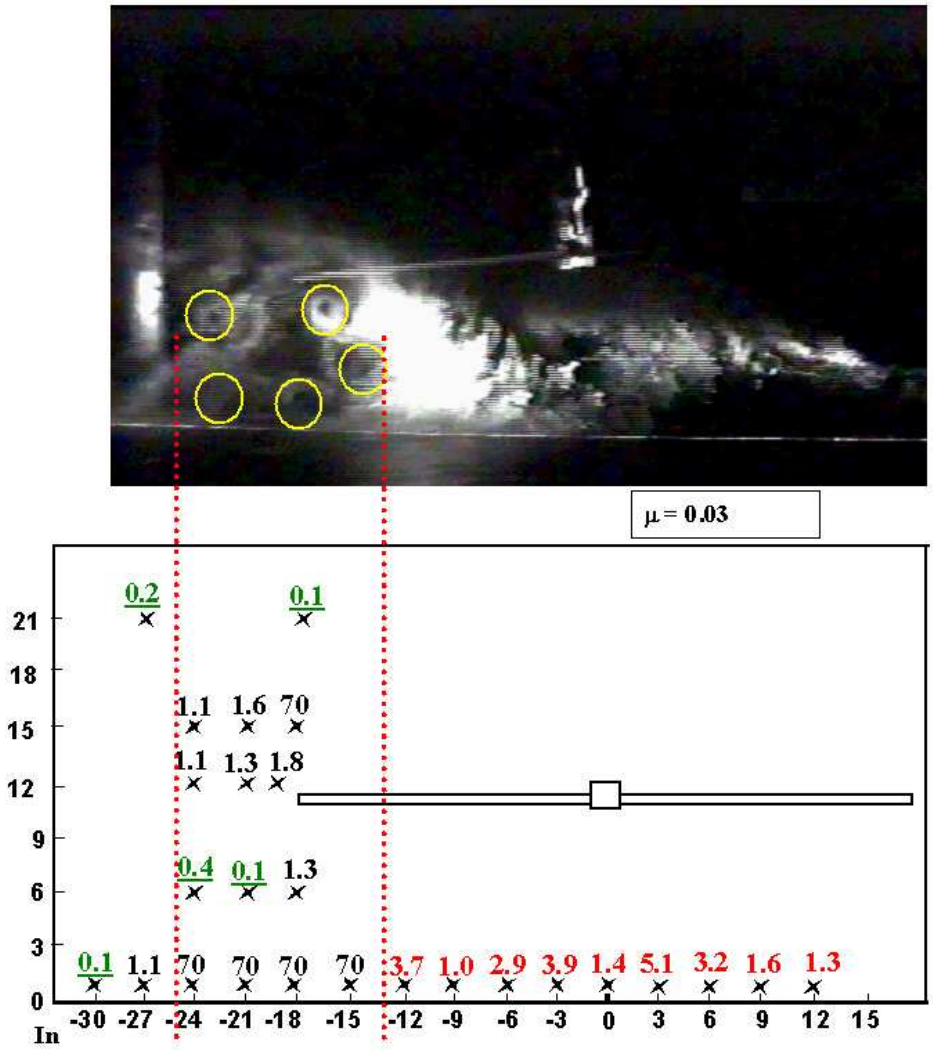

Figure 30: Hotwire Measurement Peak Frequencies (Hz) $\mu = 0.03$

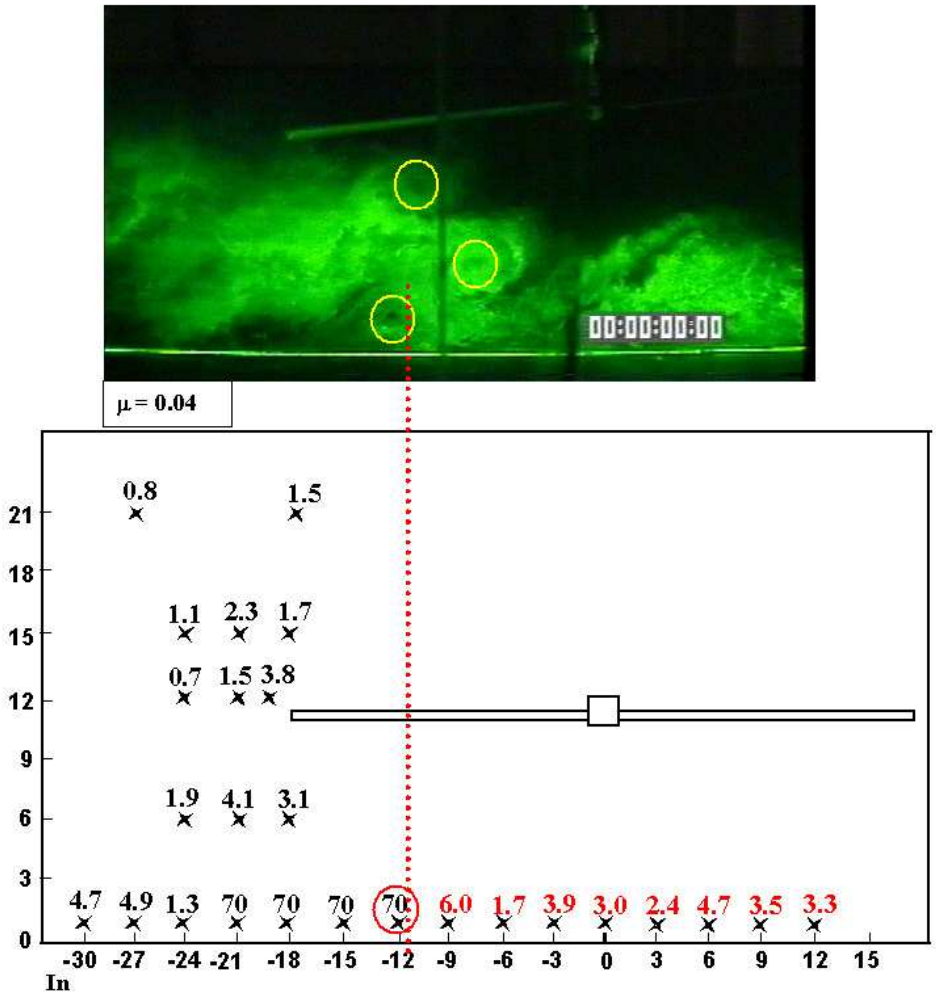

Figure 31: Hotwire Measurement Peak Frequencies (Hz) $\mu = 0.04$

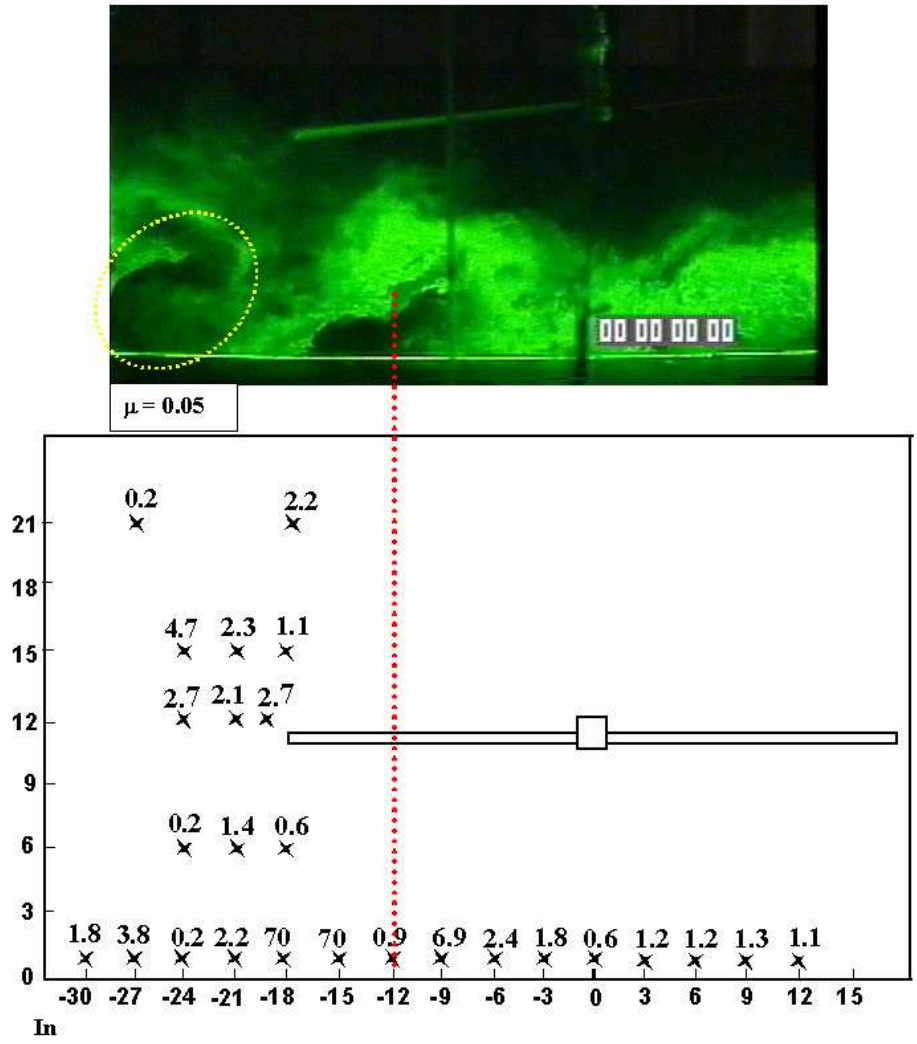

Figure 32: Hotwire Measurement Peak Frequencies (Hz) $\mu = 0.05$

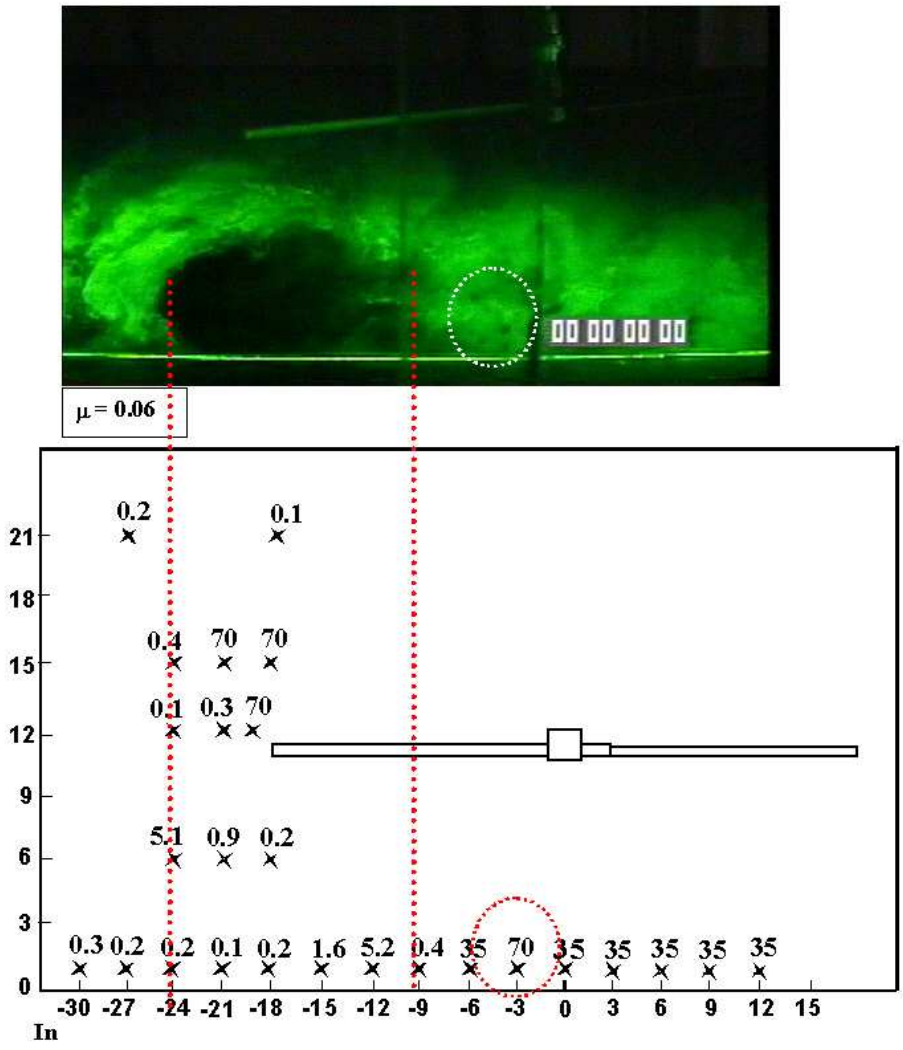

Figure 33: Hotwire Measurement Peak Frequencies (Hz) $\mu = 0.06$

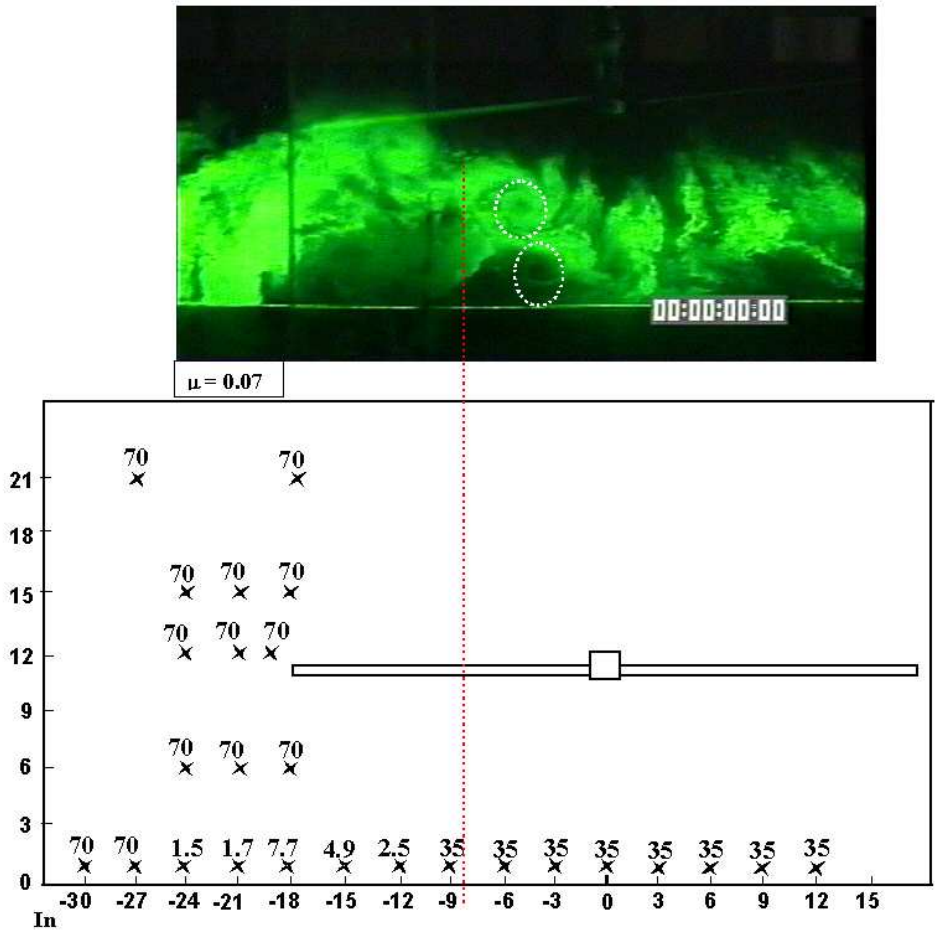

Figure 34: Hotwire Measurement Peak Frequencies (Hz) $\mu = 0.07$

4.4 Analysis of Recirculation Frequency Fluctuation at the Upwind Tip of the Rotor Disk

The frequency fluctuations of the inflow at the upwind tip of the rotor disk were further investigated. A series of long time hotwire measurements was done at the upwind tip of the rotor disk and the peak frequency of all the measurements was averaged. It was found that this average of the dominant fluctuation frequency at this location was 1.85 Hz for an advance ratio of 0.04 and 2.60 Hz for an advance ratio of 0.05. When advance ratio was $\geq$ 0.06, the dominant fluctuation frequency was the blade passage frequency, which correlated with the flow visualization observations that showed that the recirculation changed over to a ground vortex at an advance ratio of about 0.057. This also showed that the energy in the recirculation fluctuations was stronger than that in the blade passage disturbance at the upwind tip of the rotor disk when advance ratio $\leq$ 0.05.

When these fluctuation frequencies were compared with the parameters of the experimental set-up, some interesting relationships were found. First, the λ (defined as inflow ratio. In forward flight, the definition of λ is shown in Equation 3, where U_∞ is the forward velocity of the helicopter, α is the rotor disk angle of attack, Ω is the angular velocity of the rotor, v_i is the induced velocity of the rotor and R is the radius of the rotor) of the rotor was calculated.

$$\lambda = \frac{U_\infty \sin\alpha}{\Omega R} + \frac{v_i}{\Omega R} \tag{3}$$

To calculate λ the Momentum theory derivation was used [50], where μ is the advance ratio and C_T is the Coefficient of thrust. Since

$$\mu = U_\infty \cos\alpha/(\Omega R); \tag{4}$$

$$\lambda_i = \lambda_h/(2\sqrt{\mu^2+\lambda^2} \qquad And \tag{5}$$

$$\lambda_h = \sqrt{\frac{C_T}{2}} \tag{6}$$

λ from momentum theory is given by Equation 7.

$$\lambda = \mu\tan\alpha + \frac{C_T}{2\sqrt{\mu^2+\lambda^2}} \tag{7}$$

For calculating λ at $\mu = 0.04$ and 0.05, the measurements of C_T which were done by Brand in 1989 [5] were used. These were measurements of the rotor thrust without a ground plane, carried out at $\mu = 0.0$, 0.075, 0.10, 0.15, and 0.20. The C_T values at $\mu = 0.04$ and 0.05 were interpolated using a polynomial fit, as shown in Fig. 35.

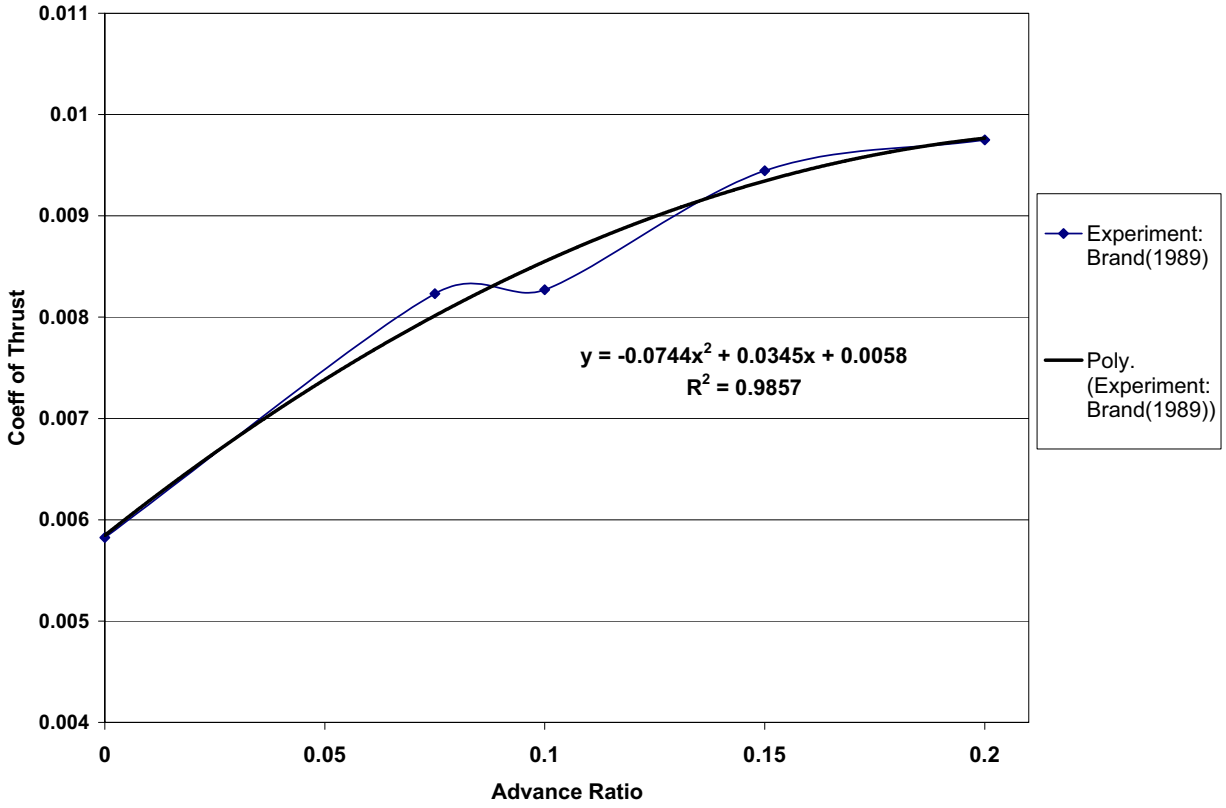

Figure 35: C_T Measurements and Polynomial Interpolation

Table 3: Frequency of Recirculation Fluctuation

Advance Ratio	Measured Frequency (Hz)	Calculated Frequency (Hz)	Error %
0.04	1.85	1.77	-4.18%
0.05	2.60	2.68	3.24%

Using these interpolated values, λ values of 0.189 at $\mu = 0.04$ and 0.229 at $\mu = 0.05$ were obtained. It should also be noted that the forward velocity at $\mu = 0.04$ is 4.02 m/s and at $\mu = 0.05$ is 5.03 m/s, and the height of the rotor (h) above the ground is 0.429 m.

It was found that the frequency of recirculation fluctuation (F_RF) was very closely linked to these parameters and is shown in Equation. 8.

$$F_RF = \frac{\lambda U_\infty}{h} \tag{8}$$

The results are shown in Table 3 and matched the measured results very closely.

4.5 Summary

The low frequency fluctuations in the inflow plane ahead of the rotor occur at about 1 to 2 Hz and appear only during the recirculation regime. These oscillations stop above an advance ratio of 0.06. The rear of the vortex is dominated by the 1 per rev component, and has high amplitude, high frequency oscillations in it. Low frequency oscillations are seen near the ground ahead of the ground vortex and are caused due to the separation of the flow ahead of the ground vortex.

It was also seen that the fluctuation frequency seems to be a function of the rotor height, inflow ratio and forward velocity. The results of the calculated frequency of fluctuation closely matched the measured frequency. This should help in scaling the frequency of fluctuations to other rotors.

CHAPTER V

FUSELAGE FORCE MEASUREMENTS

5.1 Objectives and Selection of Fuselage Shape

The hotwire results have shown that unsteady effects of a rotorcraft flying in ground effect will play a significant role in the handling characteristics during low advance ratio flight or during transition to forward flight. The hotwire measurements highlighted the long time scale unsteady effects seen in the recirculation regime. The next step was to explore the quasi-steady effects of IGE rotorcraft flight.

The effect of fuselage shape on loads was investigated, since this is an oft-reported problem by pilots while flying close to the ground [64]. The helicopter fuselage shape is governed more by the requirement for reduced radar cross section rather than its aerodynamics characteristics. Pilots have observed that there is a significant effect of fuselage shape on helicopter handling, especially while flying close to the ground. This operator feedback was the primary motivation to explore this phenomenon. Such a study has not been carried out in the past, and this study is the first to look at the effect of fuselage shape on loads both in and out of ground effect.

Since the hub moments would affect the forces on the fuselage, the fuselage was decoupled from the hub. It was not practical to test an actual helicopter fuselage because the main point of interest was to understand the effect of fuselage shape in IGE flight without making it rotorcraft specific. At the same time, it was important to select fuselage shapes that were representative of the types of fuselage shapes being used in the industry. After conducting a survey of common helicopter fuselage shapes, two generic shapes were chosen for further investigation. The first was cylindrical with a circular cross-section and the second had flattened sides. These shapes are shown in Fig. 36. Henceforth, these two shapes will be referred to as circular cross-section fuselage and flattened fuselage respectively. It can be seen that the circular cross-sectional fuselage is representative of a class of rotorcraft

including the Alouette-III and BO-105, while the flattened fuselage is more typical of craft such as the Boeing AH-64 and the Sikorsky S-92. It was expected that these two generic shapes would help study the effects on a broad spectrum of fuselage shapes in the rotorcraft industry today.

5.2 Experimental Set-up

The experimental measurement of the fuselage loads was conducted in the John Harper 7′x9′ tunnel at Georgia Tech. The set-up for the experiment is shown in Fig. 37. The fuselage loads were measured with a 6-component load cell made by ATI Technologies. The load cell was calibrated using test weights and the error in the range of measurement was found to be less than 1% of the largest force measured. The fuselage was yawed using a stepper motor from -60° to +60° . The error estimate in the measurements is discussed later in this chapter.

The co-ordinate system of the forces on the fuselage is shown in Fig. 38. It is to be noted that all forces are non-dimensionalized by density, tip speed and circular cross-section fuselage planform area as shown in Equation 9.

$$C_F = \frac{F}{\rho A_F {V_{Tip}}^2} \tag{9}$$

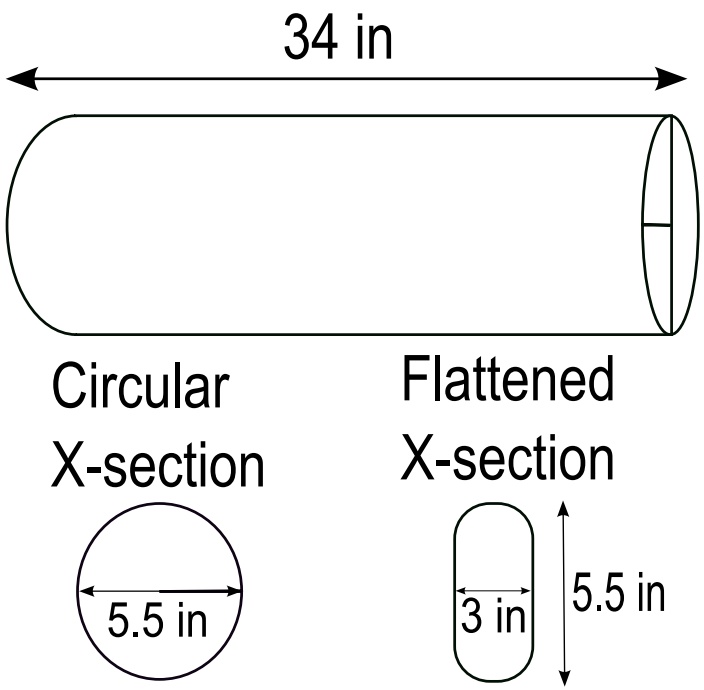

Figure 36: Test Fuselage Specifications

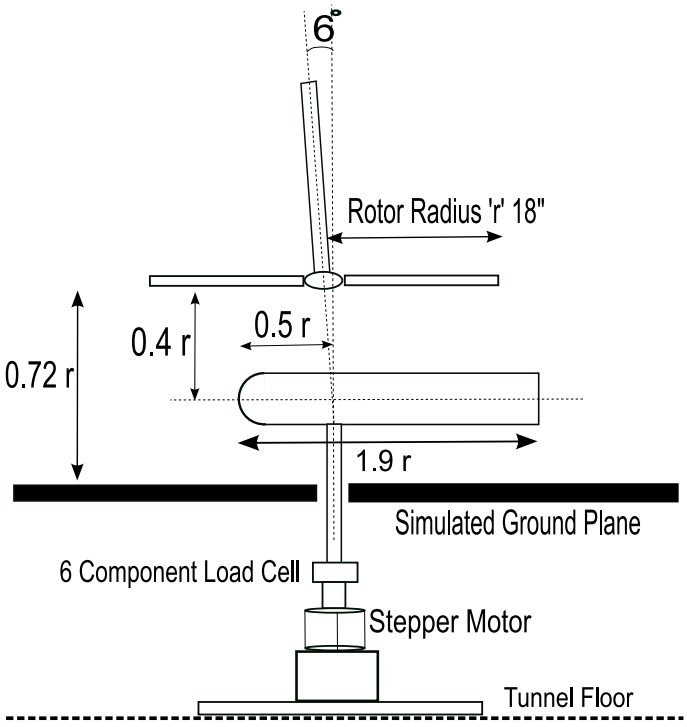

Figure 37: Fuselage Load Measurement Experimental Setup

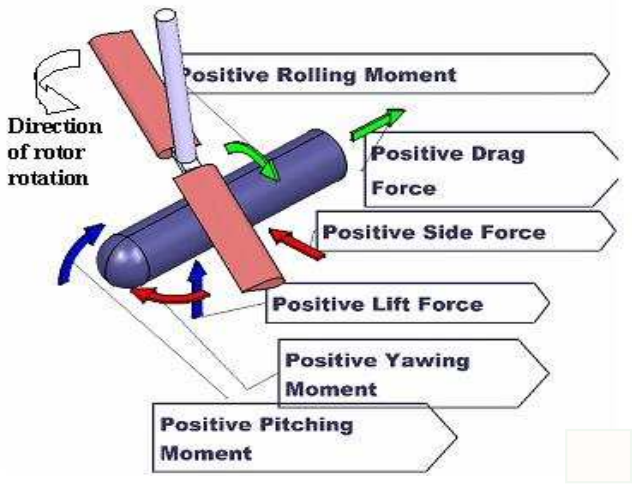

Figure 38: Fuselage Load Measurement Experimental Setup

5.3 Results and Discussion

5.3.1 Frequency Components of Fuselage Load Measurements

The first step in the fuselage load measurements was to check the frequency components of the forces. This was to understand if the fluctuations seen in the inflow region were being felt on the fuselage. It was found that none of the force components displayed the low frequency fluctuations seen in the velocity in the inflow plane. The only components discernible on the loads were the 1 and 2 per rev components along with the natural frequency of the fuselage system. The natural frequency of the fuselage system was measured by providing an impulsive forcing function to the fuselage system. This was to be expected since the velocity fluctuations were only seen in the upstream part of the rotor disk, and any such fluctuation was expected to be negligible when integrated over the entire surface of the fuselage. This means that a constant advance ratio, the unsteady effect of the inflow was not very significant on the fuselage loads.

5.3.2 Circular Cross-section Fuselage Forces

The first set of tests that were conducted were for the circular cross-section fuselage. The forces on the fuselage were measured both in and out of ground effect from hover to an advance ratio of 0.1.

5.3.2.1 Circular Cross-section Fuselage Downforce

The measured downforce for the circular cross-section fuselage is shown in Fig. 39. Fig. 39 A shows the downforce for a circular cross-section fuselage out of ground effect, while Fig. 39 B shows the downforce for circular cross-section fuselage in ground effect. Fig. 39 C shows the downforce for a circular cross-section fuselage at 0° yaw both in and out of ground effect. The layout of the plots is explained below.

Figs. 39 A and B are comprehensive plots that shows the downforce at yaw angles between -60° and +60° from hover to an advance ratio of 0.09. Fig. 39 C extracts the information at 0° yaw that shows the downforce for a rotorcraft fuselage as it accelerates from hover to an advance ratio of 0.1. It shows the difference between the downforce on a

rotorcraft fuselage as it accelerates out of hover in and out of ground effect.

It can be seen from Figs. 39 A and B that the downforce distribution changes considerably in and out of ground effect. The downforce is much less IGE than OGE. This is to be expected because the inflow is cut down considerably IGE. The symmetric distribution seen OGE also breaks down IGE. Fig. 39 C shows the downforce at 0° yaw. It can be seen that the fuselage IGE actually encounters an upforce at hover due to the presence of the ground. The other interesting aspect IGE is the blip in downforce between advance ratio of 0.05 and 0.08. It can be seen by correlating this to flow visualization results that this occurs at the advance ratio where the ground vortex forms and moves under the fuselage.

5.3.2.2 Circular Cross-section Fuselage Side Force

The measured side force for the circular cross-section fuselage is shown in Fig. 40. Fig. 40 A shows the side force for a circular cross-section fuselage out of ground effect, while Fig. 40 B shows the side force for the circular cross-section fuselage in ground effect. Fig. 39 C shows the side force for a circular cross-section fuselage at 0° yaw both in and out of ground effect. Figs. 40 A and B are comprehensive plots that show the side force at yaw angles between -60° and +60° from hover to an advance ratio of 0.09. Fig. 40 C extracts the information at 0° yaw that shows the side force for a rotorcraft fuselage as it accelerates from hover to an advance ratio of 0.1. It shows the difference between the side force on a rotorcraft fuselage as it accelerates out of hover in and out of ground effect.

It can be seen from Figs. 40 A and B that the symmetric distribution of side force OGE breaks down IGE. It can also be seen that the magnitude of side force at higher yaw angles is much less IGE. Another interesting phenomenon is the sudden variation in side force between yaw angles +20° and +40° and is marked on Fig. 40 B with a red ellipse.

Figs. 40 C shows the side force on a circular section fuselage while accelerating from hover to an advance ratio of 0.09. It can be seen that behavior of the fuselage IGE and OGE differs drastically. While the side force at hover in and out of ground effect is almost the same, the trend changes significantly when the rotorcraft accelerates out of hover. The side force OGE immediately shifts to a negative value and remains almost unchanged till

an advance ratio of 0.07 and then reduces slightly up to an advance ratio of 0.09. This appears to be a function of the wake angle and the extent of the fuselage that is exposed to the wake. On the other hand, the fuselage side force IGE remains at about the hover value until about an advance ratio of 0.05 and then changes direction at an advance ratio of 0.07. It is to be noted that this coincides with the formation of the ground vortex under the fuselage. The IGE side force then approaches the OGE value at an advance ratio of 0.09.

The moment arm of the side force was calculated to find the point at which the side force acted. This was done by dividing the yawing moment by the side force obtained from the six component load cell. The plot is shown in Fig. 41. It can be seen that the change in direction of the side force IGE is accompanied by a rapid forward shift of the side force moment arm. This appears to indicate a loss of side force in the rear section of the fuselage due to the formation of the ground vortex and the separation associated with it.

5.3.2.3 Circular Cross-section Fuselage Drag Force

The measured drag force for the circular cross-section fuselage is shown in Fig. 42. Fig. 42 A shows the drag force for a circular cross-section fuselage out of ground effect, while Fig. 42 B shows the drag force for the circular cross-section fuselage in ground effect. Fig. 39 C shows the drag force for a circular cross-section fuselage at 0° yaw both in and out of ground effect. Figs. 42 A and B are comprehensive plots that shows the drag force at yaw angles between -60° and +60° from hover to an advance ratio of 0.09. Fig. 42 C extracts the information at 0° yaw that shows the drag force for a rotorcraft fuselage as it accelerate from hover to an advance ratio of 0.1.

It can be seen from Fig. 42 C that the fuselage drag increases steadily OGE as the rotorcraft accelerates from hover. However, the behavior is quite different IGE. The drag force remains almost constant until an advance ratio of 0.05 and then sharply decreases until an advance ratio of 0.07, and then increases gradually again. It is interesting to note that the sudden decrease of fuselage drag occurs with the formation of the ground vortex under the fuselage. If we looked at this effect alone, it could be destabilizing for the pilot

while hovering in the presence of a headwind. The combination of thrust and tip path angle necessary for a steady hover with a headwind equivalent to advance ratio of 0.05, would be destabilizing if the wind speed increased to advance ratio of 0.07. Not only does the drag on the fuselage decrease, but the upward lift on the fuselage also increases as shown in Fig. 39 C. Therefore, neglecting all other factors such as hub moments and tail rotor effectiveness, this scenario would lead to a sudden feeling of forward acceleration and upward lift to the pilot of the rotorcraft. But this feeling would be temporary, since the effects of decreasing drag and increasing lift on the fuselage diminish, either in the case of advance ratio increasing above 0.07 or decreasing below 0.05. Thus, the situation feeds into a scenario where the pilot is likely to over compensate while flying close to the ground.

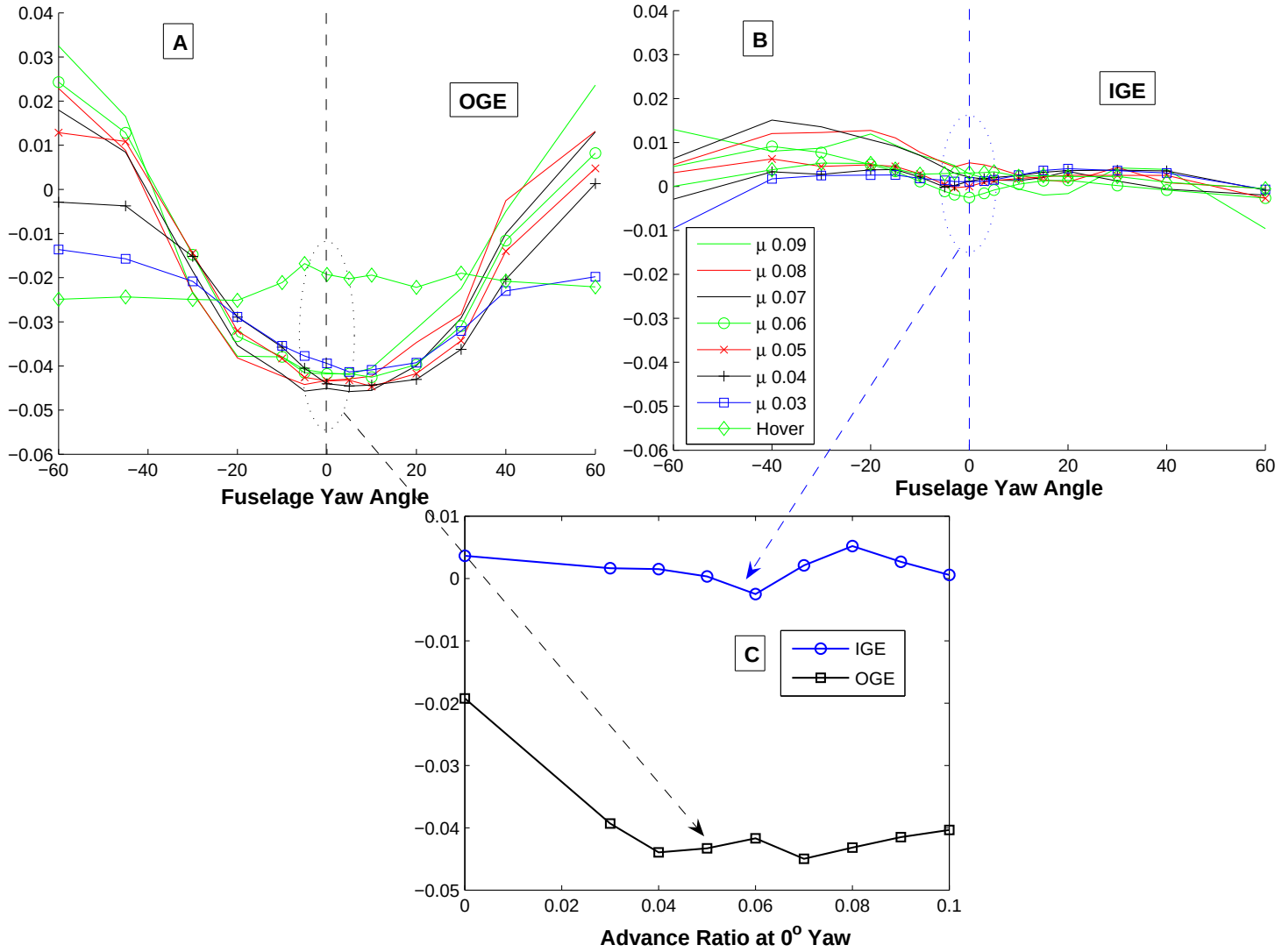

Figure 39: Circular Cross-section Fuselage Downforce. Non-dimensionalized by density, tip speed and circular cross-section fuselage planform area.

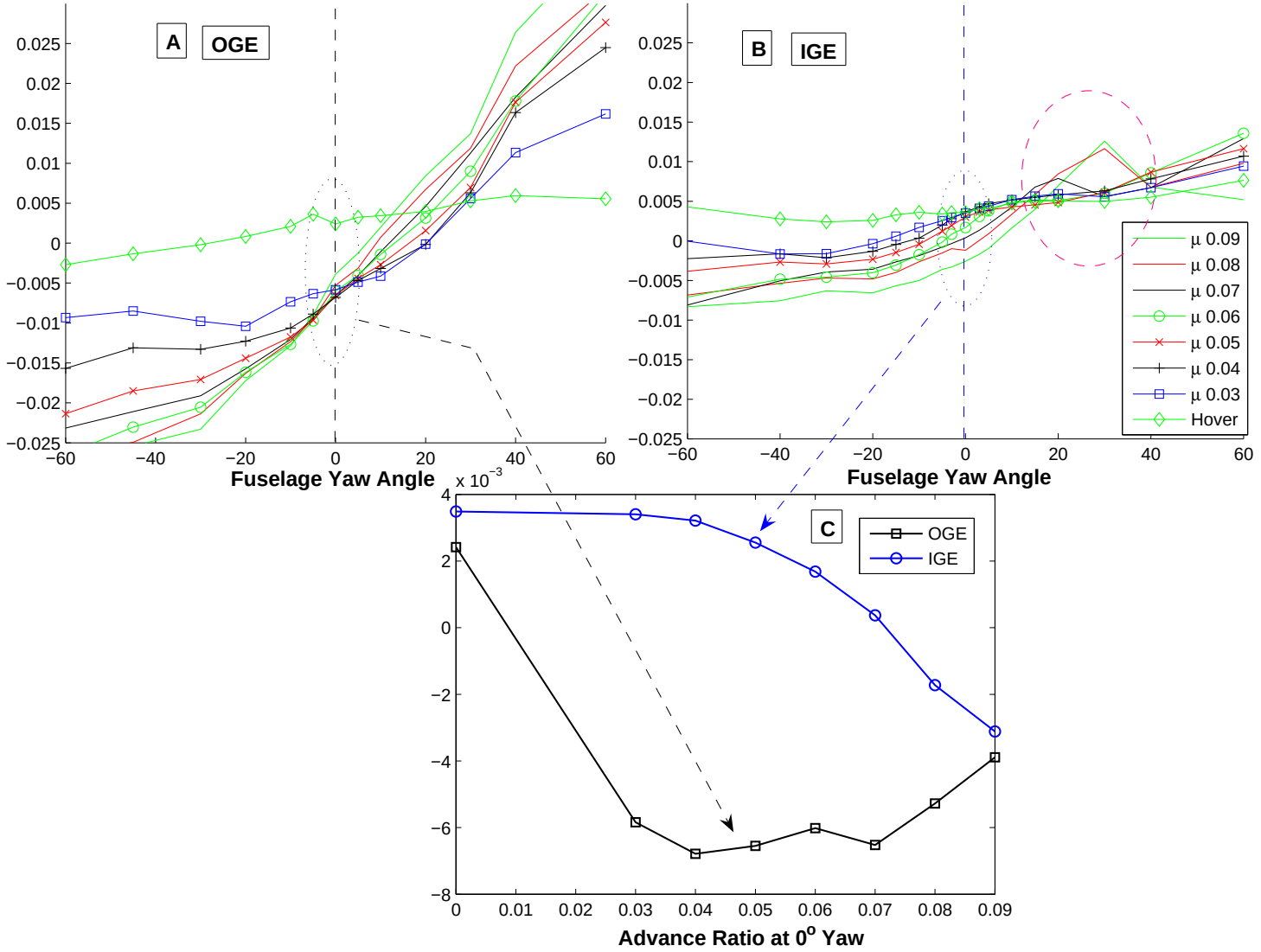

Figure 40: Circular Cross-section Fuselage Side force. Non-dimensionalized by density, tip speed and circular cross-section fuselage planform area.

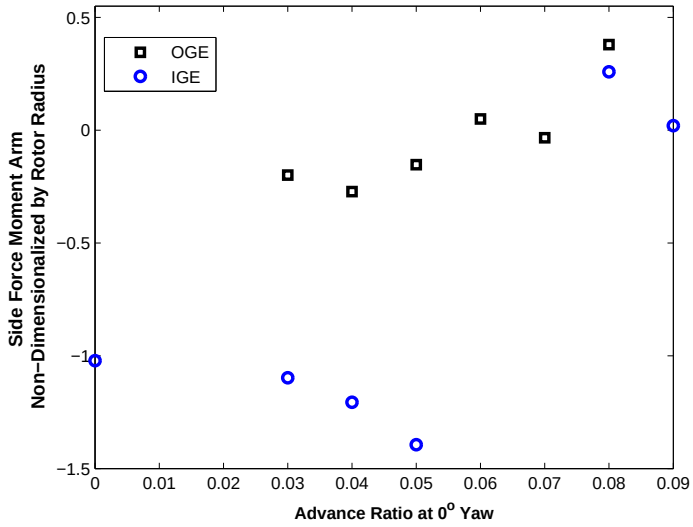

Figure 41: Side Force Center of Pressure

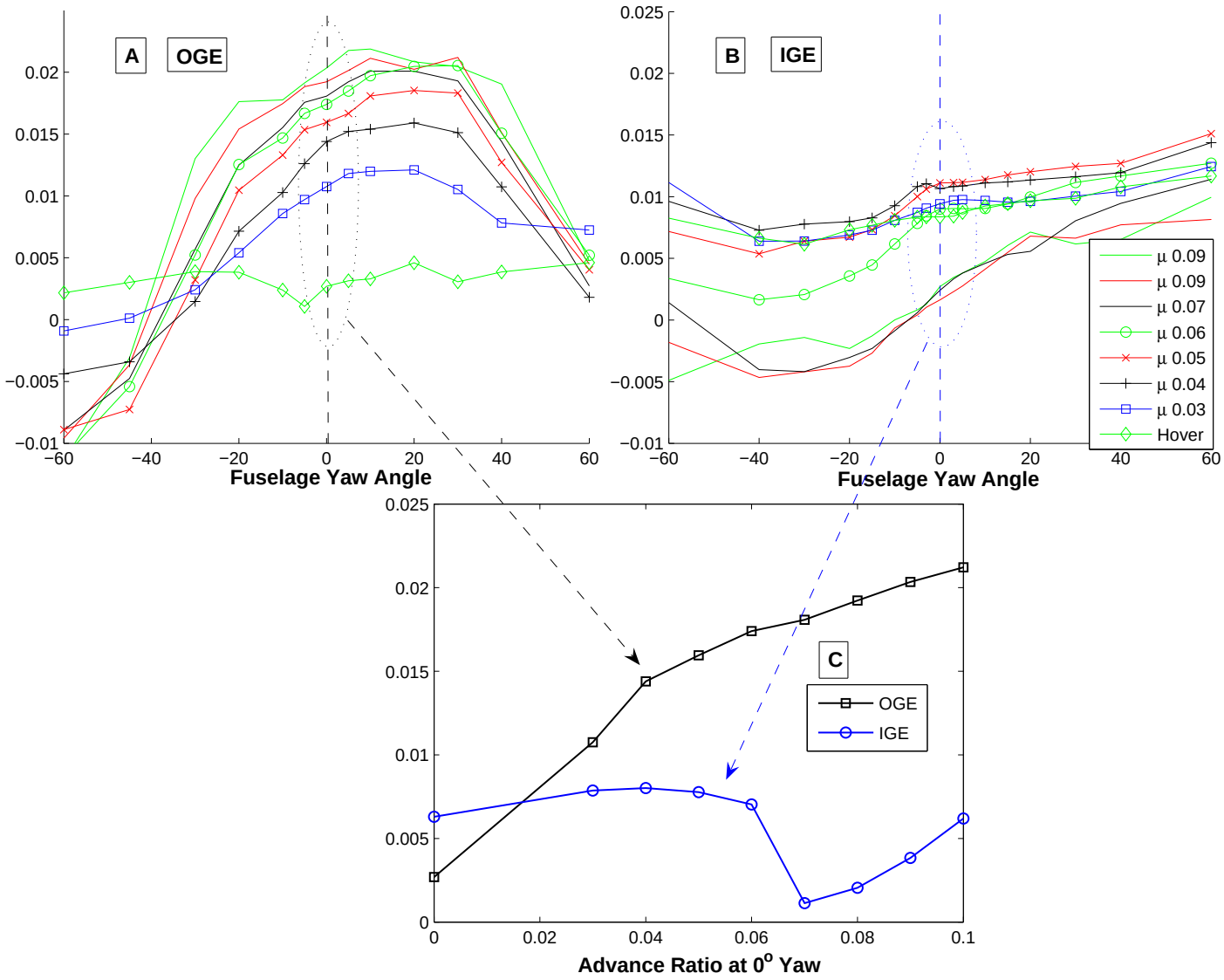

Figure 42: Circular Cross-section Fuselage Drag force. Non-dimensionalized by density, tip speed and circular cross-section fuselage planform area.

5.3.3 Comparison of Circular Cross-section and Flattened Fuselage Loads

The next step was to measure the forces on the flattened fuselage. The plots include error bars, which indicate the maximum expected error in the measurements. A discussion of the error estimate is included in the next section.

5.3.3.1 Comparison of Lift Force

Fig. 43 shows the comparison of the lift force on the two kinds of fuselages at 0° yaw from hover to an advance ratio of 0.1. It can be seen that the down force of a circular cross-section fuselage is much greater than that of the flattened fuselage while out of ground effect. This is to be expected since a smaller area is exposed to the inflow in the case of a flattened fuselage. It can also be seen that both the fuselages IGE show an increase in downforce between advance ratio of 0.03 and 0.05, followed by an increase in upward lift on the fuselage in the 0.06 to 0.08 advance ratio range. However, the increase in upward lift is of a greater magnitude in the case of the flattened fuselage IGE.

5.3.3.2 Comparison of Drag Force

Fig. 44 shows the comparison of the drag force on the two kinds of fuselages at 0° yaw from hover to an advance ratio of 0.1. It can be seen that the drag force of both fuselages increase steadily while out of ground effect. However, the rate of increase is higher in the case of the circular cross-section fuselage. The drag force IGE show a similar trend for both fuselages. The sudden dip in drag can be seen between advance ratio of 0.06 and 0.08 and the increase thereafter can be seen.

5.3.3.3 Comparison of Side Force

Fig. 45 shows the comparison of the side force on the two kinds of fuselages at 0° yaw from hover to an advance ratio of 0.1. During discussions with helicopter pilots, the difference in side forces had always been emphasized as a point of concern by them. The measurements found that the side force showed the most variation depending on the fuselage shape. It can be seen that the side force IGE varies considerably depending on fuselage shape. While the side force OGE for a circular cross-section fuselage immediately switches to a negative

value when the helicopter fuselage accelerates to an advance ratio of 0.03, the flattened fuselage stays at a positive side force value until an advance ratio of 0.04 before changing to a negative value. The values of the side forces OGE for the two fuselages approach each other till they almost overlap at an advance ratio of 0.09.

The behavior of the side force on the two types of fuselages IGE is considerably different. The side force for a circular cross-section fuselage IGE remains at a positive value until an advance ratio of 0.07. This is accompanied by a rapid forward shift in the moment arm as shown in Fig. 41. The side force of a flattened fuselage IGE shows a distinct kink at an advance ratio of 0.06. The slope of the curve increases after the formation of the ground vortex under the fuselage.

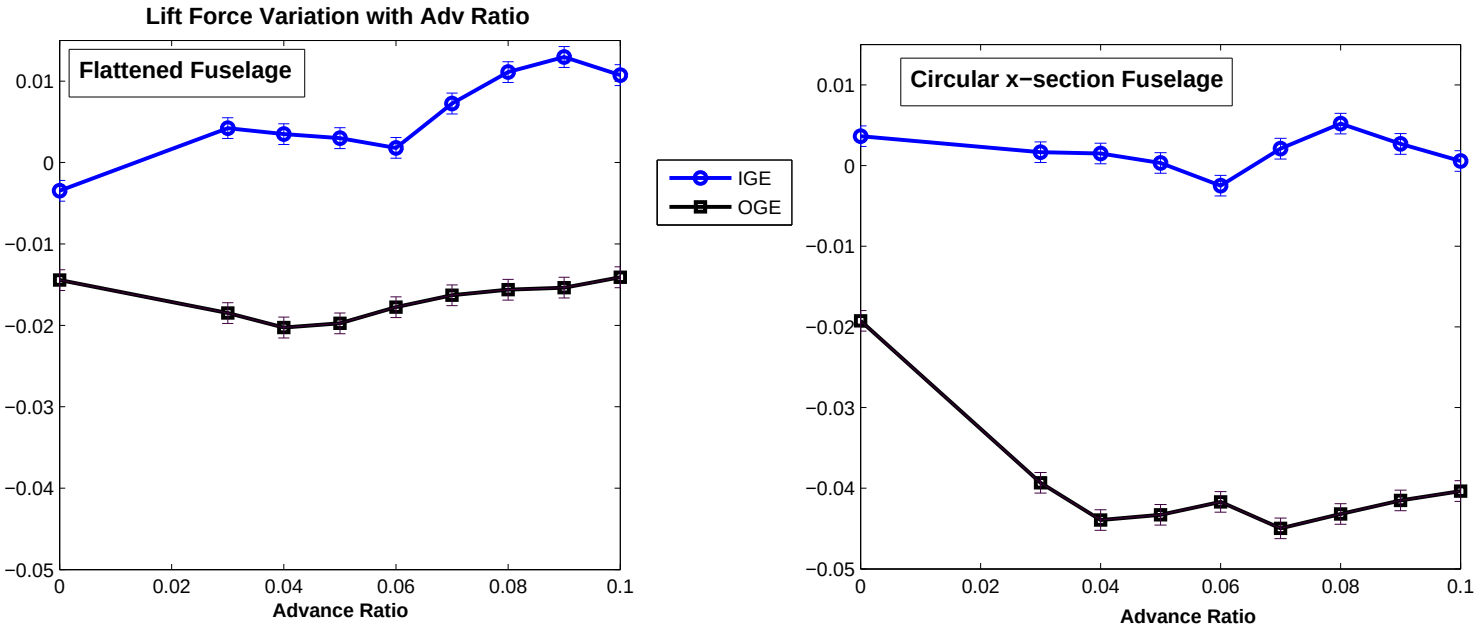

Figure 43: Comparison of Non-Dimensional Lift Force of Circular cross-section and Flattened Fuselage.

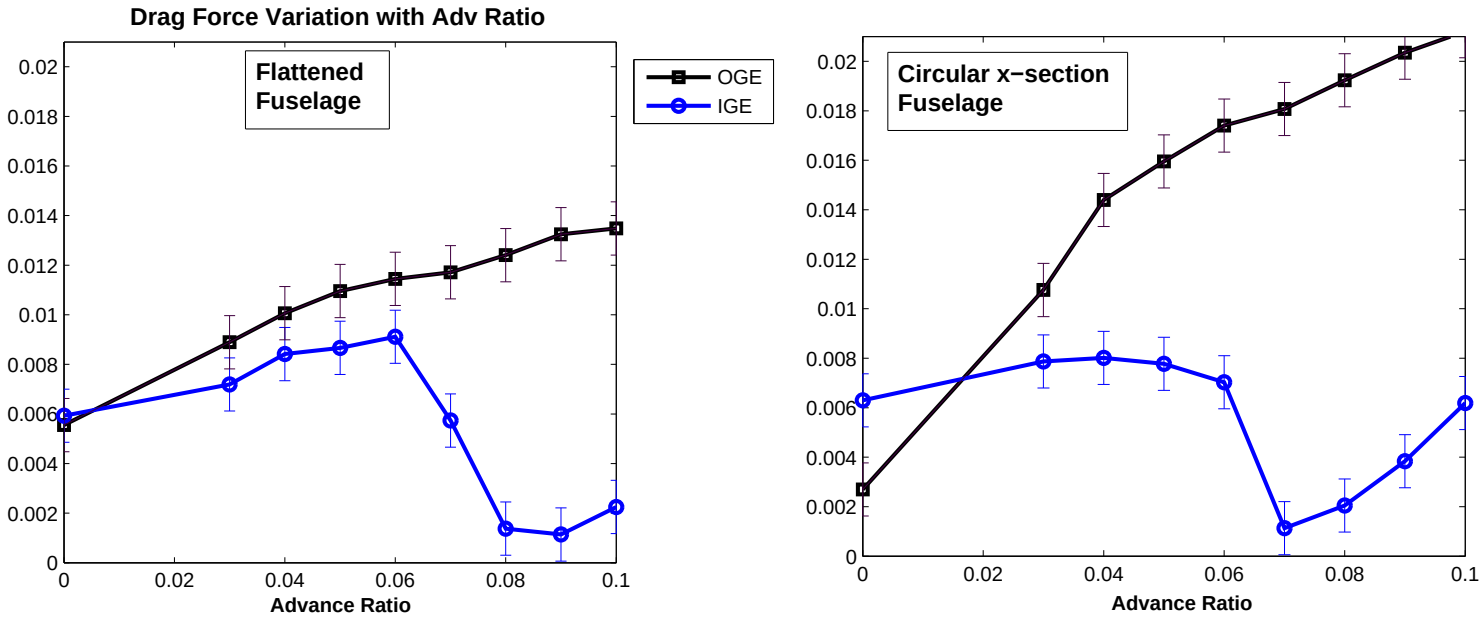

Figure 44: Comparison of Non-Dimensional Drag Force of Circular cross-section and Flattened Fuselage.

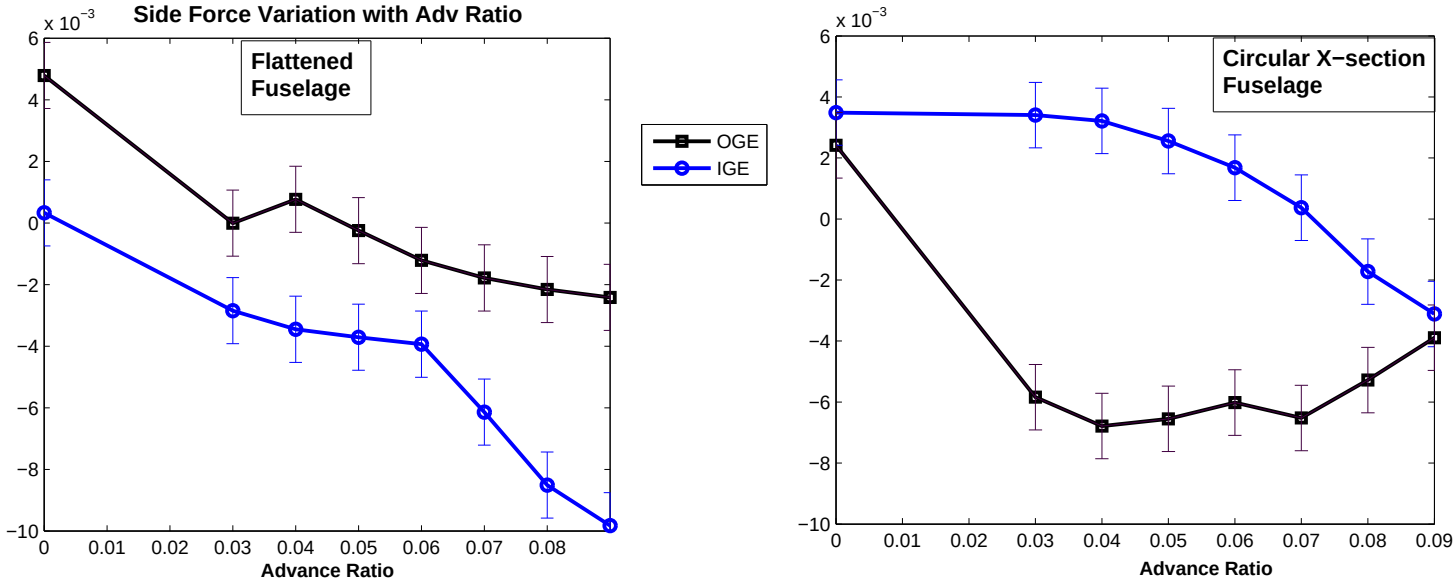

Figure 45: Comparison of Non-Dimensional Side Force of Circular cross-section and Flattened Fuselage.

5.4 Discussion on Measurement Error

The error in the measurements was estimated with the help of a calibration run on the load cell. The load cell was loaded with precision weights in all three components up to the full scale, and the errors in the readings were recorded. A conservative approach was followed, and the *maximum error* recorded in each component was taken to be the error estimate of the load cell in that axis. The maximum error amounted to 0.48N on the downforce component, which amounted to an error 0.12% of full scale. The maximum error on the side and drag force components was 0.403N, which amounted to 0.31% of full scale.

5.5 Conclusion

The following conclusions can be drawn from this analysis.

1. The low frequency fluctuations seen in the inflow and in the region around the ground vortex are not noticeable in the fuselage force measurements.

2. The downforce of a circular cross-section fuselage is much greater than the flattened fuselage. Both fuselages show a decrease in downforce between advance ratio of 0.06 and 0.08 with the formation of the ground vortex. The magnitude of the reduction of downforce is greater in the case of the flattened fuselage.

3. There is a sudden decrease in drag force between advance ratio of 0.06 and 0.08 with the formation of the ground vortex.

4. The two cross-sectional fuselages have distinct differences in the case of side force. In ground effect, the circular cross-section sideforce changes direction at an advance ratio of 0.07, which is accompanied by a sudden forward shift of the point at which the side force acts. This behavior is not seen in the case of the flattened fuselage. This implies that the side force felt on a circular cross section fuselage IGE would be considerably different from that experienced OGE. This kind of behavior is not seen in the flattened fuselage. This could pose a problem for helicopter pilots who change the type of rotorcraft that they fly IGE due to the change in the side forces felt by the fuselage.

CHAPTER VI

SURFACE FLOW VISUALIZATION OF GROUND VORTEX

6.1 Objectives

Information about the flow is useful in understanding the wake structure of a rotorcraft. To this end, surface flow visualization was carried out on the ground plane for a rotorcraft at low advance ratios in ground effect. This visualization was carried out using tufts that were attached to the ground plane. A picture of the experiment is shown in Fig. 46. The motivation of the experiment was to carry out a study of the ground vortex structure. Surface flow visualization provides important qualitative information about the flow direction close to the ground. This also provides information for validating computational fluid dynamics (CFD) analysis to check the accuracy with which it models the flow structure and the wake structure in the presence of the ground plane.

6.2 Experimental Setup

The surface flow visualization was carried out by affixing tufts on the ground plane. The schematic of the experimental set-up is shown in Fig. 47.

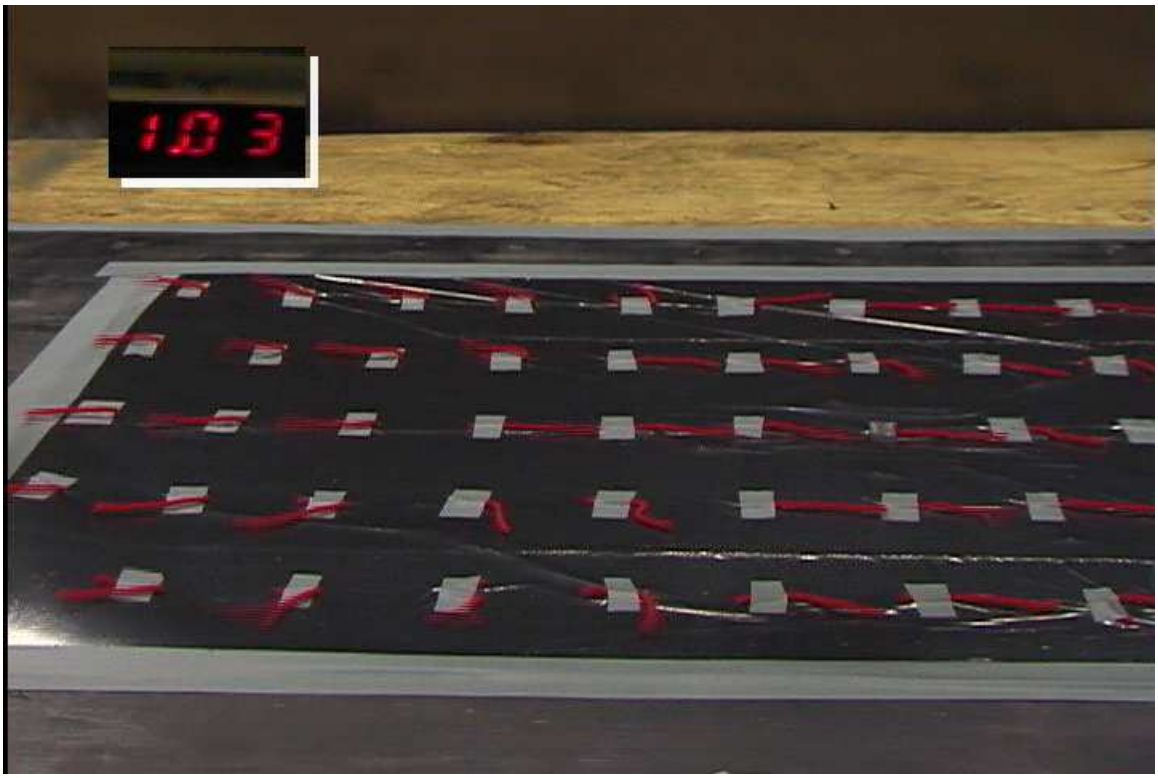

Figure 46: Tuft Surface Visualization Experiment

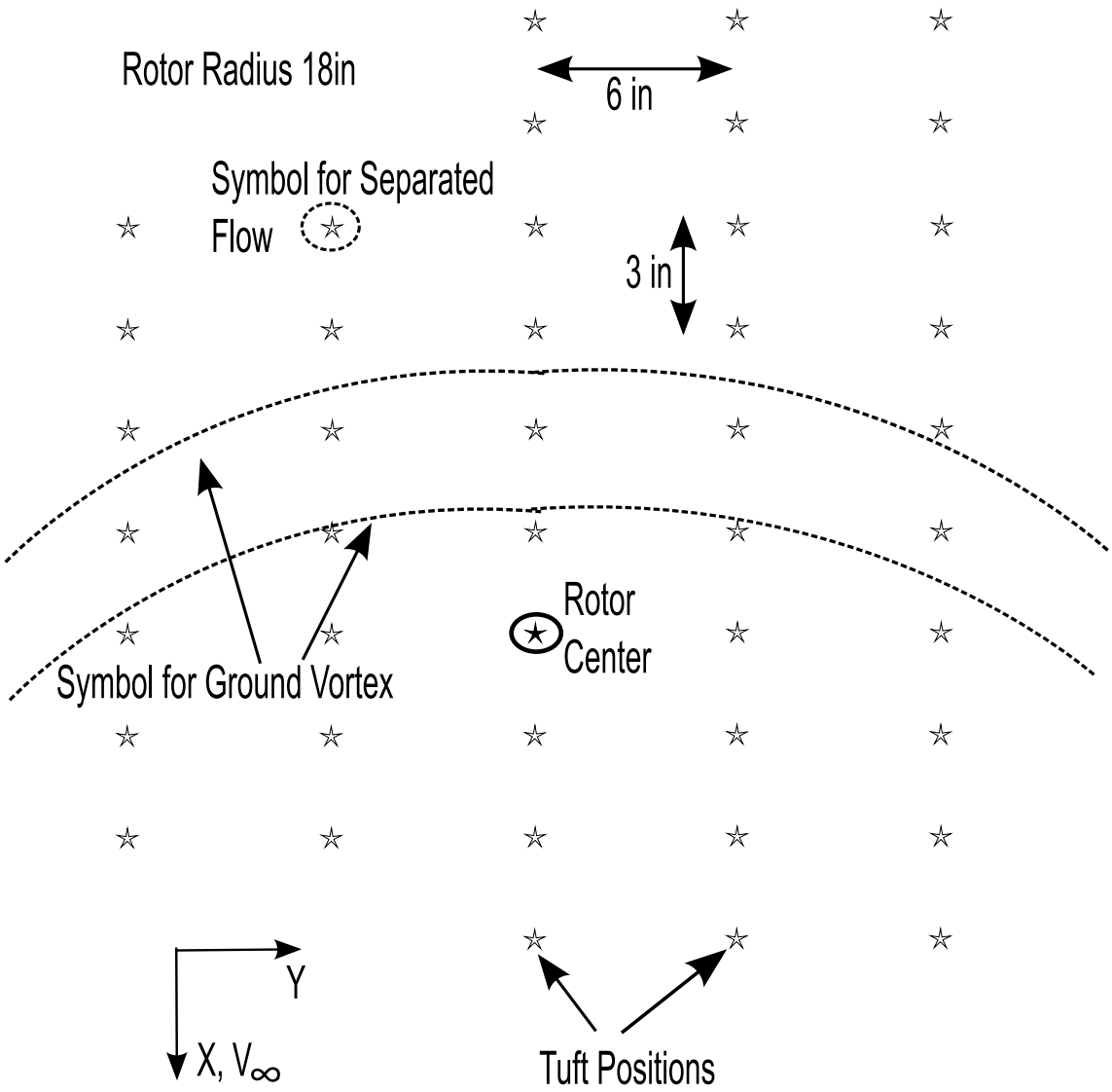

Figure 47: Schematic of Tuft Surface Visualization Experimental Set-up

The tuft positions are shown by the star symbol. It can be seen that the X co-ordinate is along the freestream direction and the Y direction is along the 90 ° - 270 ° rotor azimuth position. The distance between the tufts in the X direction is 3 inches and the distance between the tufts in the Y direction is 6 inches. The tuft that is below the rotor center is marked with a solid black ellipse. The tufts that lie in the region of separated flow are marked with a dashed black ellipse. The estimated position of the ground vortex is shown with two dashed lines that encompass the position of the ground vortex. It is to be noted that the tuft positions indicate only the average direction of flow.

6.3 Results and Discussion

6.3.1 Advance Ratio 0.03

The surface flow visualization results at an advance ratio of 0.03 is shown in Fig. 48. The tuft directly below the rotor center is marked by a solid black ellipse, and tufts in the region of separated flow are marked with a dashed ellipse. It can be seen that flow at the surface moves upstream about 9 inches ahead of the rotor center. This is the forward directed flow that is re-ingested in to the disk plane in the recirculation regime. There is a region of separated flow between the regions of upstream and downstream directed flow.

6.3.2 Advance Ratio 0.04

The surface flow visualization results at an advance ratio of 0.04 are shown in Fig. 49. The flow structure is similar to that at μ 0.03. The reversed flow ahead of the rotor center can be seen that is part of the recirculation flow in the forward part of the rotor disk.

6.3.3 Advance Ratio 0.05

The surface flow visualization results at an advance ratio of 0.05 are shown in Fig. 50. The recirculation flow still dominates at the ground plane. The flow structure is clearly defined with a forward facing flow about 12 inches in front of the rotor center, along with outward flow in the Y direction.

6.3.4 Advance Ratio 0.06

The surface flow visualization results at an advance ratio of 0.06 are shown in Fig. 51. This is the advance ratio where the ground vortex begins to form. However, the ground vortex is not well defined. The forward facing flow moves back to about 9 inches ahead of the rotor center, and the change over from forward facing flow to downstream flow is more clearly defined than at lower advance ratios.

6.3.5 Advance Ratio 0.07

The surface flow visualization results at an advance ratio of 0.07 are shown in Fig. 52. The ground vortex has formed and can be seen as separated flow about 18 inches ahead of the rotor center. The position of the ground vortex is marked with two dashed arcs. The forward facing flow has now moved back to about 6 inches ahead of the rotor center.

6.3.6 Advance Ratio 0.08

The surface flow visualization results at an advance ratio of 0.08 are shown in Fig. 53. The ground vortex has moved back to about 15 inches ahead of the rotor center and its shape is more clearly defined.

6.3.7 Advance Ratio 0.09

The surface flow visualization results at an advance ratio of 0.09 are shown in Fig. 54. The ground vortex has moved back to about 12 inches ahead of the rotor center and the flow upstream of the ground vortex can now be seen. The ground vortex also begins to bend and forms a greater angle with respect to the X axis.

6.3.8 Advance Ratio 0.10

The surface flow visualization results at an advance ratio of 0.10 are shown in Fig. 55. The ground vortex has moved significantly backward to about 9 inches ahead of the rotor center and is now considerably bent with respect to the X axis. The flow ahead of the ground vortex is turned outward by the presence of the ground vortex. The radial flow in the ground vortex can be seen in the core of the ground vortex.

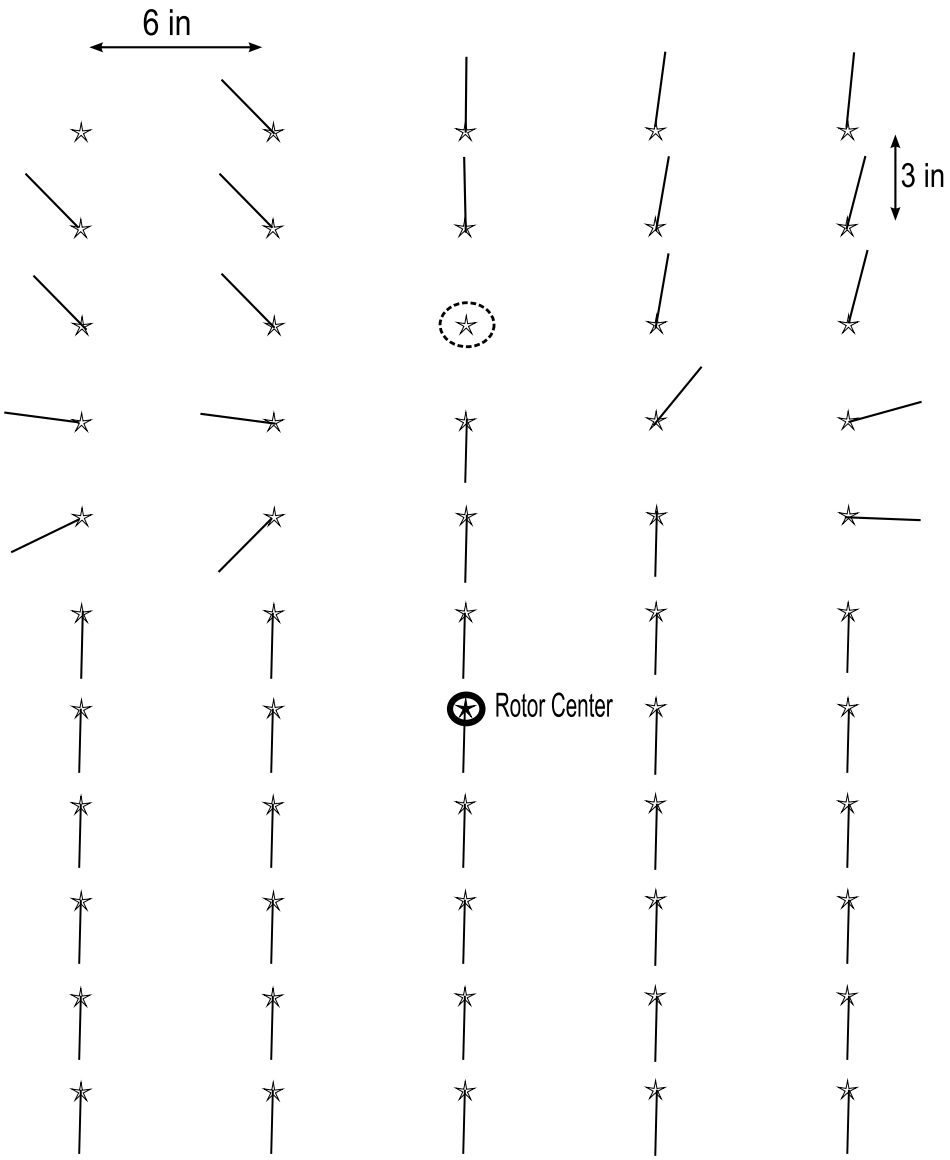

Figure 48: Tuft Surface Visualization at advance ratio 0.03

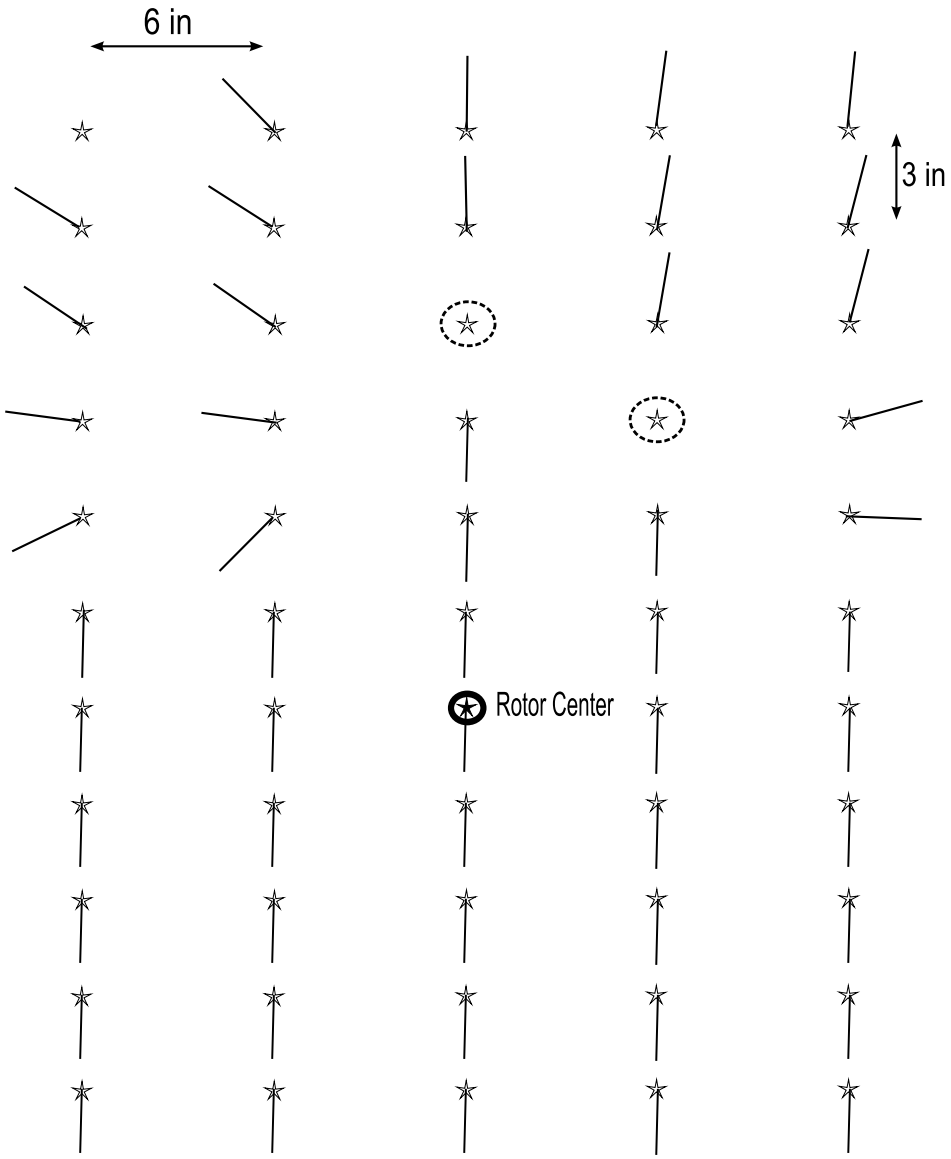

Figure 49: Tuft Surface Visualization at advance ratio 0.04

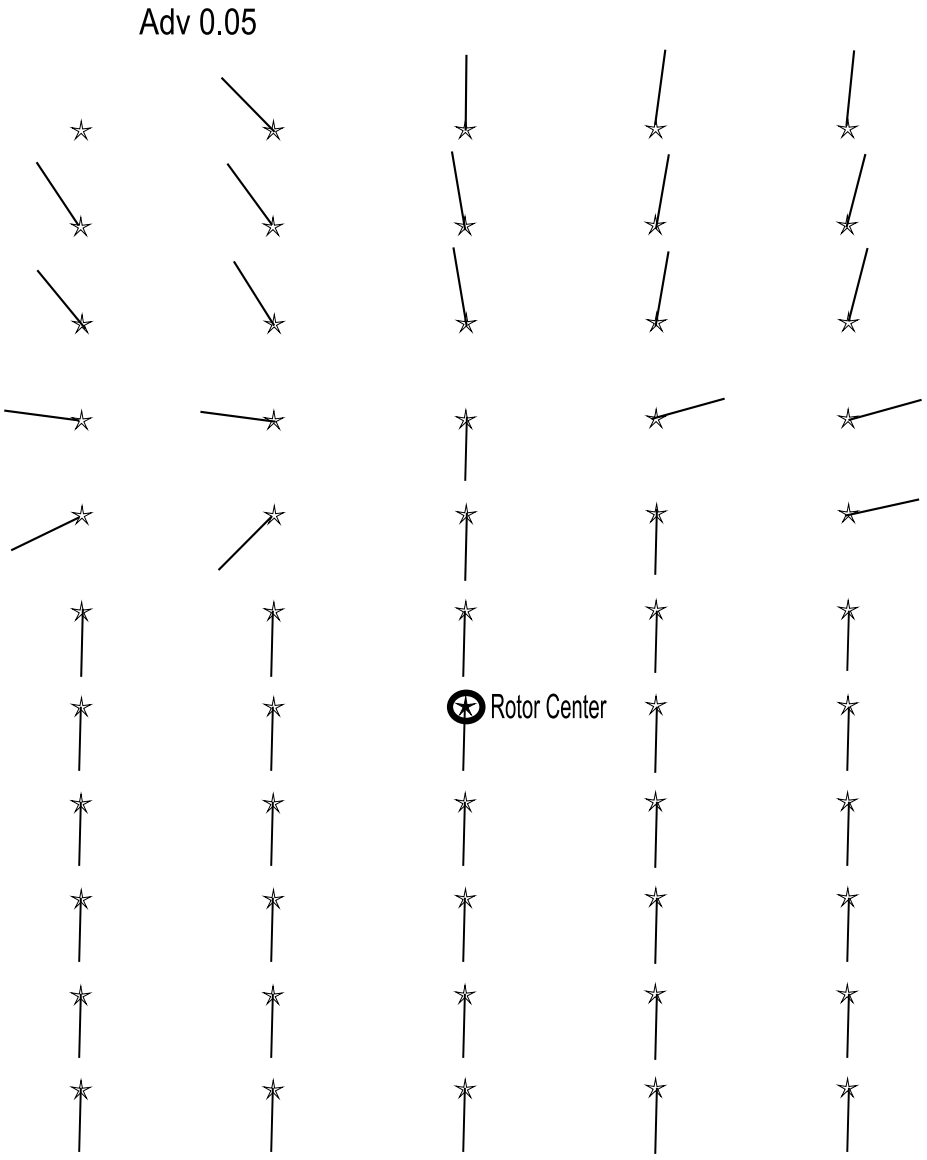

Figure 50: Tuft Surface Visualization at advance ratio 0.05

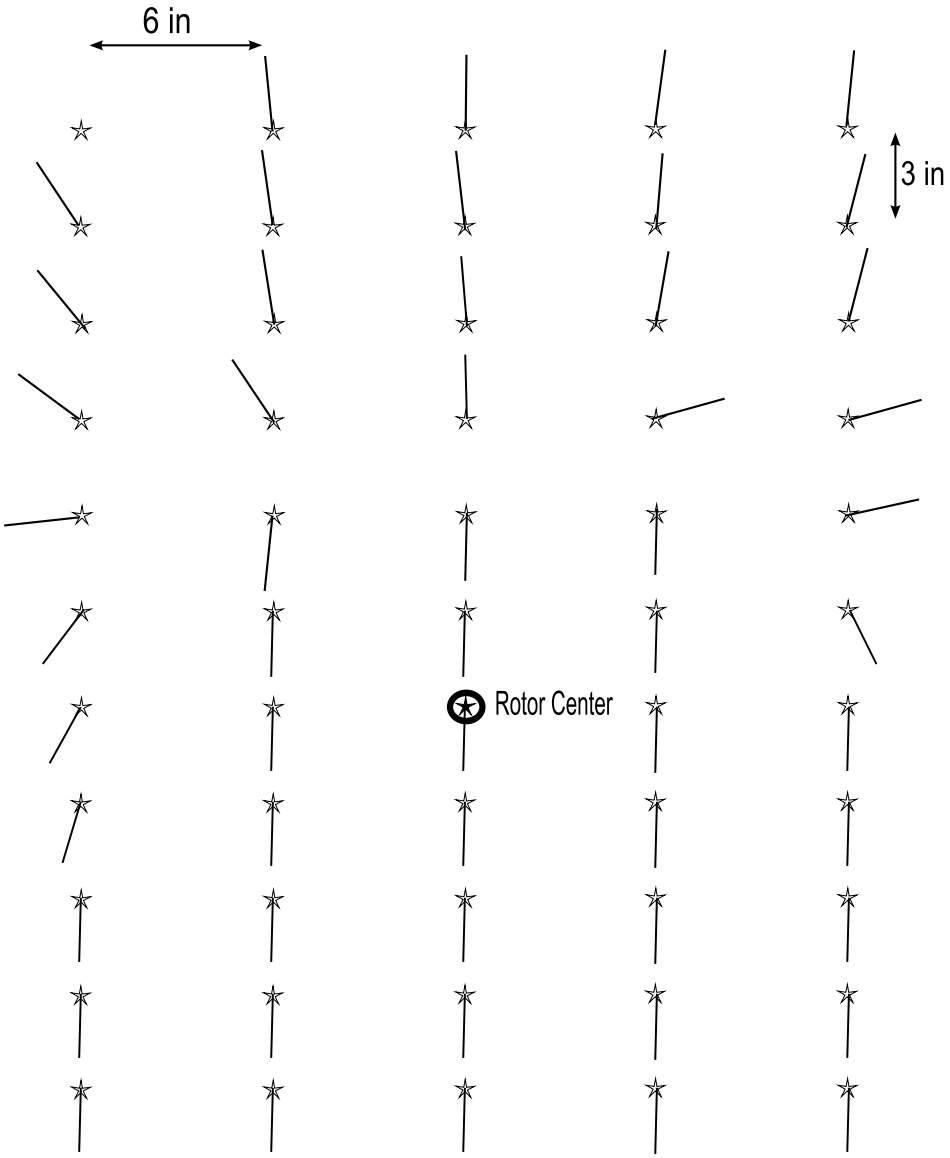

Figure 51: Tuft Surface Visualization at advance ratio 0.06

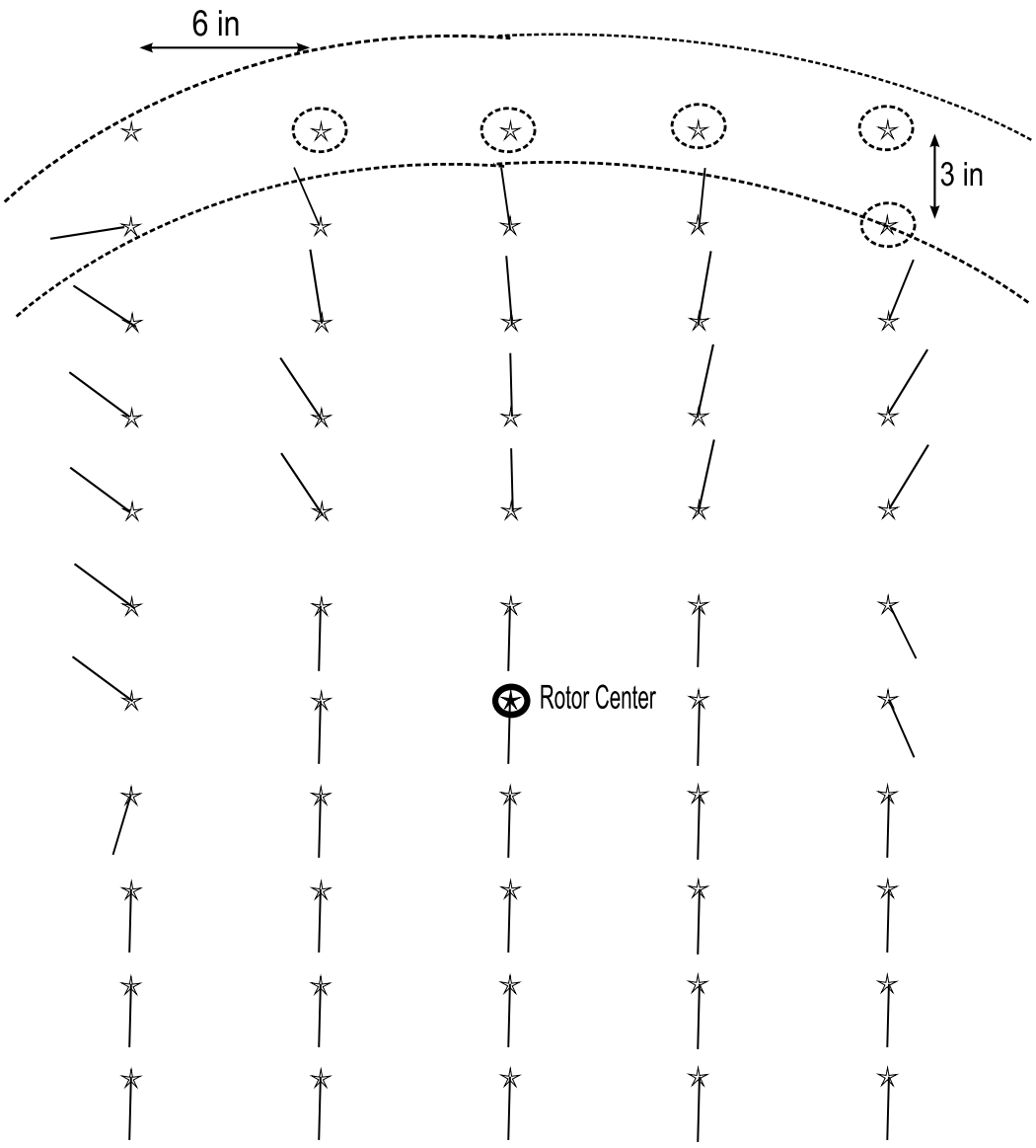

Figure 52: Tuft Surface Visualization at advance ratio 0.07

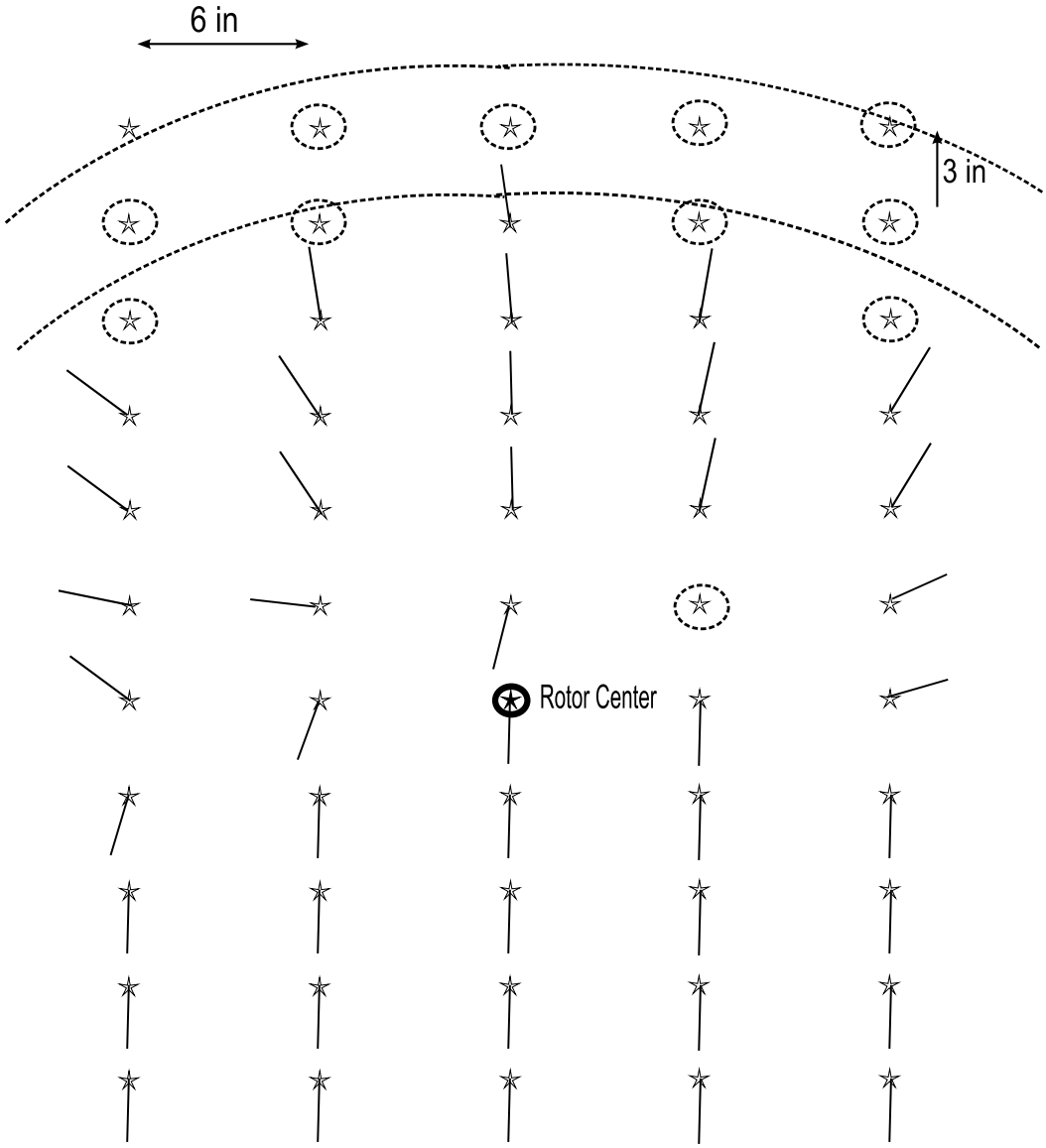

Figure 53: Tuft Surface Visualization at advance ratio 0.08

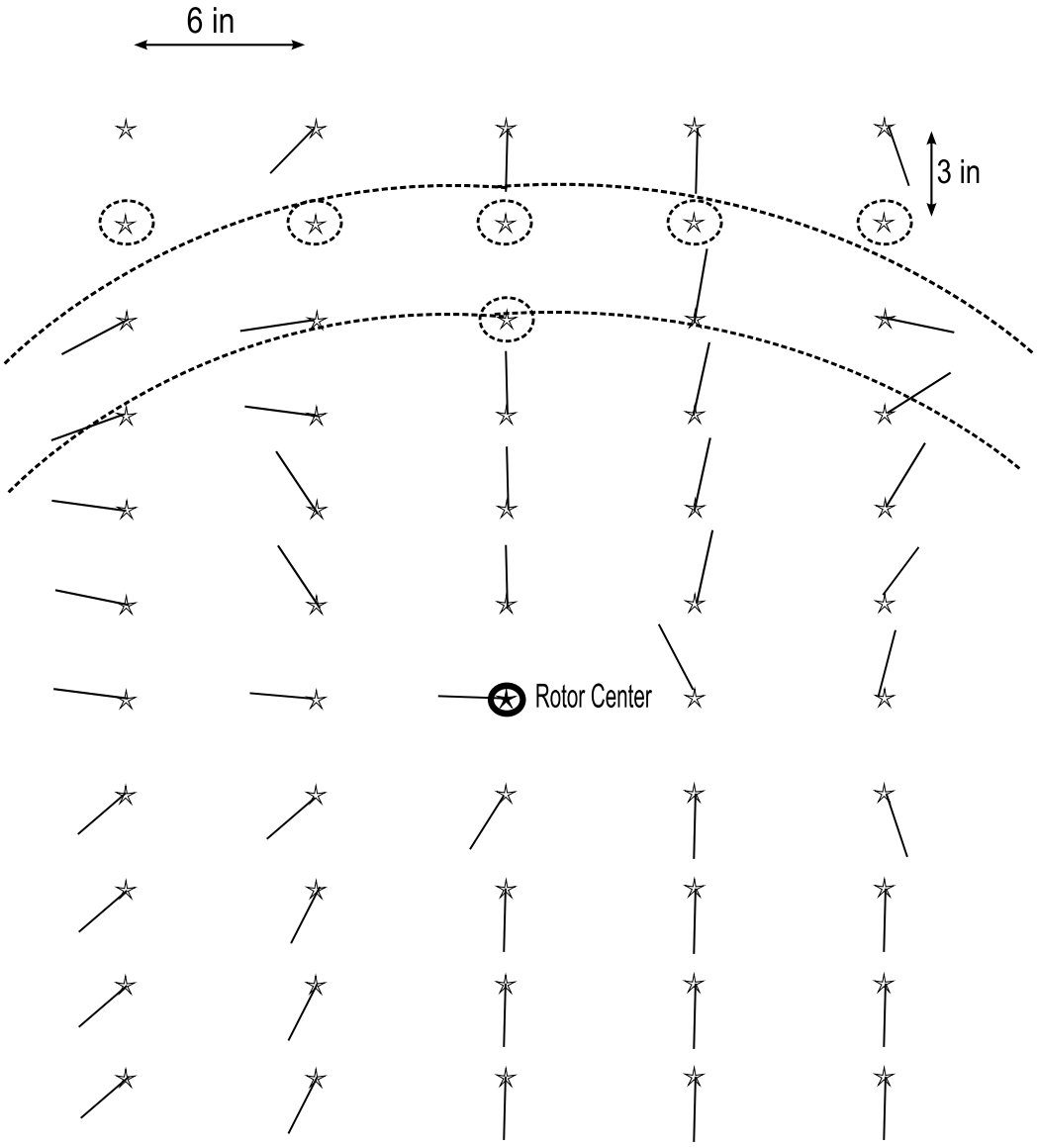

Figure 54: Tuft Surface Visualization at advance ratio 0.09

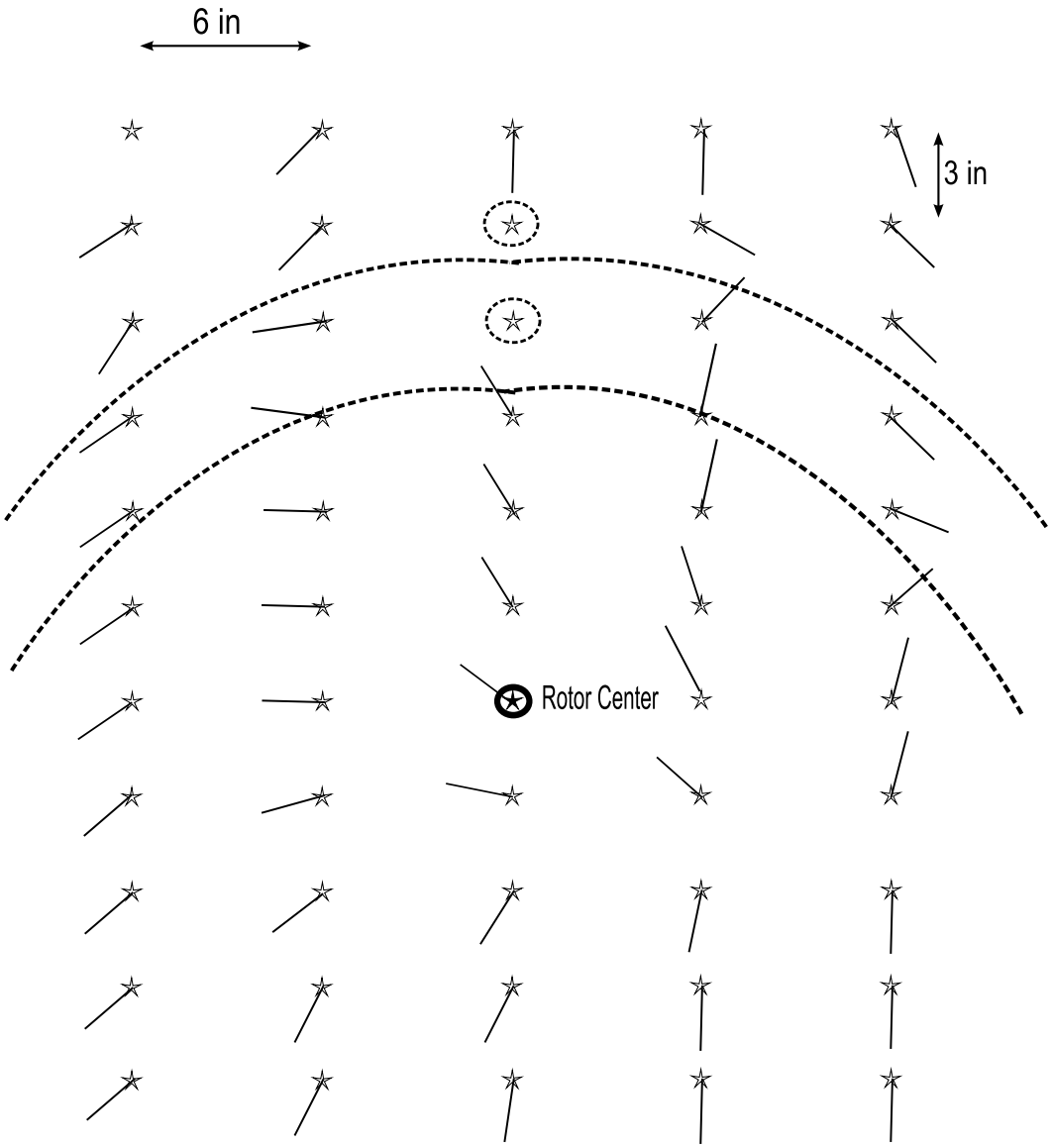

Figure 55: Tuft Surface Visualization at advance ratio 0.10

6.4 Conclusions

Surface flow visualization of the ground vortex shows that forward facing flow in the re-circulation regime persists up to an advance ratio of 0.06. The ground vortex can be seen above an advance ratio of 0.07 and it moves back and is bent more with respect to the X axis with increasing advance ratio. The radial flow in the core of the ground vortex can be seen. A more quantitative study of the flow structure using Particle Imaging Velocimetry will provide further insight into the structure of the ground vortex.

CHAPTER VII

MEASUREMENT OF ROTOR POWER

7.1 Objectives

One of the main issues with correlating experimental results in helicopter aerodynamics with computational calculations is that of accurately matching the operating conditions of the experimental rotor with that simulated in the computational model. To this end, it is necessary to provide information about the performance of the rotor.

7.2 Experimental Plan

The rotor at the John Harper Wind Tunnel is driven by a DC electric motor, and the experiment was designed to measure the power required by the motor to drive the rotor. The current to the motor was measured using a closed loop current transducer using Hall Effect. The rated accuracy is less than 0.65%. The current measurement system was tested by measuring known currents that were supplied by a high accuracy power supply and the error was validated to be between 0.0125% and 0.59%. Voltage was measured using a Labview PCI6052 analog to digital conversion card. This is a 16 bit analog to digital converter with a resolution of 0.0025 mV. The rated accuracy for this card is less than 4.747 mV. This card was validated using a known voltage supplied by a precision power supply and the accuracy of the card was calibrated to be less than 0.2%.

It was necessary to ensure that the experiment measured the power required to drive the rotor alone. To achieve this, the power required to drive the rotor shaft without the rotor blades was measured at 2100 RPM. This ensured that the frictional effects and the power required to drive the shaft was captured within this tare measurement. This power measurement was subsequently subtracted from the rotor power measurements to obtain the power required to drive the rotor blade.

7.3 Results and Discussion

7.3.1 Measurement Validation

The power measurements were validated by comparing the hover measurements with the thrust measurement that was done by Brand at the John Harper Wind Tunnel for the same rotor setup in 1989[4]. The C_P (Coefficient of Power) was calculated from Momentum theory using Equation 10, where $C_{P\,Momentum}$ is the ideal value of C_P obtained from Momentum theory and C_T is the measured value of the coefficient of thrust.

$$C_{P\,Momentum} = \frac{C_T^{3/2}}{\sqrt{2}} \tag{10}$$

This value of $C_{P\,Momentum}$ that was obtained was corrected using the non-ideal correction factor κ, which accounts for the non-ideal effects such as non–uniform inflow, tip losses, wake swirl *etc.* The final value of C_P was then obtained from Equation 11 by multiplying the correction factor κ by the $C_{P\,Momentum}$. It has been found empirically that the correction factor κ is usually between 1.1 and 1.25.

$$C_P = \kappa \times C_{P\,Momentum} \tag{11}$$

It was found for this measurement that the power measurement matched the momentum theory C_P obtained from the 1989 thrust measurement when $\kappa = 1.275$.

This was the first step of the measurement validation for the power measurement during hover. The next step was to check the power measurement in ground effect by using the measured C_T value modified by the IGE correction Equation. 1, plotted in Fig. 8. The momentum theory C_P obtained from the modified IGE value of thrust matched the measured value when $\kappa = 1.24$.

7.3.2 C_P Measurements

The plot of the C_P measurements is shown in Fig. 56. The values obtained through the momentum theory analysis is also plotted on the chart to compare with the measurements. It can be seen that the power required for the rotor out of ground effect rises linearly with increase in advance ratio. The power required at hover IGE is higher than the power

required at hover OGE. This is to be expected because the rotor is a fixed pitch rotor, and the thrust increases with the reduction in inflow. In a real situation, the pilot would reduce the collective to maintain hover flight conditions, and thus reduce power consumption.

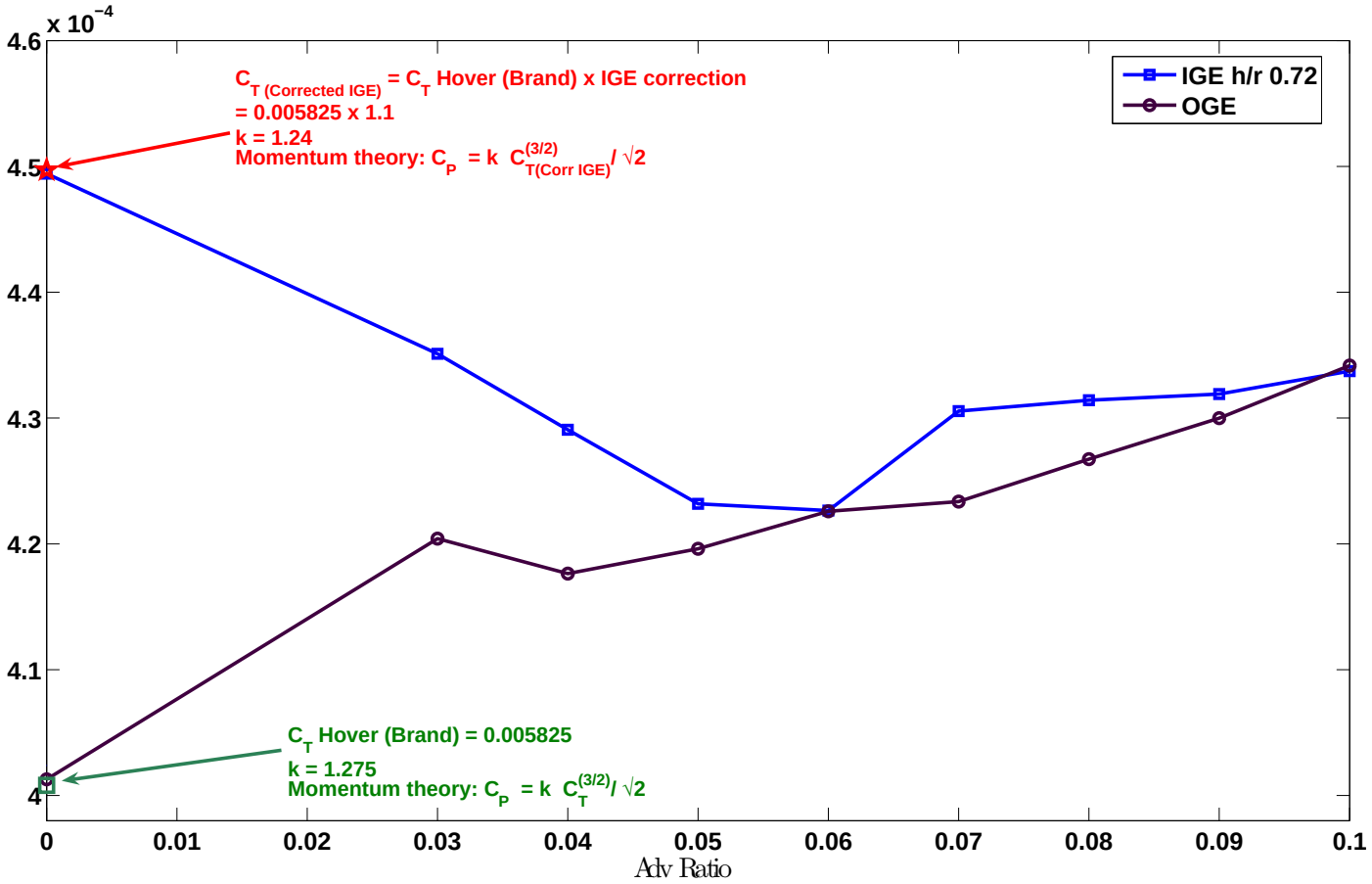

Figure 56: Power Measurements in and out of Ground Effect

It can be seen that the effect of the reduced inflow reduces with the formation of the ground vortex and the power required approaches the OGE value at an μ of 0.06. The C_P again increases between a μ of 0.07 and 0.09 before aligning itself with the OGE value at μ of 0.1.

7.4 Conclusion

The C_P for the John Harper Wind Tunnel rotor was measured in and out of ground effect. The C_P values at hover were validated using momentum theory and the C_T values measured by Brand. It was found that the C_P OGE increased linearly with advance ratio. The C_P IGE for this fixed pitch rotor was higher till the formation of the ground vortex, when it matched the OGE value. It then increased again between advance ratios of 0.07 and 0.09. The C_P got back to the OGE value at an advance ratio of 0.1, when the ground vortex was overrun.

CHAPTER VIII

PIV OF THE GROUND VORTEX

8.1 Objectives

The ground vortex has been visualized and studied by various researchers in the past. They have looked at vortex position and its effect on rotor thrust and power requirements. This research looked at hotwire measurements around the ground vortex. However, while hotwire measurements are useful to resolve the high frequency components, they are point measurements. They are also not very good to resolving the directional components of the velocities. Particle Image Velocimetry (PIV) provides an effective way to capture velocity field measurements accurately. The PIV experiment would help in quantifying the flow field under the rotor in ground effect, and to better understand the structure of the ground vortex.

8.2 Introduction to PIV

A PIV system consists of four components- a laser to visualize the flow, seed particles to scatter the light, a camera to record the images and a computer to analyze the images. PIV works by flashing the laser in two pulses separated by a known interval to illuminate the flowfield of interest, which is seeded with tracer particles. The change in the position of the particles on the images associated with the time interval provides the velocity of the particles. Early systems depended on tracking individual particles, but correlation based PIV is a more efficient way to calculate the velocities of the particles. Correlation based PIV can be based on auto-correlation, where one image is exposed twice to the laser flashes, or on cross-correlation, where two separate images are obtained for the laser pulses. The technique used in this study is the cross-correlation PIV. The two images are divided into small regions known as interrogation spots and the cross correlation function is calculated for each spot to provide one vector per spot. The determination of velocity is done by

spatial cross correlation of the images. The location of the highest correlation peak in the correlation plane corresponds to the most likely average particle displacement in the interrogation area [3]. Sub-pixel accuracy of the displacement is usually obtained by fitting a Gaussian function to the correlation peak, and finding the exact peak location. More details of the cross correlation process can be found in References [1] and [11].

Signal-to-noise ratio begins to degrade for particle displacements exceeding 1/4th of the interrogation spot size [59] and about 7 to 10 particles in each interrogation spot is necessary for accurate PIV measurements [39]. The ideal size of seeding particles is between 3 and 4 pixels. The other requirements for optimum accuracy for PIV measurements are summed up in [3].

8.3 Experimental Plan

The PIV experiments were conducted on the rotor at the John Harper Wind Tunnel and the setup is the same as described in Chapter-3. The description of the equipment specific to the PIV measurements will be done in the following paragraph. A picture of the experimental set-up is shown in Fig. 57.

A 10 bit SharpVision CCD camera of 1360x1024 pixel resolution was used to obtain double exposed flow images. The frame separation was set to 25 microseconds keeping the expected maximum velocity to stay well within this threshold, and also to minimize the probability of particle loss due to out-of-plane movement. Seeding was done with a mineral oil atomizer, and the atomized flow was sent through a bent tube to filter out particles larger than 0.25 mm. A calibration check was done on the particles in the image plane and the particles fell into the range of 0.19mm (+ 0.07mm -0.05mm), which meant that particle size ranged from 1.9 to about 4 pixels.

A frequency doubled Nd-YAG laser at 532 nm was used to provide the illumination for the PIV study. A timing and synchronization unit was used to trigger the laser at the 90° – 270° position of the rotor. The laser sheet was aligned along the center line under the rotor in the upwind-downwind direction along the tunnel axial direction. The pulse separation was determined by estimating the velocity in the measurement region with the help of the

hotwire measurements. This was used to calculate the pulse separation to give a particle pixel shift of between 4 and 6 pixels while ensuring that the out-of-plane movement of the particles were not greater than about 1/3 the sheet thickness [59].

The co-ordinate system of the PIV set-up is shown in Fig. 58. The rotor shaft is tilted forward 6° and the positive X direction is in the upwind direction. The positive Y direction is toward the inflow region of the rotor. The positive u component of velocity is in the upwind direction and positive v component of velocity is upward. Note that the zero position of the co-ordinate system is the center of the shaft at the teetering pivot of the rotor.

Since a relatively large area had to be covered while capturing the fine flow details, it was decided that the field of interest would be divided into smaller measurement areas. This would ensure that finer flow details and higher spatial scales would be captured. So the area of interest was divided into 24 sub-grids, and the layout is shown in Fig. 59.

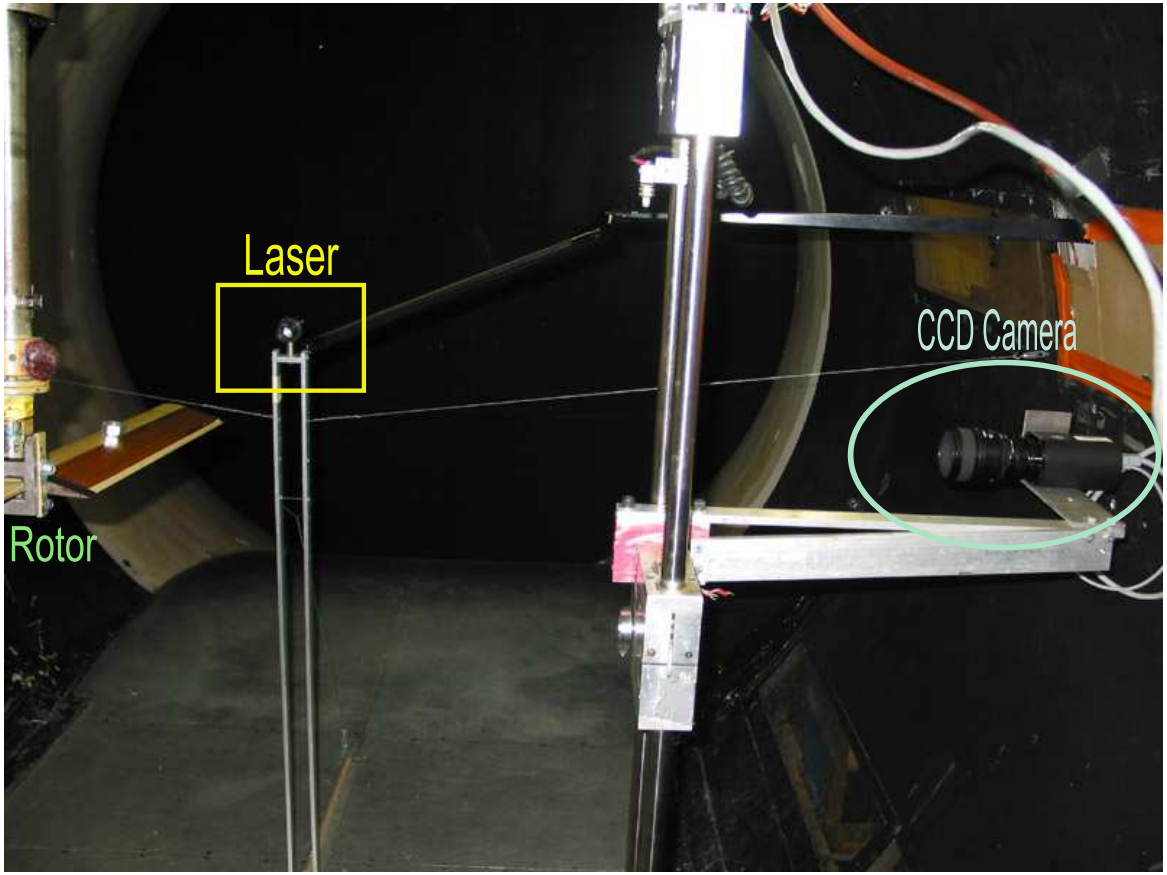

Figure 57: PIV Experimental Setup

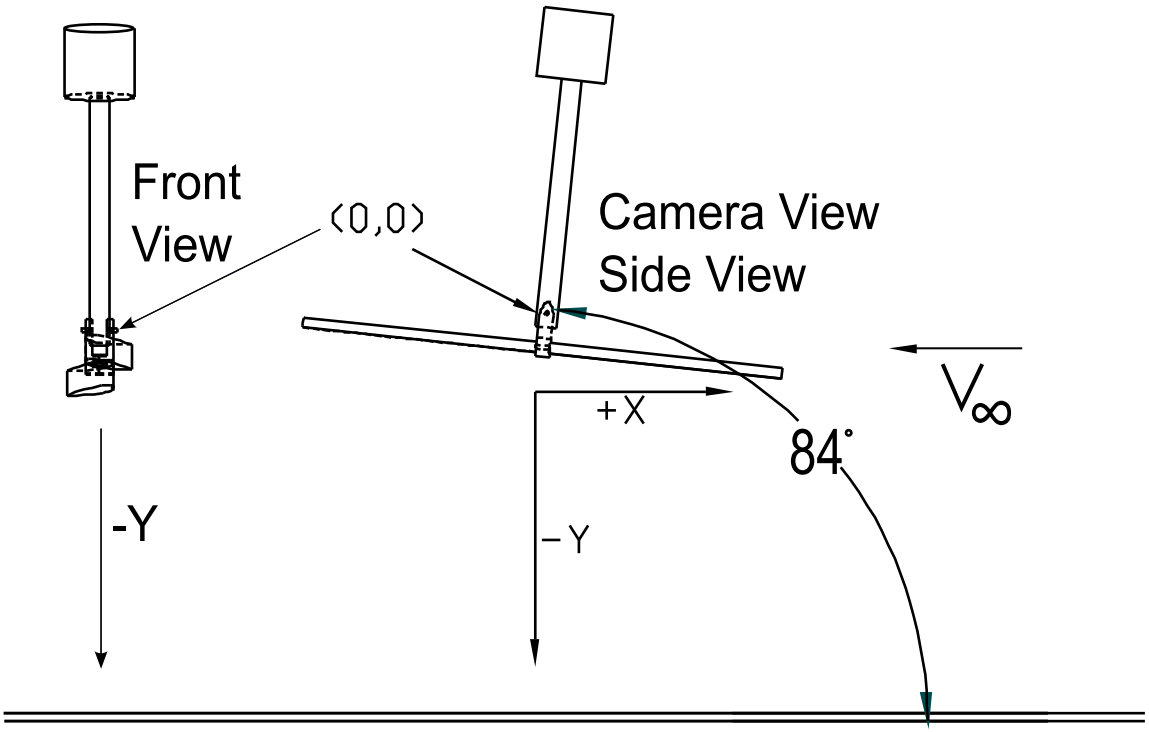

Figure 58: PIV Co-ordinate System

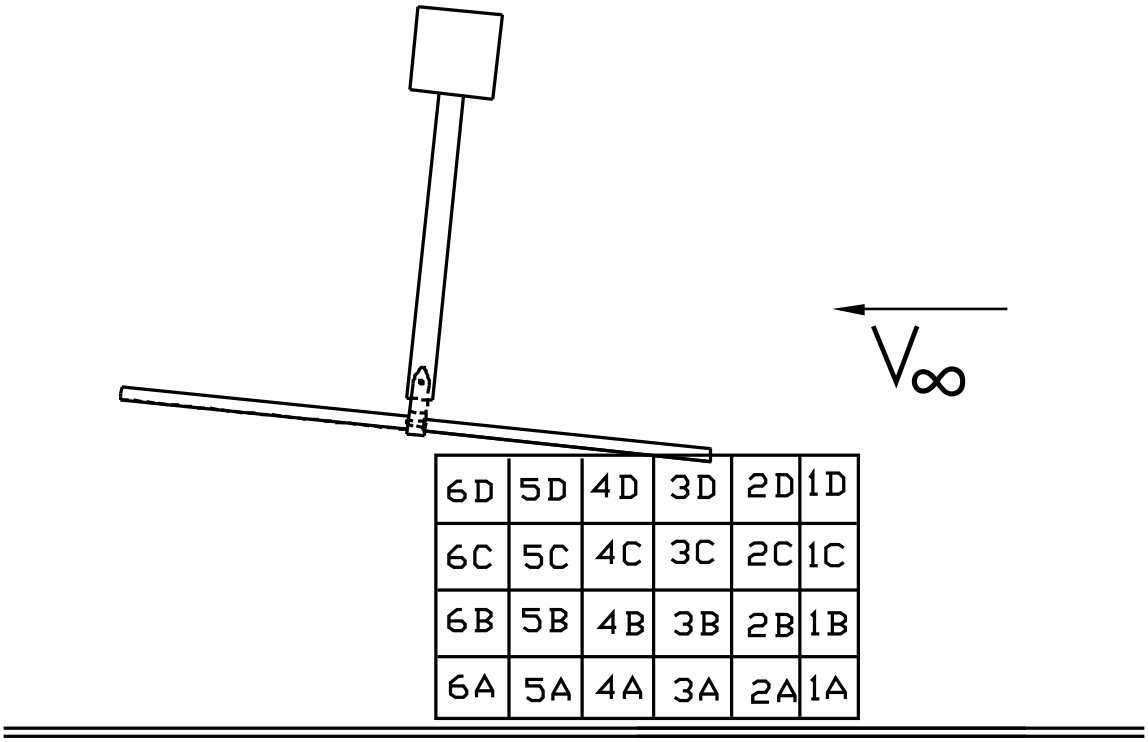

Figure 59: PIV Measurement Grid

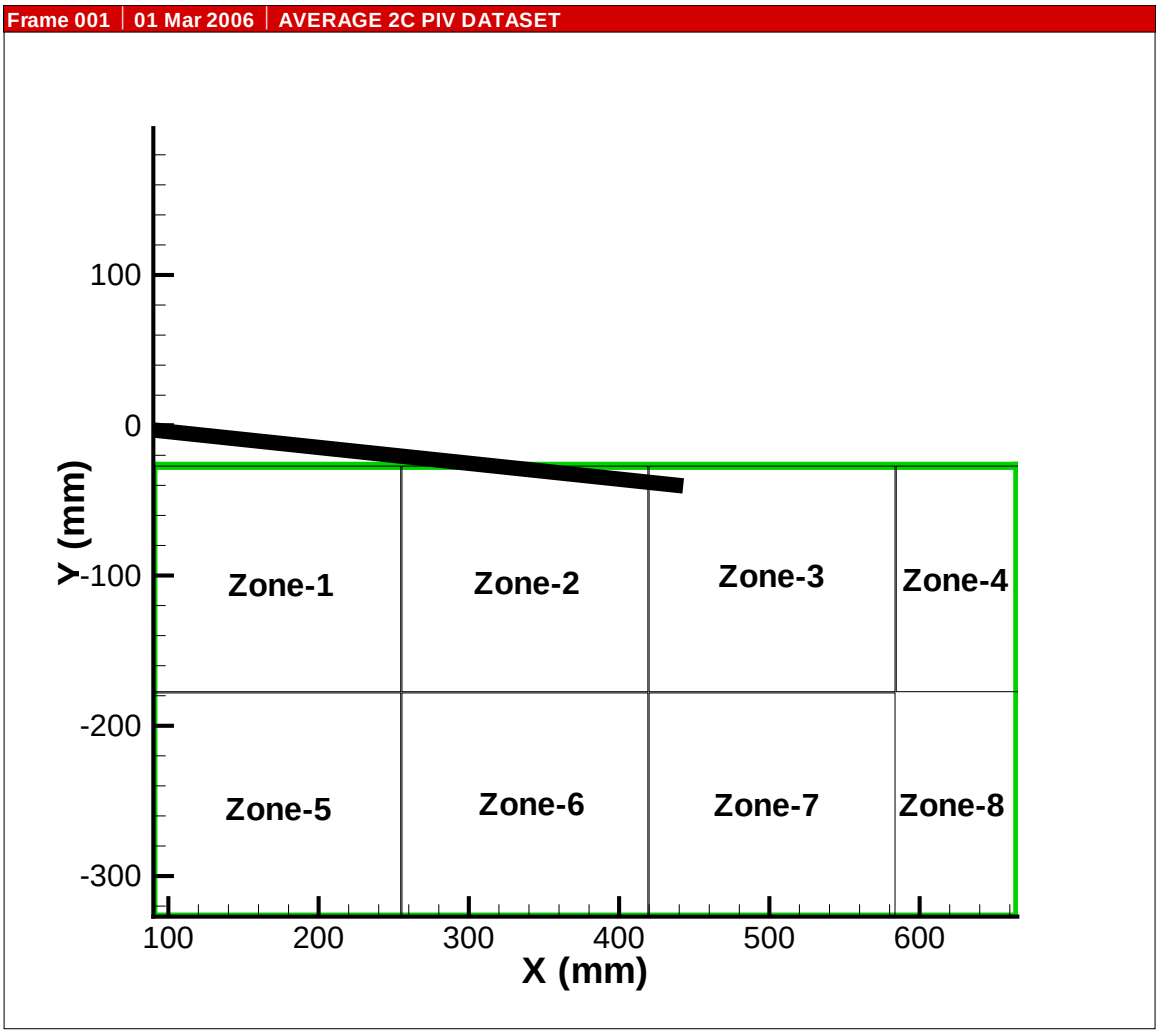

Figure 60: Coverage Area Details

8.4 Results

The results will be plotted for the whole area of coverage to give an overview of the flowfield and to get a holistic view of the flowfield around the ground vortex. This wide area view will then be broken up into 8 zones to get a closer look at the flow features. The coverage area and the details of the eight zones are given in Fig. 60. It is to be noted that the X and Y axes on all the plots are denoted in mm and all the velocity values are in m/s. The total coverage area and the individual zones can also be seen in the figure.

8.4.1 Advance Ratio 0.05

The flowfield at μ of 0.05 is shown in Fig. 61. The tip vortex and the inboard wake can be seen. This is a transitional stage between the recirculation and ground vortex regime. The nascent ground vortex can be seen, though it is raised quite a bit above the ground.

The velocity vectors at zone 1 through zone 8 can be seen from Figs. 62 to 69. The u velocity contours in all the zones can be seen from Fig. 70 to 77. The v velocity contours can be seen from Fig. 78 to Fig. 85.

The tip vortex can be seen with the associated velocity gradient in zone 2 in Figs. 63, 71 and 79. The stagnation region under the rotor where the downflow diverges can be seen in zone 5 (Figs. 66, 74 and 82). The recirculating flow can be seen in zone 6 (Figs. 67, 75 and 83).

8.4.2 Advance Ratio 0.06

The flowfield at μ of 0.06 is shown in Fig. 86. The ground vortex has completely formed. One can also notice that the ground vortex has moved backward and closer to the ground with an increase in advance ratio.

The velocity vectors at zone 1 through zone 8 can be seen from Figs. 87 to 94. The u velocity contours in all the zones can be seen from Fig. 95 to 102. The v velocity contours can be seen from Fig. 103 to Fig. 110.

The core of the ground vortex can be seen in zone 6 (Figs. 92, 100 and 108). The tip vortex can be seen with the associated velocity gradient in zone 2 in Figs. 88, 96 and 104. The stagnation region under the rotor where the downflow diverges can be seen in zone 5 (Figs. 91, 99 and 107).

8.4.3 Advance Ratio 0.07

The flowfield at μ of 0.07 is shown in Fig. 111. The ground vortex is now visible with a tight core and has moved under the rotor. The tip vortex from the previous blade can be seen and it can be seen that the tip vorticity is being incorporated into the ground vortex.

The velocity vectors at zone 1 through zone 8 can be seen from Figs. 112 to 119. The u

velocity contours in all the zones can be seen from Fig. 120 to 127. The v velocity contours can be seen from Fig. 128 to Fig. 135.

The core of the first tip vortex can be seen in zone 2 (Figs. 113, 121 and 129). The tip vortex from the previous blade can be seen with the associated velocity gradient in zone 5 in Figs. 116, 124 and 132. The core of the ground vortex can be seen in zone 6 (Figs. 117, 125 and 133). The separation region ahead of the ground vortex can be seen in zone7 (Figs. 118, 126 and 134).

8.4.4 Advance Ratio 0.08

The flowfield at μ of 0.08 is shown in Fig. 136. The ground vortex is now tighter and has moved further rearward. Two older tip vortices can be seen and the tip vorticity is being ingested into the ground vortex.

The velocity vectors at zone 1 through zone 8 can be seen from Figs. 137 to 144. The u velocity contours in all the zones can be seen from Fig. 145 to 152. The v velocity contours can be seen from Fig. 153 to Fig. 160.

The interaction between the tip vortex and the ground vortex can be seen in zones 5 and 6 (Figs. 141, 149, 157, 142, 150, and 158). The separation region in front of the ground vortex has become considerably bigger and can be seen in zone 7 (Figs. 143, 151 and 159).

8.5 Discussion

Apart from the flow field measurements and ground vortex location that can be used by computational studies for validation, this study highlights two important observations that help us in understanding ground effect operations of rotorcraft better. Firstly, it is clear that the vorticity from the tip vortex is incorporated into the ground vortex, which definitely negates the common opinion that the ground vortex is comprised of the downflow turning back on itself due to the effect of the freestream velocity. This also correlates with the strong 2 per rev component measured by the hotwire around the ground vortex at an advance ratio of 0.07, while the area behind the ground vortex is dominated by the 1 per rev component. This is because the tip vorticity is being incorporated into the ground vortex, thereby introducing a strong 2 per rev component into the ground vortex.

The second important issue is the strength of the ground vortex. No study has yet measured the strength of the ground vortex. This is crucial when computational approaches use vortex models. The strength of the ground vortex was found by integrating the vorticity in a closed boundary around the ground vortex. The strength of the ground vortex from this study was found to be 1.72 m^2/s at an advance ratio of 0.08. Laser Doppler Velocimetry studies of this rotor found that the circulation of the tip vortex at its formation was 0.89 m^2/s [73], which reduced to 0.42 m^2/s at a vortex age of 20 ° [53]. The ground vortex is more than four times as strong as the tip vortex. The ground vortex appears to be a reservoir of vorticity that is added by the tip vortices. The ground vortex builds up its vorticity and then periodically sheds, which matches earlier observations and hotwire measurements done in this study. This would explain the "puffing" fluctuation that various authors have observed, who are cited in Chapter-1, and which was seen in the flow visualization portion of this study.

8.6 Error Estimation

Errors in PIV measurements can be of five types [59]. They are:

1. Random error due to noise and other measurement uncertainties
2. Bias error due to sub-pixel interpolation
3. Gradient error resulting from rotation and deformation of the flow within an interrogation spot leading to loss of correlation
4. Tracking error resulting from the inability of a particle to follow the flow
5. Acceleration error caused by approximating the local Eulerian velocity from the Lagrangian motion of tracer particles

Out of these five, the last three cannot be avoided. They can only be minimized by careful planning, by optimizing the size of the particles and the pulse separation to give the best results for the flow condition. The steps that were taken to plan these aspects were outlined at the beginning of this chapter. It is also quite difficult to quantify the last three errors.

As far as the bias error is concerned, it is manifested by a phenomenon called pixel locking, where the sub-pixel interpolation causes the velocity to be biased toward integer values of pixel shift. One way of preventing this phenomenon is to check the histograms of the pixel shift after each run to ensure that there is not a cluster around an integer value. This was carried out to obviate the possibility of this error. It has also been shown that bias error becomes sizable usually when particle image diameter ¡ 1 pixel [59]. Therefore, one can make a reasonable conclusion that this error is not sizable in this study.

It has been shown that random error scales with the particle image diameter [1] and is given by the relation in Equation. 12, where σ is the random error, d_p is the particle image diameter and c is an empirical constant that usually lies between 0.05 and 0.10.

$$\sigma = c \times d_p \tag{12}$$

Thus for this experiment the random error ranged from 0.10 pixels in the best case (0.05 x 2 pixels) to 0.4 pixels in the worst case (0.10 x 4 pixels).

The total measurement error can be quantified with Equation. 13 [63].

$$\epsilon_m \leq W_p/U_p \times 3/(ZM) \times \sigma_i \tag{13}$$

where W_p is the maximum out-of-plane component of the flow velocity, U_p is the maximum in-plane component of the flow velocity, Z is the light sheet thickness, M is the magnification, and σ_i is the random measurement error in the image plane.

W and U were taken to be 15 m/s from the hotwire measurements and the preliminary PIV measurements, both of which indicated a maximum velocity of approximately 14 m/s. The light sheet thickness was maintained between 4 and 5 mm, and the magnification of the camera was 1/16. σ as already shown varied from 0.10 pixels in the best case to 0.4 pixels for the worst case. The pixel size was 4.65 μm. σ_i therefore amounted to 4.65 $\times$ $10^{-}6 \times \sigma$. Taking these factors into account, the measurement error in the best case was 0.46% and in the worst case was 1.86%. This amounted to an absolute error of 0.07 m/s and 0.26 m/s respectively based on a 15 m/s maximum velocity.

8.7 Conclusion

PIV measurements of the flowfield around a ground vortex at advance ratios between 0.05 and 0.08 was carried out. The flowfield was quantified and the precise location of the ground vortex was mapped. It was found that the ground vortex ingests vorticity from the tip vortex. The strength of the ground vortex was found to be more than 4 times the tip vortex value.

CHAPTER IX

CONCLUSIONS AND RECOMMENDATIONS

In rotary-wing vehicles, the unsteady phenomena reported by operators IGE have not been fully explained yet. This regime of flight has seen the most number of accidents over the past 30 years. Developing a thorough understanding of the various flight regimes close to the ground will help us in accurately predicting these phenomena, which will help pilots to better anticipate the control inputs required for safe flight.

So far, there is considerable uncertainty as far as explaining the nature of close to ground flight is concerned. This study aimed at laying out a research plan that addressed various issues that were garnered from study of previous literature, phenomena observed during experiments and inputs provided from operators and research advisers at the Army Research Office and Sikorsky Aircraft Corporation. The outline of this plan was laid out in Fig. 10. The first aim of this study was to show that unsteadiness actually existed in ground effect that was absent while flying away from the ground. Once that was shown, the regimes of flight in ground effect were visualized.

The next step was to divide the study into two prongs. The first was the unsteady approach that looked at quantifying the unsteady fluctuations that seemed to occur even while the helicopter was flying at a steady advance ratio close to the ground. It also aimed at understanding the long time scale fluctuations that have been reported by pilots in the past.

The second prong of the approach was to examine the quasi-steady effects of flying close to the ground. To this end, the effect of fuselage cross-section shape on fuselage loads was investigated. This was a recommendation from Sikorsky researchers and Army/ NASA reviewers who felt that operators seemed to feel different loads depending on the shape of the fuselage of the helicopter that they were piloting close to the ground. The other aspect was to quantify the flowfield around the ground vortex using PIV, and to better

understand the structure of the ground vortex. The study also provided power data for the experimental configuration to help numerical researchers to correlate their results with experimental data.

9.1 Summary of Results

9.1.1 General Results

1. Two distinct flow regimes were seen for a rotor flying at low advance ratios in ground effect. Recirculation of the rotor wake occurs at lower advance ratios and formation of a ground vortex occurred above an advance ratio ≈ 0.058.

2. The ground vortex moves further downstream and decreases in size as the advance ratio increases.

9.1.2 Results: Unsteady Phenomena

1. The jitter of the tip vortices were quantified during flow visualization and was found to be much greater IGE when compared to OGE.

2. The low frequency fluctuations in the inflow plane ahead of the rotor occur at about 1 to 2 Hz and appear only during the recirculation regime. These oscillations stop above an advance ratio of 0.06. These fluctuations were further quantified using hotwire measurements.

3. The rear of the vortex is dominated by the 1 per rev component, and has high amplitude, high frequency oscillations in it. Low frequency oscillations are seen near the ground ahead of the ground vortex and is caused due to the separation of the flow ahead of the ground vortex. Two per rev components indicating ingestion of tip vorticity is seen around the ground vortex.

4. Hotwire measurements showed that the fluctuation frequency in the inflow region was a function of the rotor height, inflow ratio and forward velocity. This would help in generalizing the results and scaling it for other rotors.

5. The fluctuations in the inflow and around the ground vortex do not significantly affect fuselage loads

9.1.3 Results: Quasi-steady Phenomena

1. The downforce on a circular cross-section fuselage is much greater than that on the flattened fuselage. Both fuselages show a decrease in downforce between advance ratio of 0.06 and 0.08 with the formation of the ground vortex. The magnitude of the reduction of downforce is greater in the case of the flattened fuselage.

2. There is a sudden decrease in drag force between advance ratio of 0.06 and 0.08 with the formation of the ground vortex.

3. The two cross-sectional fuselages have distinct differences in the case of side force. In ground effect, the circular cross-section sideforce changes direction at an advance ratio of 0.07, which is accompanied by a sudden forward shift of the point at which the side force acts. This behavior is not seen in the case of the flattened fuselage. Thus, it is the circular cross-section fuselage's sideforce IGE that is distinctly different from the sideforces felt in other regimes of flight.

4. It was found that the C_P OGE increased linearly with advance ratio. The C_P IGE for this fixed pitch rotor was higher until the formation of the ground vortex, when it matched the OGE value. It then increased again between advance ratios of 0.07 and 0.09. The C_P got back to the OGE value at an advance ratio of 0.1, when the ground vortex was overrun.

5. The flowfield around the ground vortex was quantified using PIV and the precise location of the ground vortex was mapped. It was found that the ground vortex ingests vorticity from the tip vortex. The strength of the tip vortex was found to be more than 4 times the tip vortex value.

9.2 Conclusions

1. Unsteadiness IGE: The unsteadiness IGE is considerably higher than that seen OGE.

The increased jitter of the tip vortices IGE indicates that there are considerable interactions between the preceding vortices and the ground vortex.

2. Determination of long time disturbance: The recirculation fluctuation frequency at the upwind tip of the rotor disk was related to the inflow ratio, height above the ground and the forward velocity. The measured results matched this relation very closely. This will have an effect on the rotor thrust. More significantly, it will have a long time fluctuating effect on the hub moments. The relation derived in this study will help in scaling the results to a real life scenario.

3. Structure of ground vortex: The hotwire study of the ground vortex revealed 2 per rev components on the periphery of the ground vortex. The ground vortex incorporates tip vorticity, and not just a separation induced vortex as postulated by various authors, who have compared it to the horseshoe vortex formed by a jet in crossflow. This correlates with the PIV study also revealed that the high velocity edge of the ground vortex was being fed by the vorticity from the tip vortices.

4. Loads and fuselage shape: It was seen that the sideforce felt by a circular crosssection fuselage IGE was distinctly different from that felt by the flattened fuselage. The sideforce behavior IGE of the circular crosssection fuselage was also different from its behavior OGE. The change in sideforce of a circular crosssection fuselage is accompanied by a sudden change in the moment. This implies that the pilot of a circular crosssection fuselage is most likely to encounter unexpected sideforces when flying close to the ground. This quantifies the intuitive difference reported by helicopter operators of handling differences based on fuselage shapes for this particular configuration as a function of advance ratio.

5. Strength of ground vortex: The flowfield around the ground vortex was quantified using PIV and it was shown that the strength of the ground vortex was more than four times greater than the tip vortex. This implies that the performance of a helicopter close to the ground would be dominated by the effects of the tip vortex.

9.3 Recommendations

The following recommendations are made based on the results from this research study.

1. The recirculation fluctuations seen in the inflow plane are long time scale disturbances that can be modeled with potential methods. A scaling relation has been proposed to relate the disturbance to flow parameters. This function has to be related to other conditions.

2. Another important issue is the effect of dynamic operations close to the ground. Ground effect experiments done on fixed wing aircraft point out two key differences between IGE wind tunnel experiments and real world flight close to the ground. The first is the presence of a ground boundary layer in wind tunnel experiments with a fixed ground plane [13] and it is often addressed with the use of a moving ground belt. The second is the effect of a dynamic ground plane that incorporates variable sink rates, gusts, and dynamically varying pitch angles [10], [7], [40]. The effect of the ground boundary layer is not expected to be significant since the ground vortex has been shown to be much stronger than the tip vortex, and will therefore be much stronger than the ground boundary layer. The other issue that can be explored is the effect of dynamic changes in helicopter pitch angle, sink rates, sideward motion and gusts.

3. The experiments with the fuselage were with generic models. It was shown that the side force on a circular crosssection fuselage was distinctly different IGE from a flattened fuselage. Lower order models can be derived to convert these loads into handling qualities.

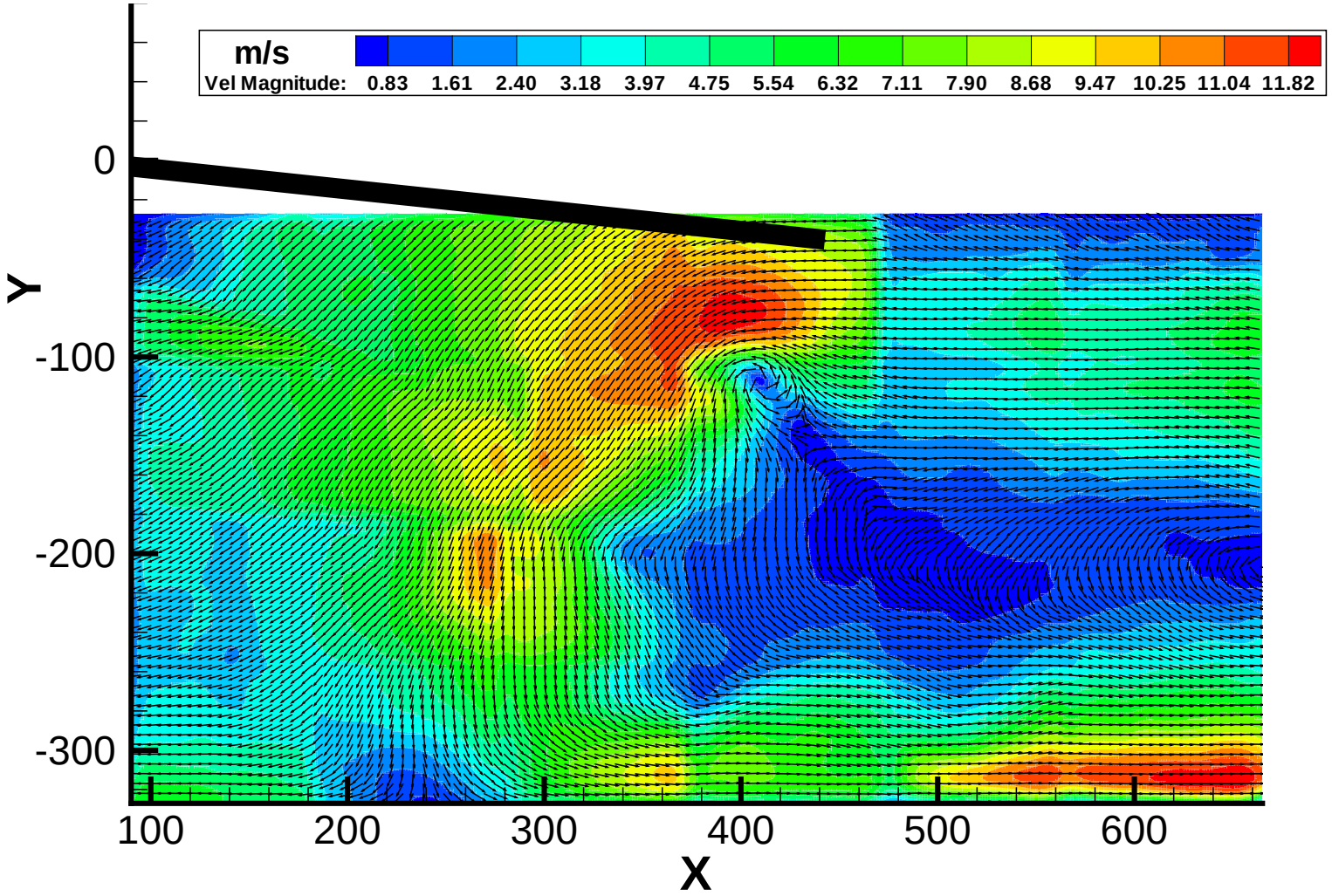

Figure 61: Flowfield at Advance Ratio 0.05. Axes in mm.

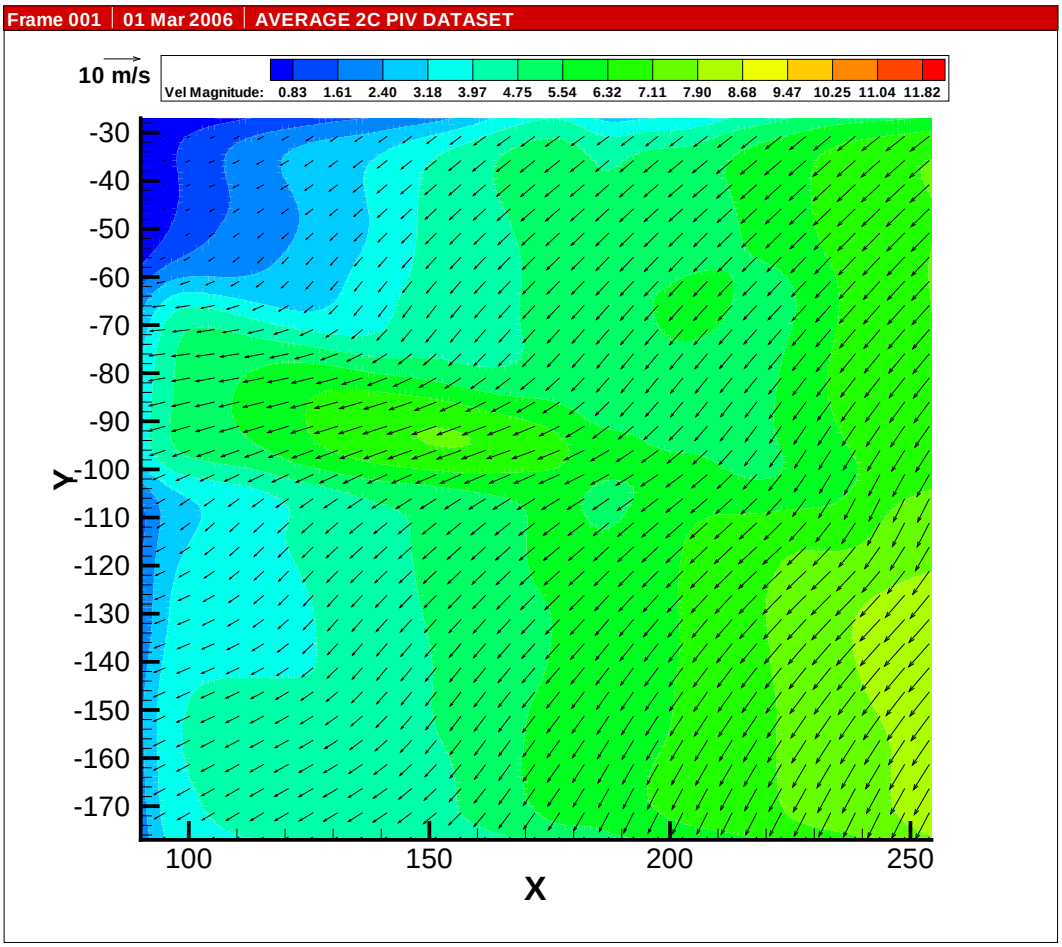

Figure 62: Flowfield at Advance Ratio 0.05- zone 1. Axes in mm.

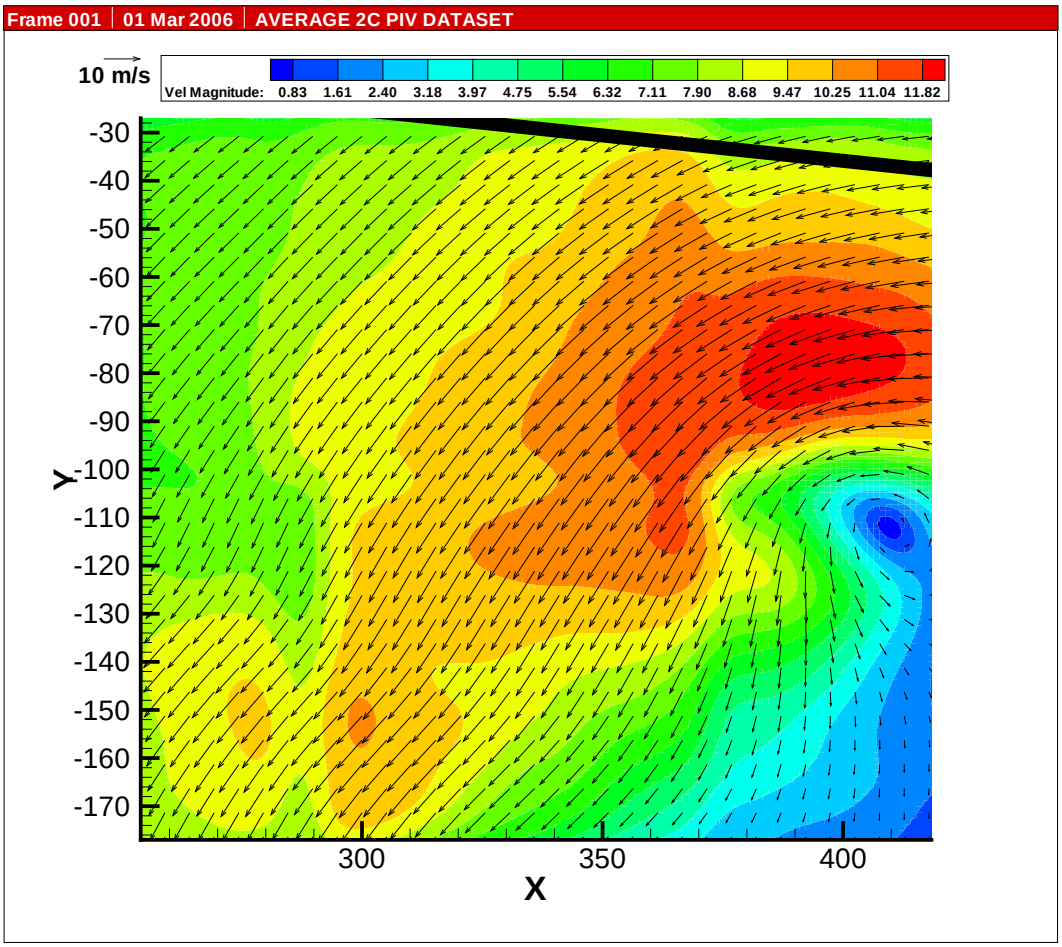

Figure 63: Flowfield at Advance Ratio 0.05- zone 2. Axes in mm.

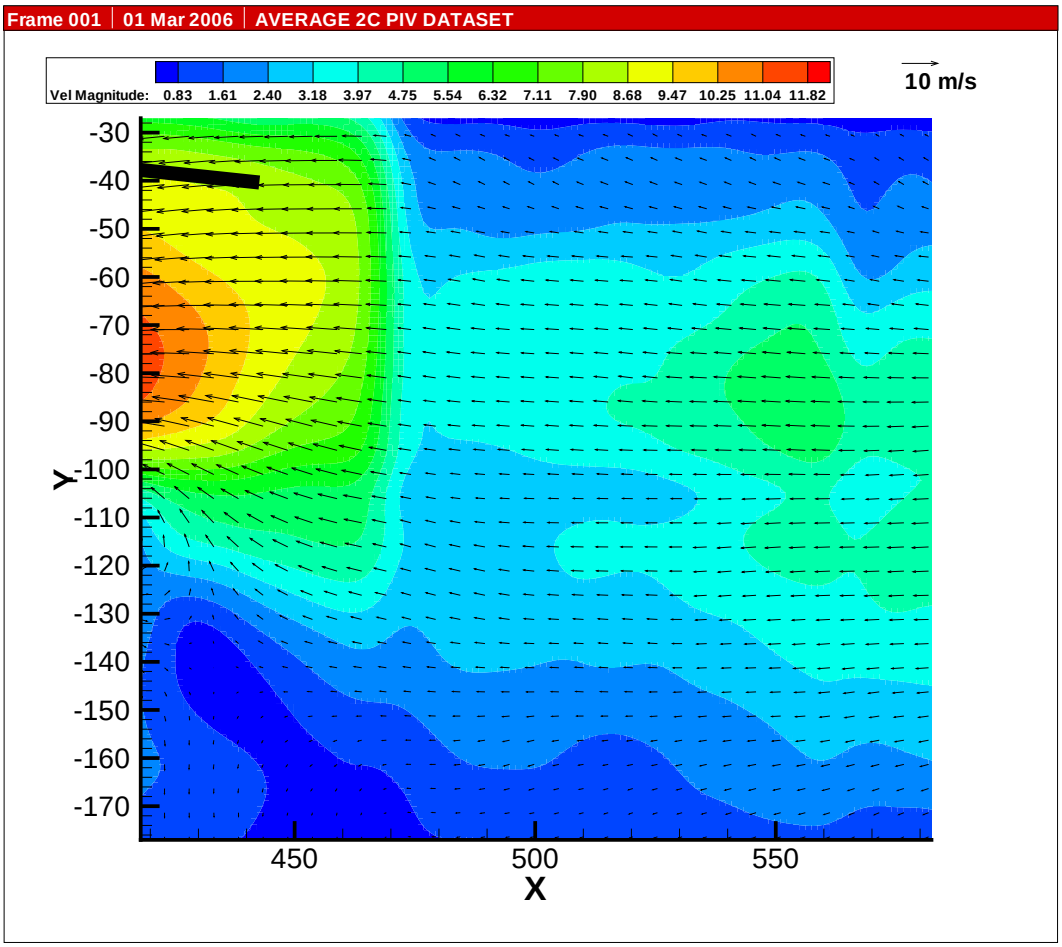

Figure 64: Flowfield at Advance Ratio 0.05- zone 3. Axes in mm.

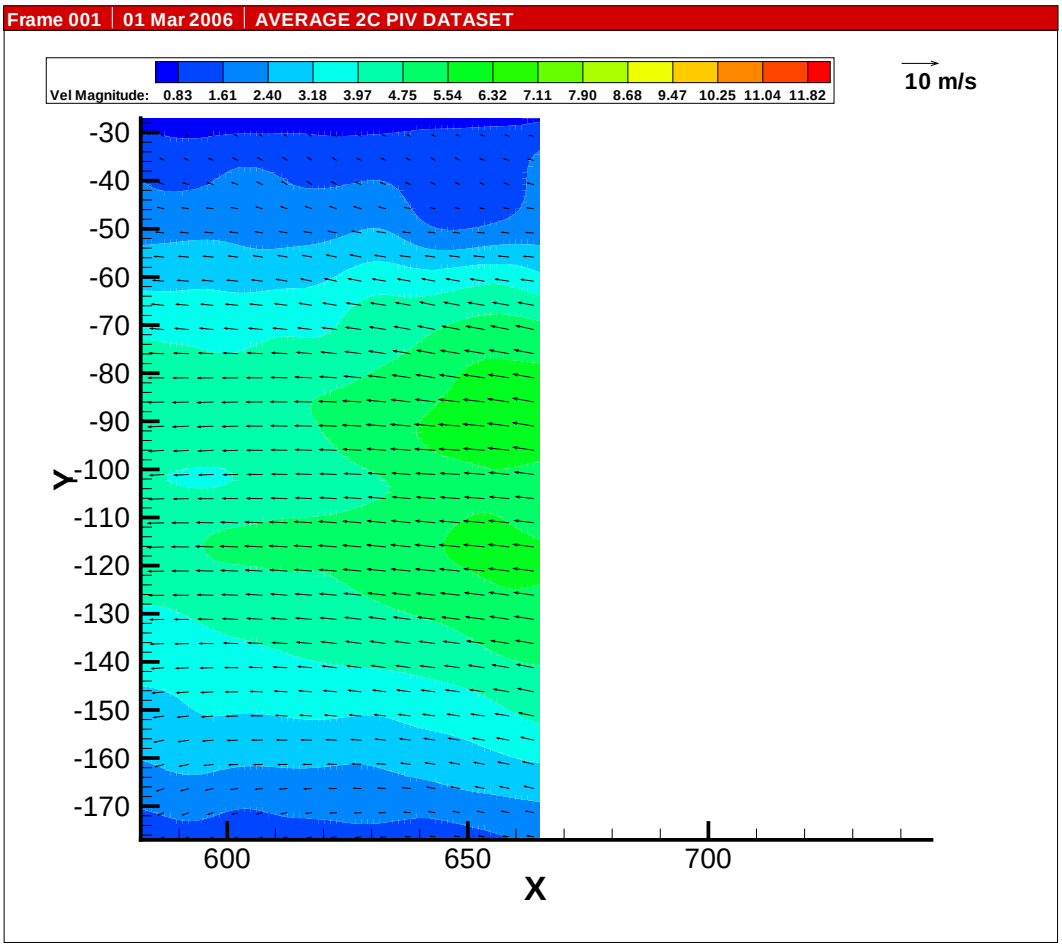

Figure 65: Flowfield at Advance Ratio 0.05- zone 4. Axes in mm.

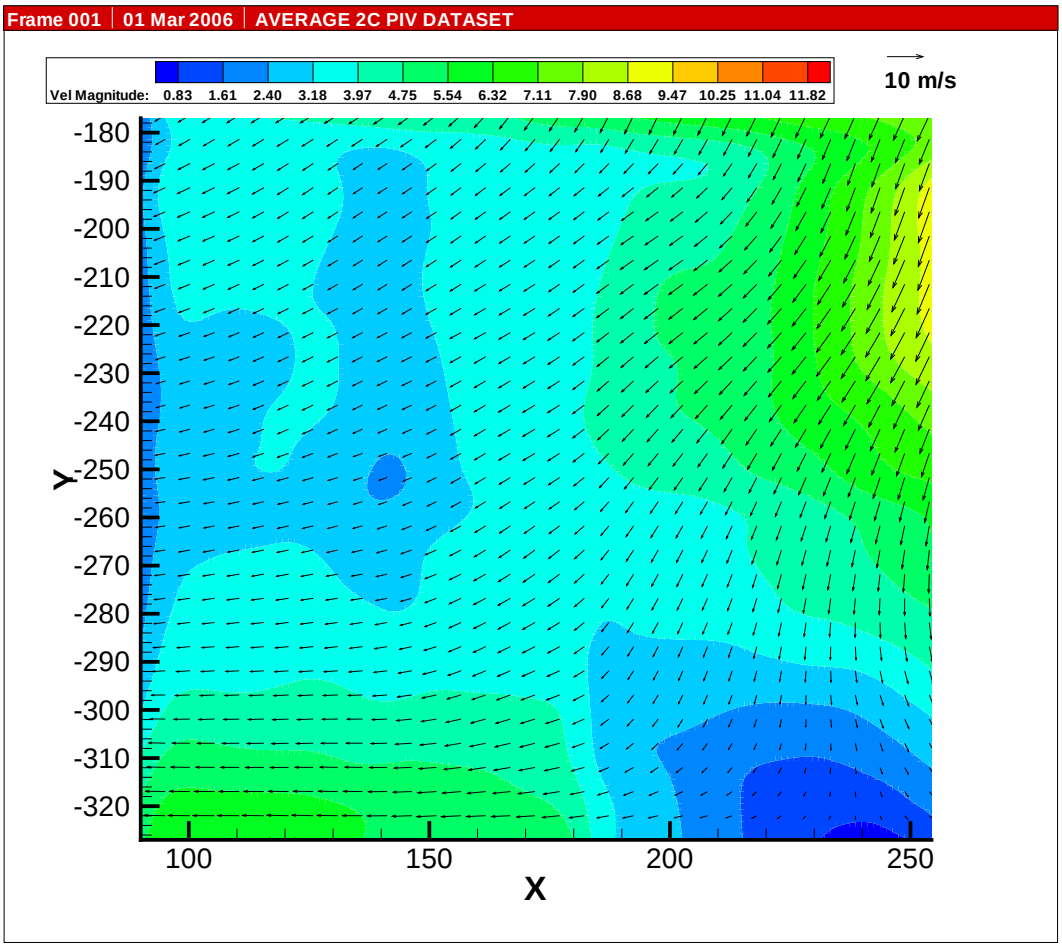

Figure 66: Flowfield at Advance Ratio 0.05- zone 5. Axes in mm.

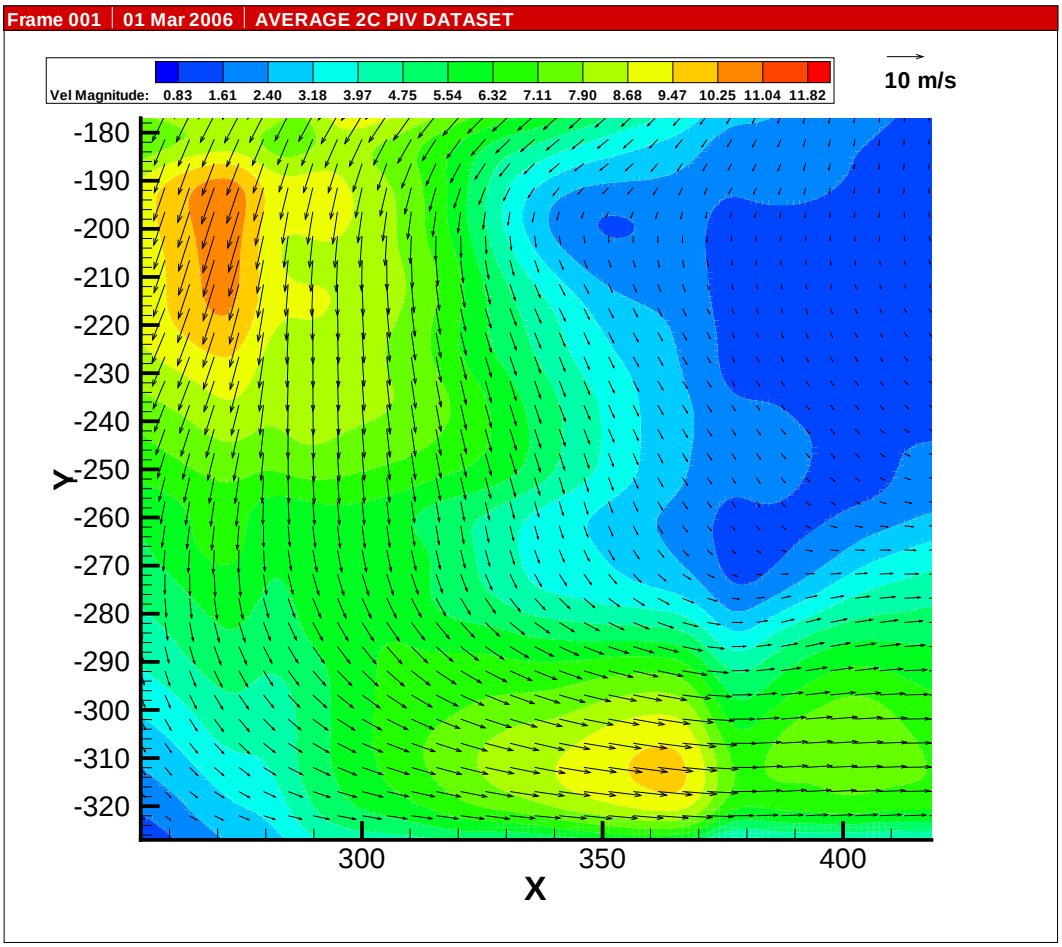

Figure 67: Flowfield at Advance Ratio 0.05- zone 6. Axes in mm.

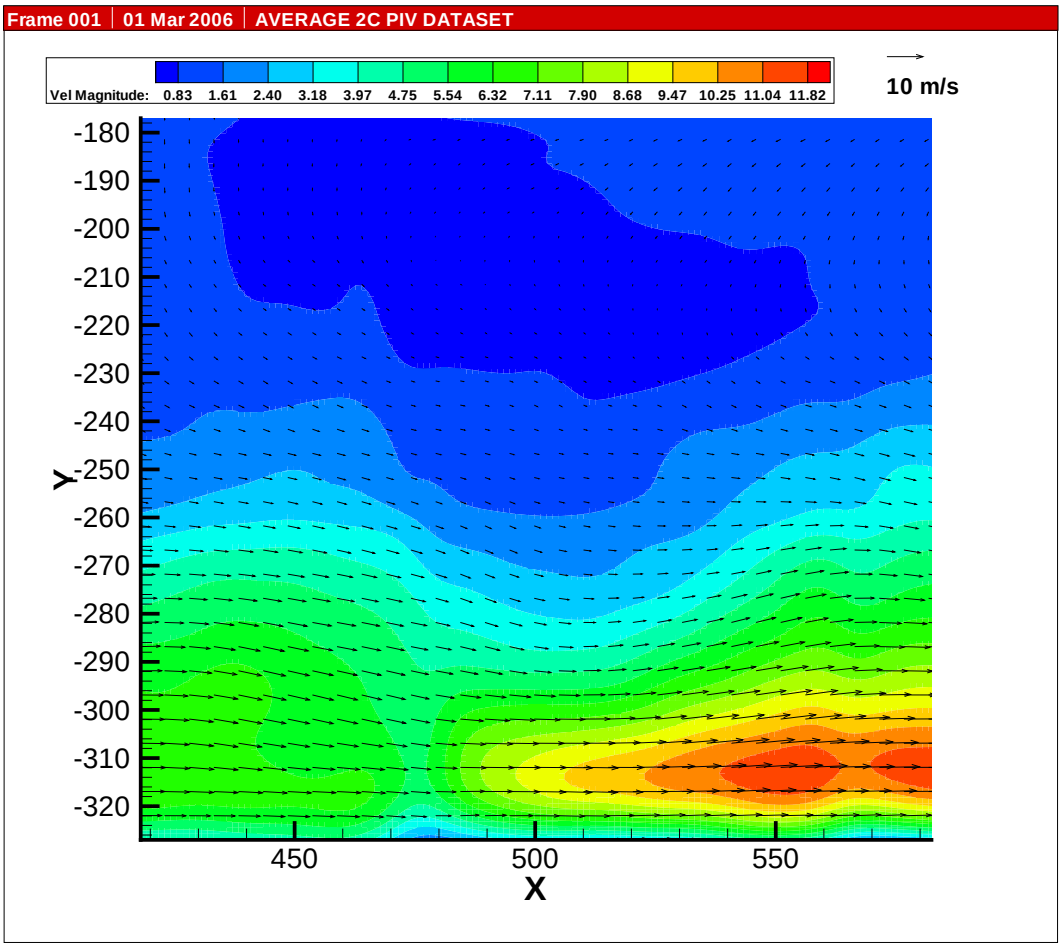

Figure 68: Flowfield at Advance Ratio 0.05- zone 7. Axes in mm.

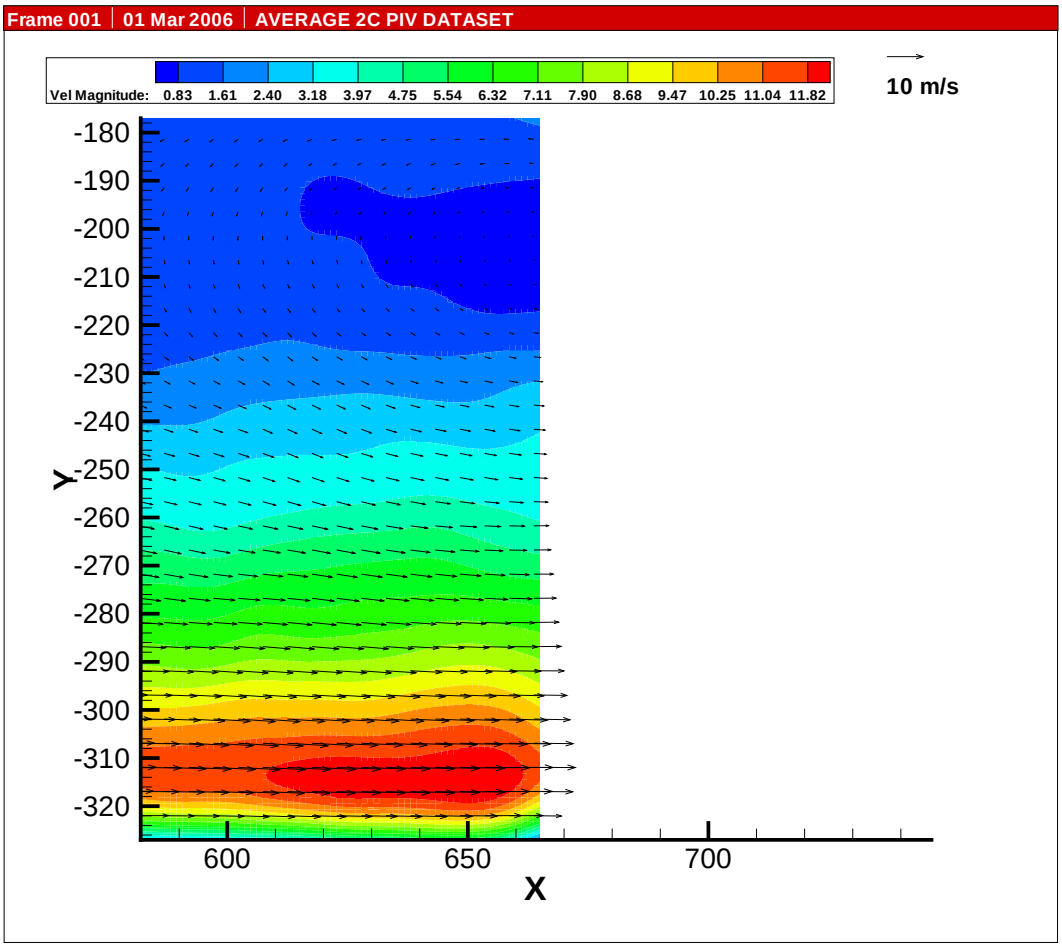

Figure 69: Flowfield at Advance Ratio 0.05- zone 8. Axes in mm.

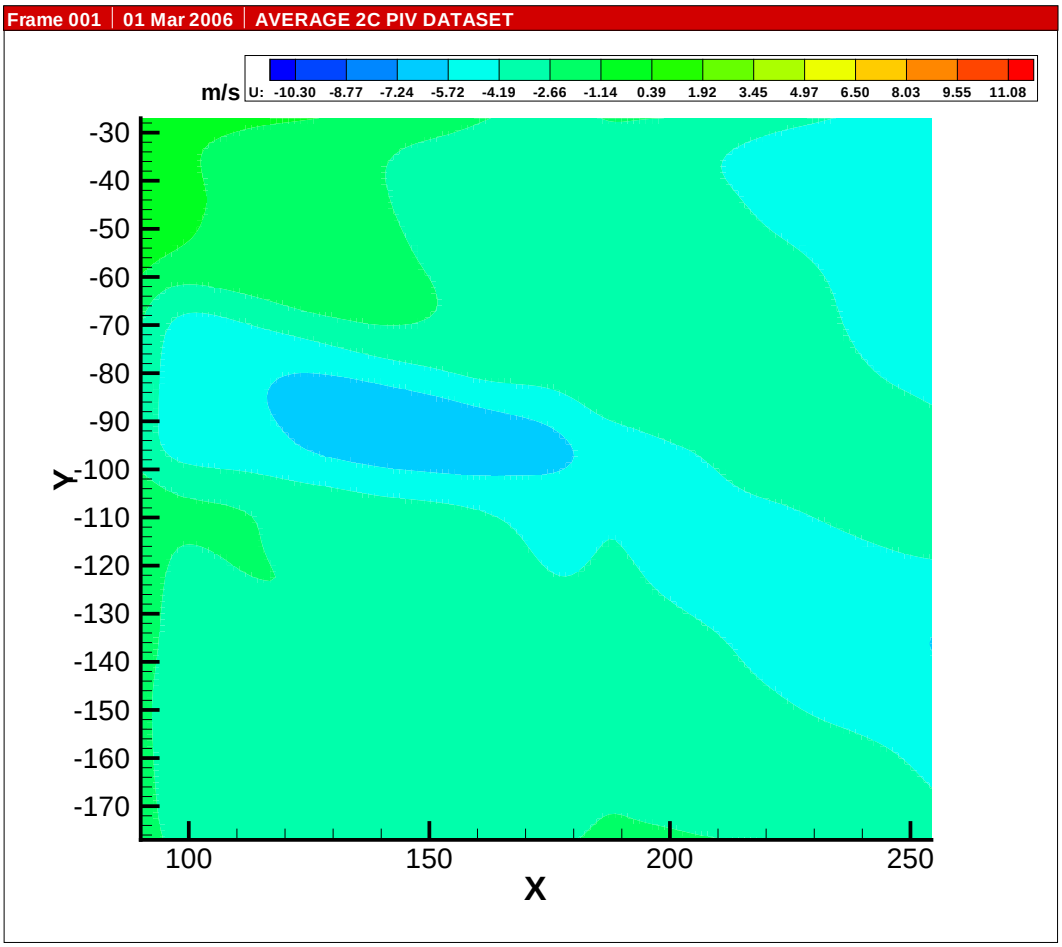

Figure 70: u Velocity at Advance Ratio 0.05- zone 1. Axes in mm.

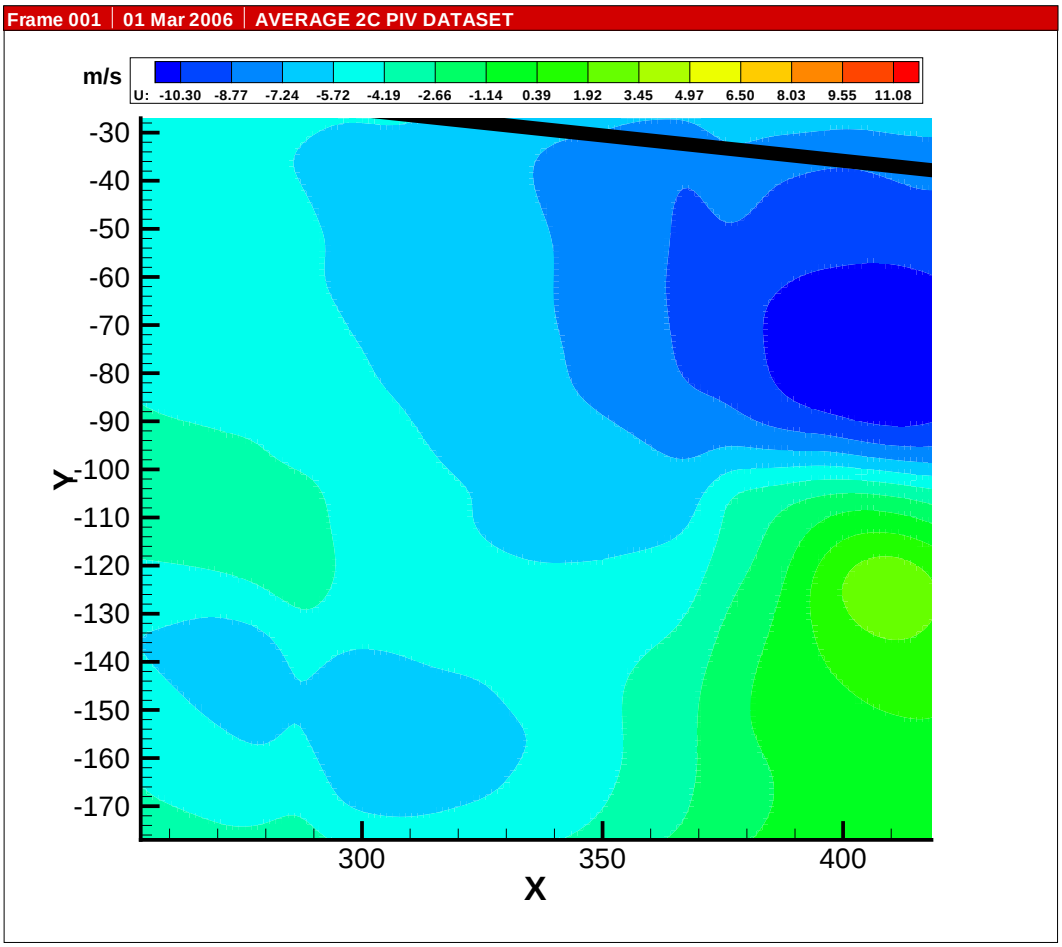

Figure 71: u Velocity at Advance Ratio 0.05- zone 2. Axes in mm.

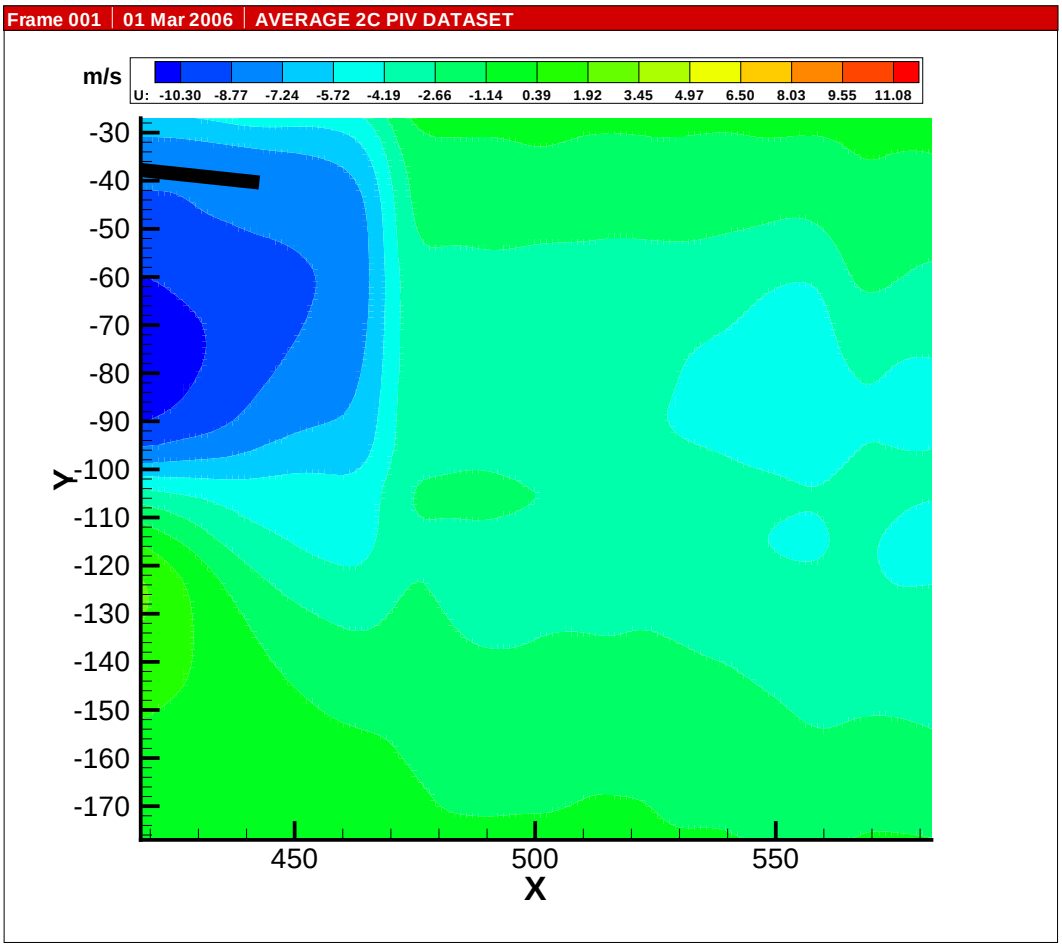

Figure 72: u Velocity at Advance Ratio 0.05- zone 3. Axes in mm.

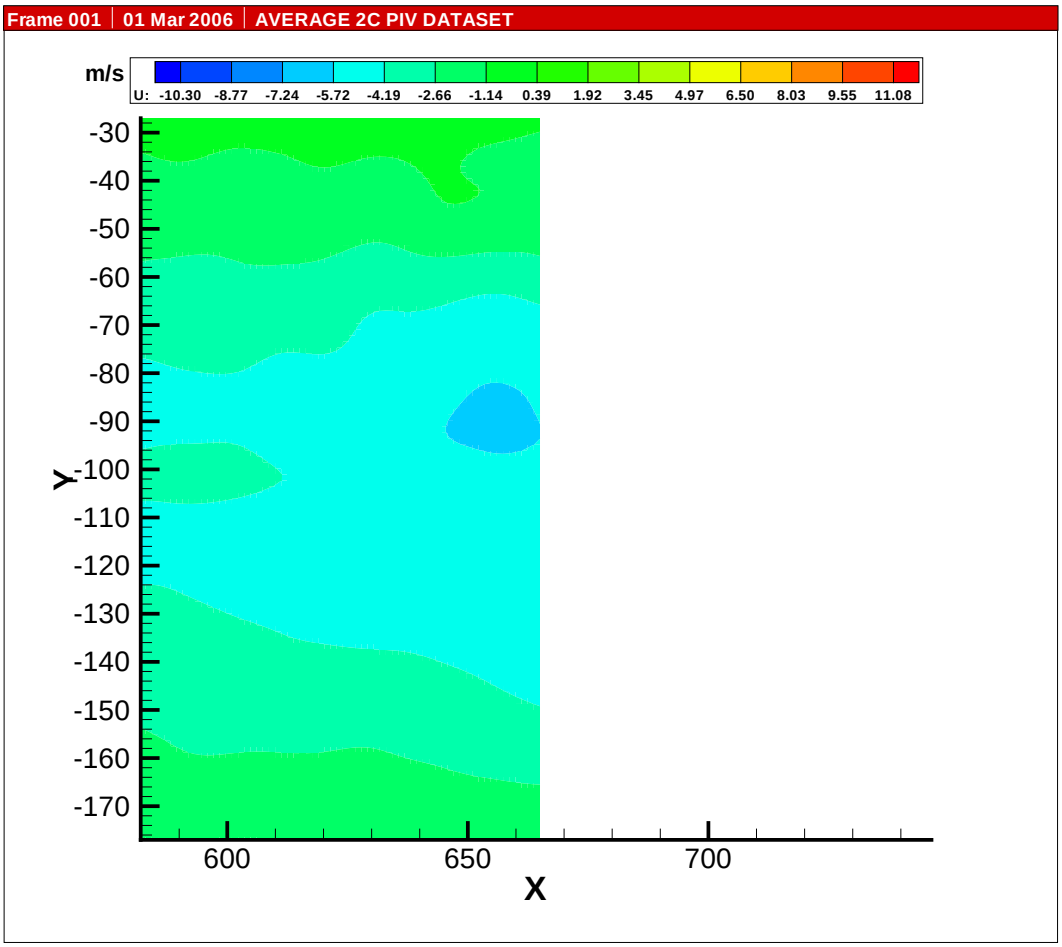

Figure 73: u Velocity at Advance Ratio 0.05- zone 4. Axes in mm.

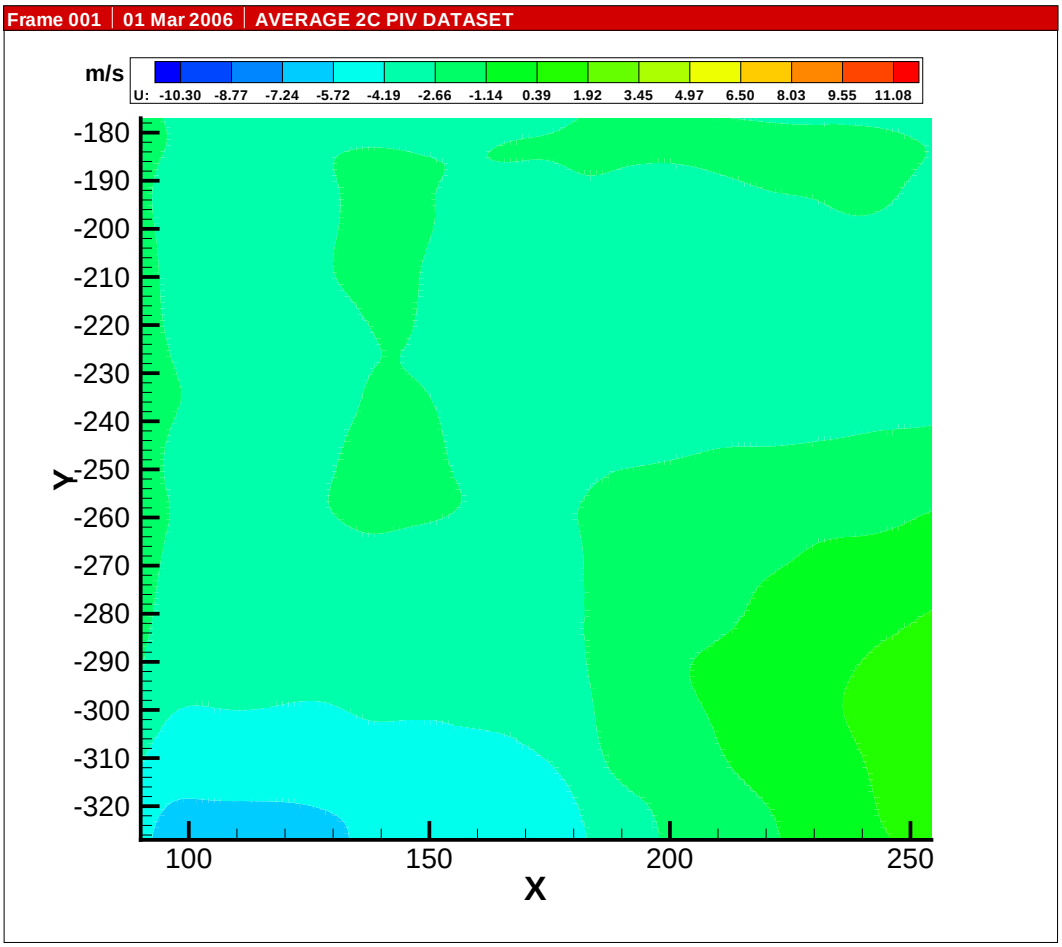

Figure 74: u Velocity at Advance Ratio 0.05- zone 5. Axes in mm.

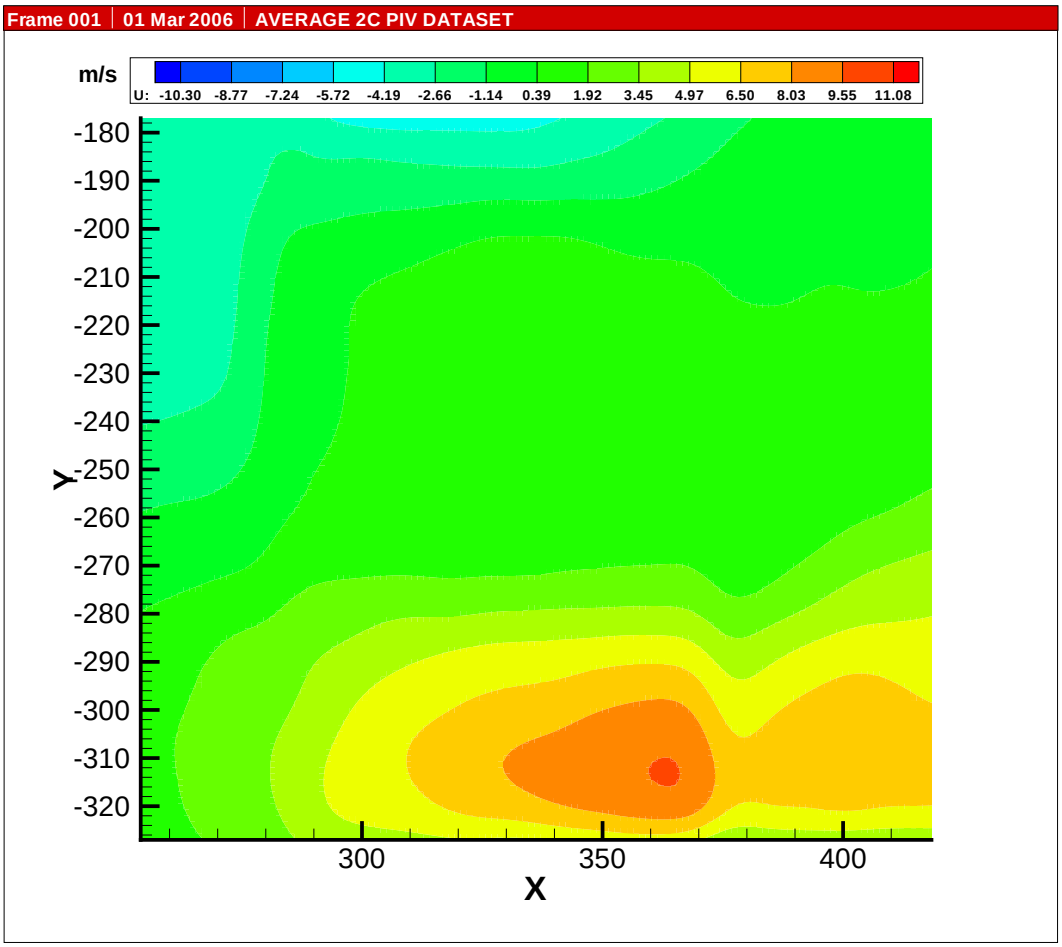

Figure 75: u Velocity at Advance Ratio 0.05- zone 6. Axes in mm.

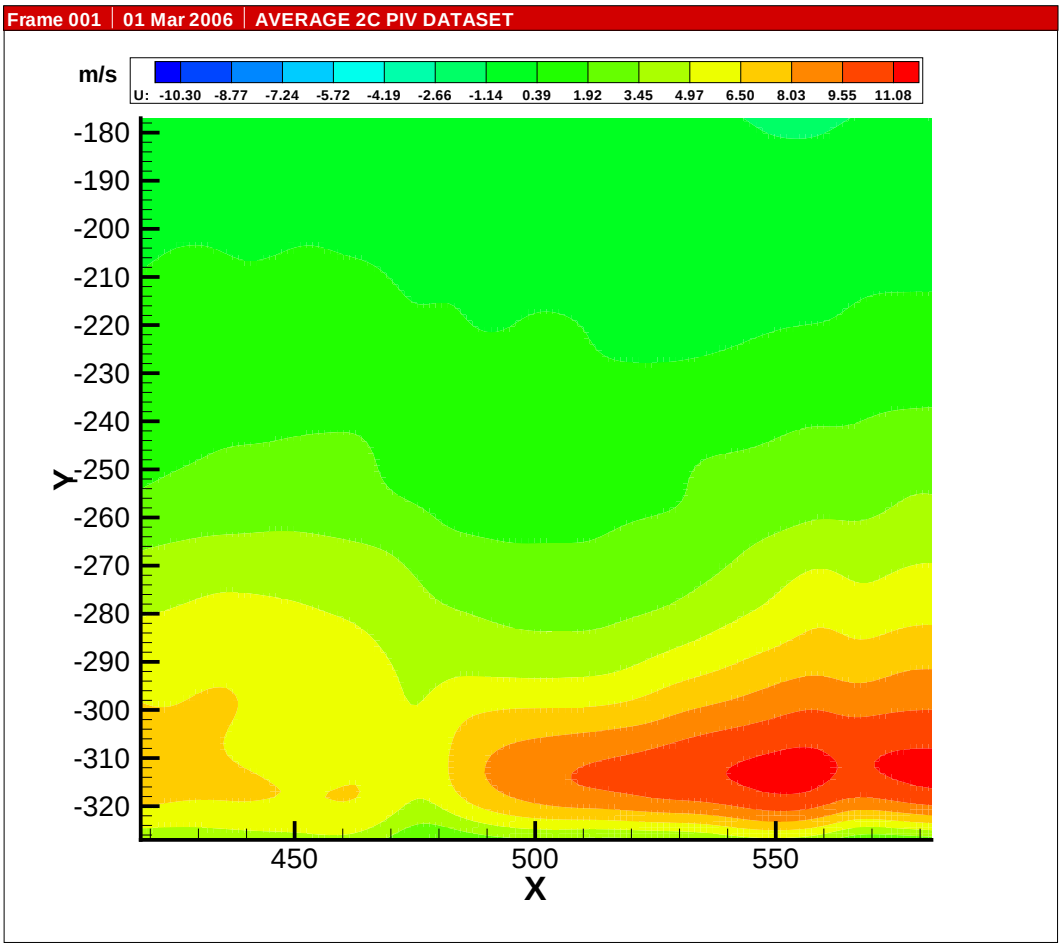

Figure 76: u Velocity at Advance Ratio 0.05- zone 7. Axes in mm.

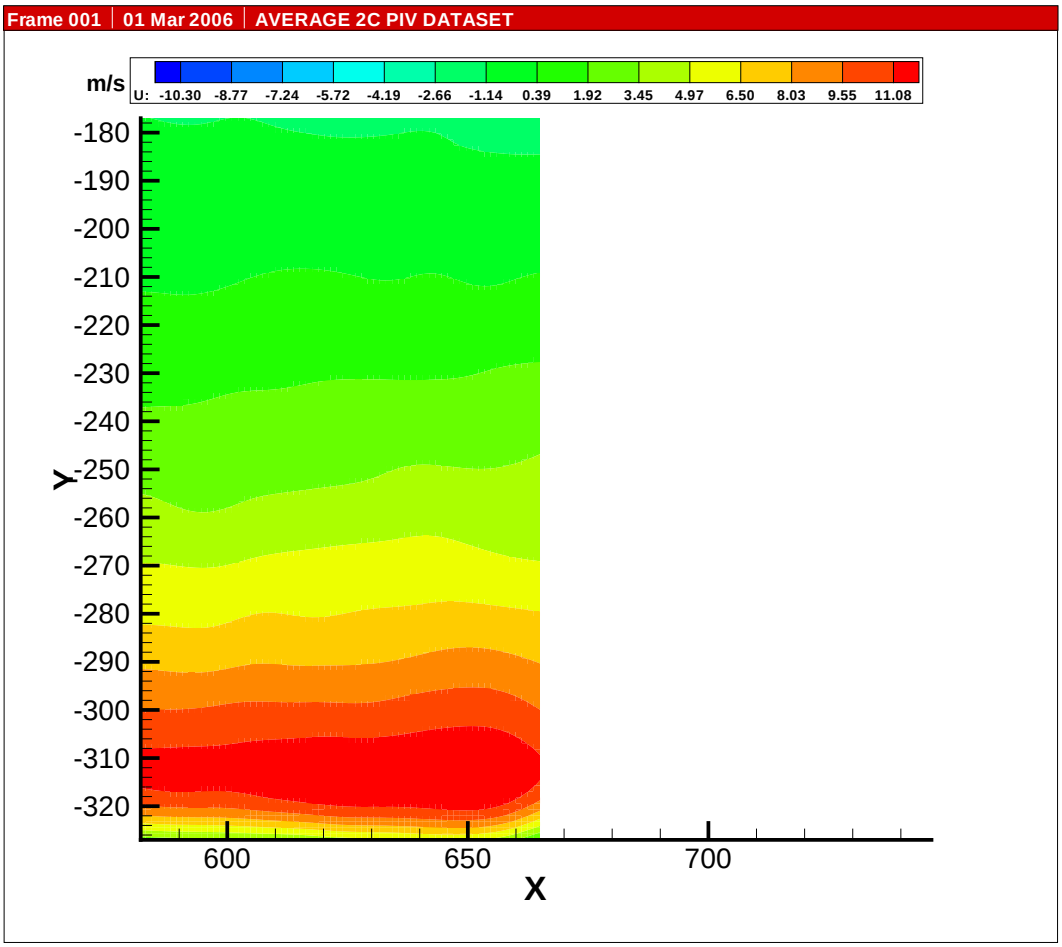

Figure 77: u Velocity at Advance Ratio 0.05- zone 8. Axes in mm.

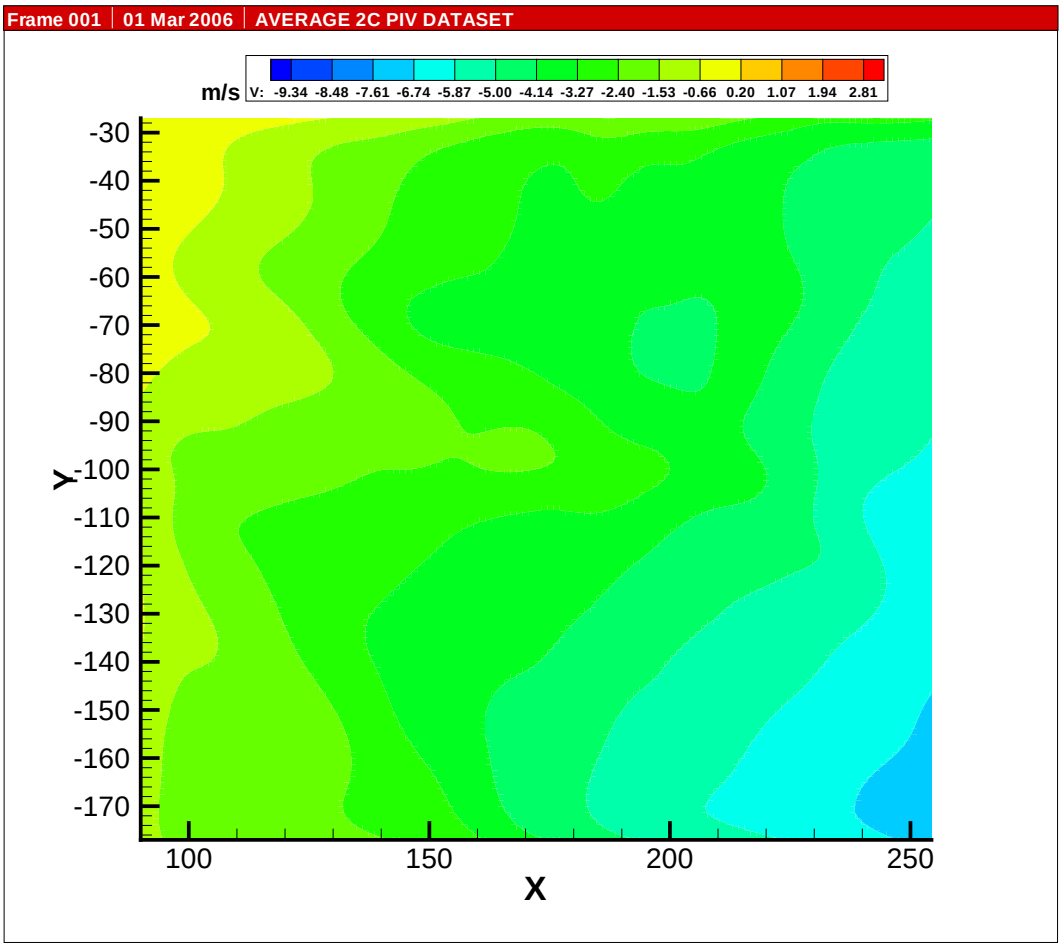

Figure 78: v Velocity at Advance Ratio 0.05- zone 1. Axes in mm.

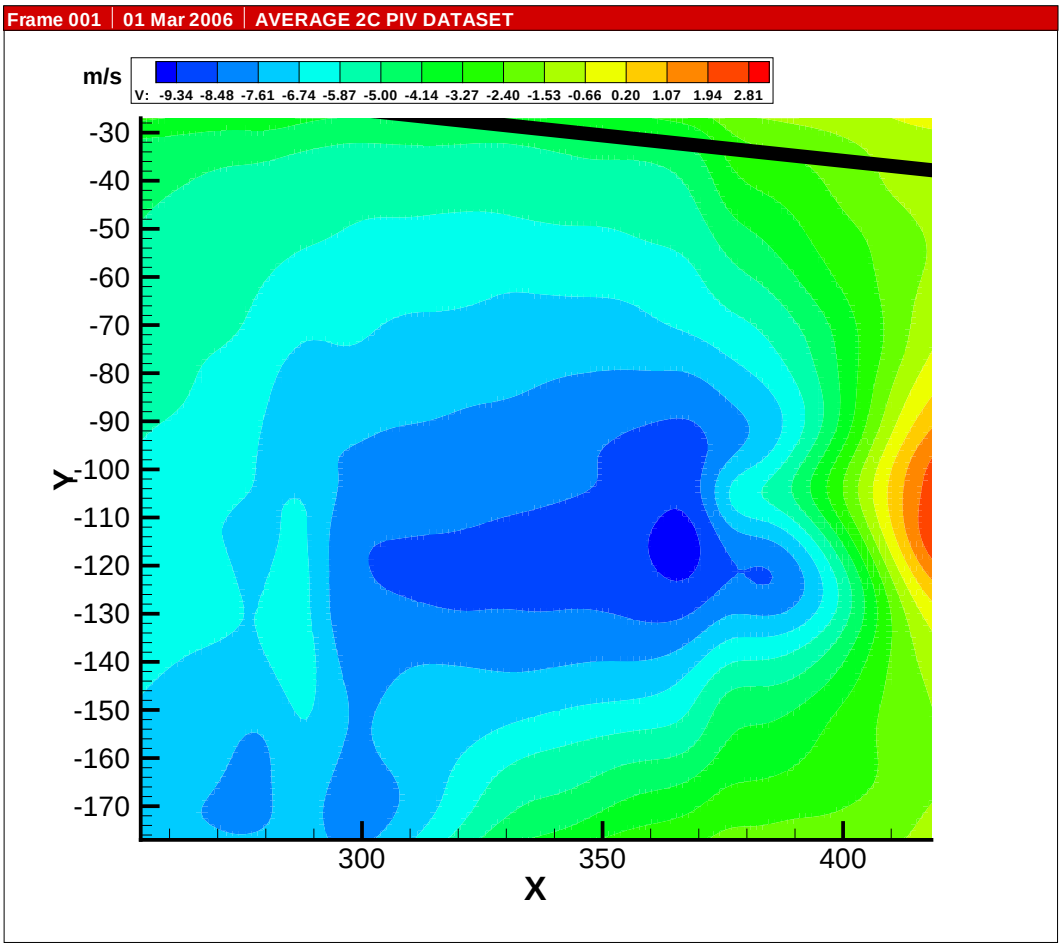

Figure 79: v Velocity at Advance Ratio 0.05- zone 2. Axes in mm.

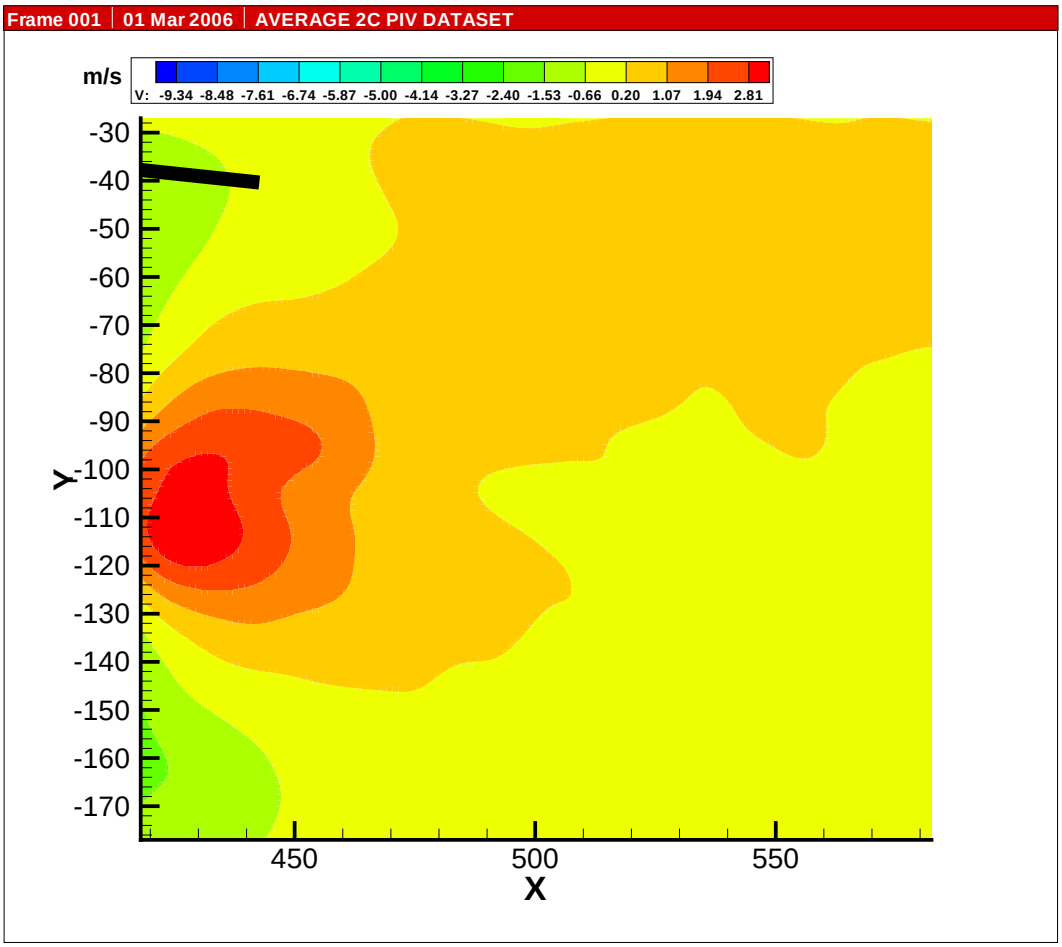

Figure 80: v Velocity at Advance Ratio 0.05- zone 3. Axes in mm.

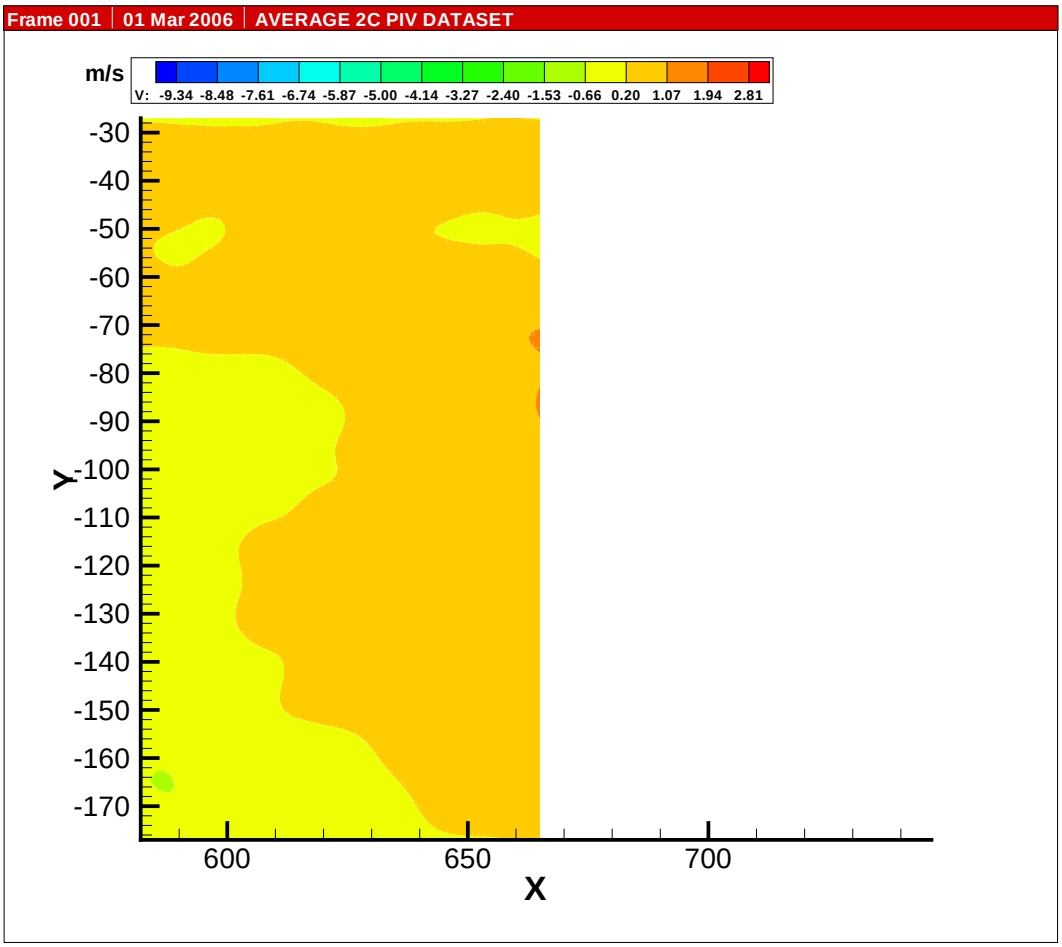

Figure 81: v Velocity at Advance Ratio 0.05- zone 4. Axes in mm.

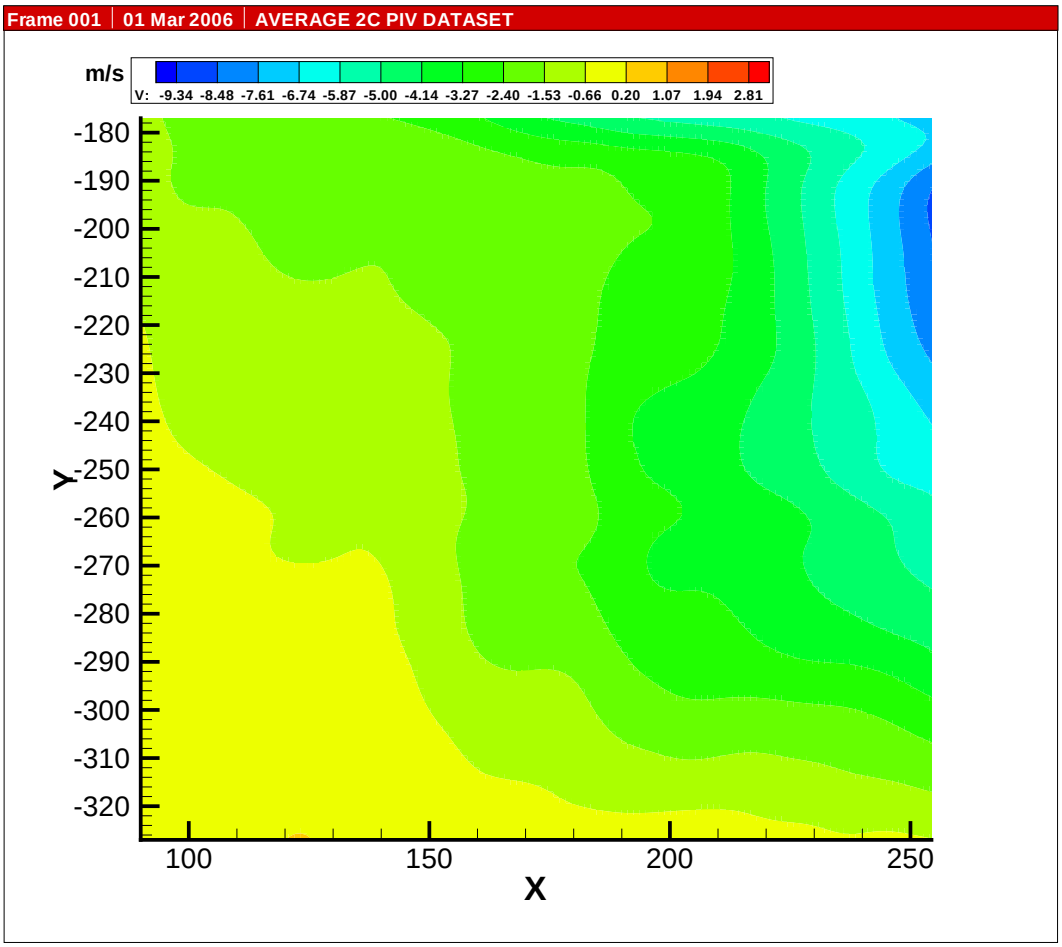

Figure 82: v Velocity at Advance Ratio 0.05- zone 5. Axes in mm.

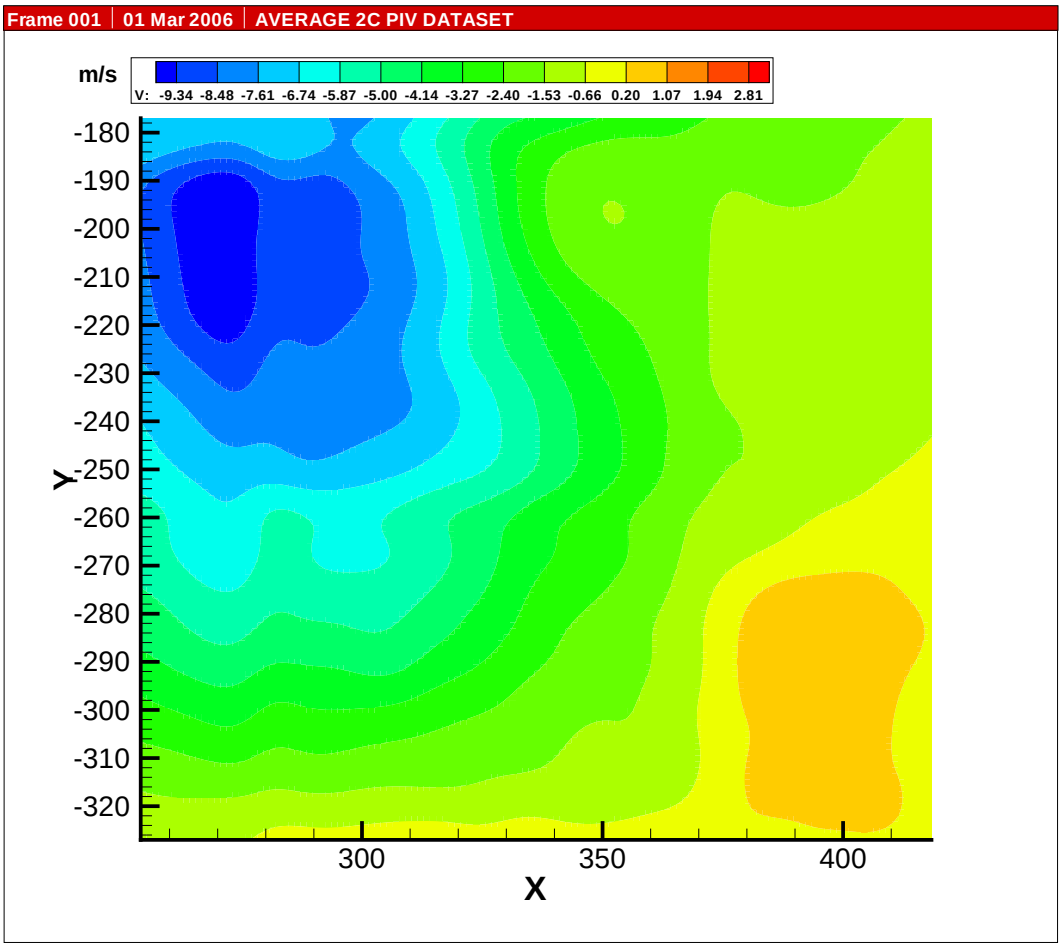

Figure 83: v Velocity at Advance Ratio 0.05- zone 6. Axes in mm.

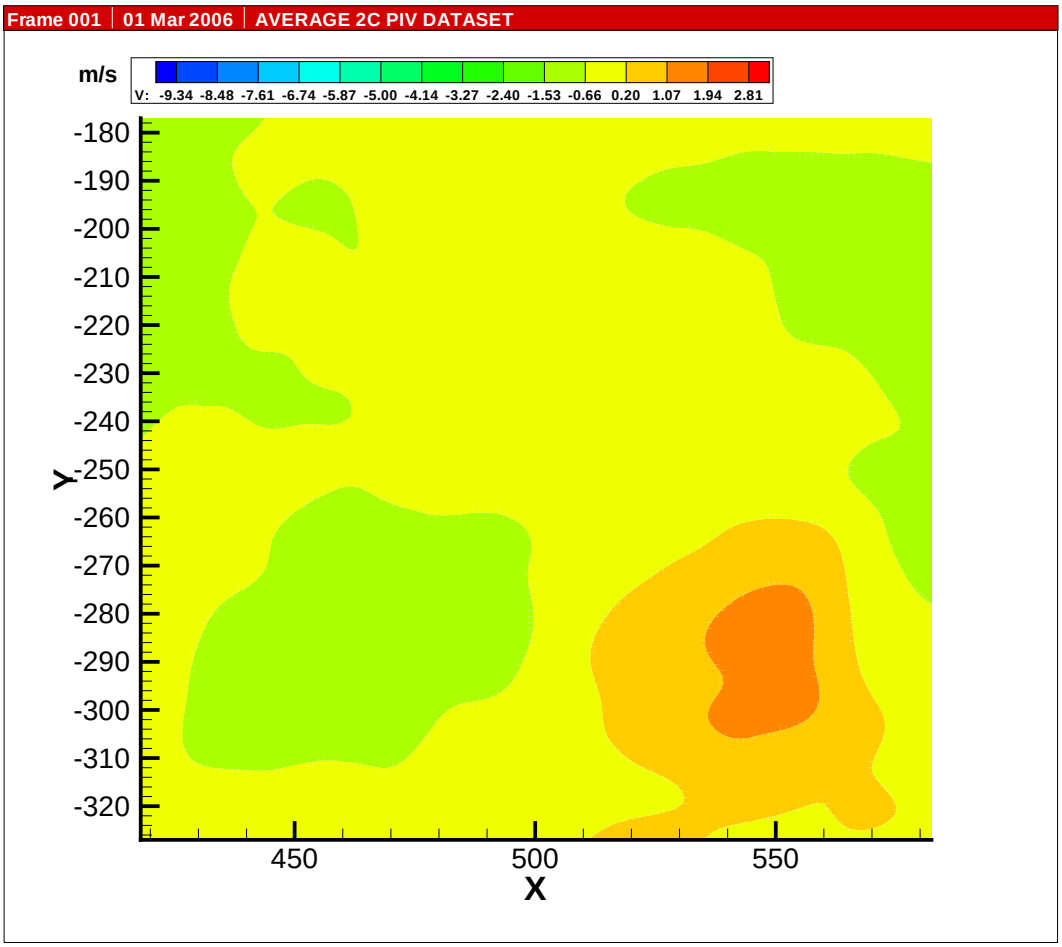

Figure 84: v Velocity at Advance Ratio 0.05- zone 7. Axes in mm.

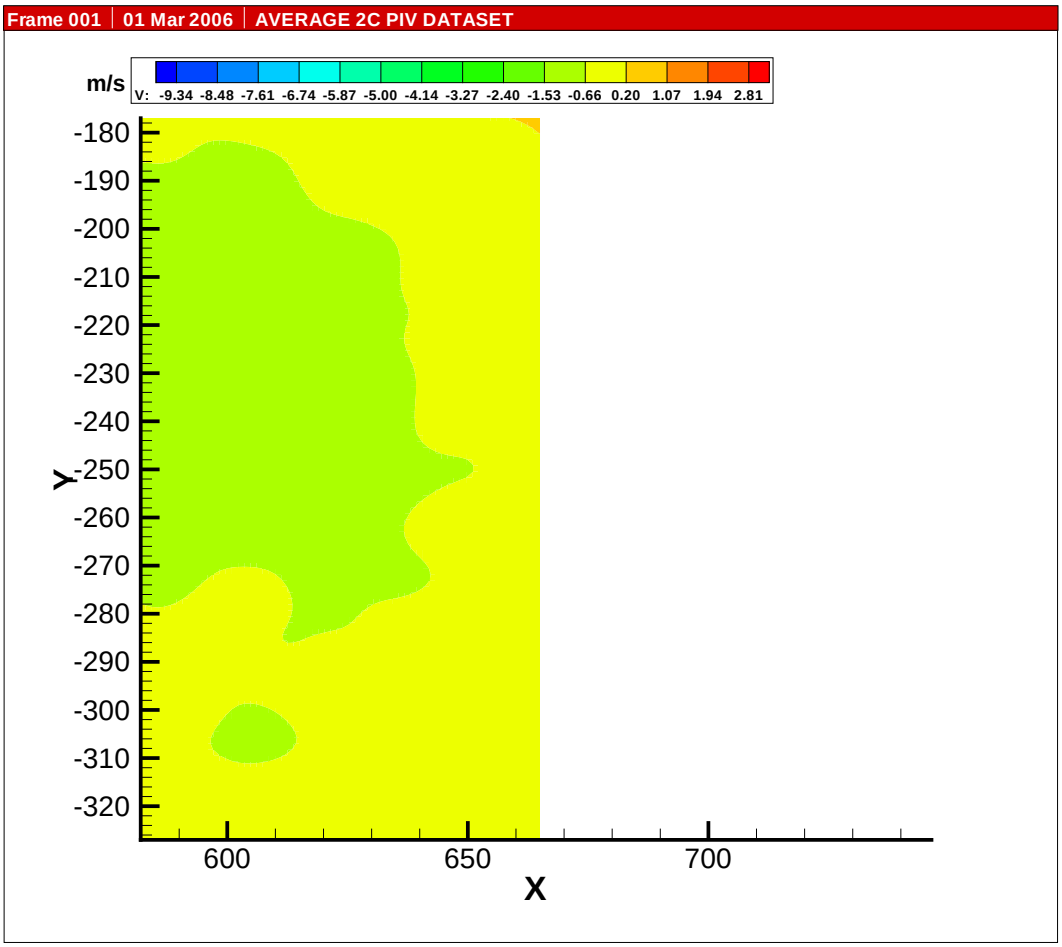

Figure 85: v Velocity at Advance Ratio 0.05- zone 8. Axes in mm.

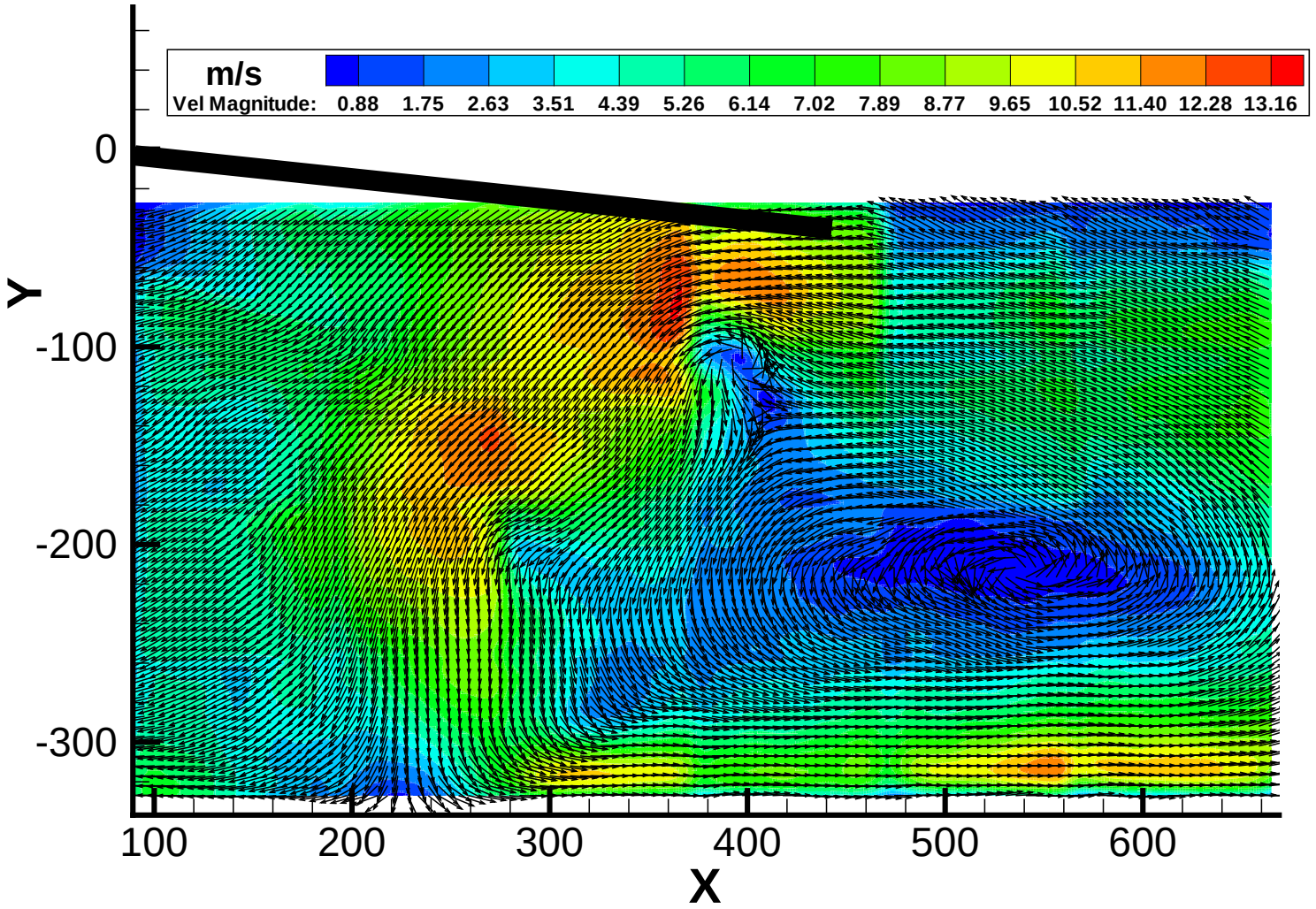

Figure 86: Flowfield at Advance Ratio 0.06. Axes in mm.

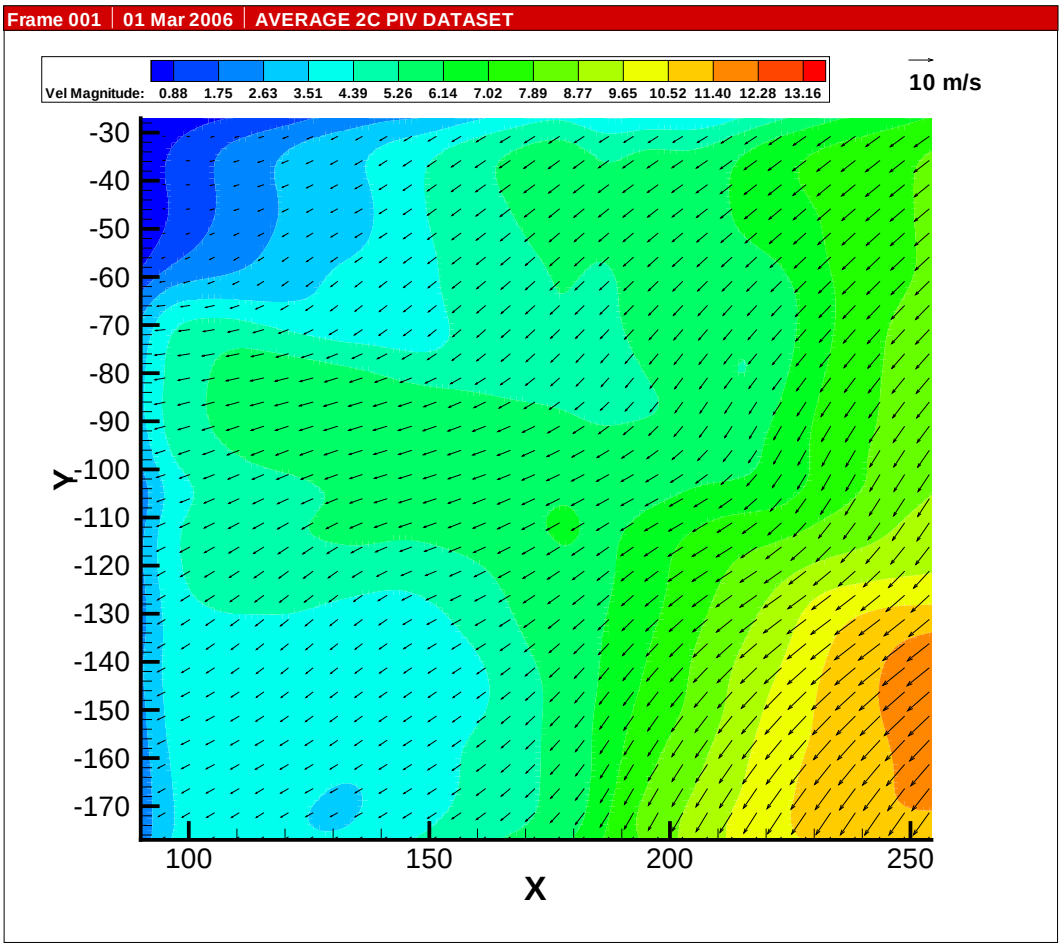

Figure 87: Flowfield at Advance Ratio 0.06- zone 1. Axes in mm.

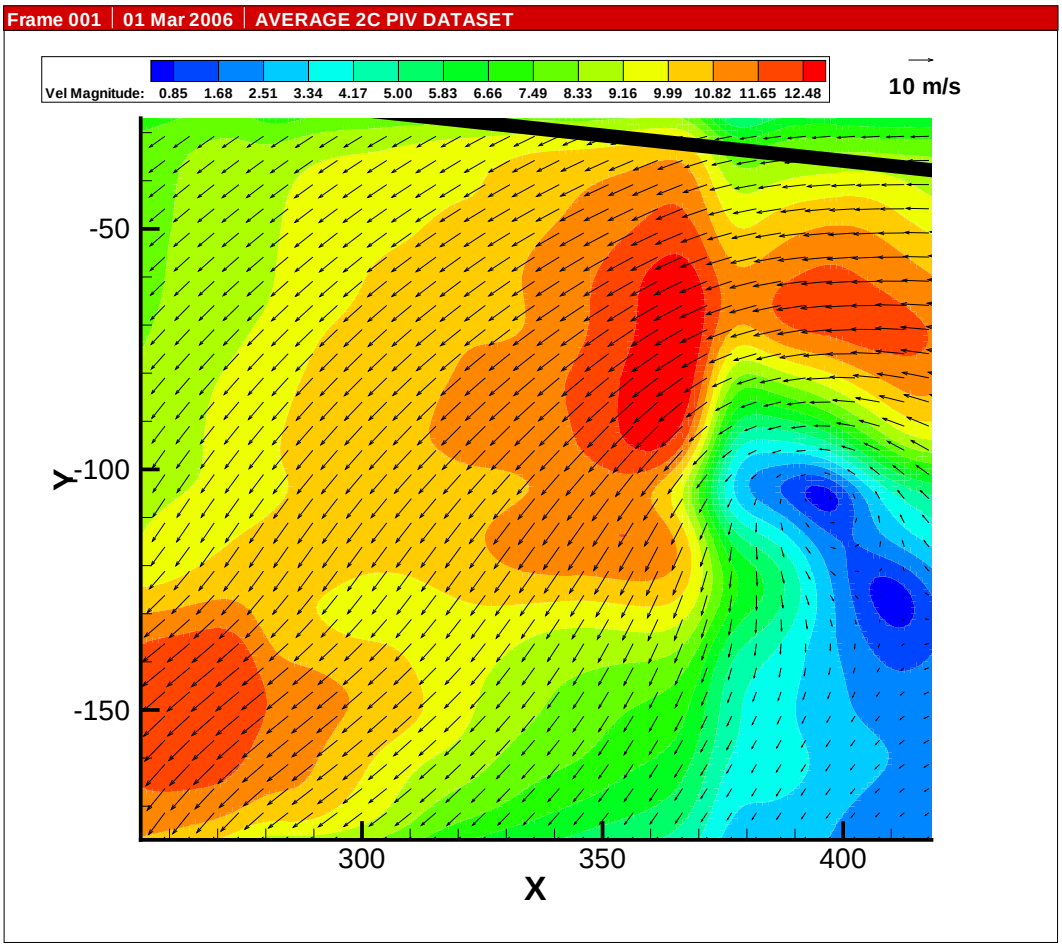

Figure 88: Flowfield at Advance Ratio 0.06- zone 2. Axes in mm.

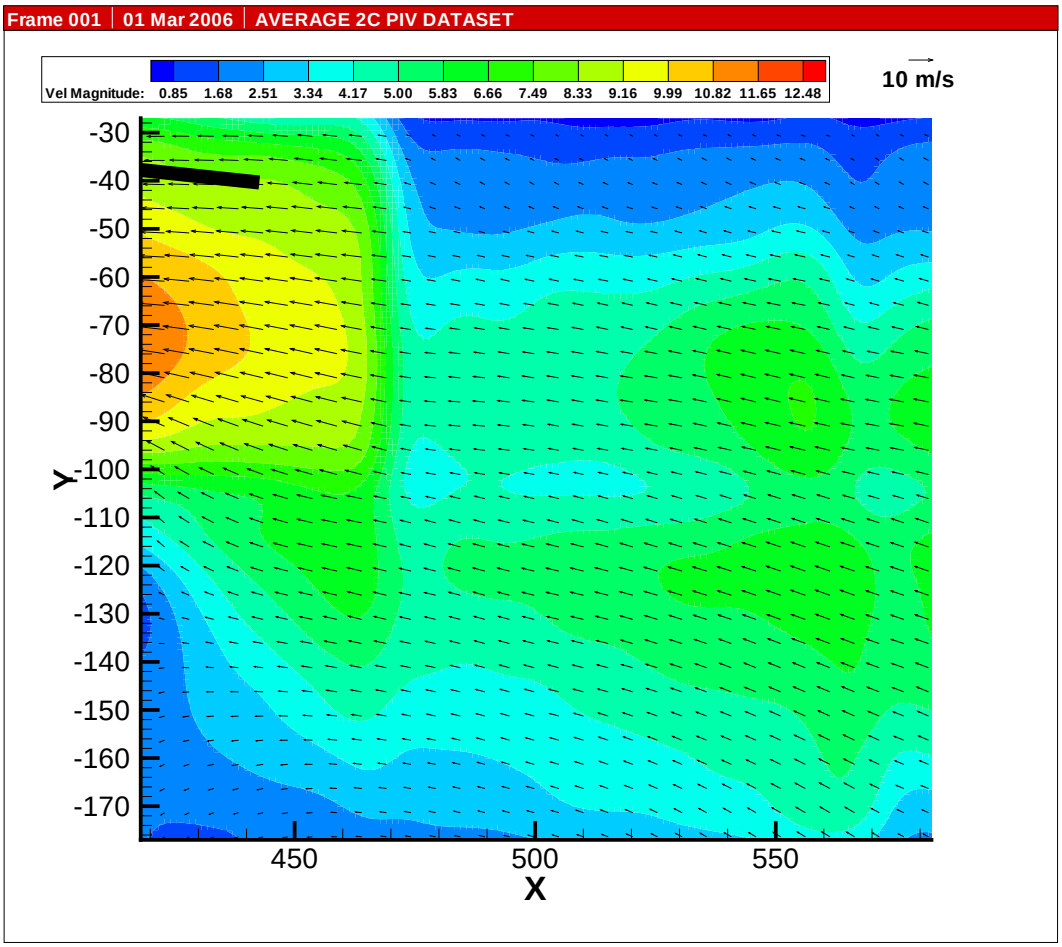

Figure 89: Flowfield at Advance Ratio 0.06- zone 3. Axes in mm.

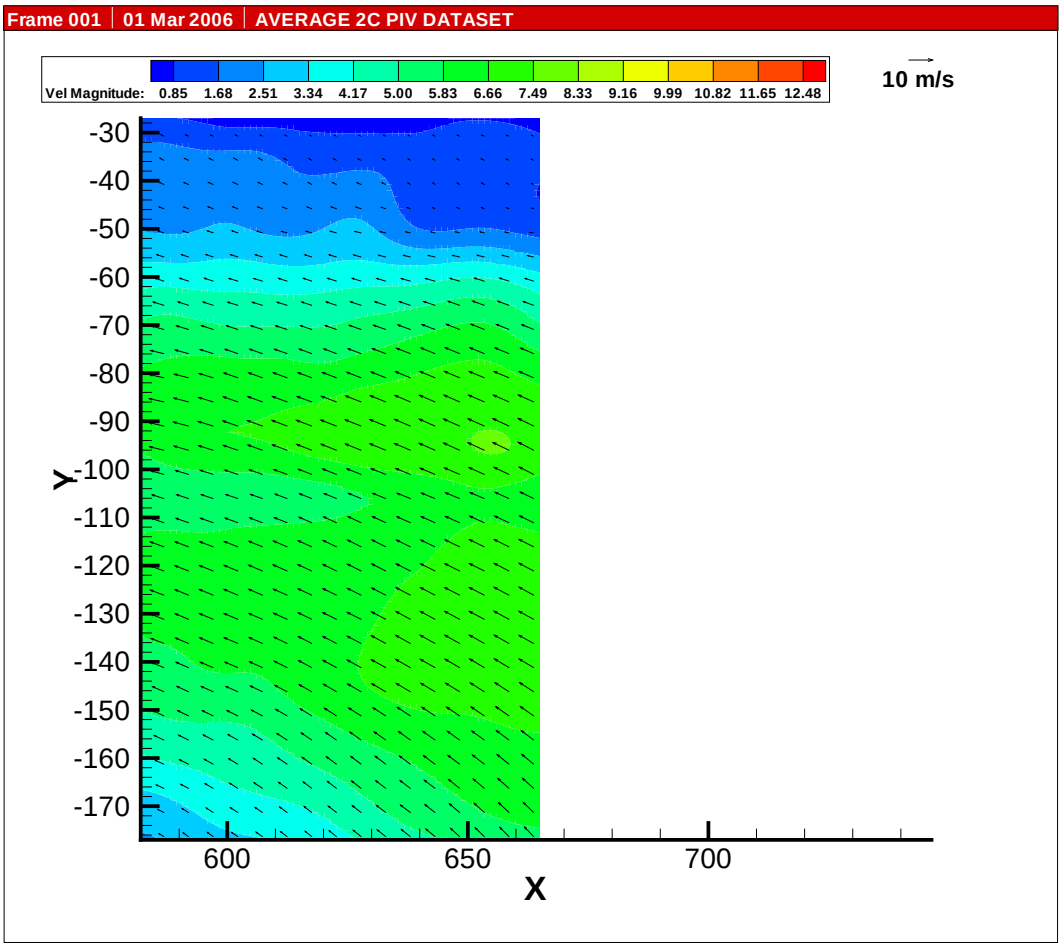

Figure 90: Flowfield at Advance Ratio 0.06- zone 4. Axes in mm.

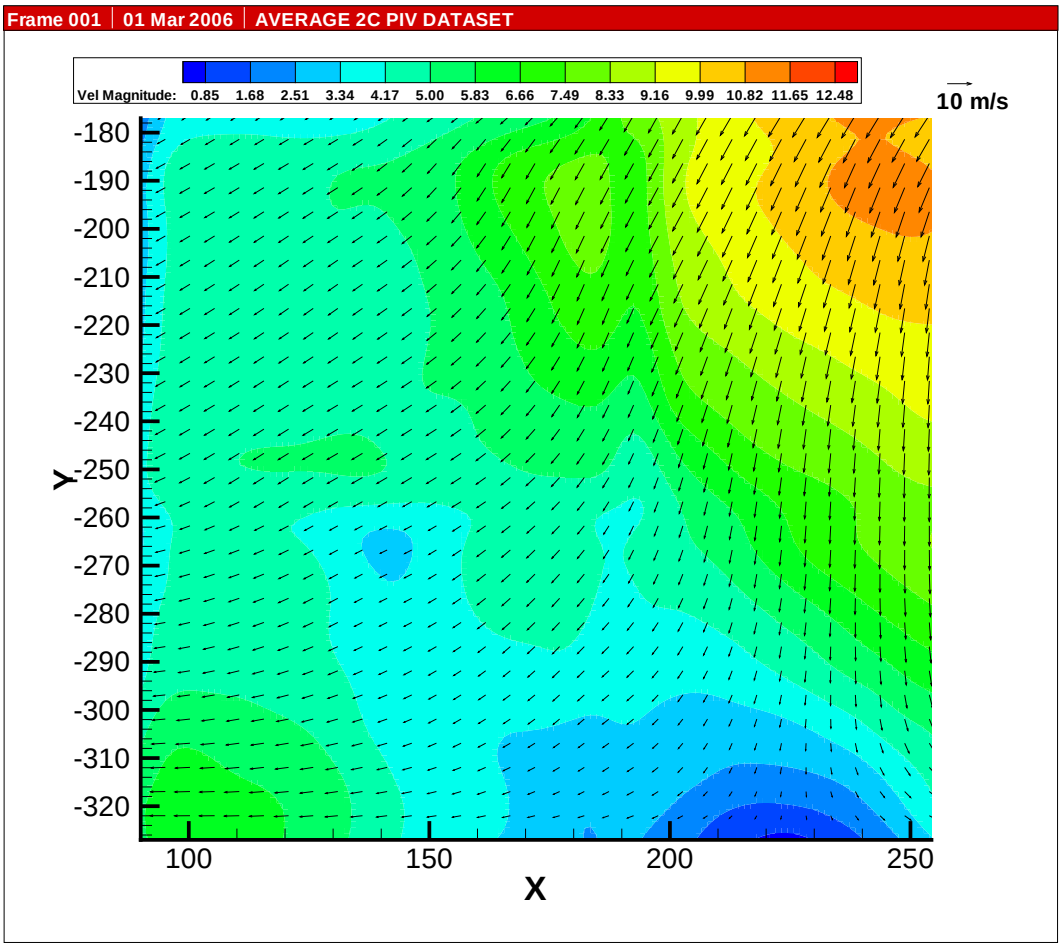

Figure 91: Flowfield at Advance Ratio 0.06- zone 5. Axes in mm.

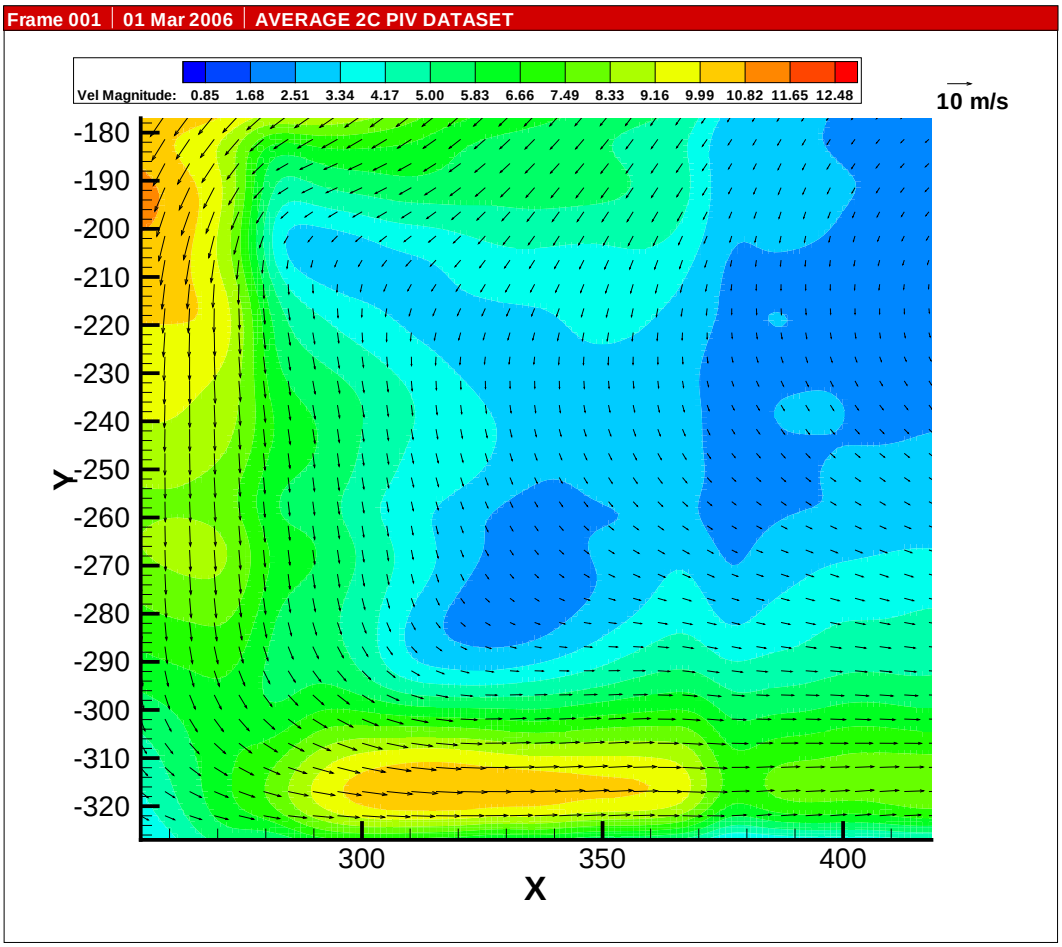

Figure 92: Flowfield at Advance Ratio 0.06- zone 6. Axes in mm.

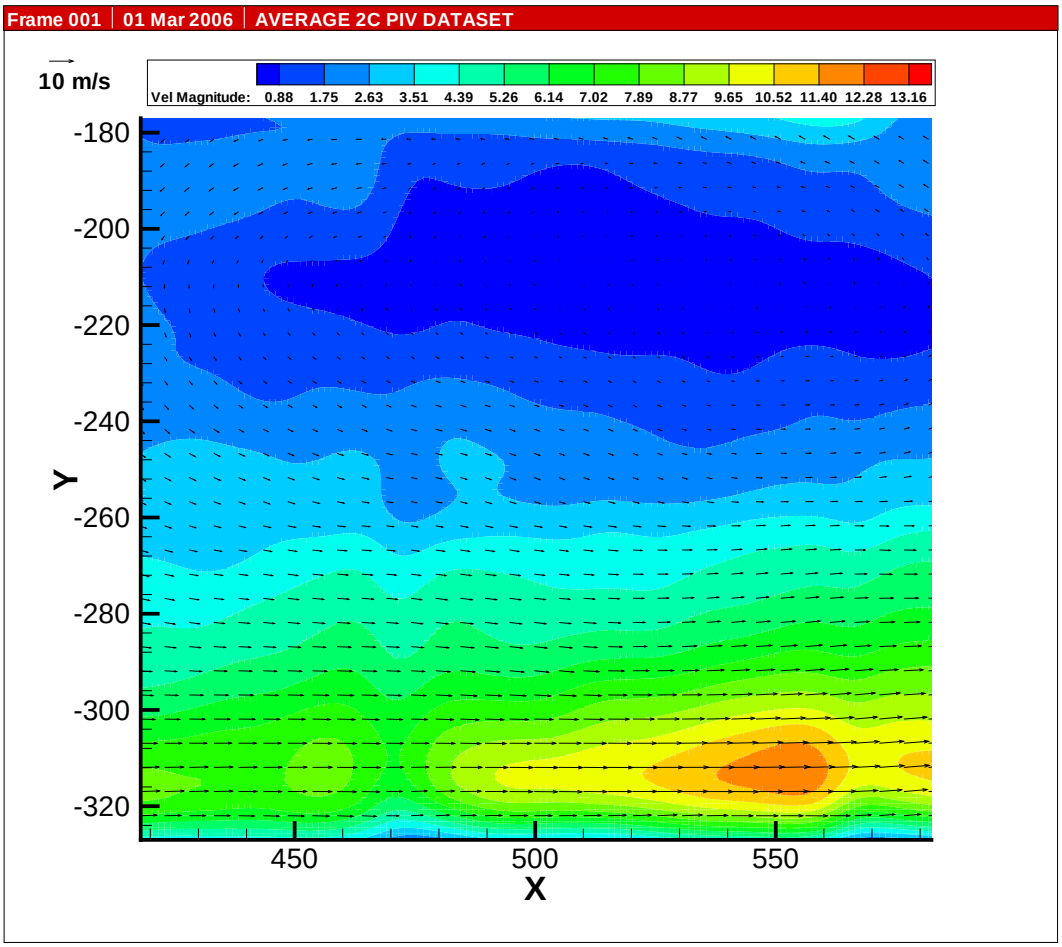

Figure 93: Flowfield at Advance Ratio 0.06- zone 7. Axes in mm.

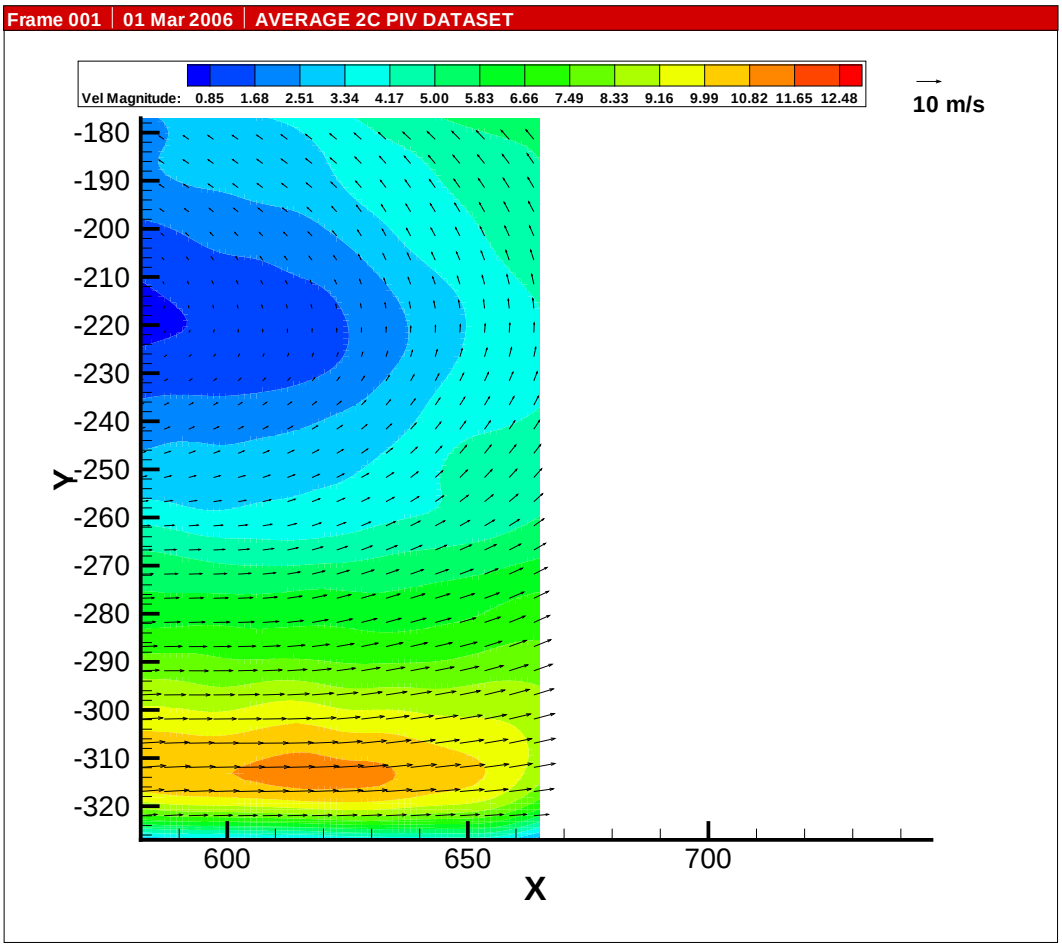

Figure 94: Flowfield at Advance Ratio 0.06- zone 8. Axes in mm.

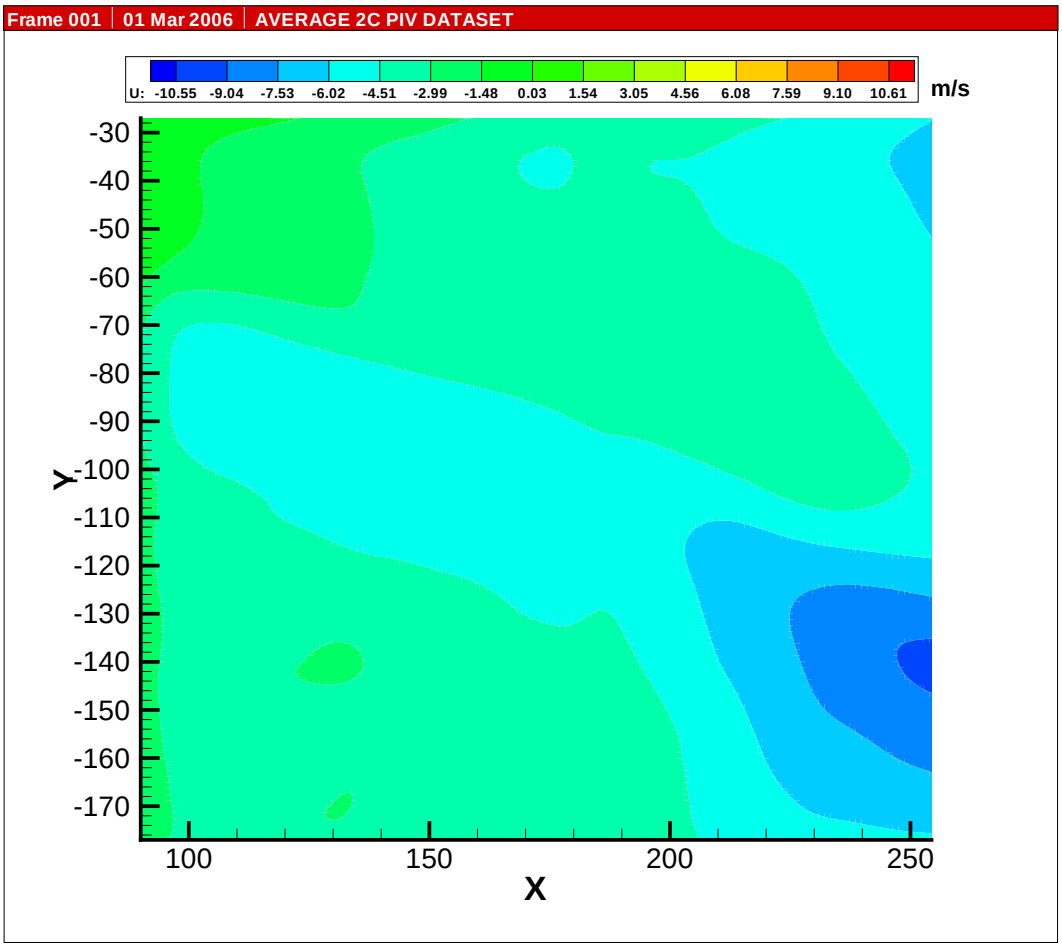

Figure 95: u Velocity at Advance Ratio 0.06- zone 1. Axes in mm.

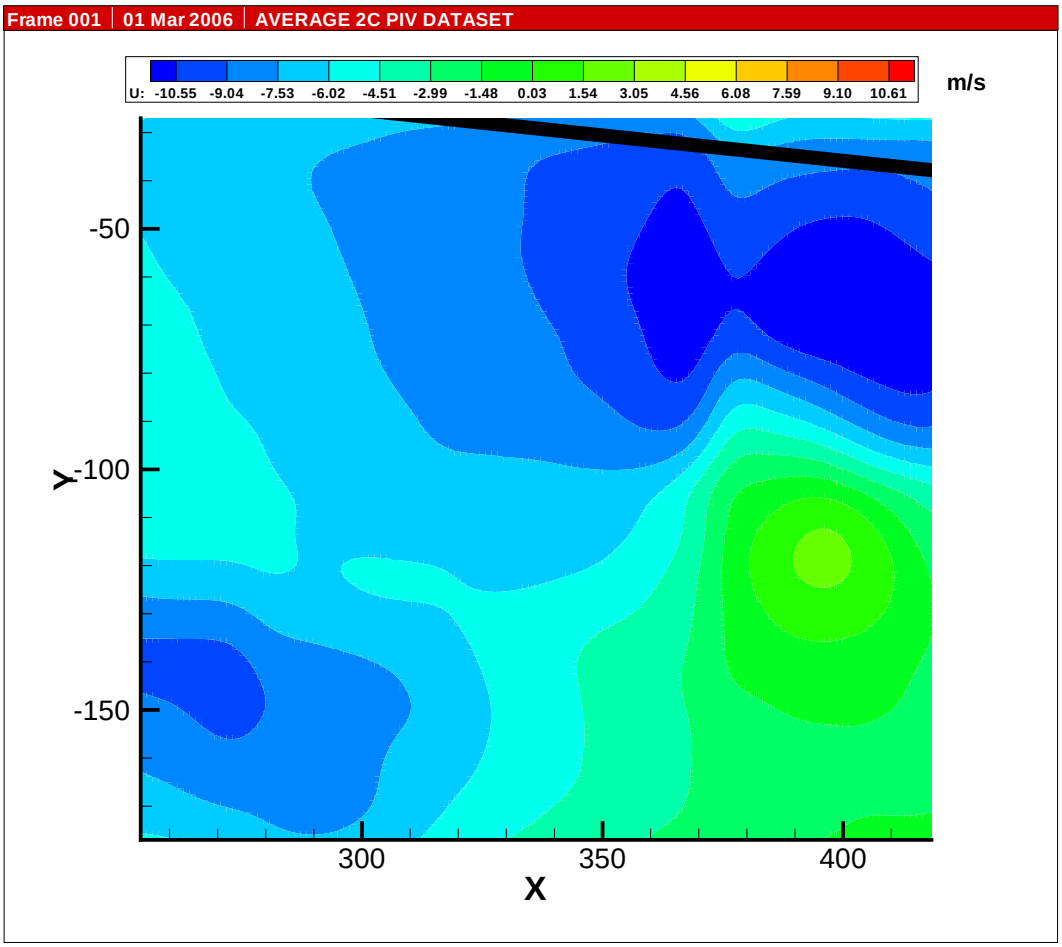

Figure 96: u Velocity at Advance Ratio 0.06- zone 2. Axes in mm.

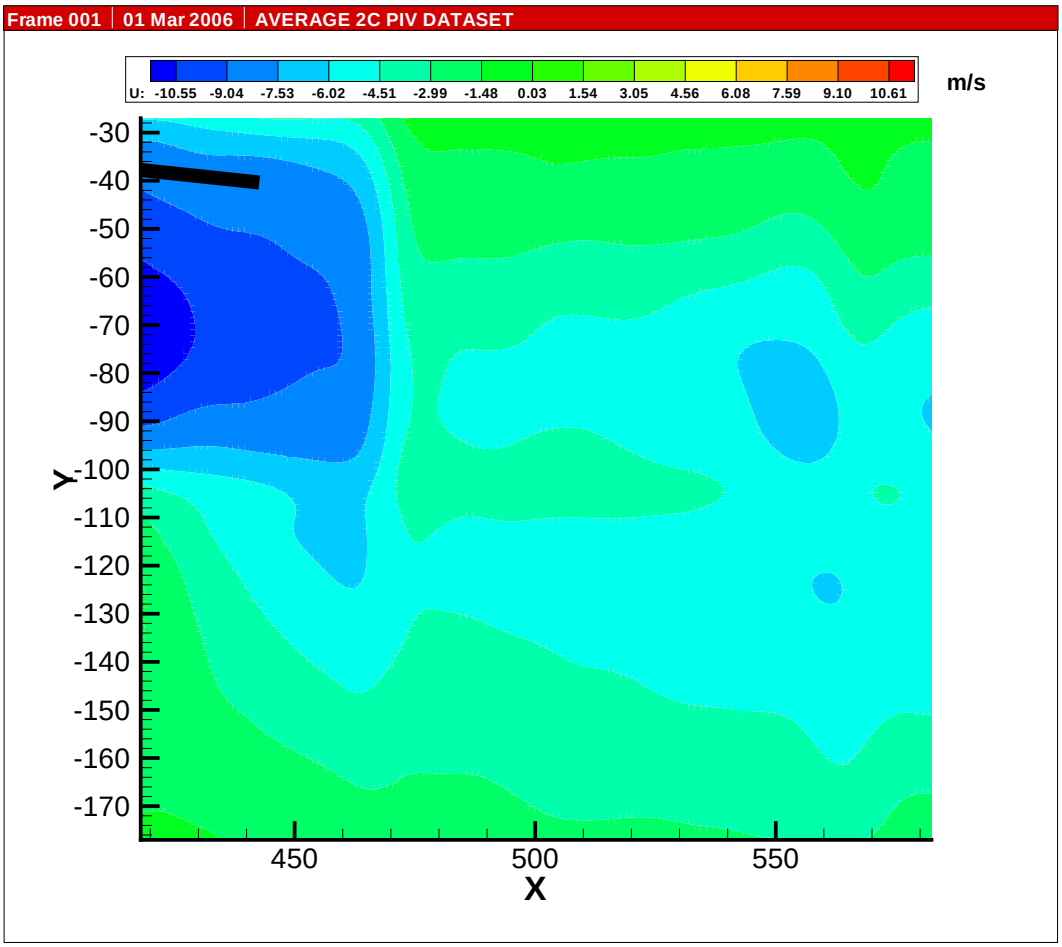

Figure 97: u Velocity at Advance Ratio 0.06- zone 3. Axes in mm.

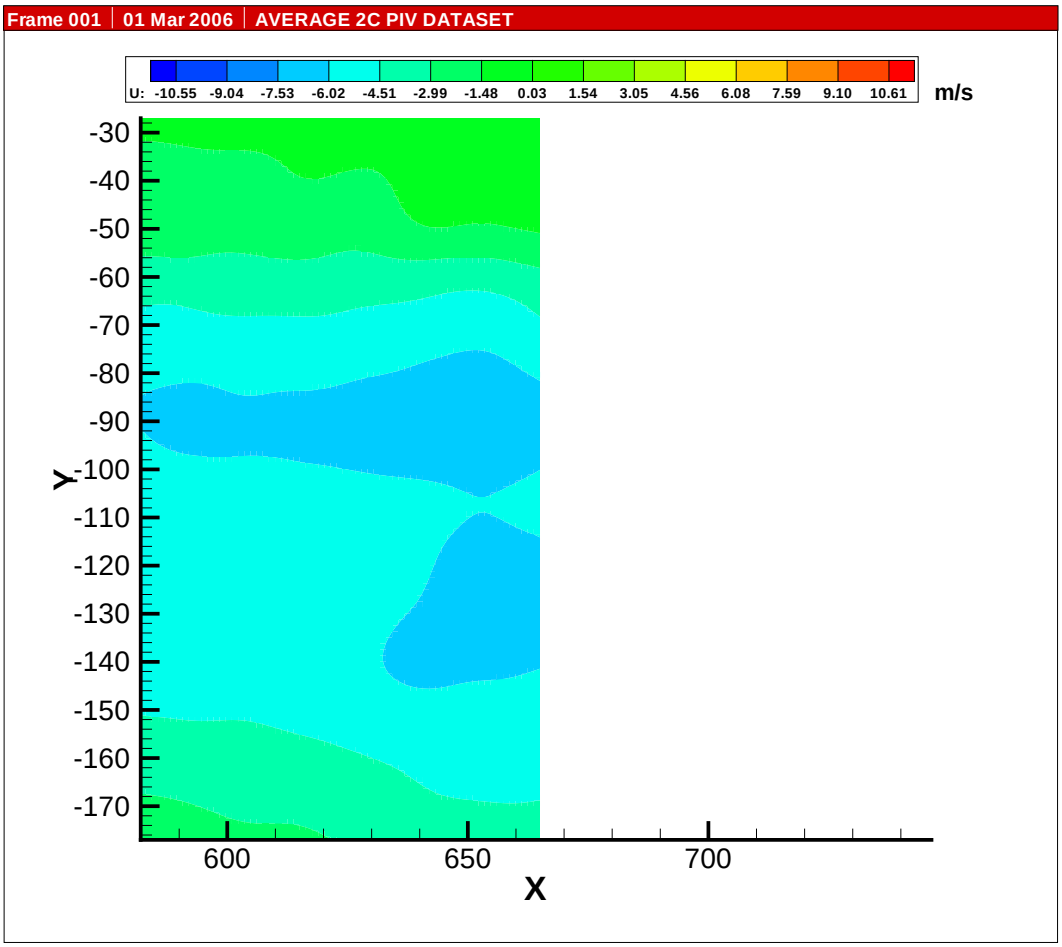

Figure 98: u Velocity at Advance Ratio 0.06- zone 4. Axes in mm.

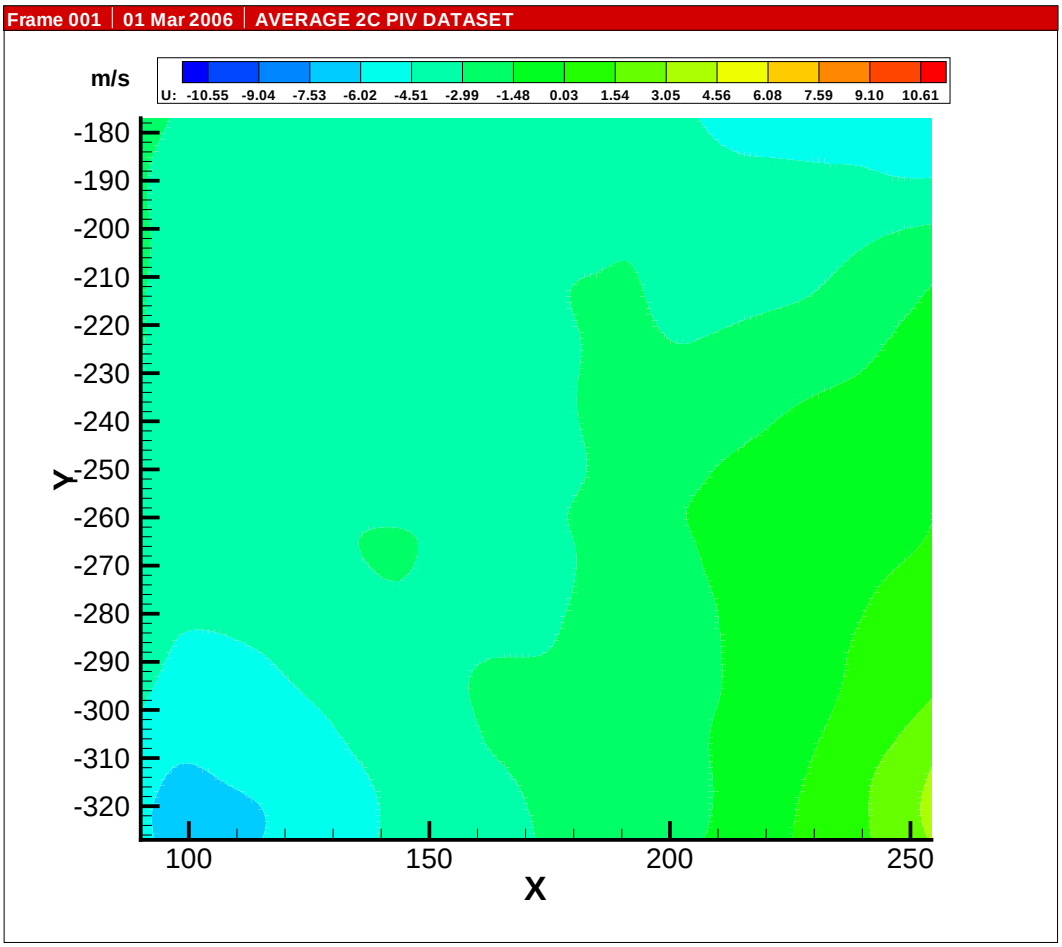

Figure 99: u Velocity at Advance Ratio 0.06- zone 5. Axes in mm.

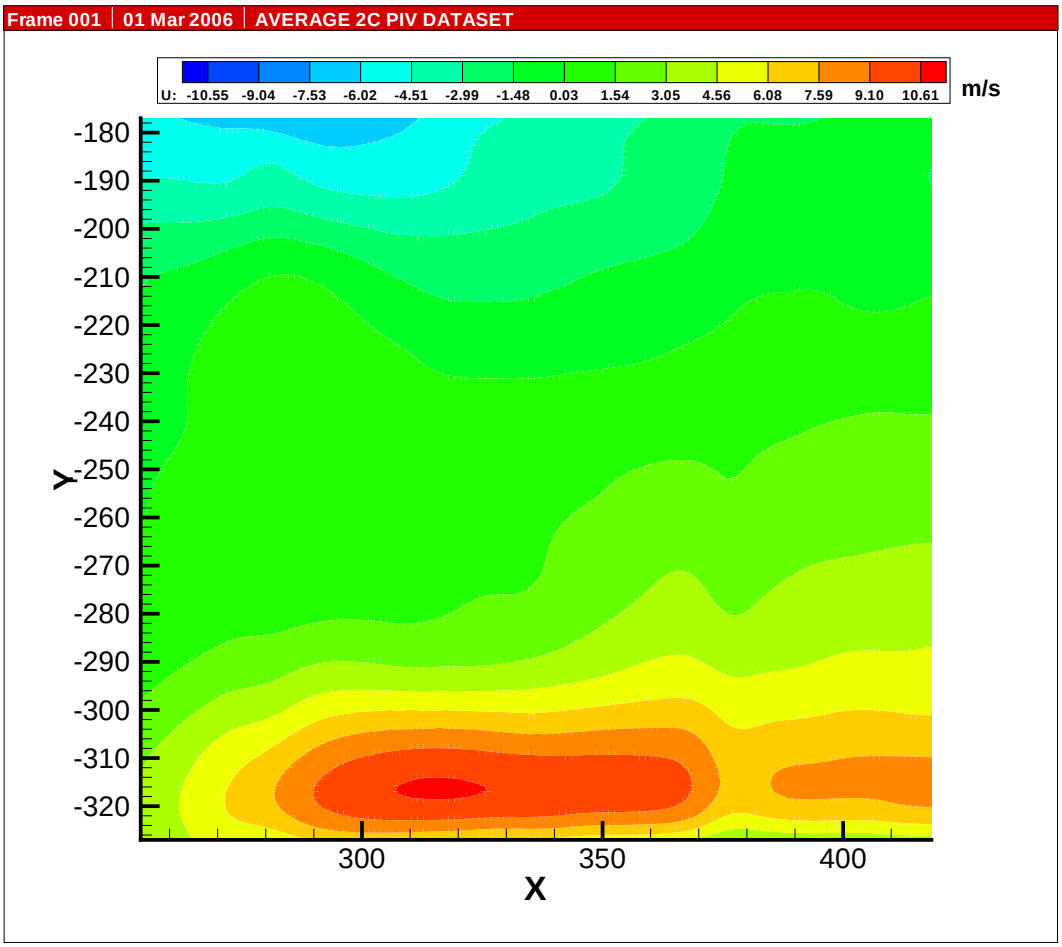

Figure 100: u Velocity at Advance Ratio 0.06- zone 6. Axes in mm.

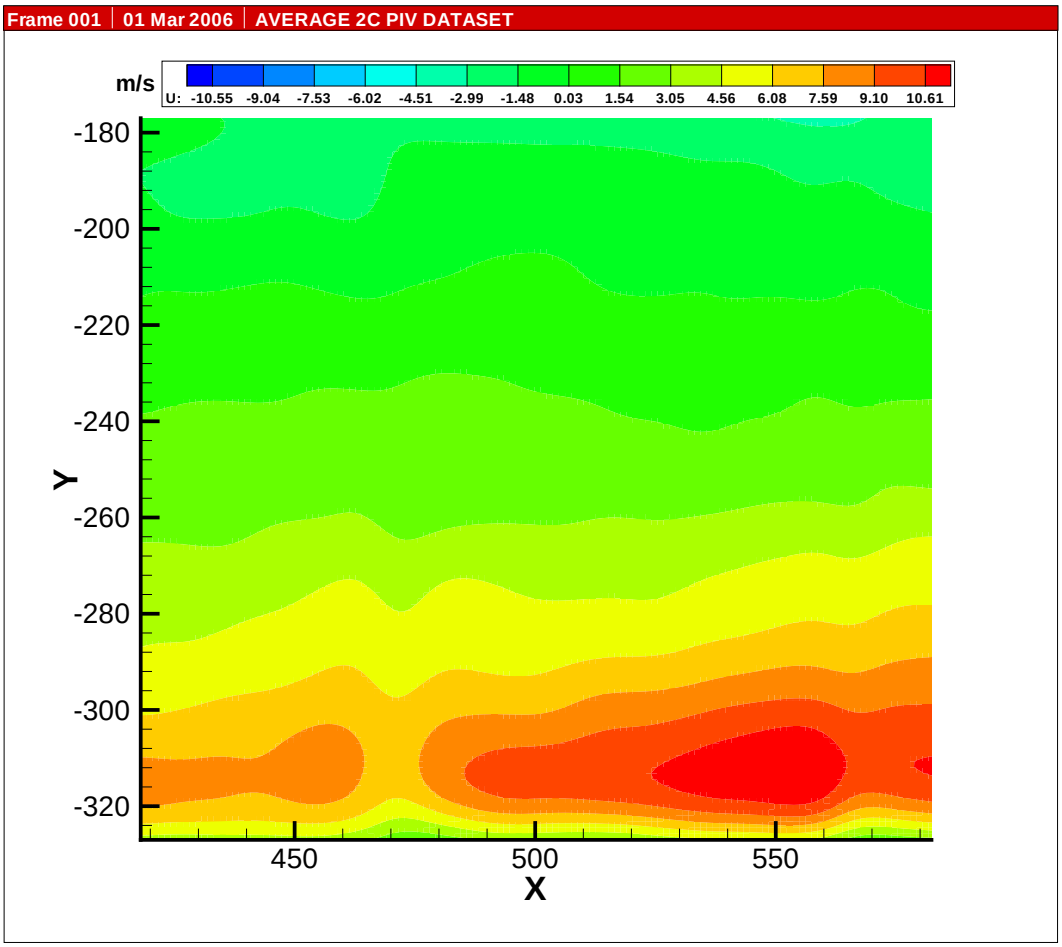

Figure 101: u Velocity at Advance Ratio 0.06- zone 7. Axes in mm.

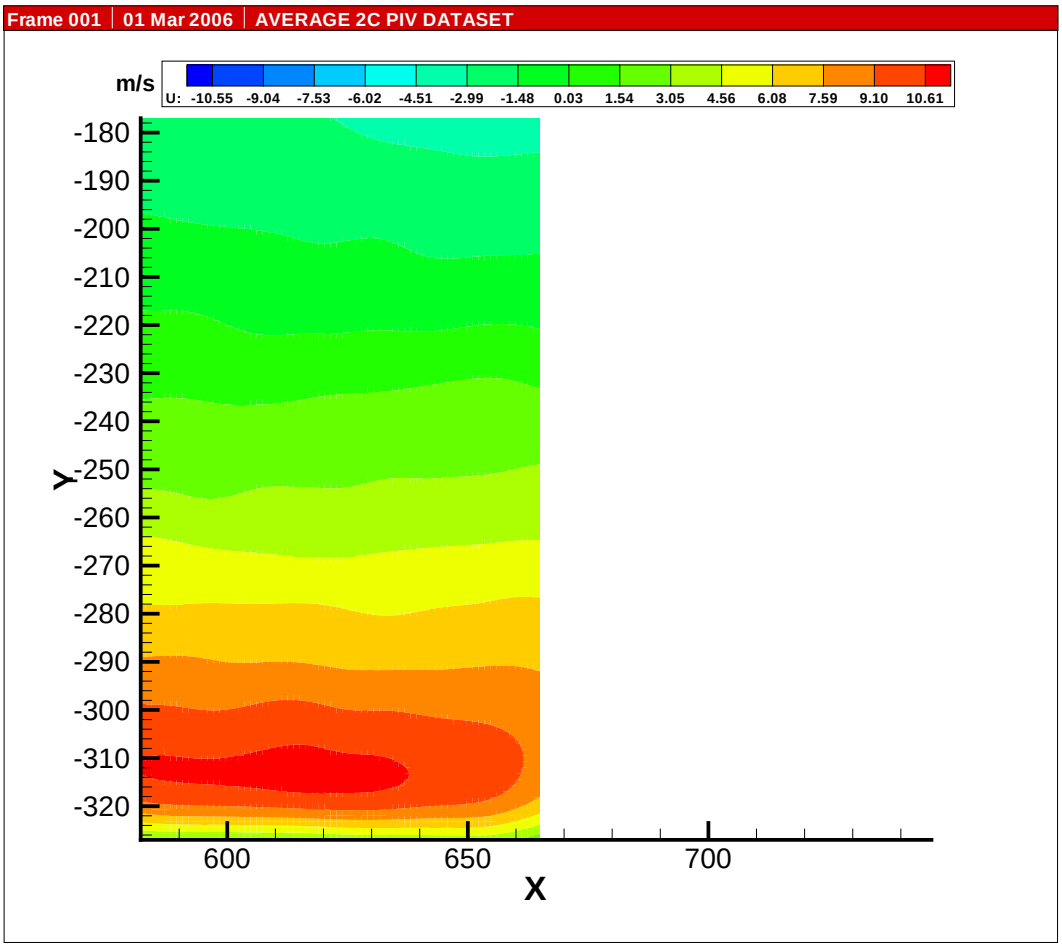

Figure 102: u Velocity at Advance Ratio 0.06- zone 8. Axes in mm.

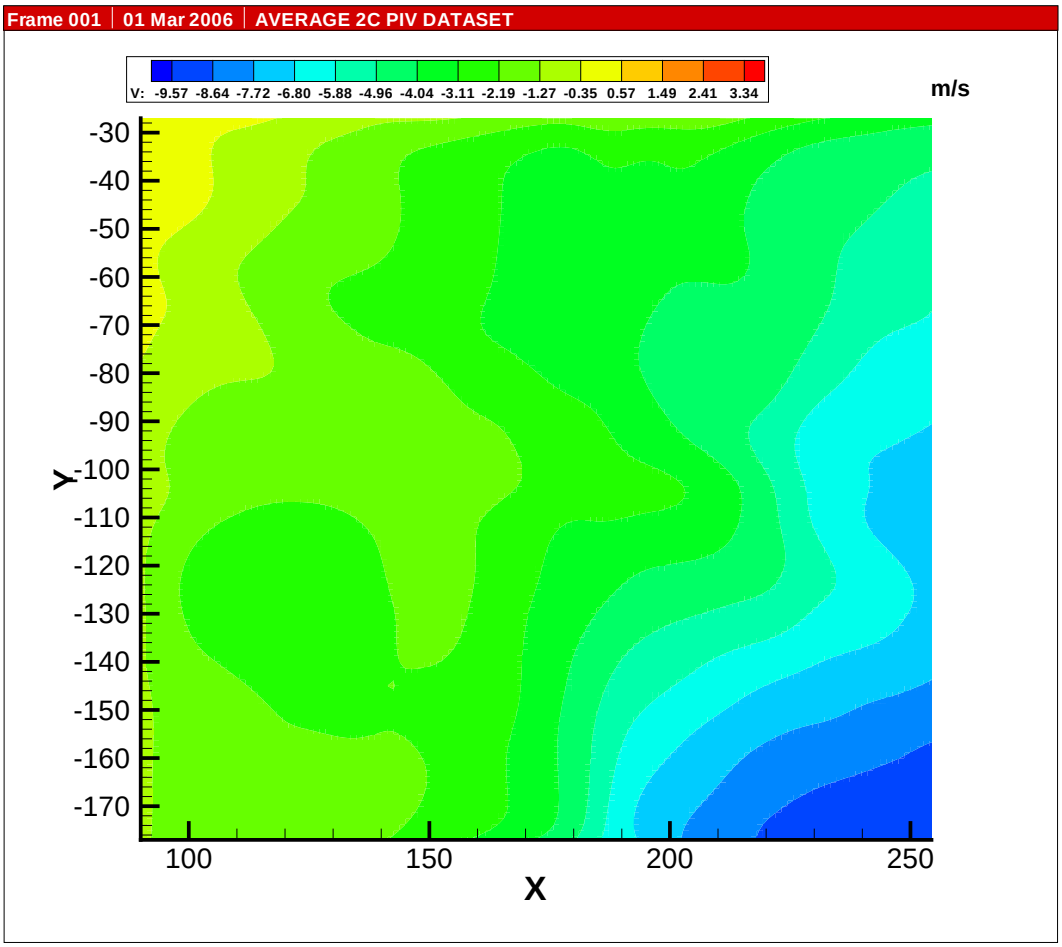

Figure 103: v Velocity at Advance Ratio 0.06- zone 1. Axes in mm.

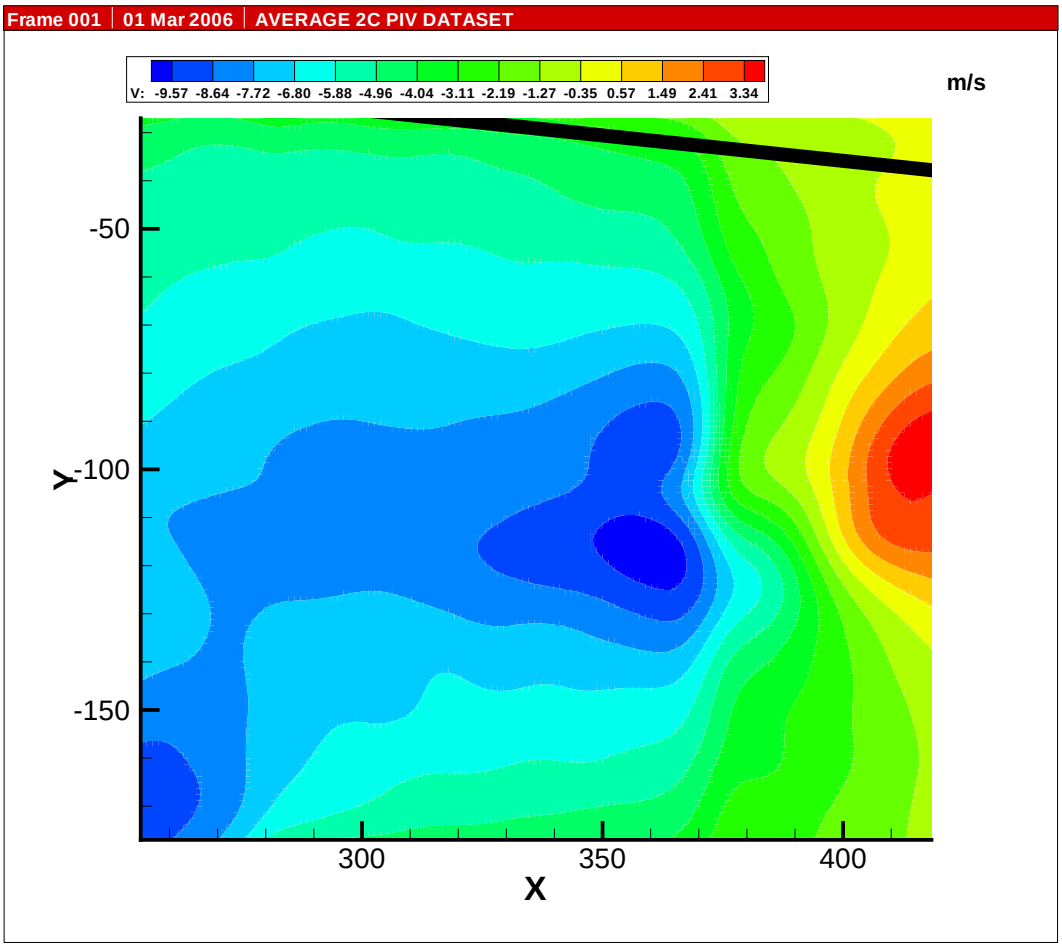

Figure 104: v Velocity at Advance Ratio 0.06- zone 2. Axes in mm.

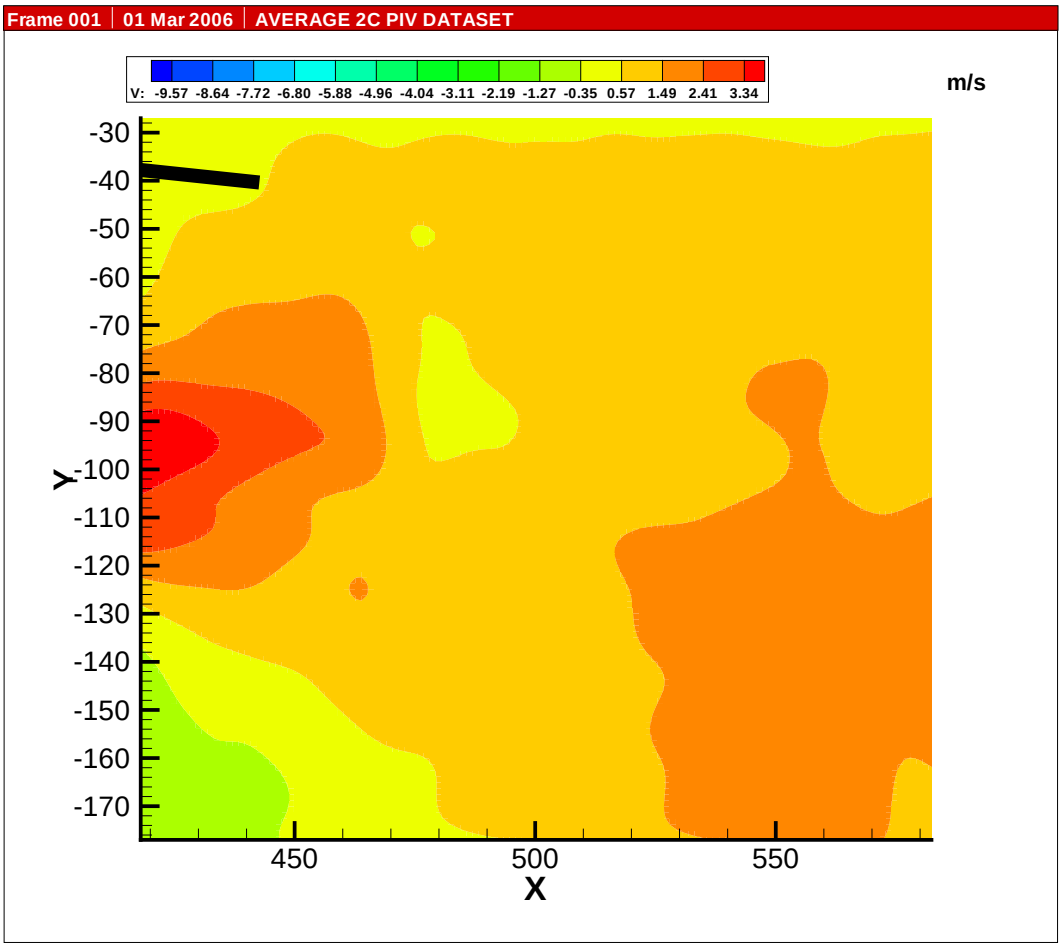

Figure 105: v Velocity at Advance Ratio 0.06- zone 3. Axes in mm.

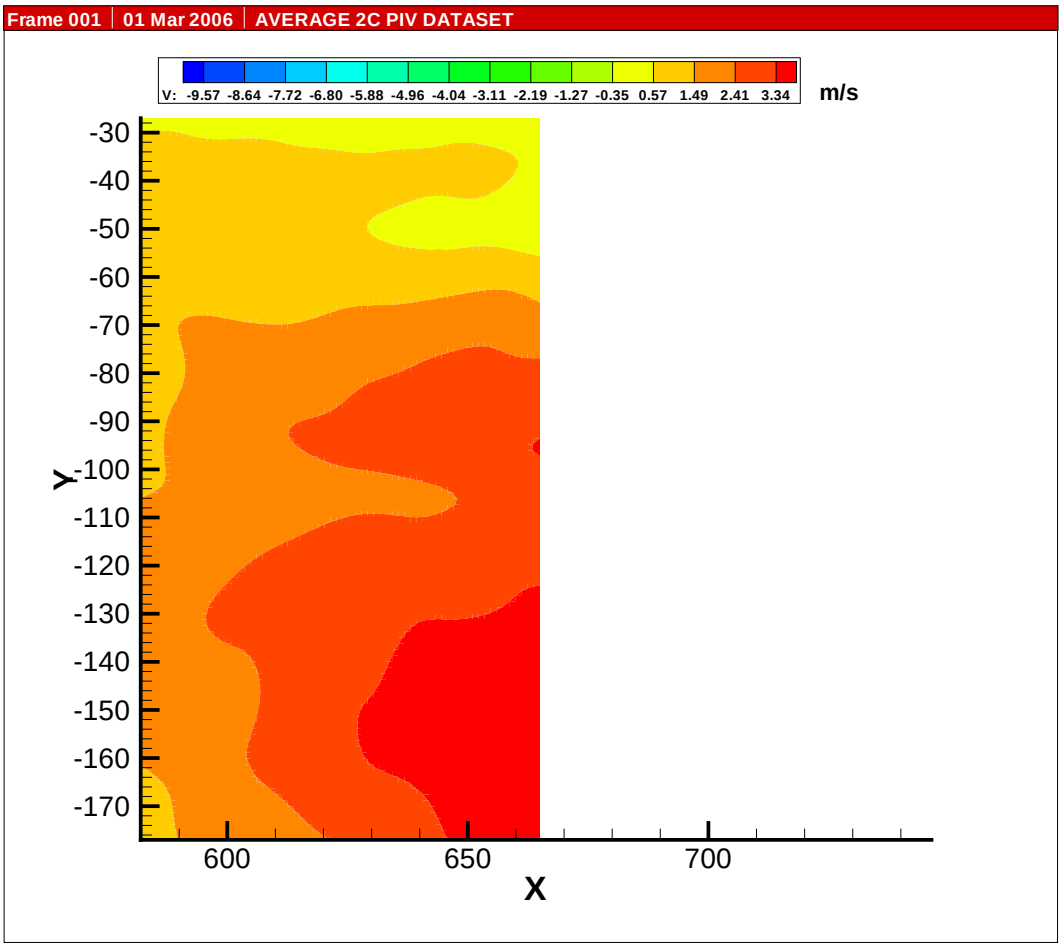

Figure 106: v Velocity at Advance Ratio 0.06- zone 4. Axes in mm.

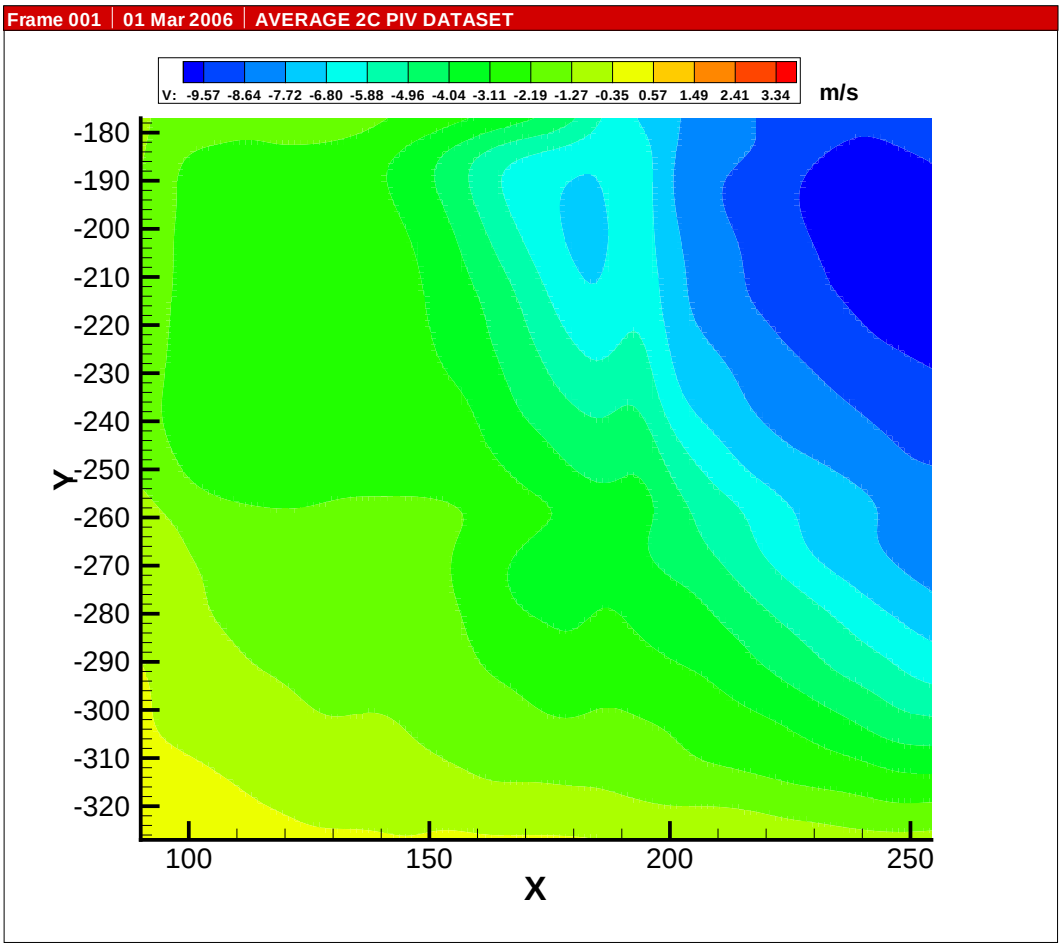

Figure 107: v Velocity at Advance Ratio 0.06- zone 5. Axes in mm.

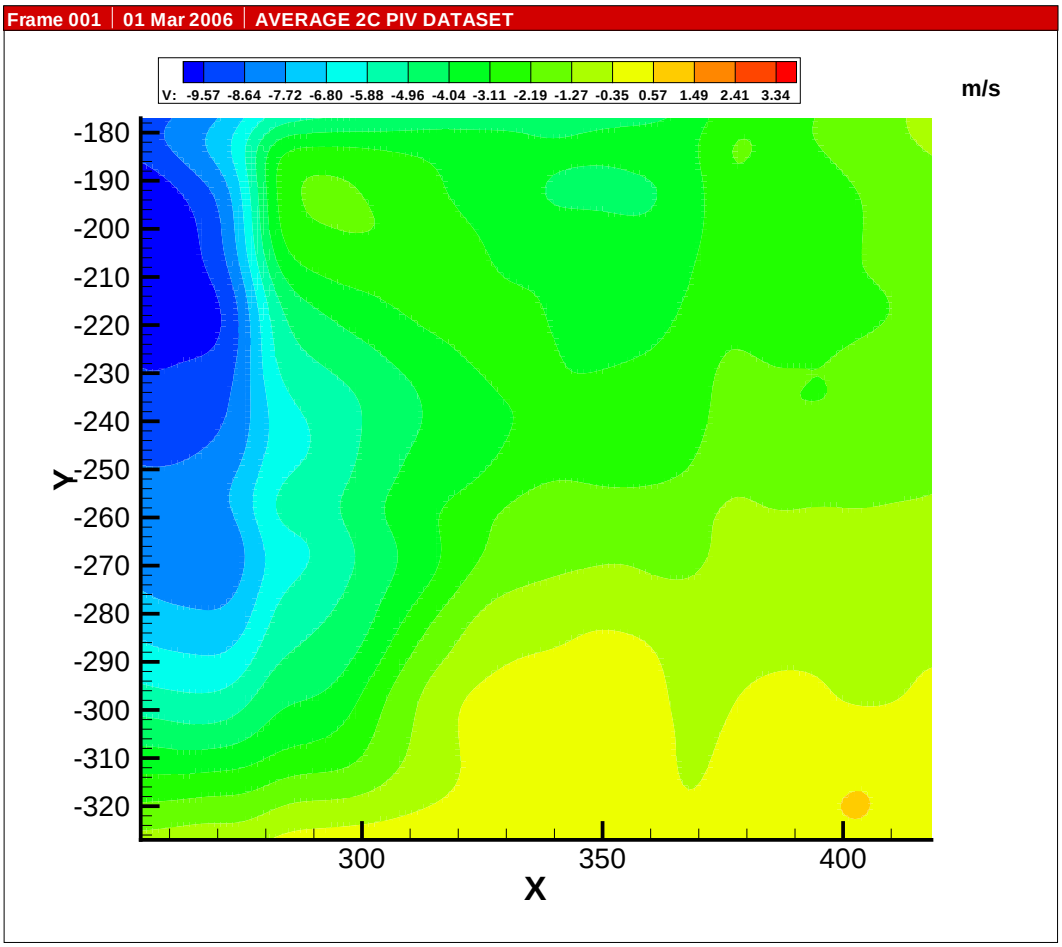

Figure 108: v Velocity at Advance Ratio 0.06- zone 6. Axes in mm.

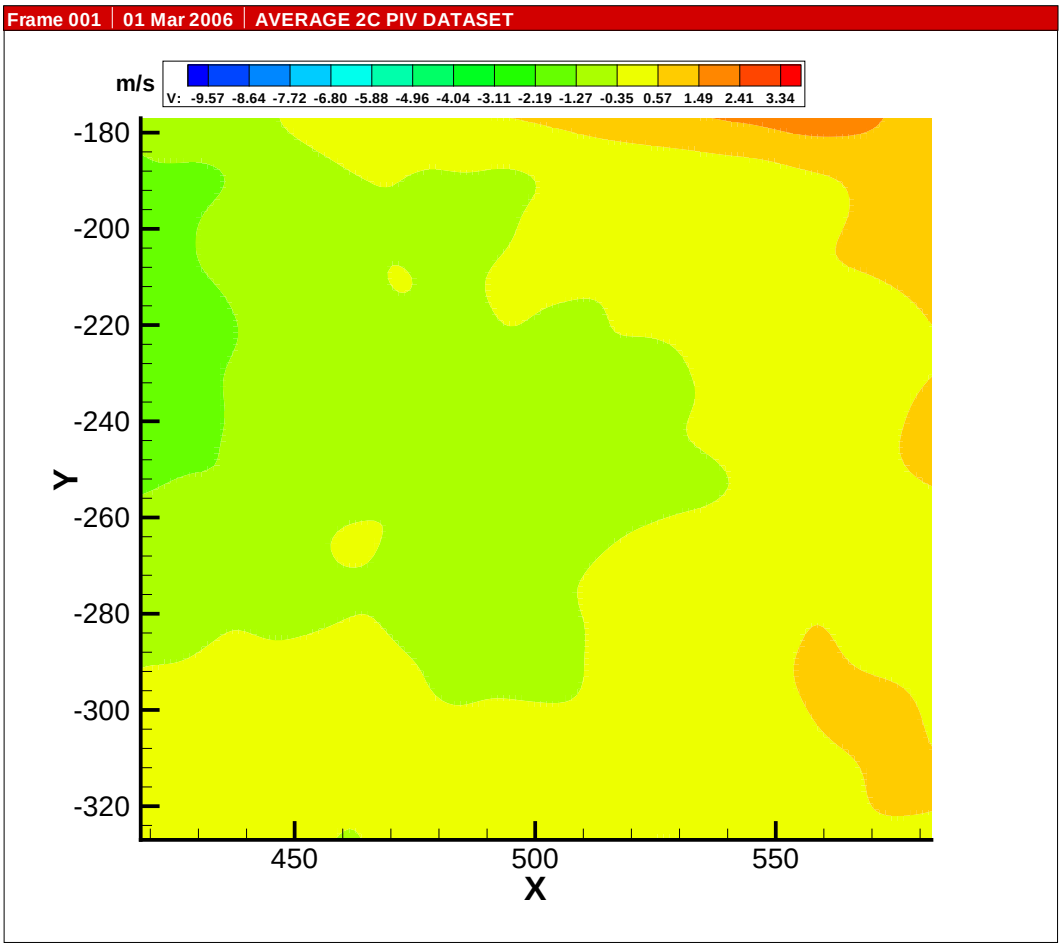

Figure 109: v Velocity at Advance Ratio 0.06- zone 7. Axes in mm.

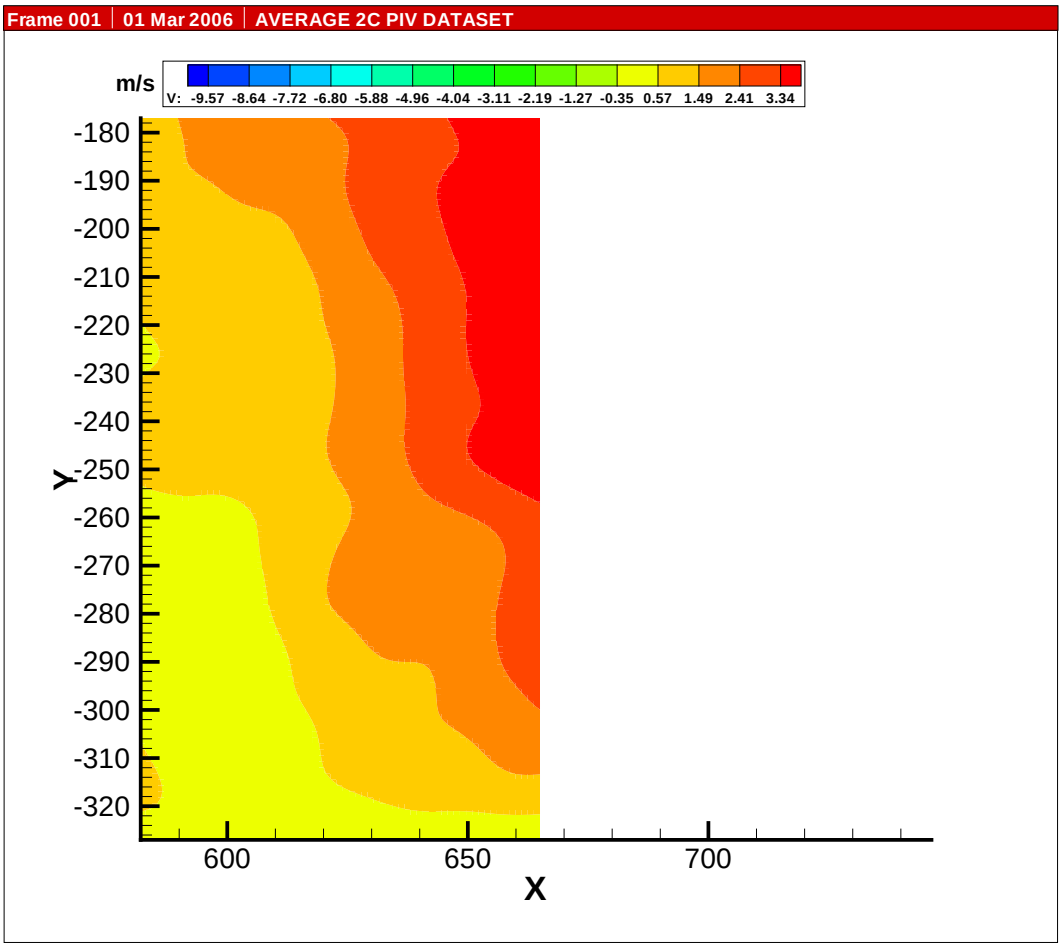

Figure 110: v Velocity at Advance Ratio 0.06- zone 8. Axes in mm.

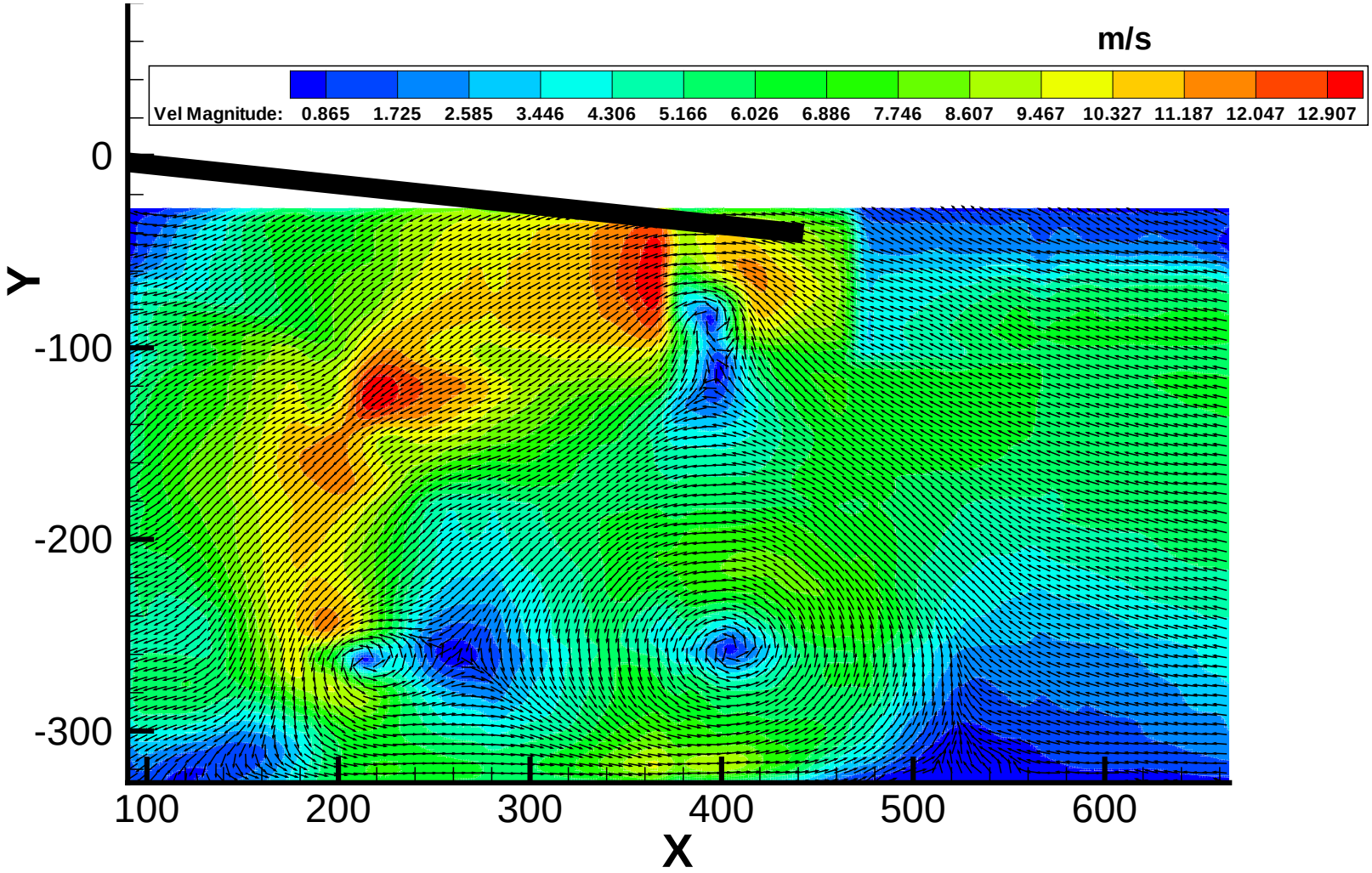

Figure 111: Flowfield at Advance Ratio 0.07. Axes in mm.

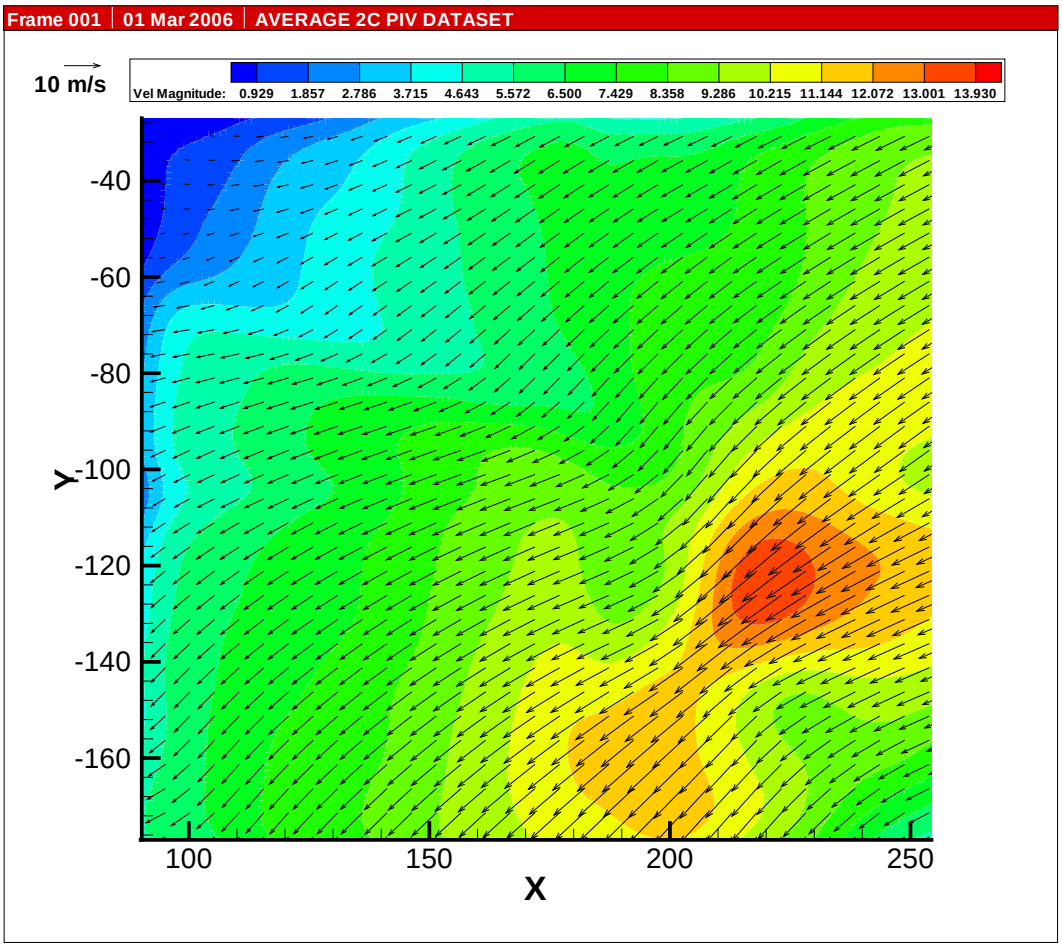

Figure 112: Flowfield at Advance Ratio 0.07- zone 1. Axes in mm.

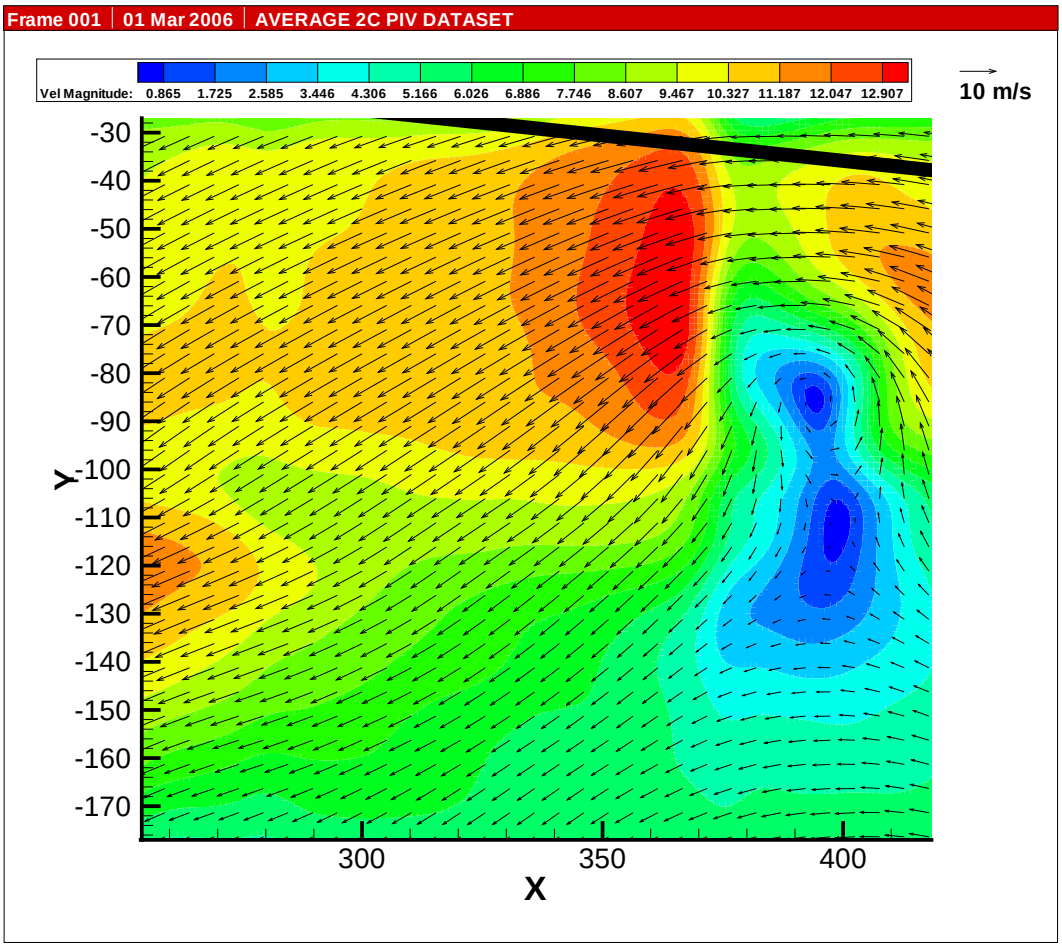

Figure 113: Flowfield at Advance Ratio 0.07- zone 2. Axes in mm.

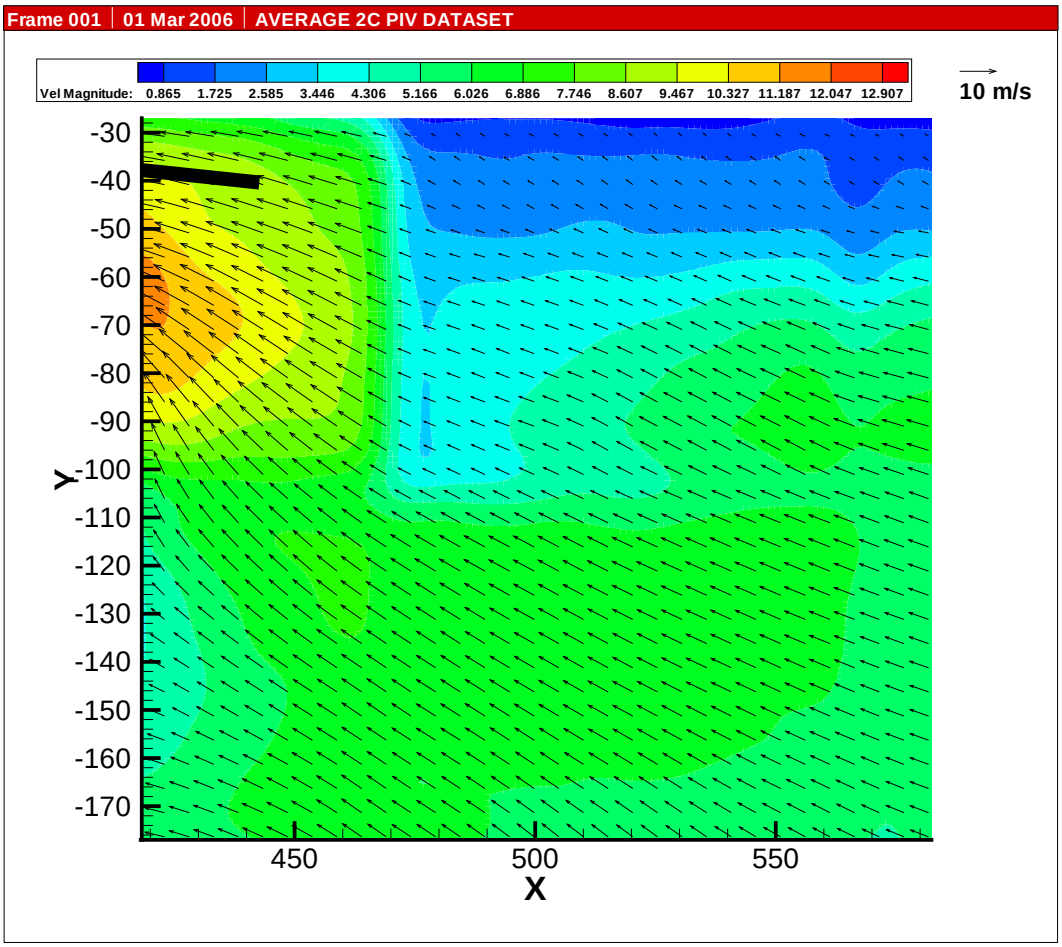

Figure 114: Flowfield at Advance Ratio 0.07- zone 3. Axes in mm.

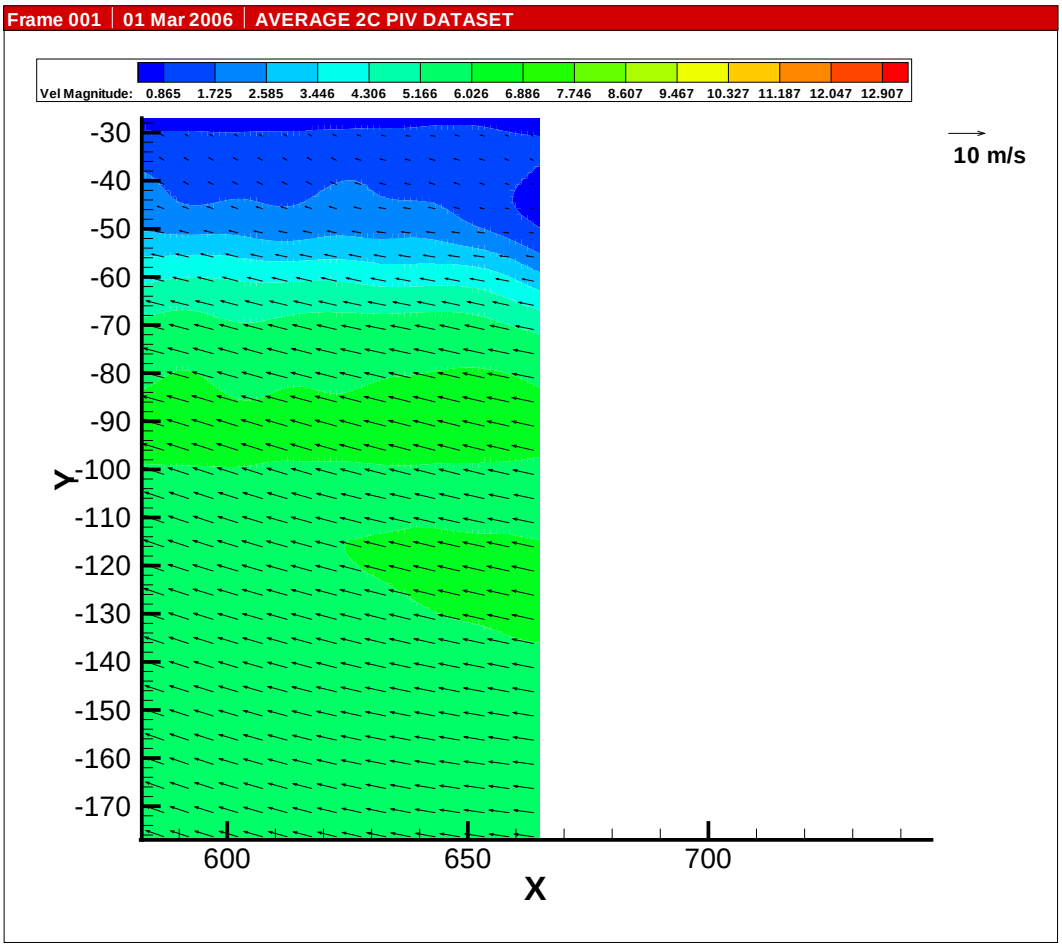

Figure 115: Flowfield at Advance Ratio 0.07- zone 4. Axes in mm.

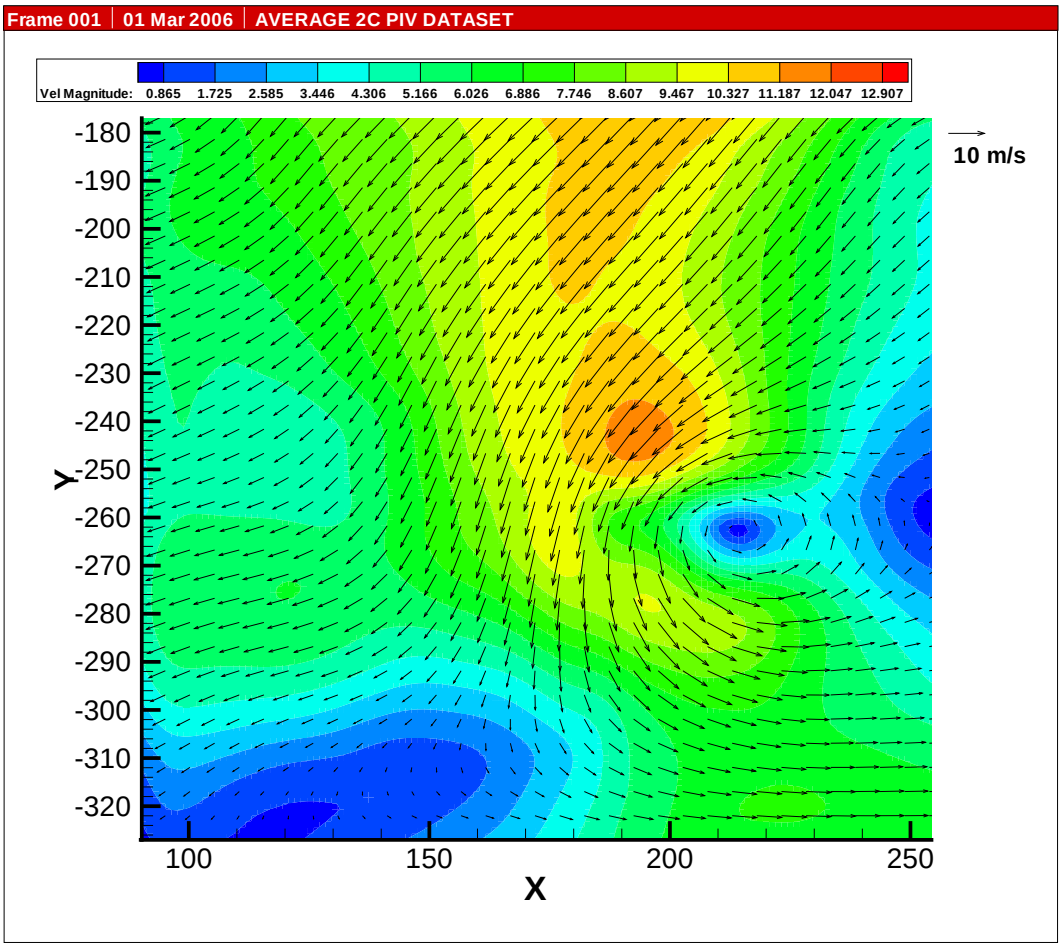

Figure 116: Flowfield at Advance Ratio 0.07- zone 5. Axes in mm.

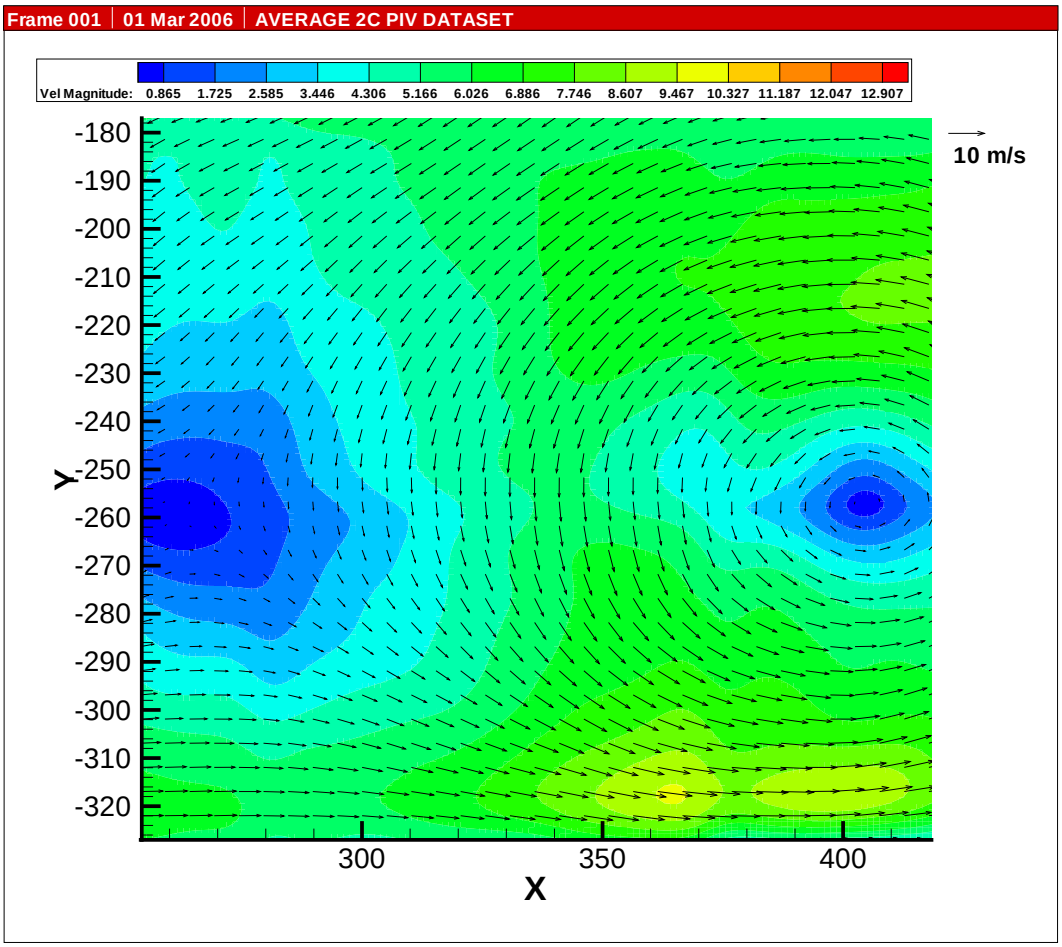

Figure 117: Flowfield at Advance Ratio 0.07- zone 6. Axes in mm.

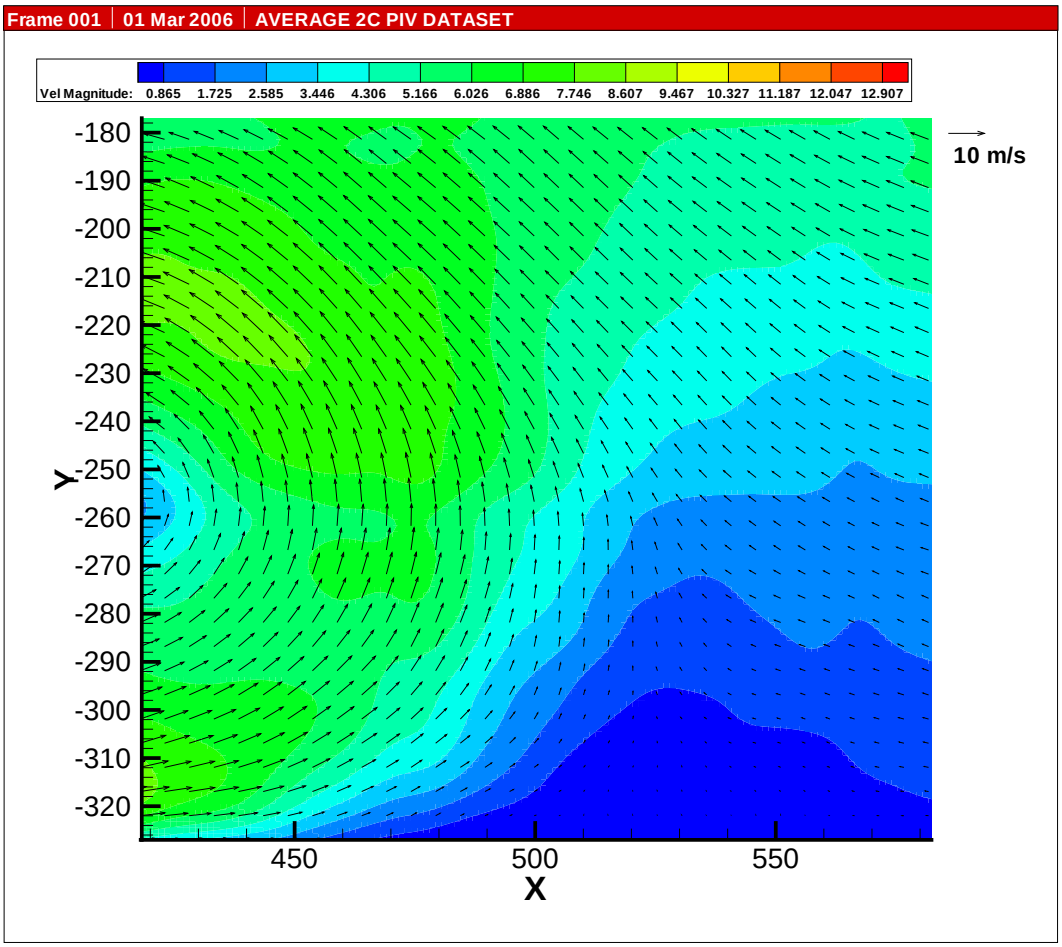

Figure 118: Flowfield at Advance Ratio 0.07- zone 7. Axes in mm.

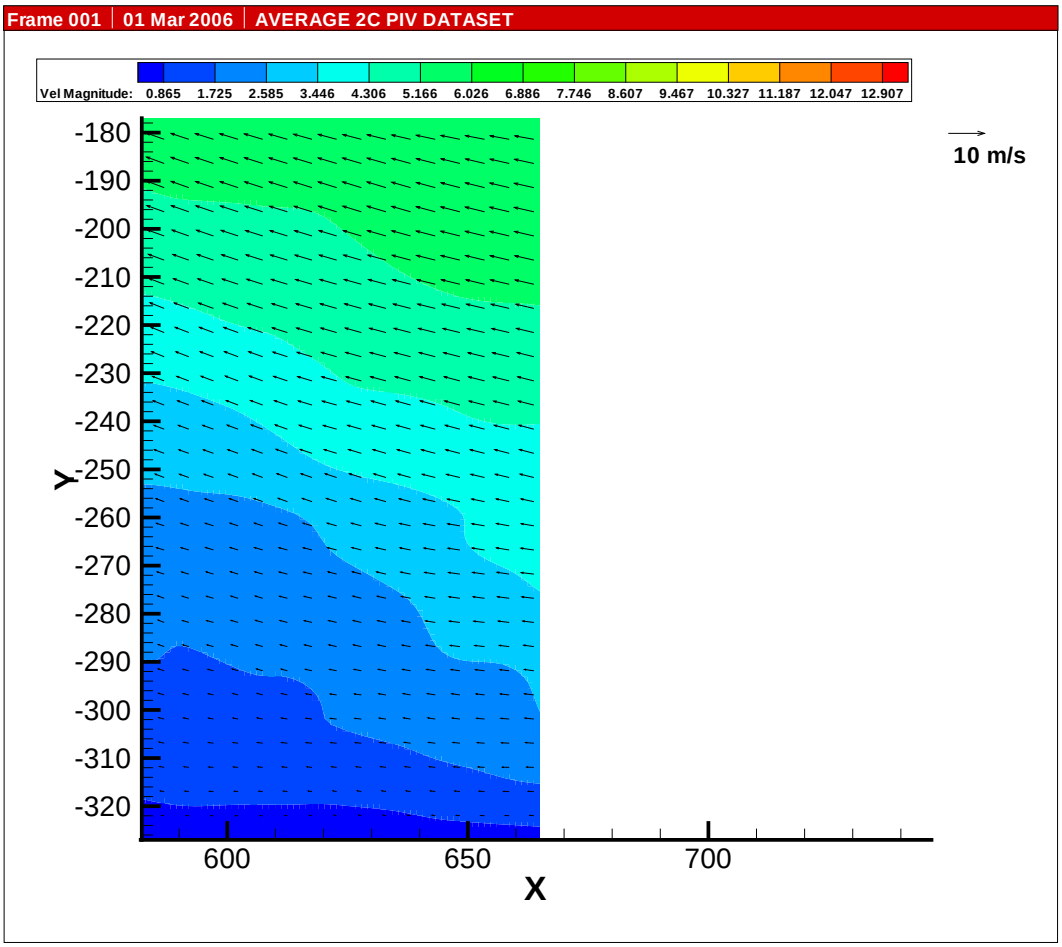

Figure 119: Flowfield at Advance Ratio 0.07- zone 8. Axes in mm.

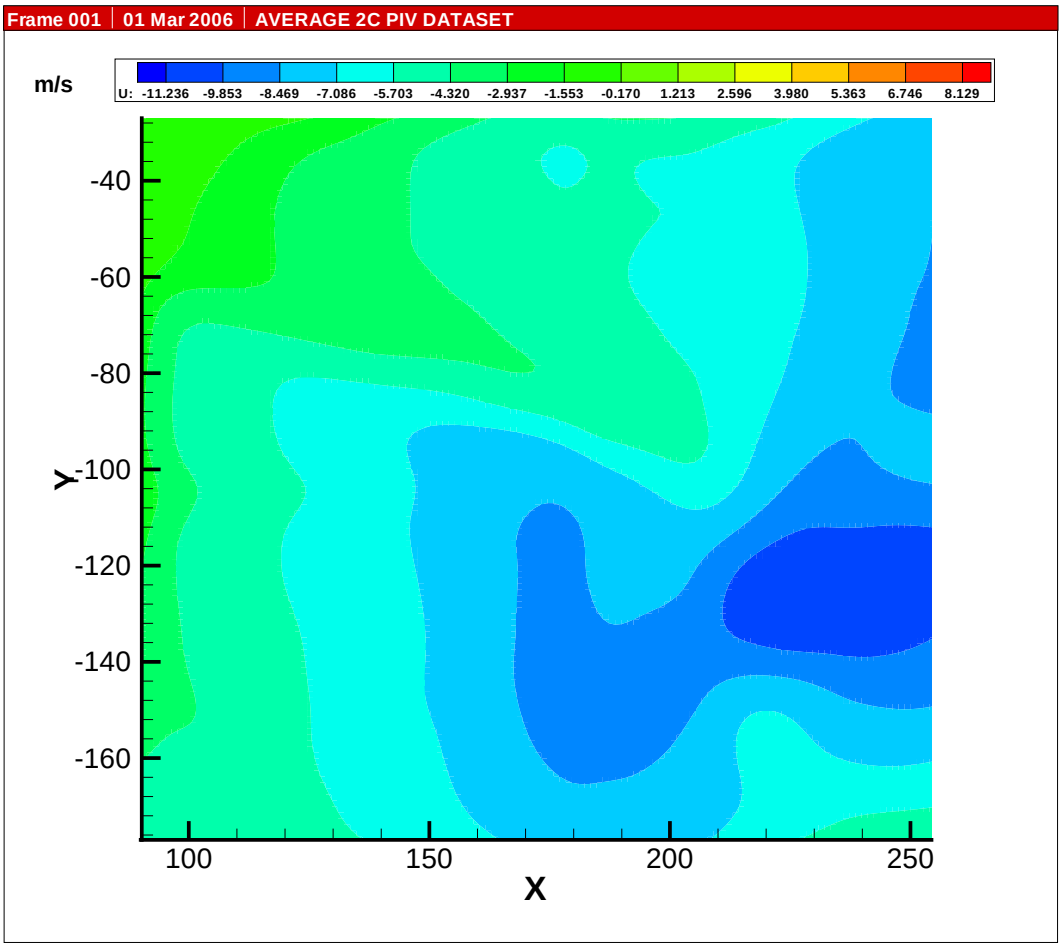

Figure 120: u Velocity at Advance Ratio 0.07- zone 1. Axes in mm.

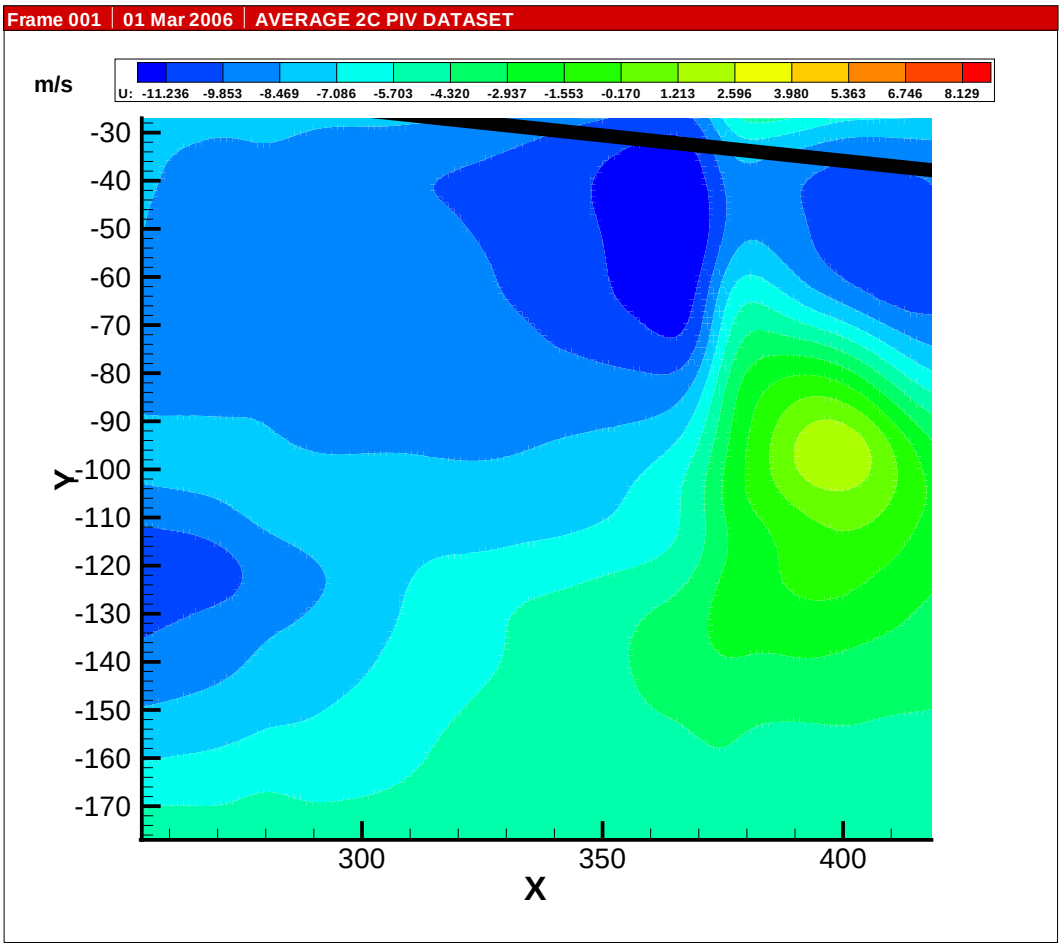

Figure 121: u Velocity at Advance Ratio 0.07- zone 2. Axes in mm.

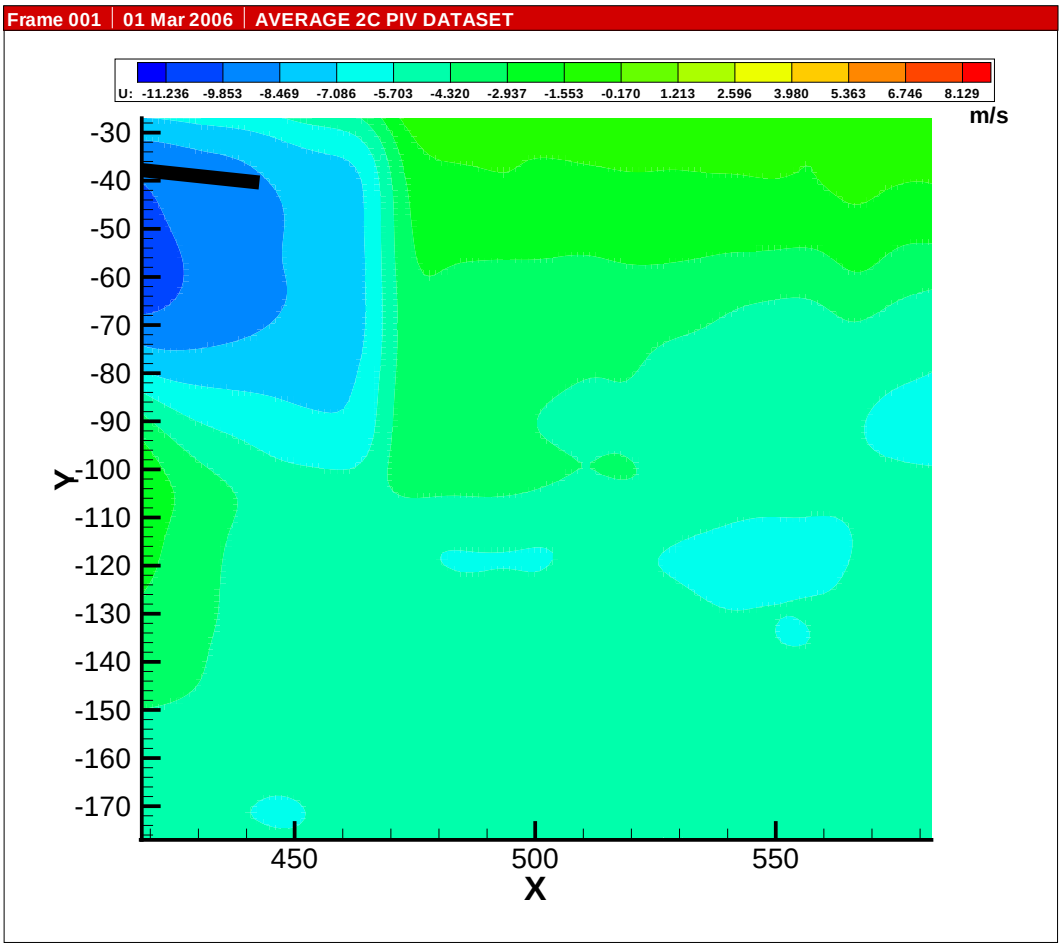

Figure 122: u Velocity at Advance Ratio 0.07- zone 3. Axes in mm.

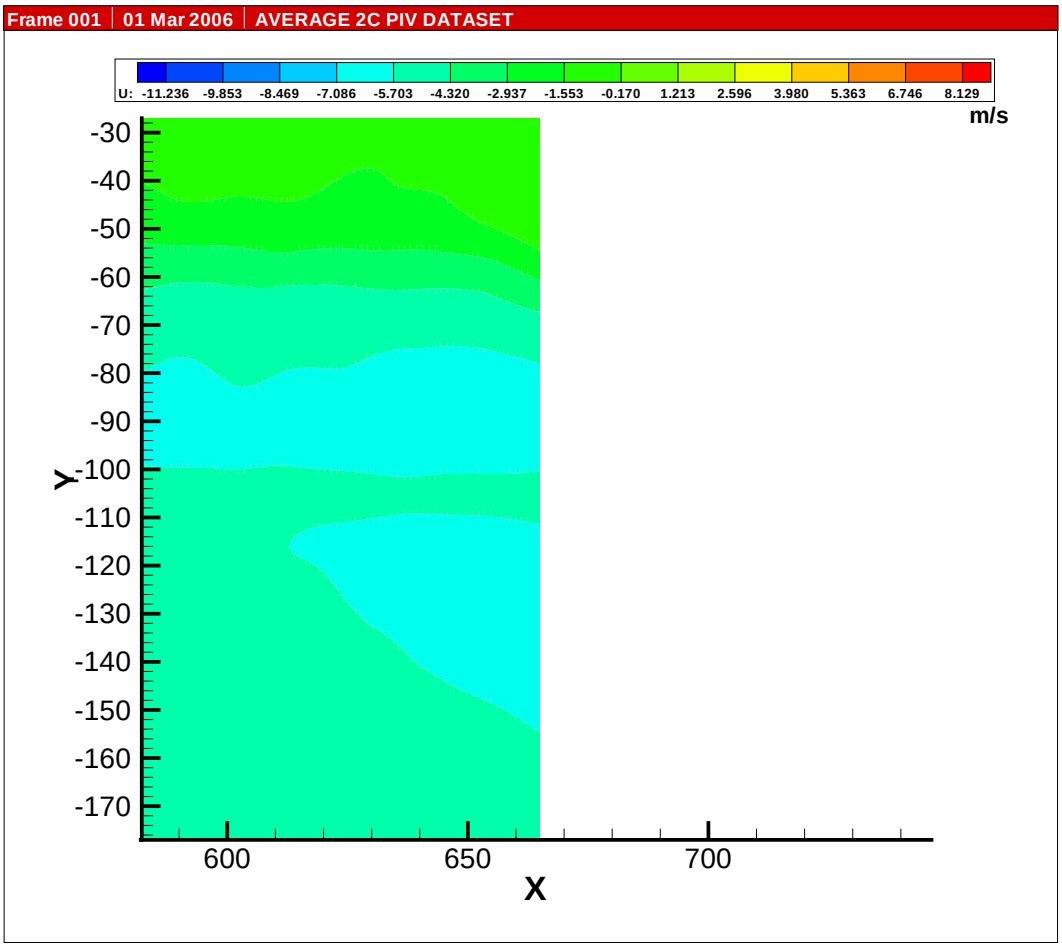

Figure 123: u Velocity at Advance Ratio 0.07- zone 4. Axes in mm.

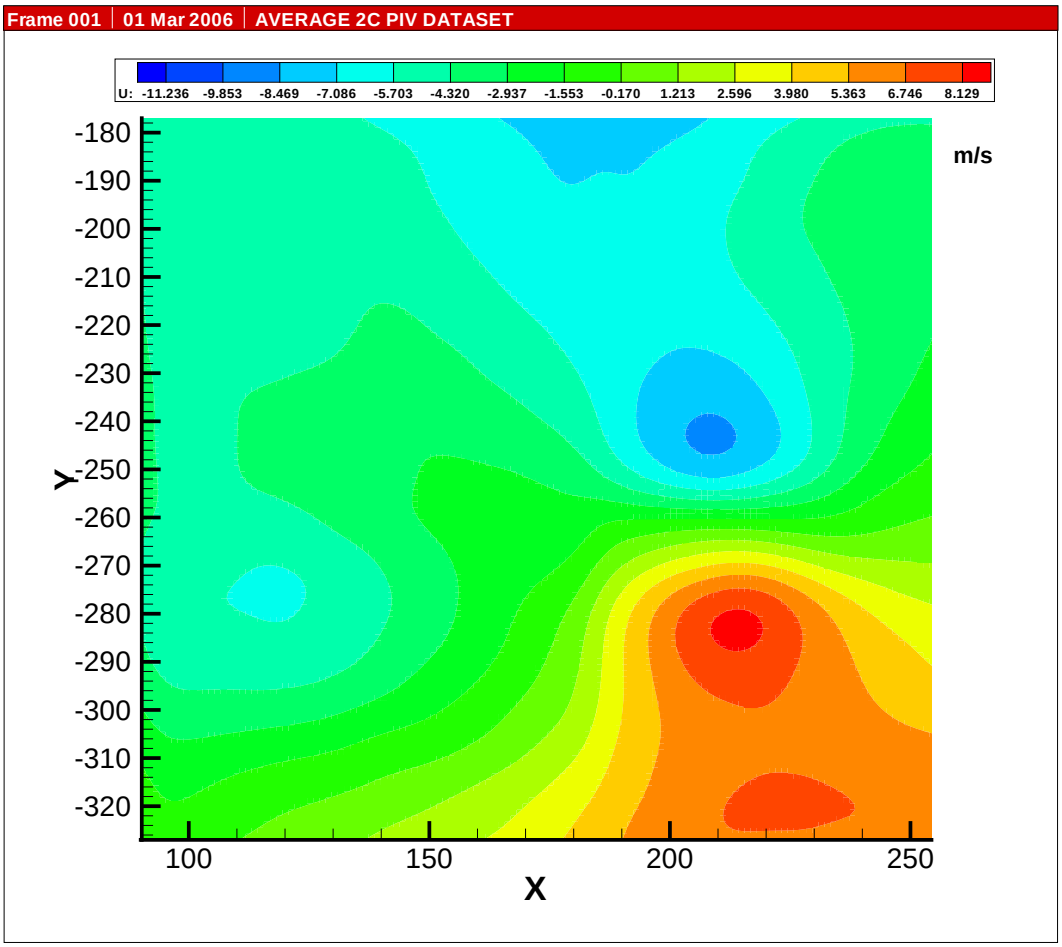

Figure 124: u Velocity at Advance Ratio 0.07- zone 5. Axes in mm.

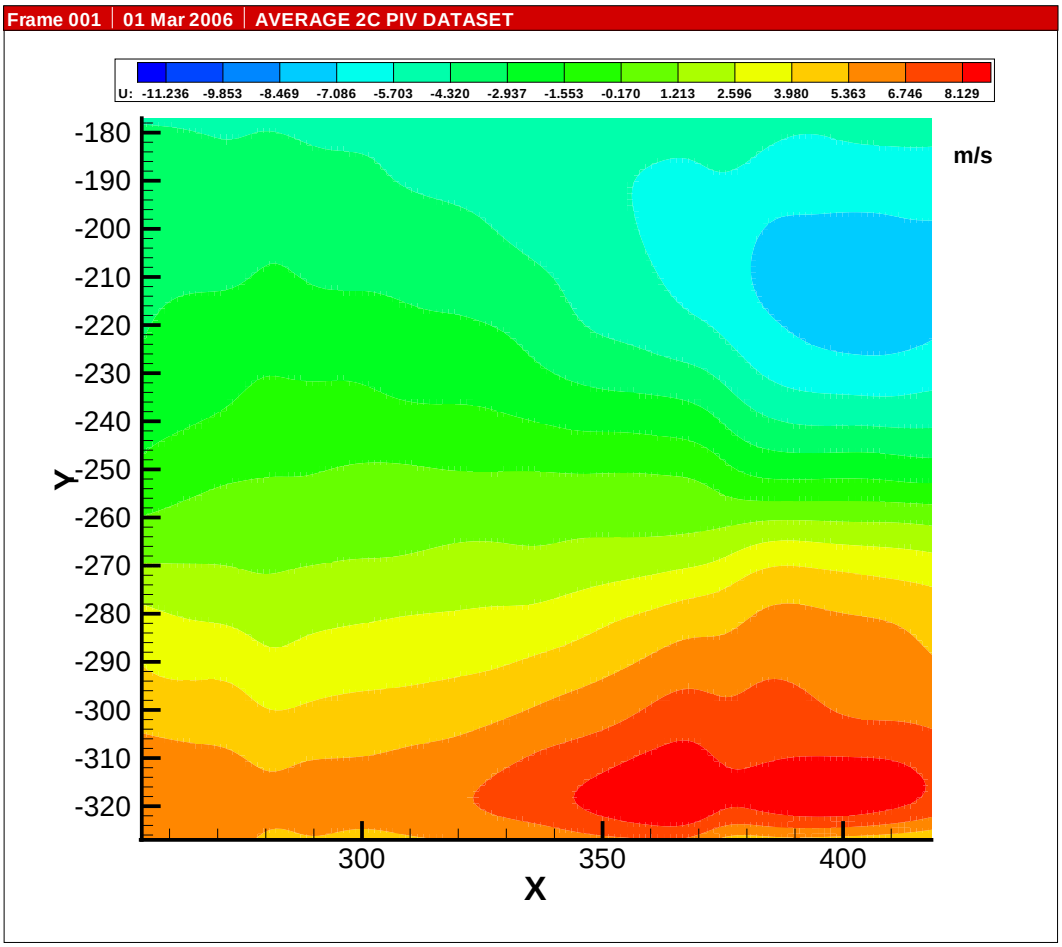

Figure 125: u Velocity at Advance Ratio 0.07- zone 6. Axes in mm.

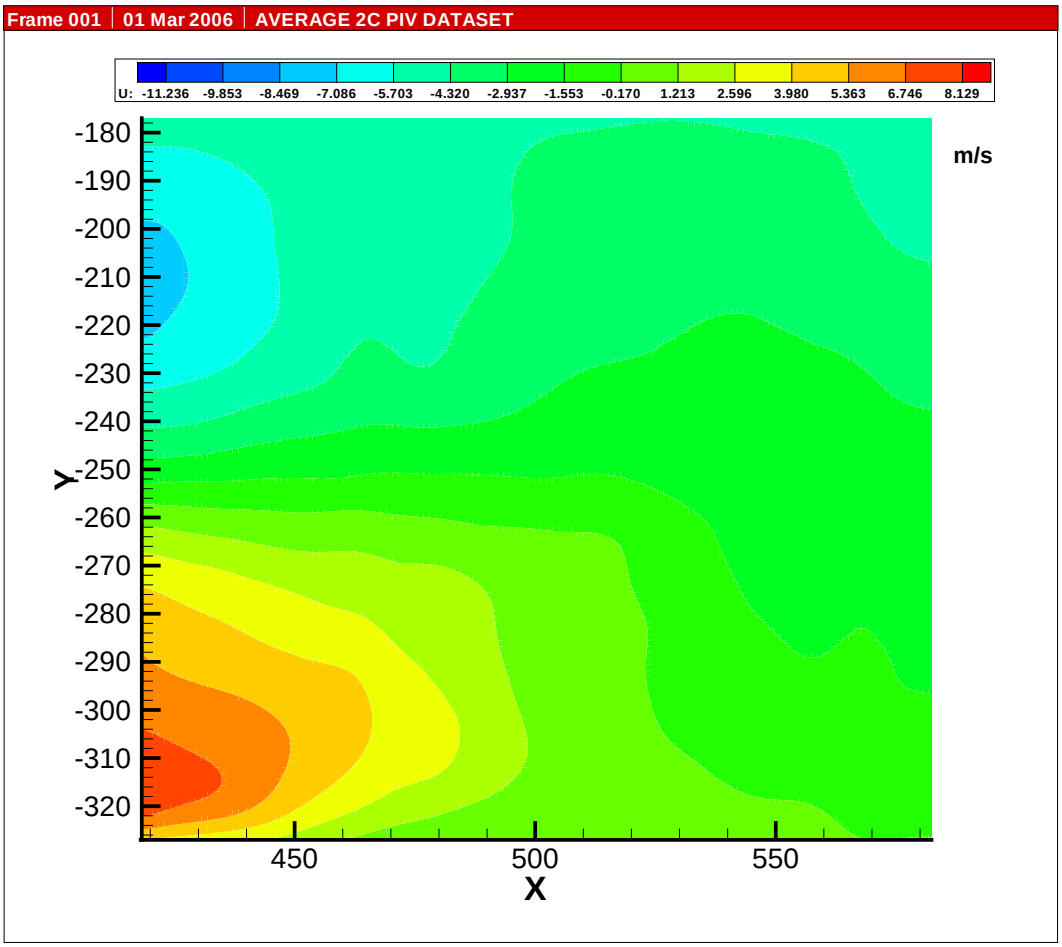

Figure 126: u Velocity at Advance Ratio 0.07- zone 7. Axes in mm.

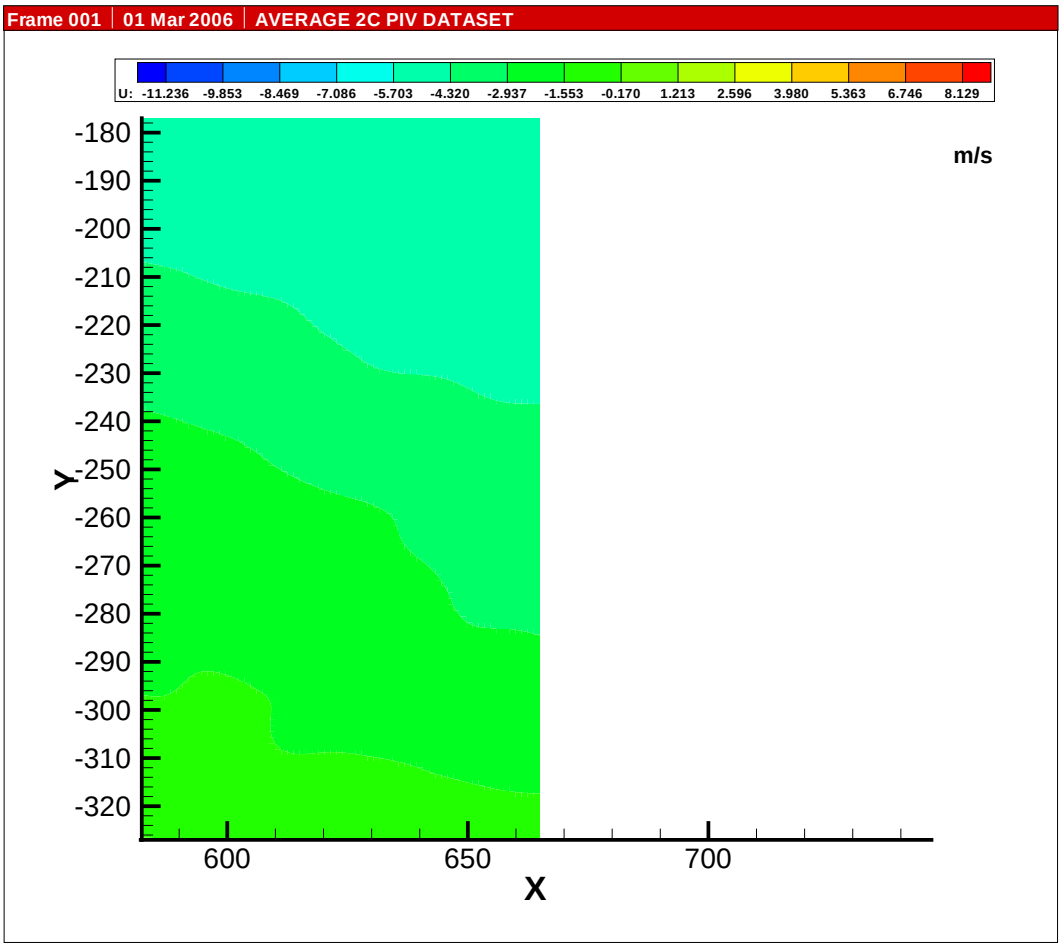

Figure 127: u Velocity at Advance Ratio 0.07- zone 8. Axes in mm.

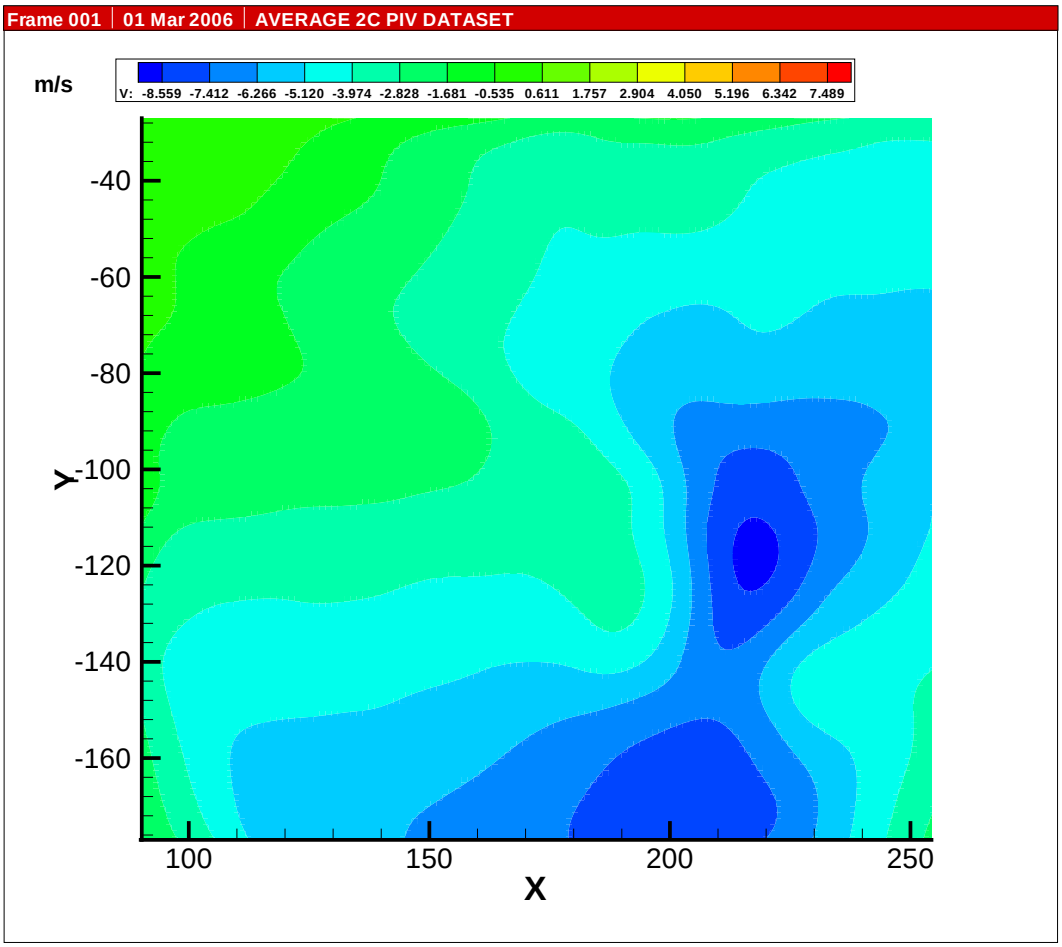

Figure 128: v Velocity at Advance Ratio 0.07- zone 1. Axes in mm.

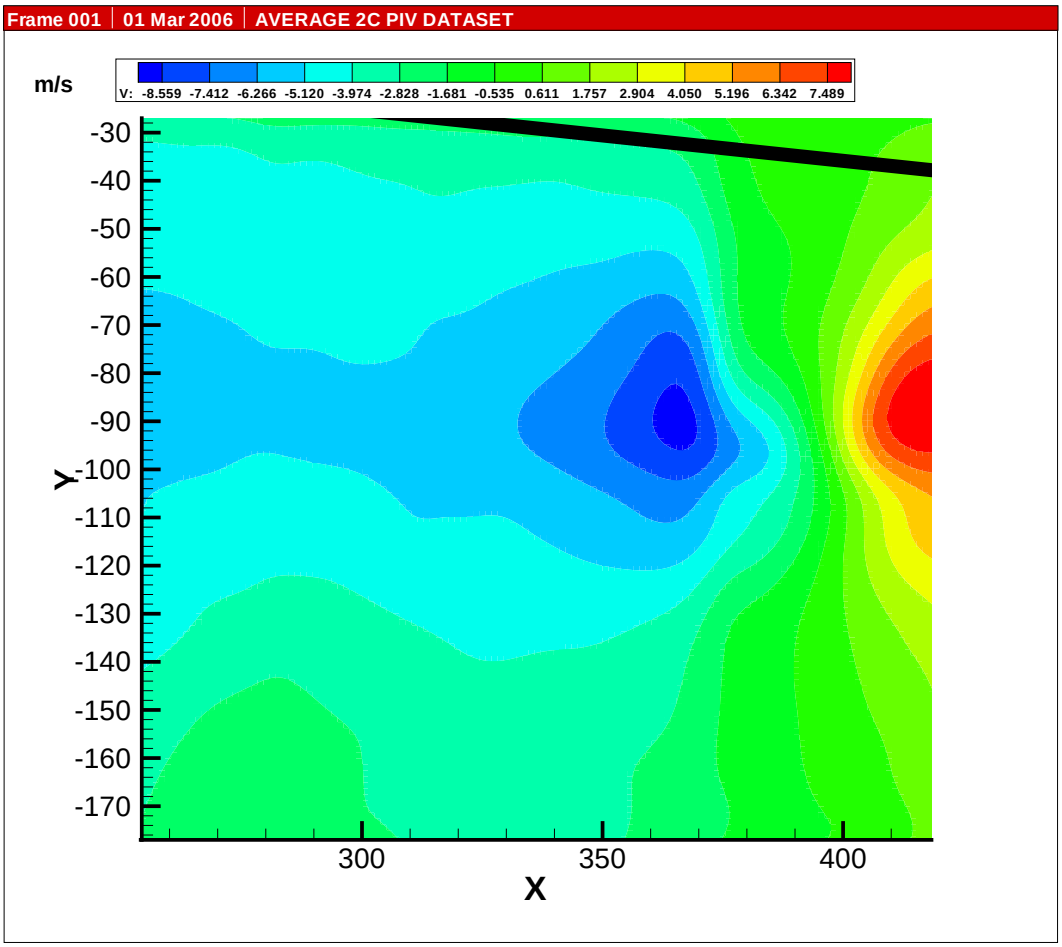

Figure 129: v Velocity at Advance Ratio 0.07- zone 2. Axes in mm.

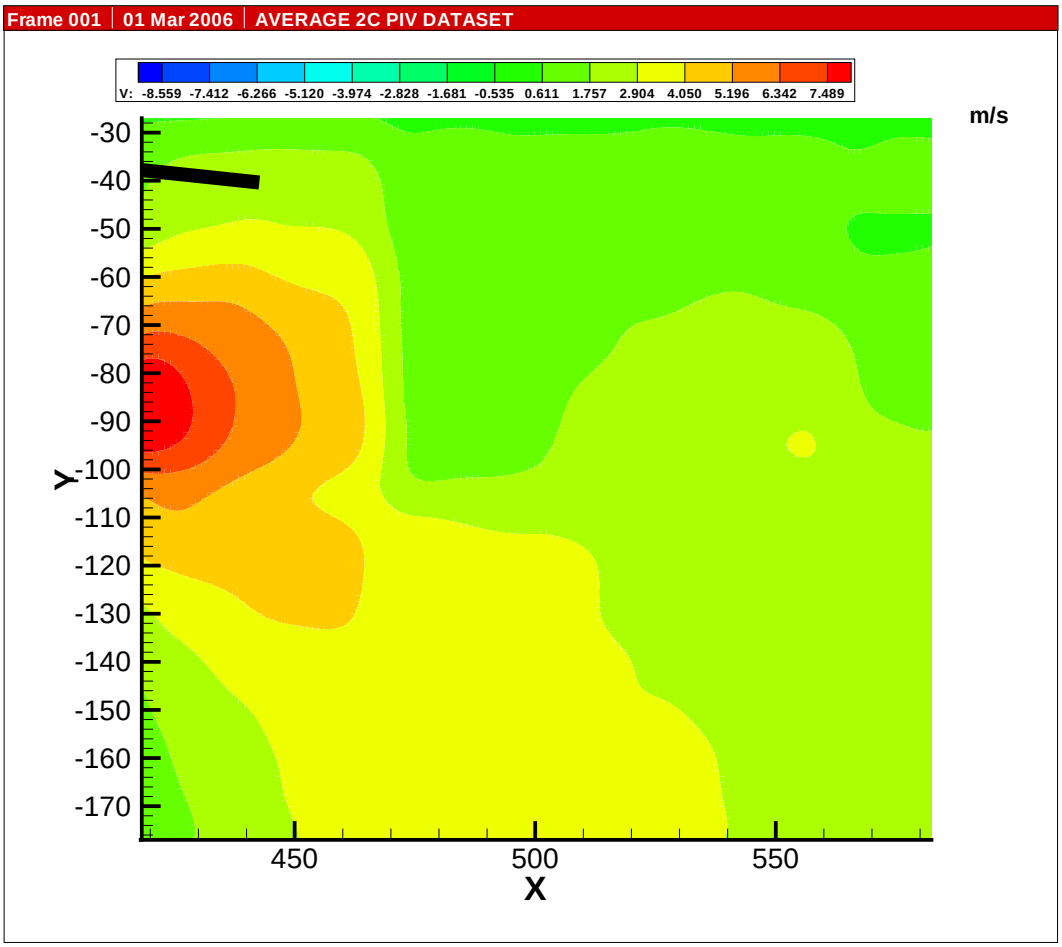

Figure 130: v Velocity at Advance Ratio 0.07- zone 3. Axes in mm.

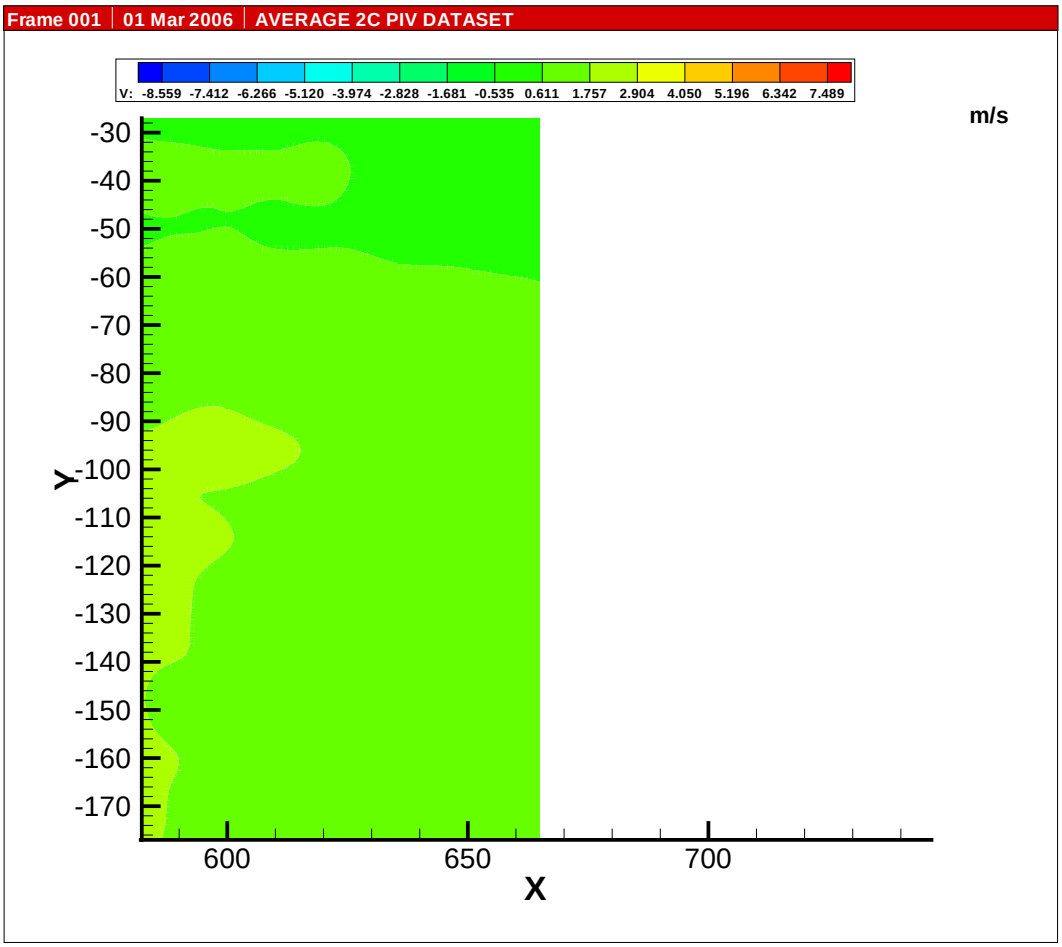

Figure 131: v Velocity at Advance Ratio 0.07- zone 4. Axes in mm.

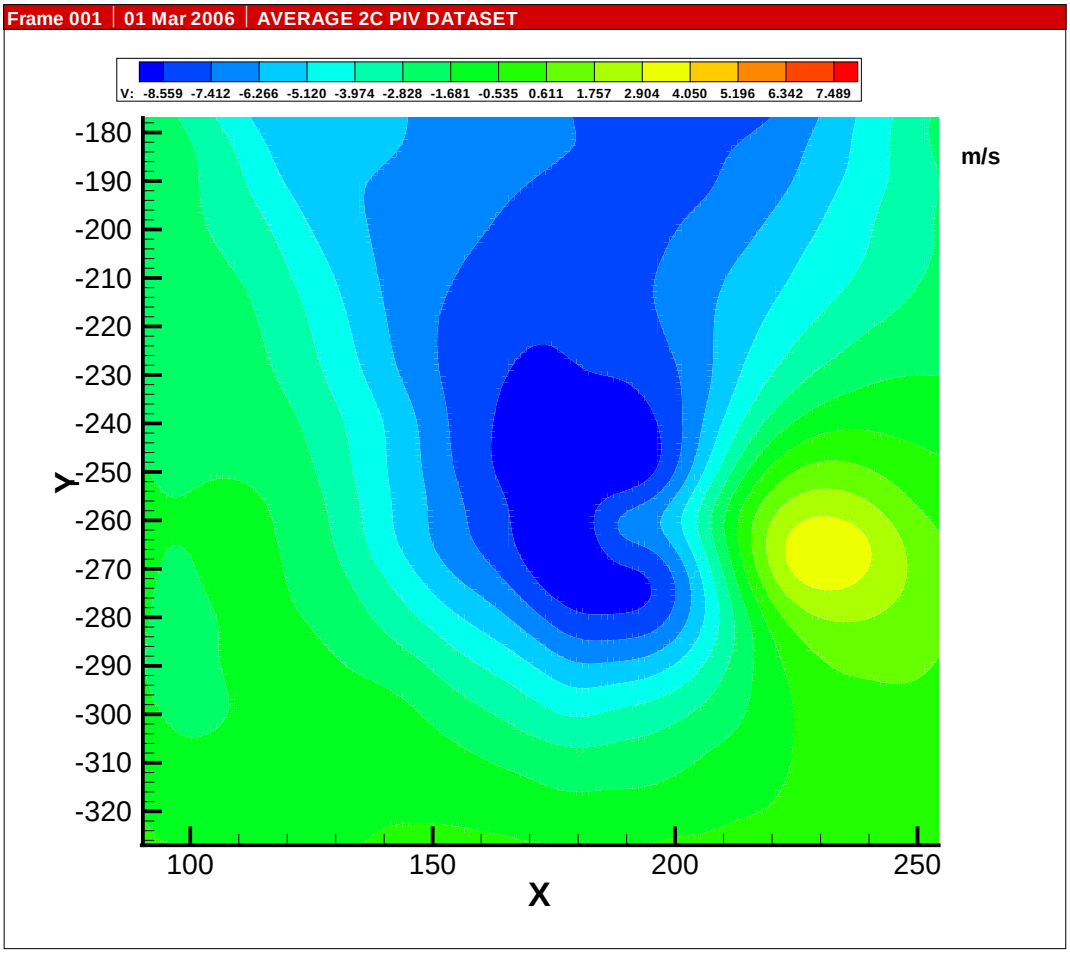

Figure 132: v Velocity at Advance Ratio 0.07- zone 5. Axes in mm.

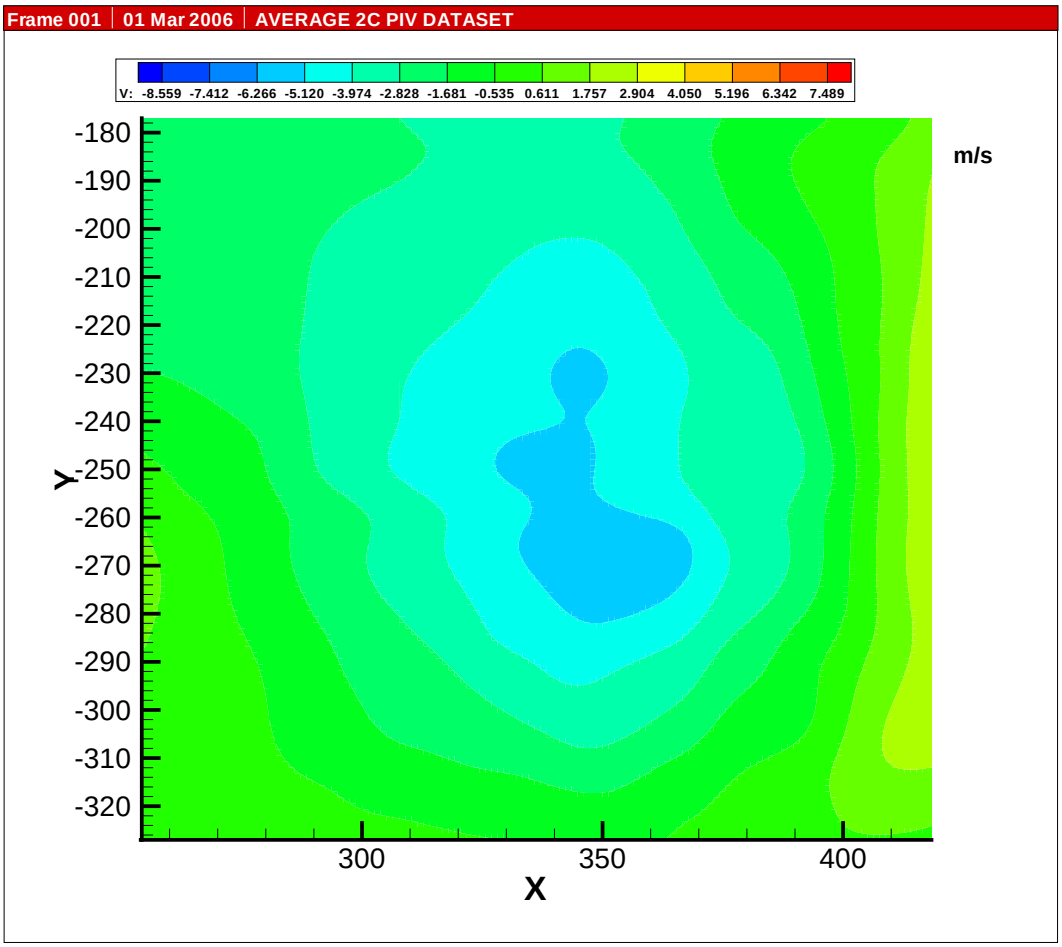

Figure 133: v Velocity at Advance Ratio 0.07- zone 6. Axes in mm.

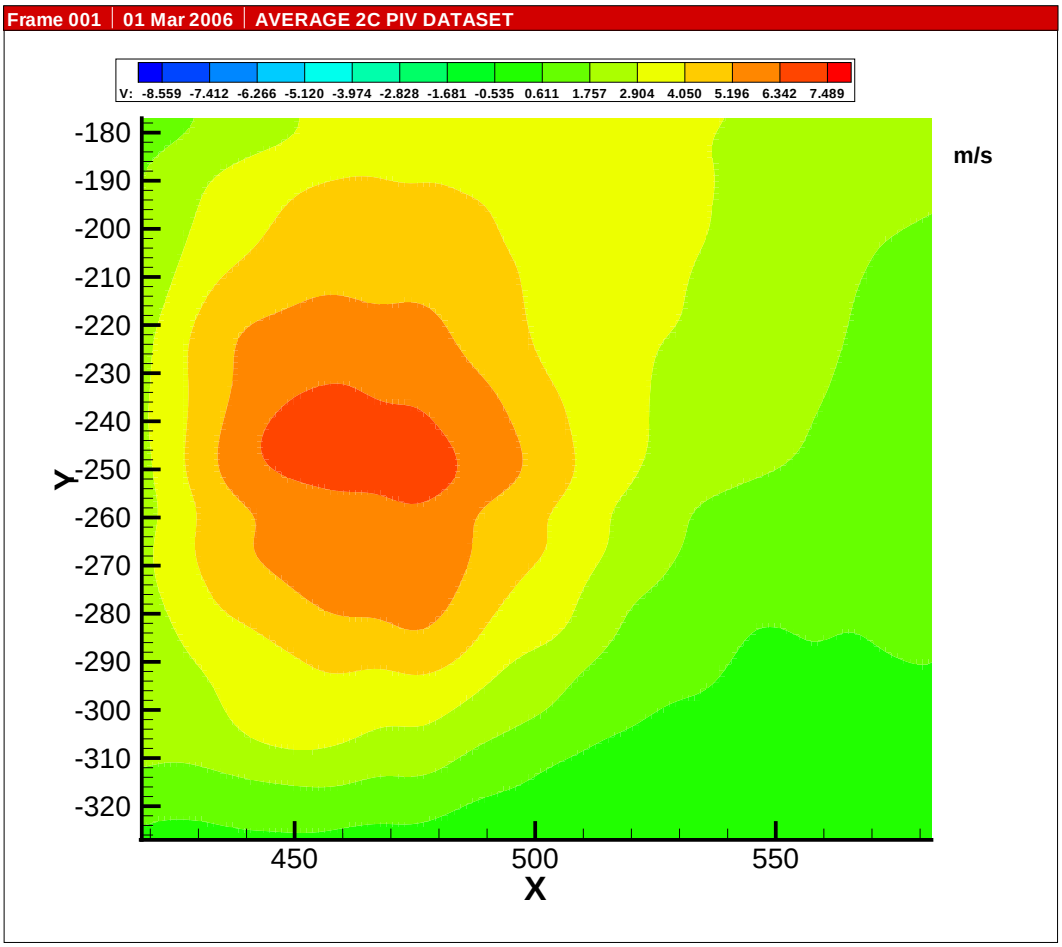

Figure 134: v Velocity at Advance Ratio 0.07- zone 7. Axes in mm.

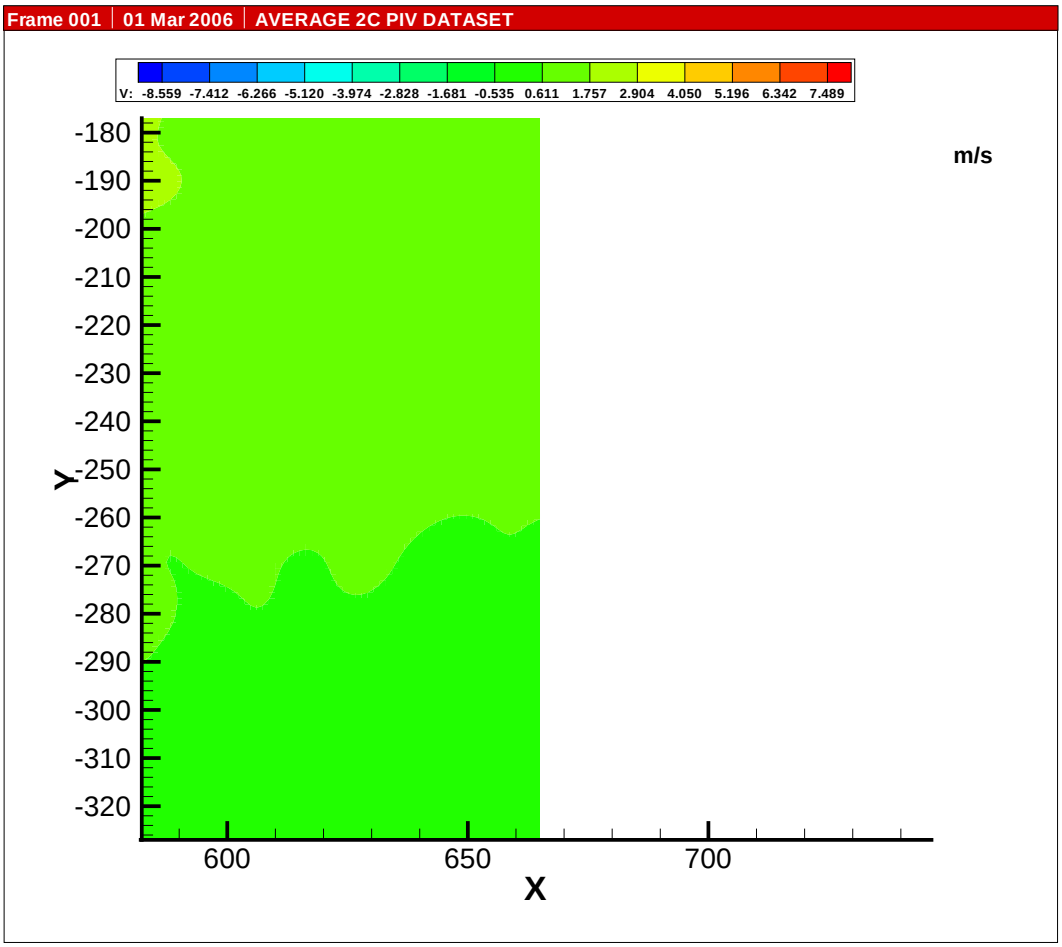

Figure 135: v Velocity at Advance Ratio 0.07- zone 8. Axes in mm.

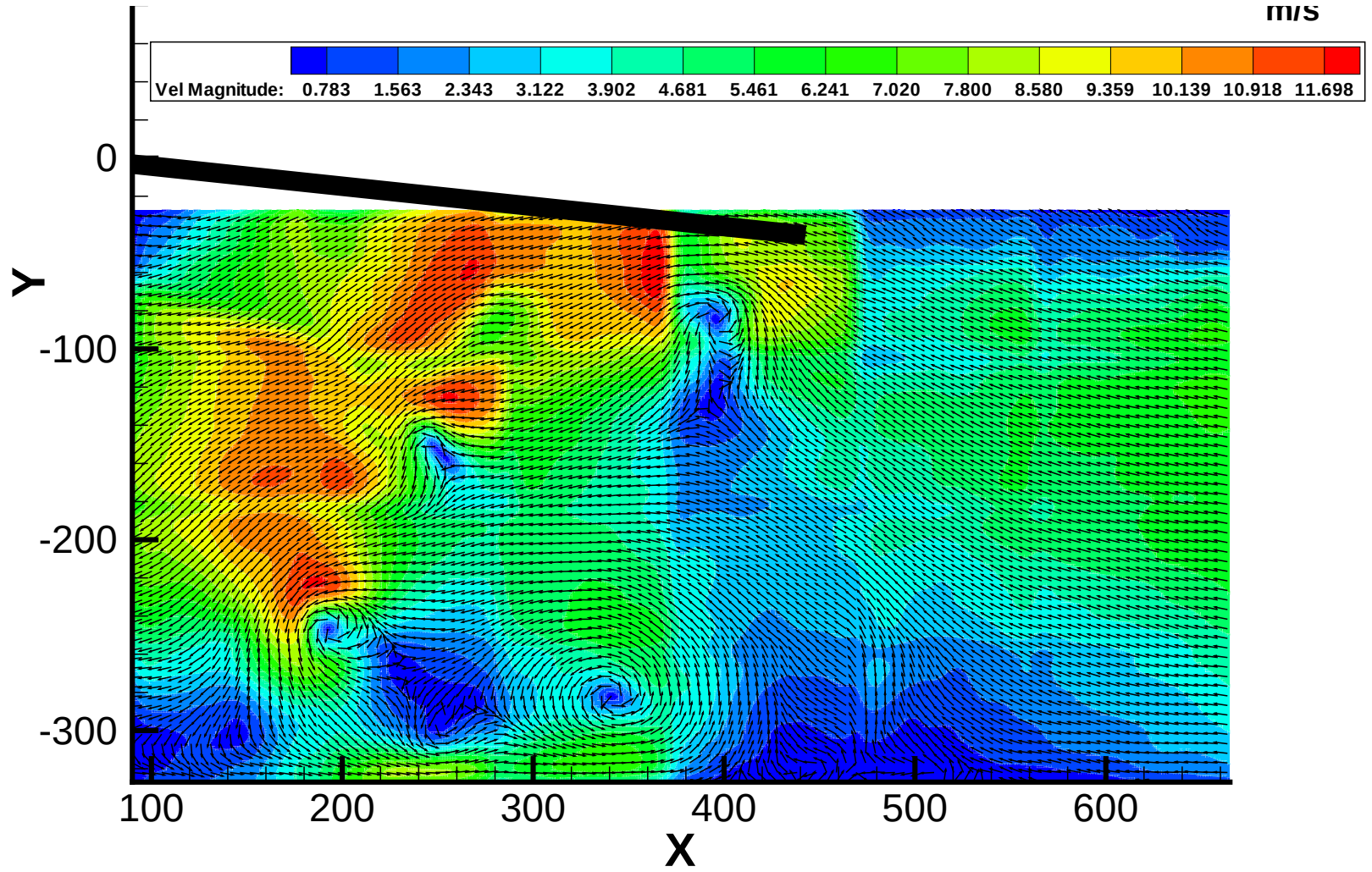

Figure 136: Flowfield at Advance Ratio 0.08. Axes in mm.

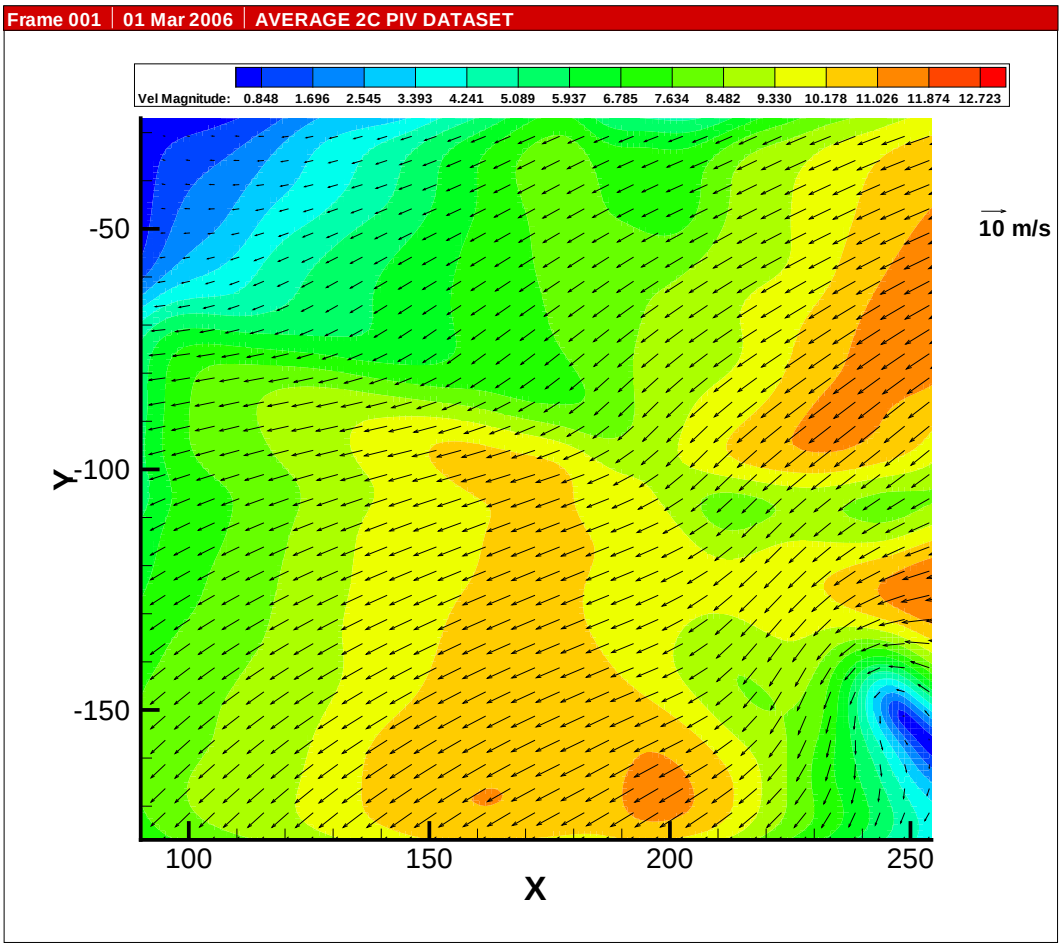

Figure 137: Flowfield at Advance Ratio 0.08- zone 1. Axes in mm.

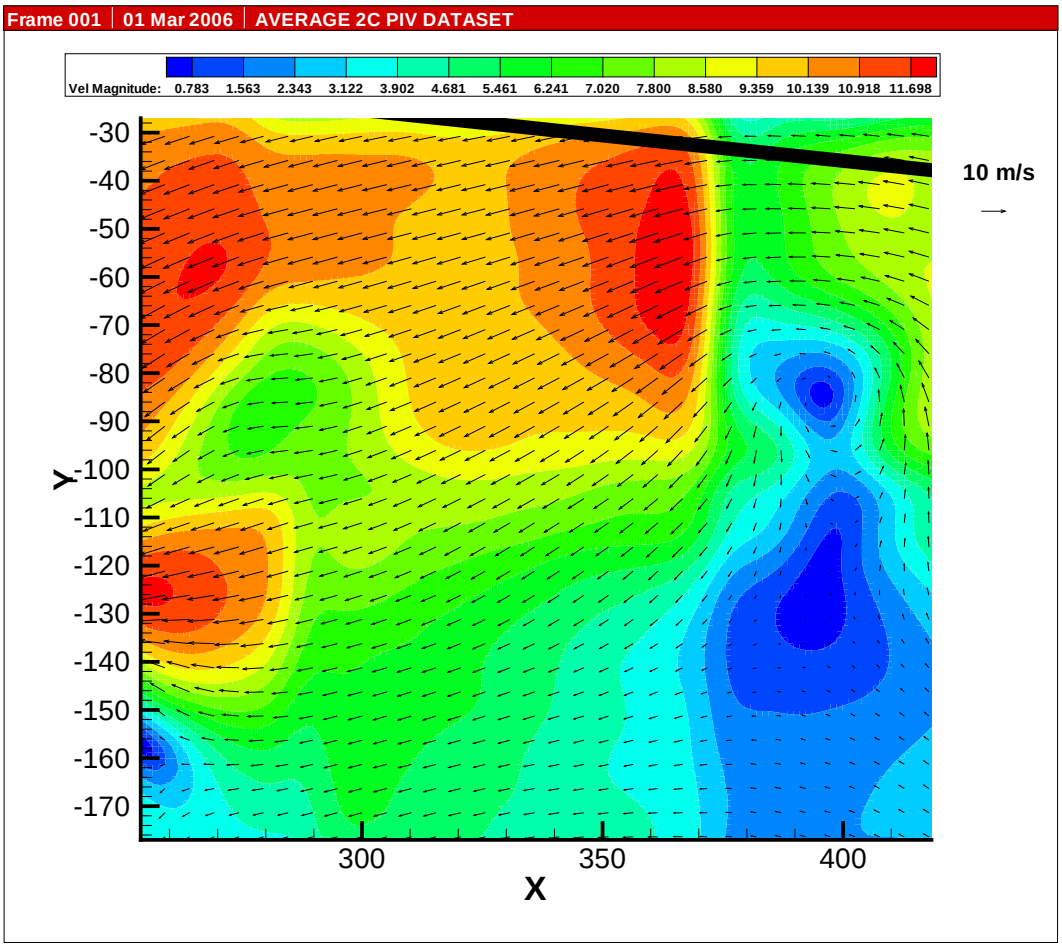

Figure 138: Flowfield at Advance Ratio 0.08- zone 2. Axes in mm.

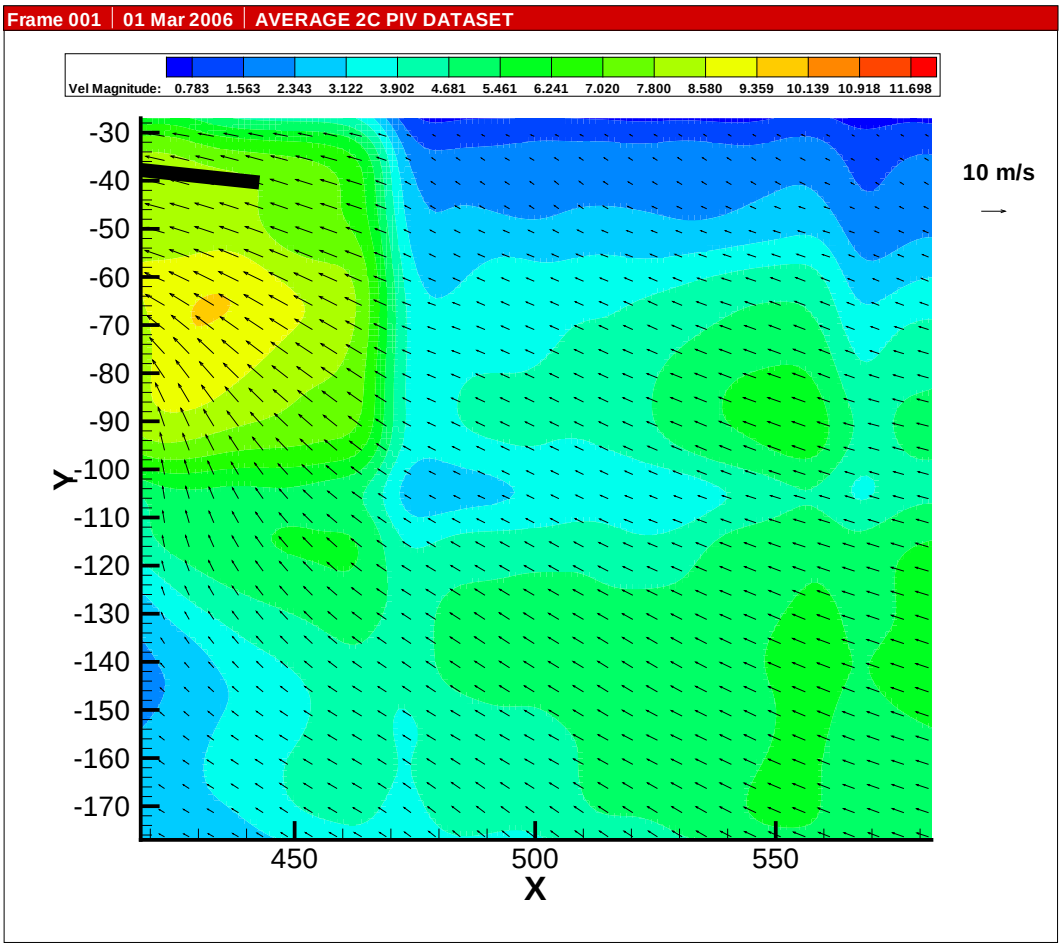

Figure 139: Flowfield at Advance Ratio 0.08- zone 3. Axes in mm.

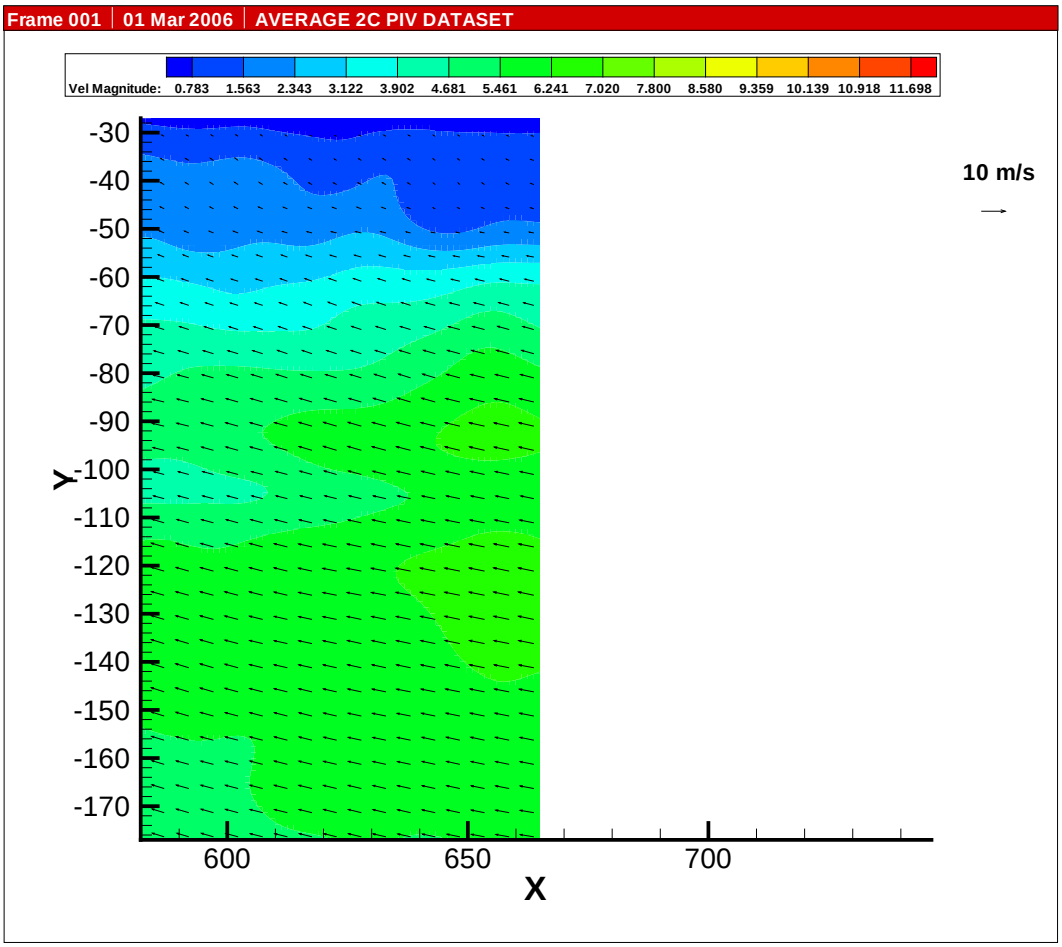

Figure 140: Flowfield at Advance Ratio 0.08- zone 4. Axes in mm.

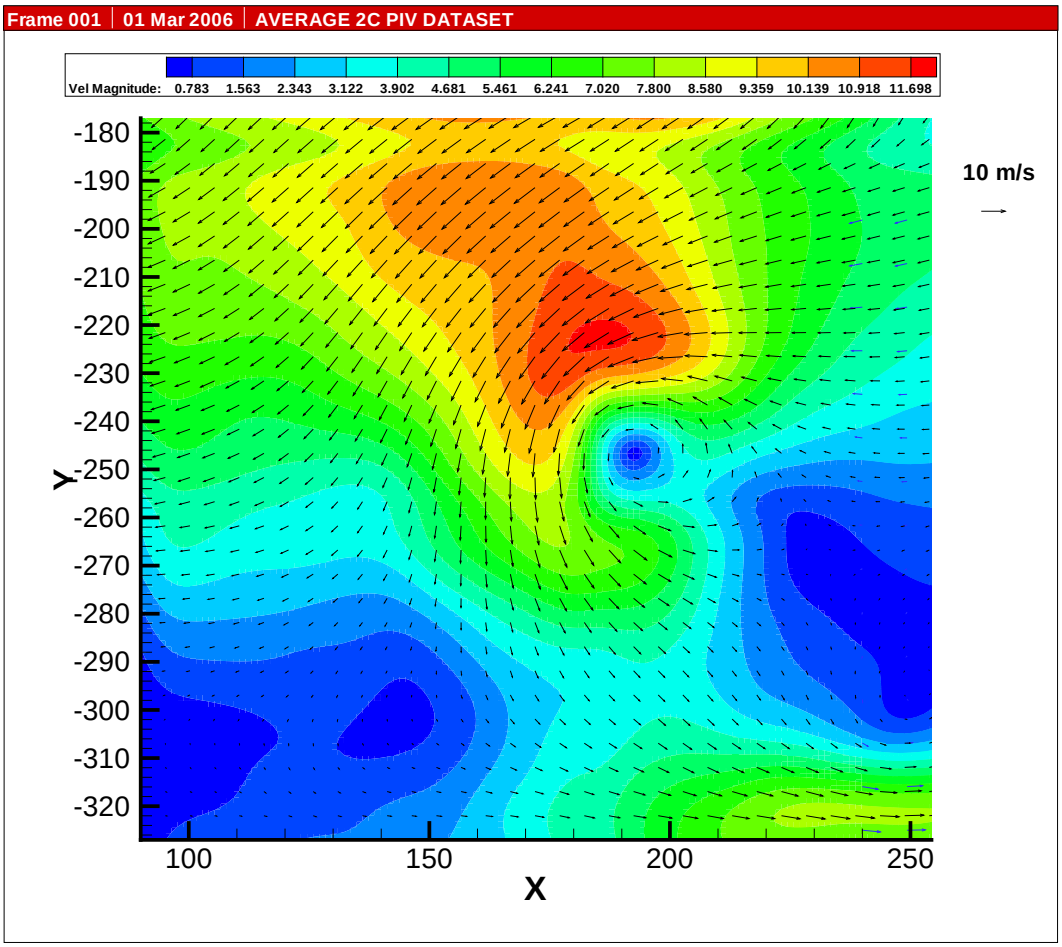

Figure 141: Flowfield at Advance Ratio 0.08- zone 5. Axes in mm.

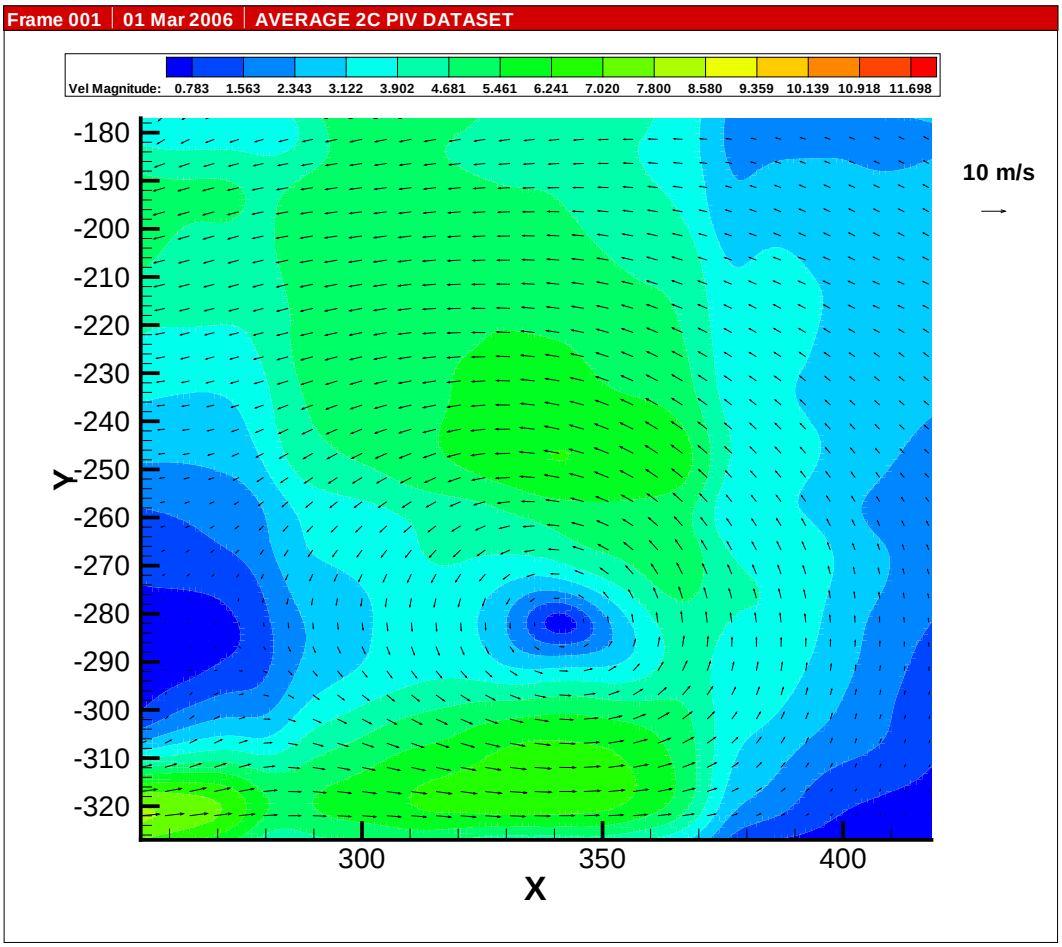

Figure 142: Flowfield at Advance Ratio 0.08- zone 6. Axes in mm.

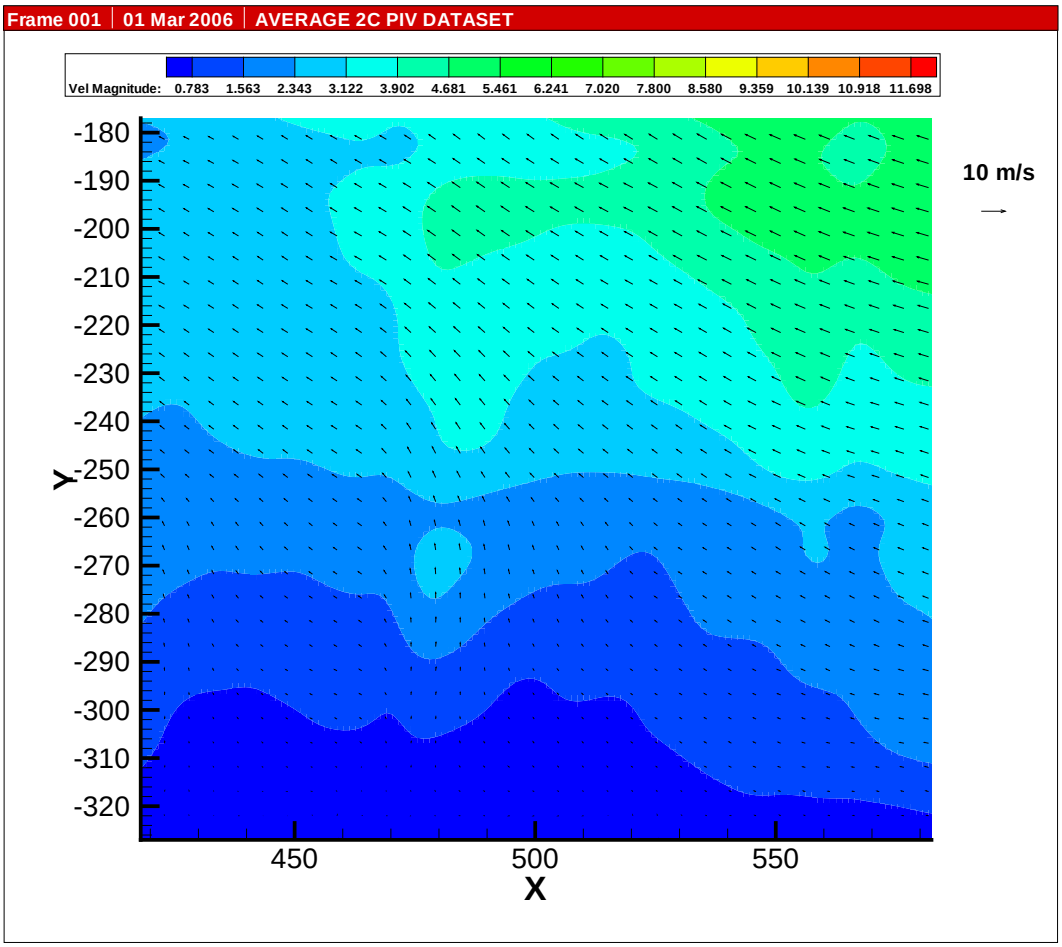

Figure 143: Flowfield at Advance Ratio 0.08- zone 7. Axes in mm.

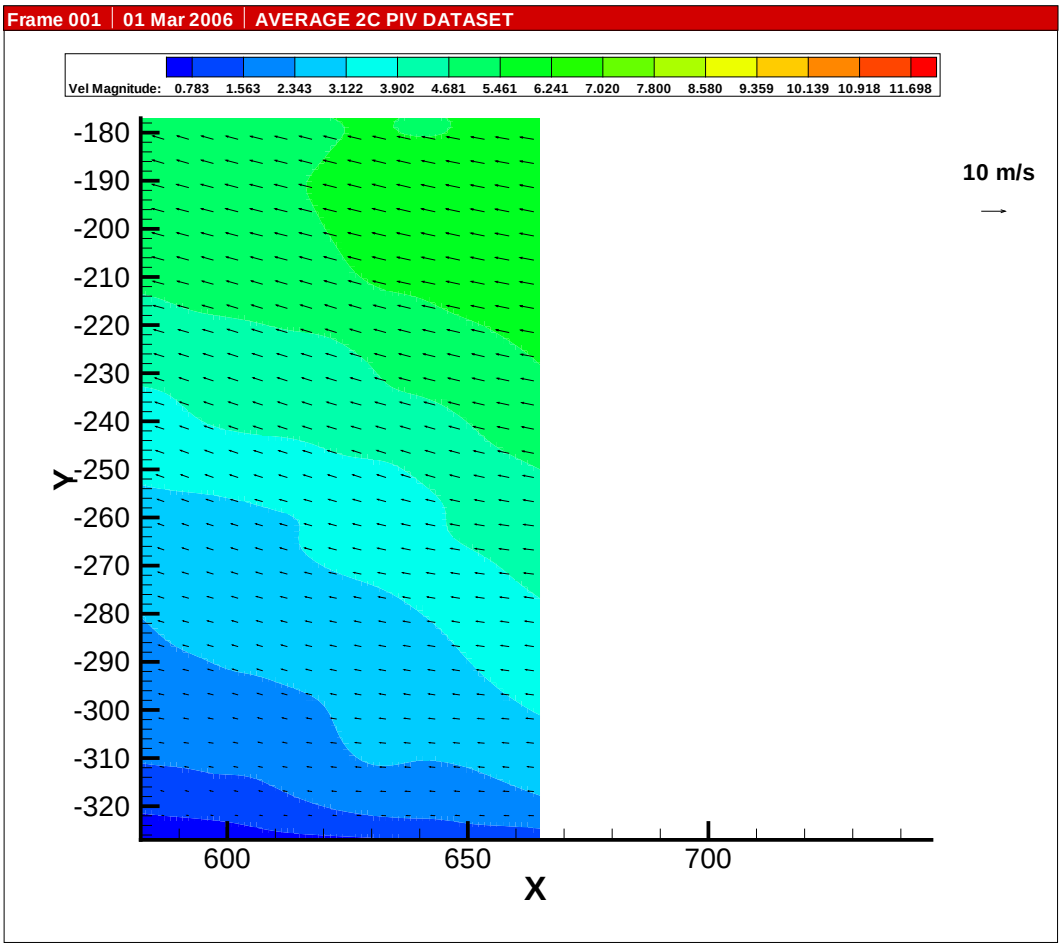

Figure 144: Flowfield at Advance Ratio 0.08- zone 8. Axes in mm.

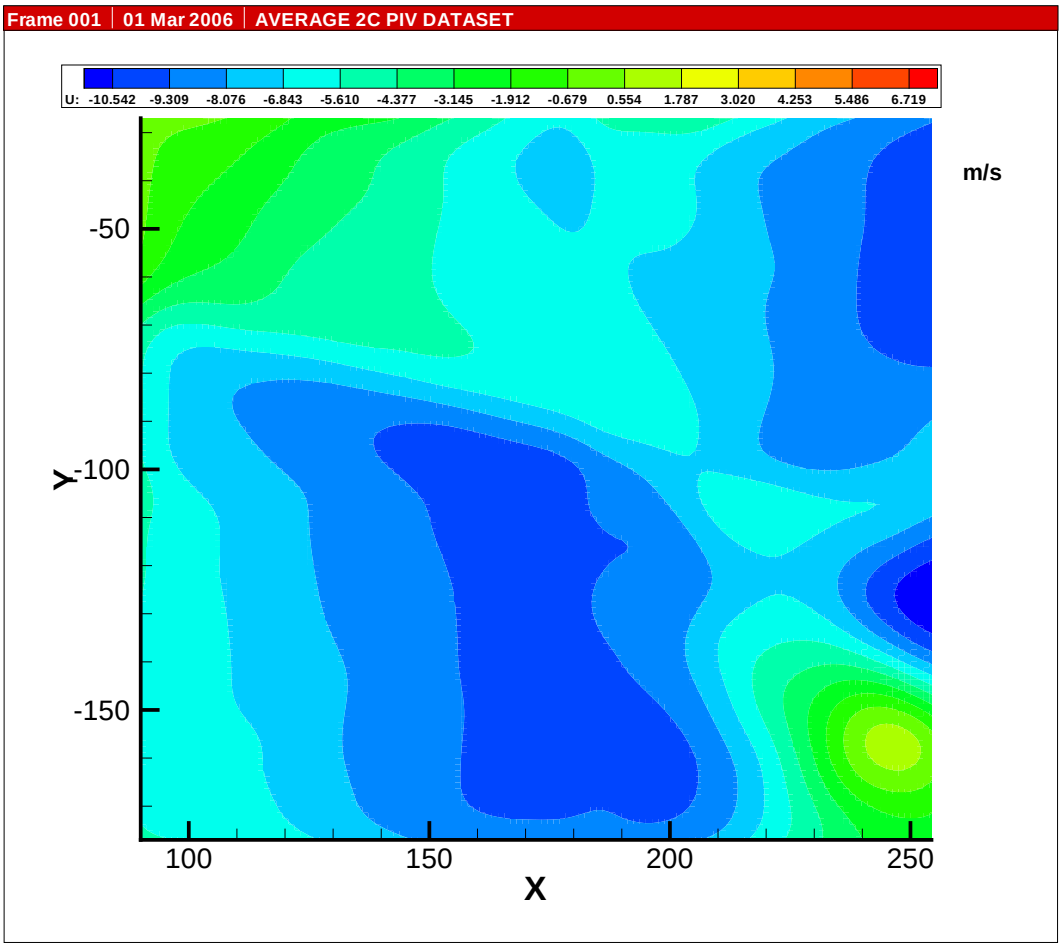

Figure 145: u Velocity at Advance Ratio 0.08- zone 1. Axes in mm.

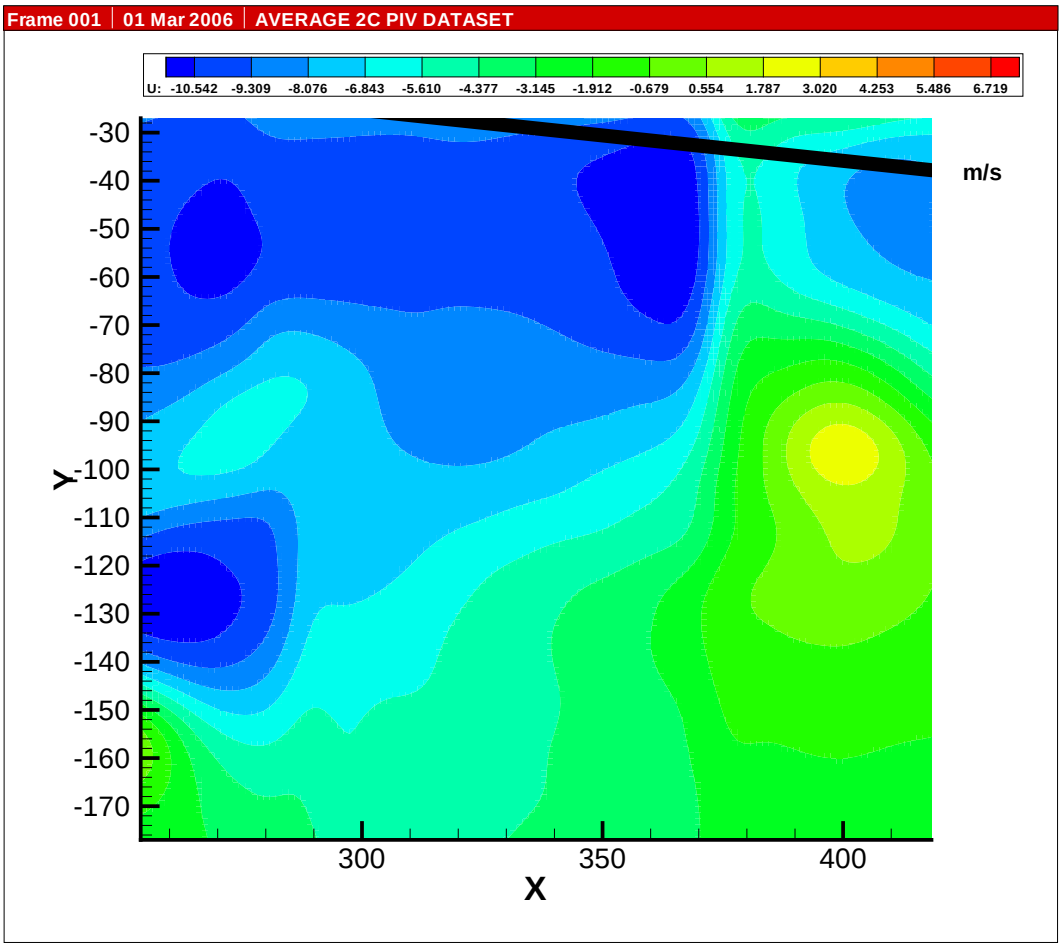

Figure 146: u Velocity at Advance Ratio 0.08- zone 2. Axes in mm.

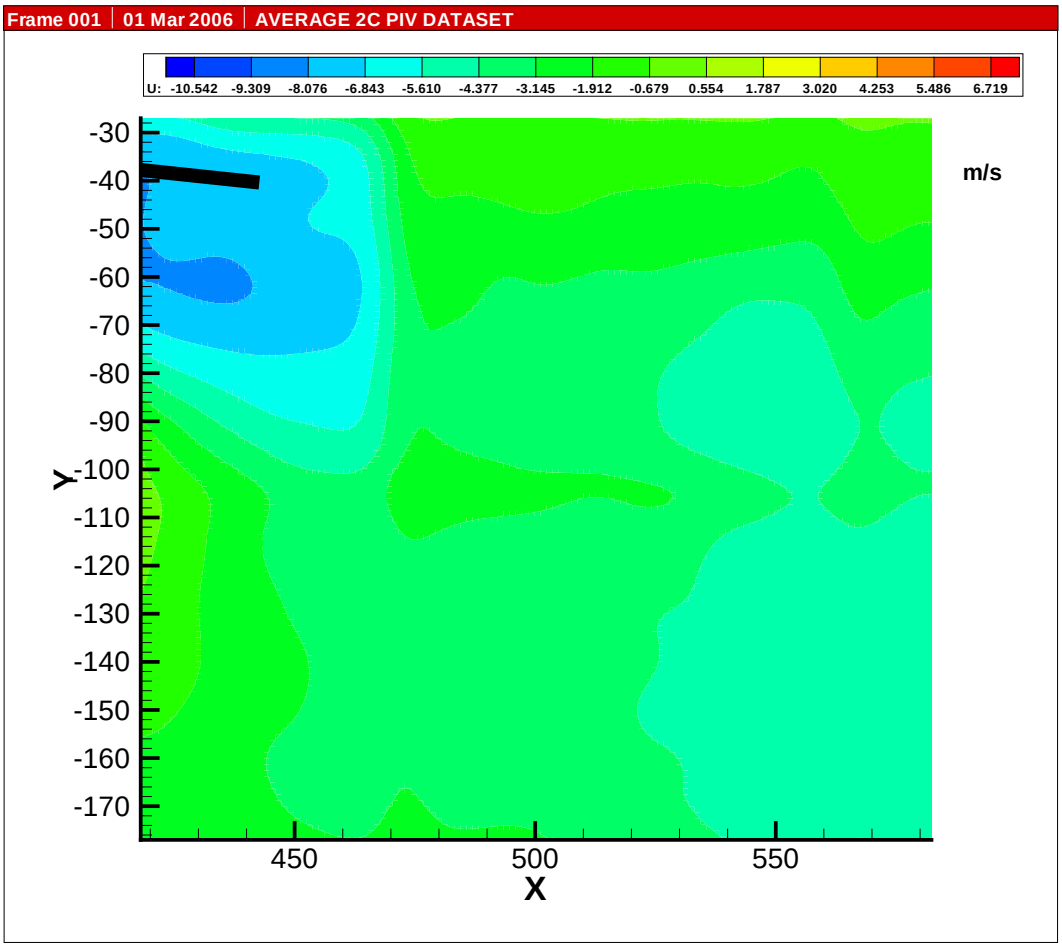

Figure 147: u Velocity at Advance Ratio 0.08- zone 3. Axes in mm.

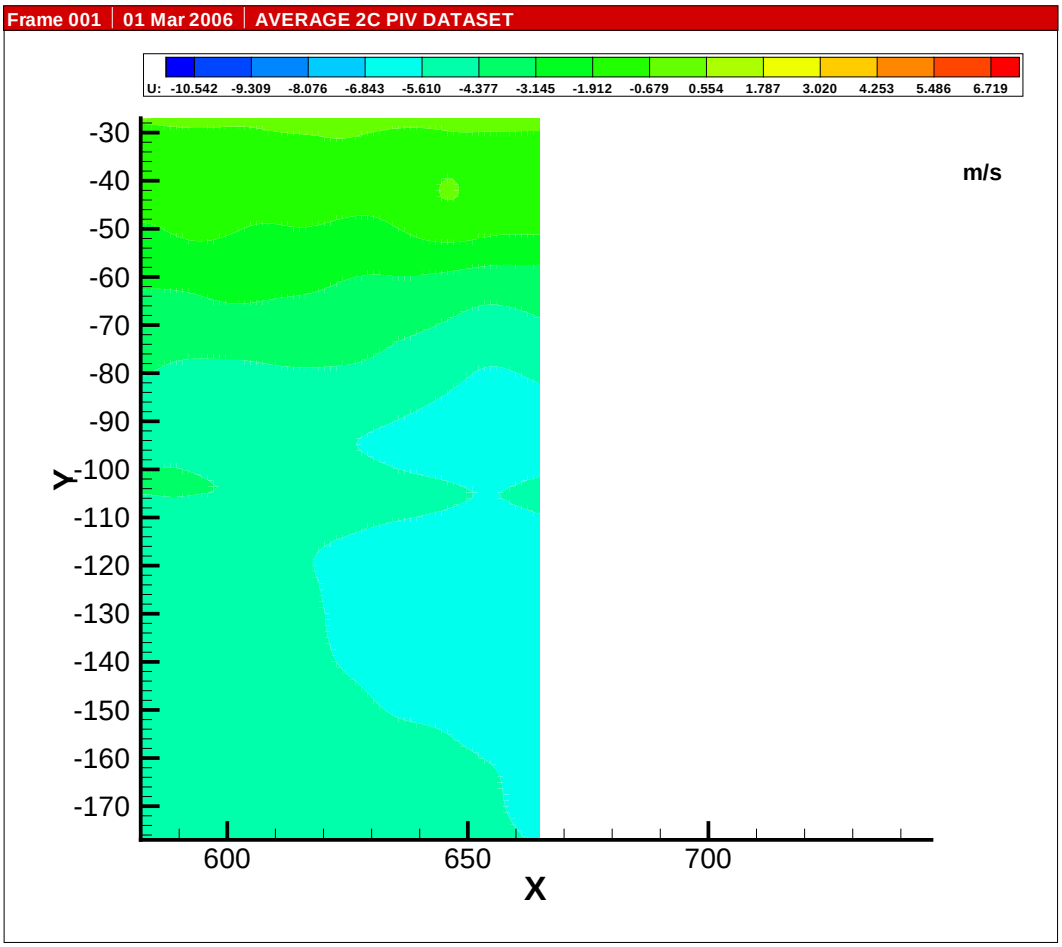

Figure 148: u Velocity at Advance Ratio 0.08- zone 4. Axes in mm.

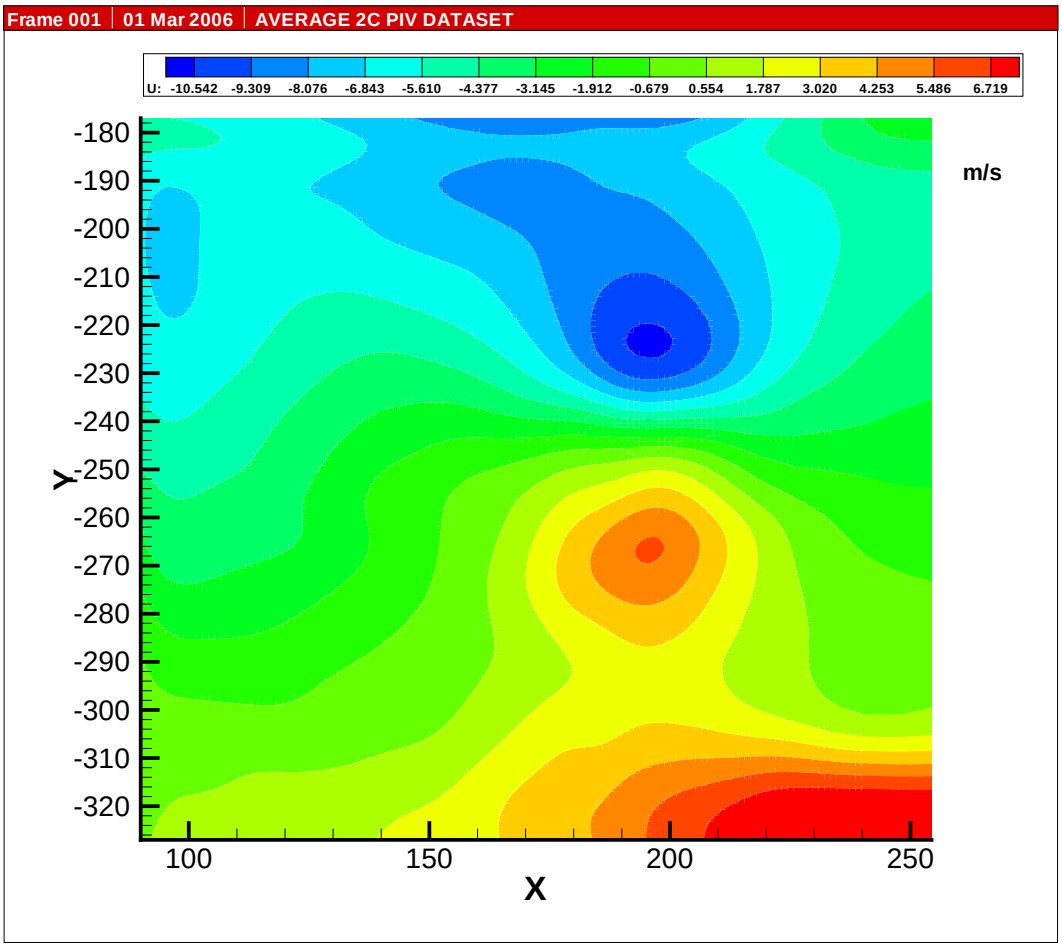

Figure 149: u Velocity at Advance Ratio 0.08- zone 5. Axes in mm.

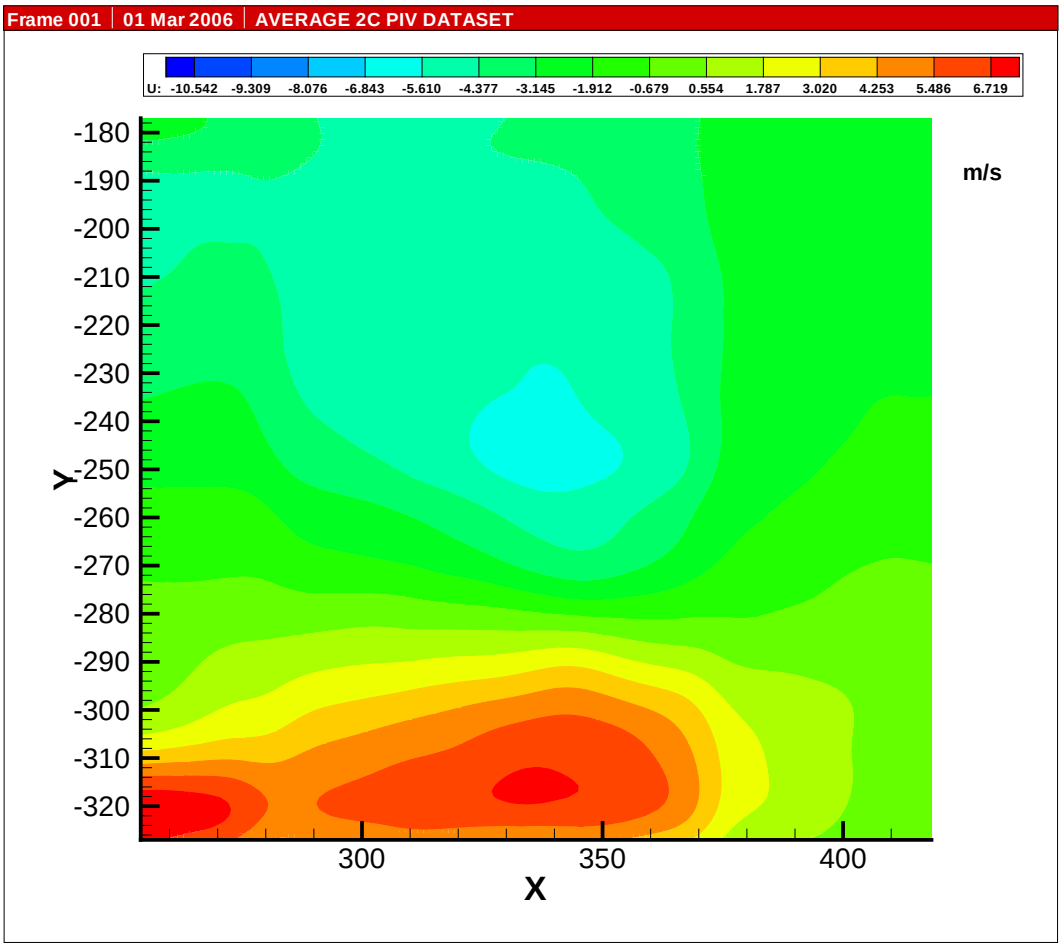

Figure 150: u Velocity at Advance Ratio 0.08- zone 6. Axes in mm.

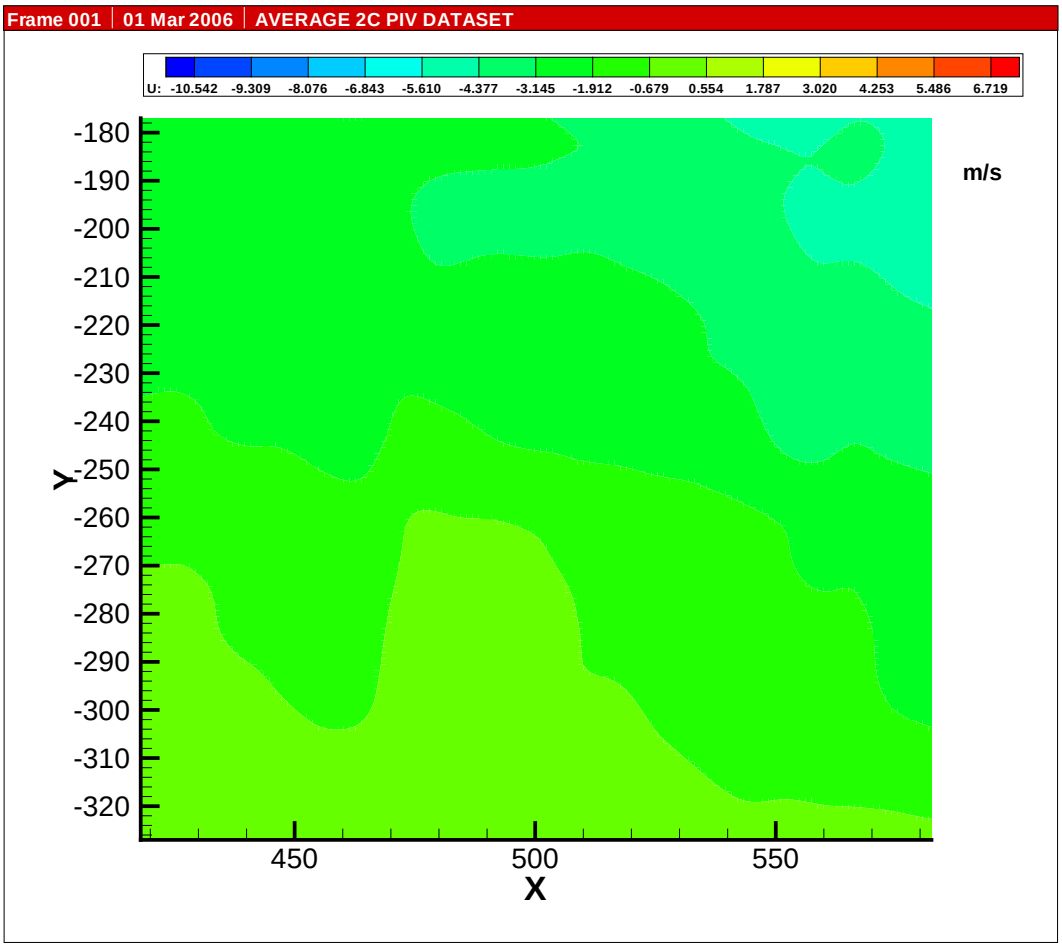

Figure 151: u Velocity at Advance Ratio 0.08- zone 7. Axes in mm.

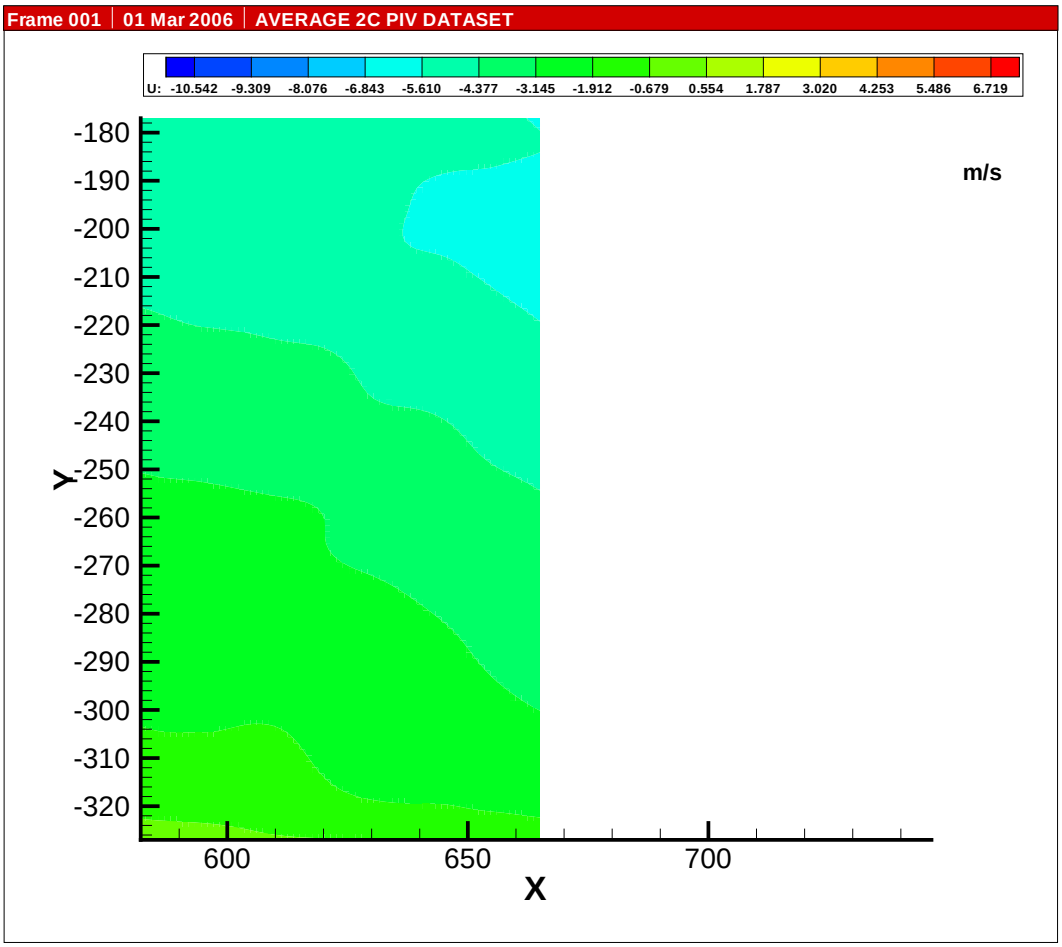

Figure 152: u Velocity at Advance Ratio 0.08- zone 8. Axes in mm.

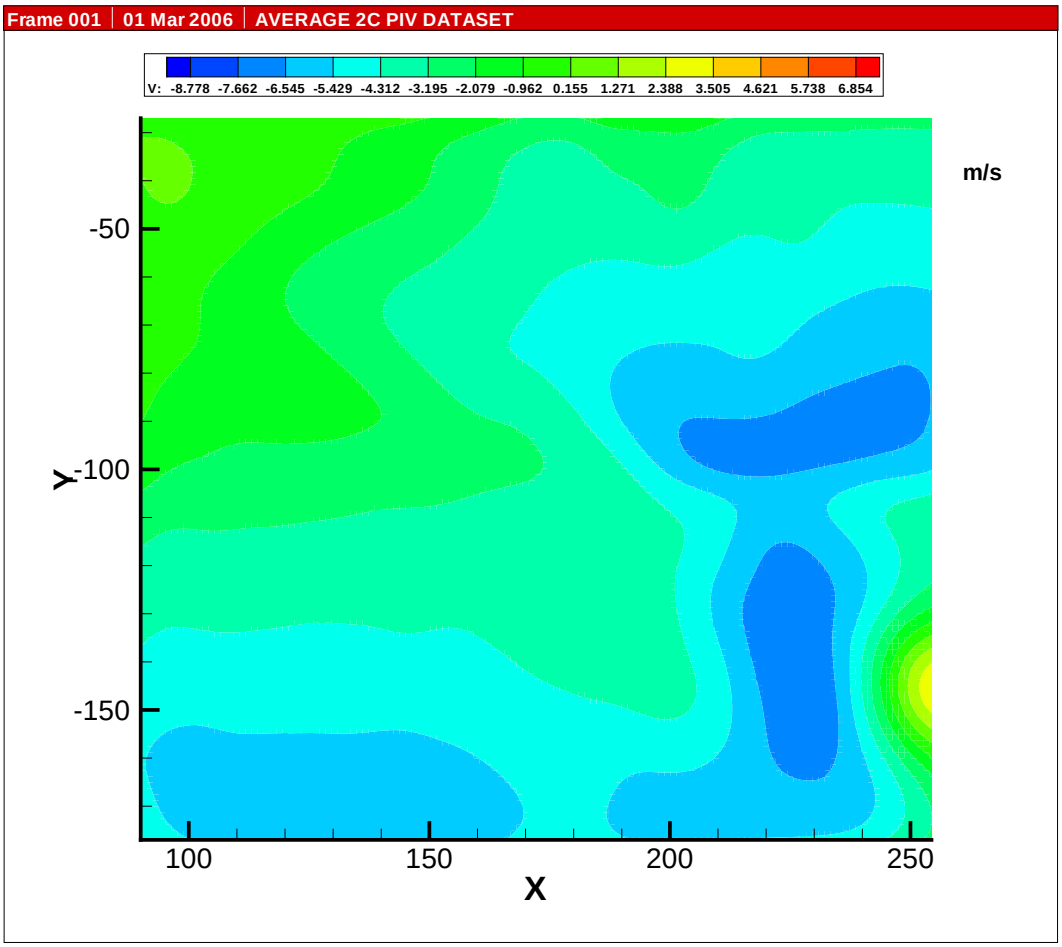

Figure 153: v Velocity at Advance Ratio 0.08- zone 1. Axes in mm.

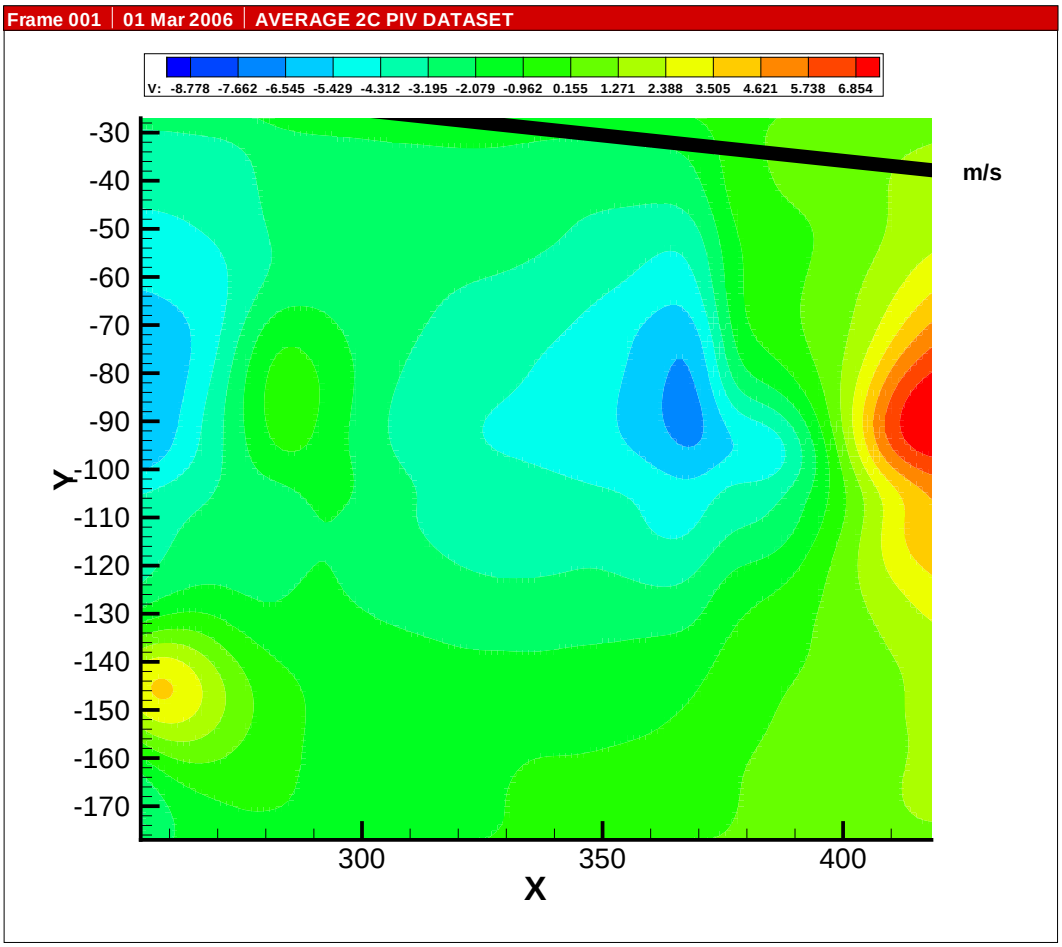

Figure 154: v Velocity at Advance Ratio 0.08- zone 2. Axes in mm.

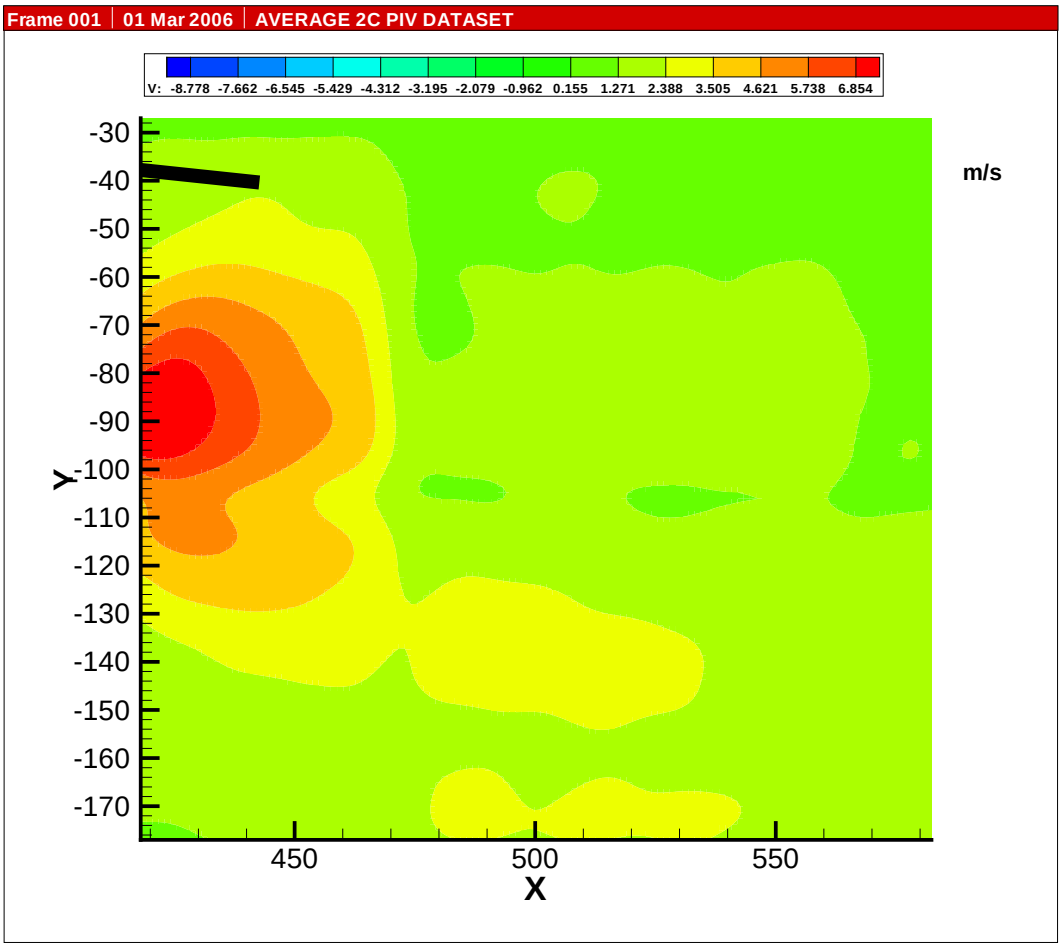

Figure 155: v Velocity at Advance Ratio 0.08- zone 3. Axes in mm.

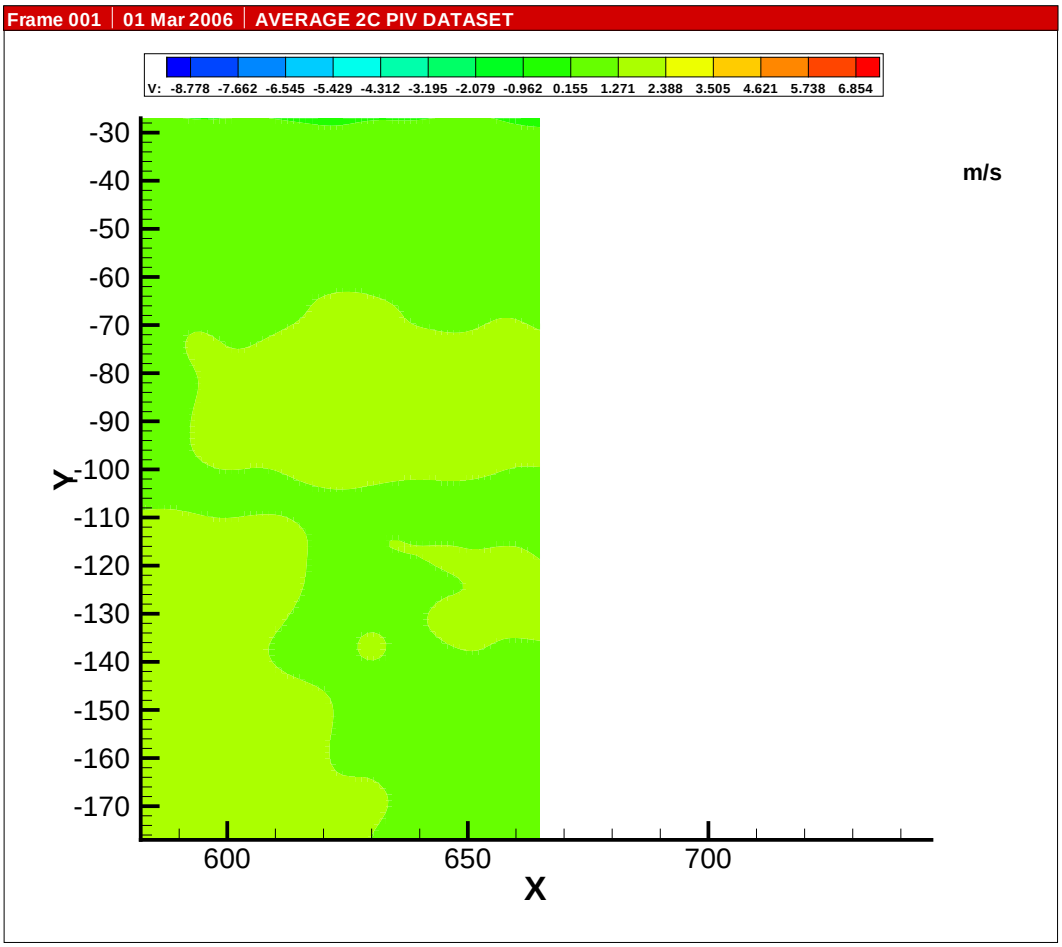

Figure 156: v Velocity at Advance Ratio 0.08- zone 4. Axes in mm.

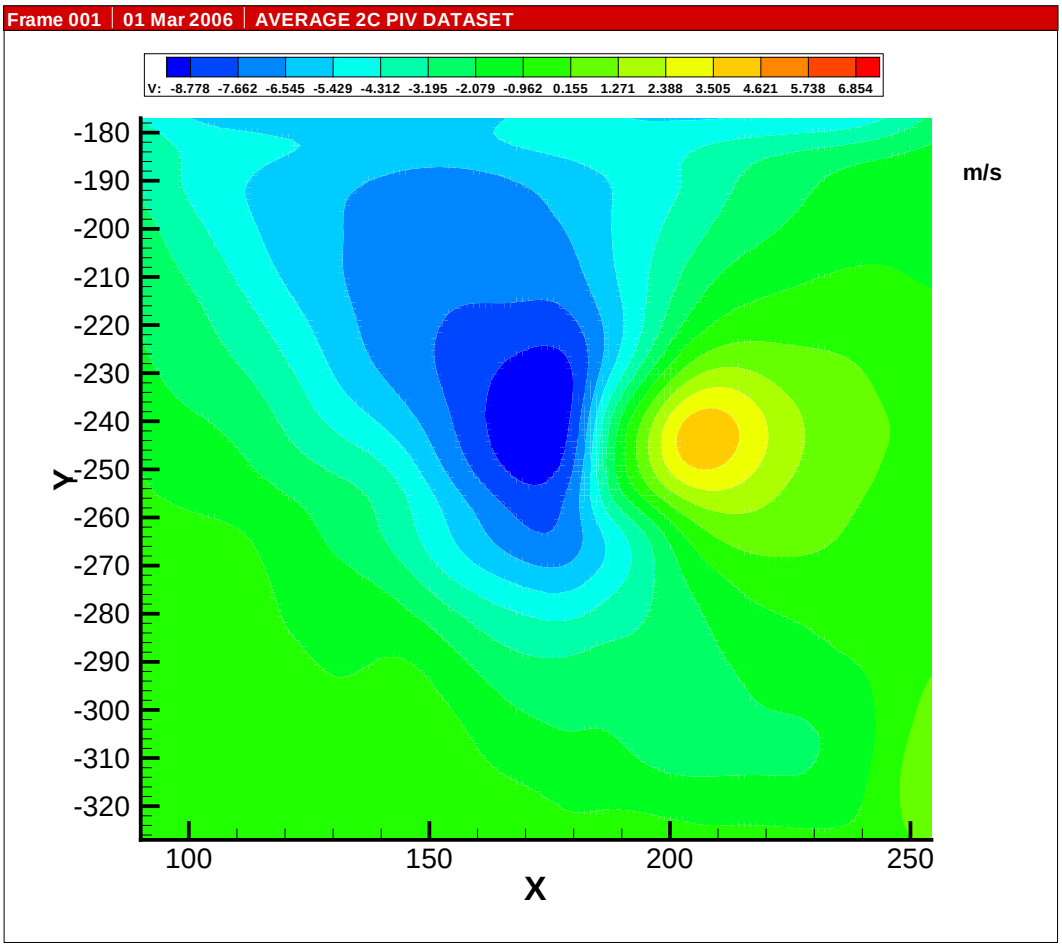

Figure 157: v Velocity at Advance Ratio 0.08- zone 5. Axes in mm.

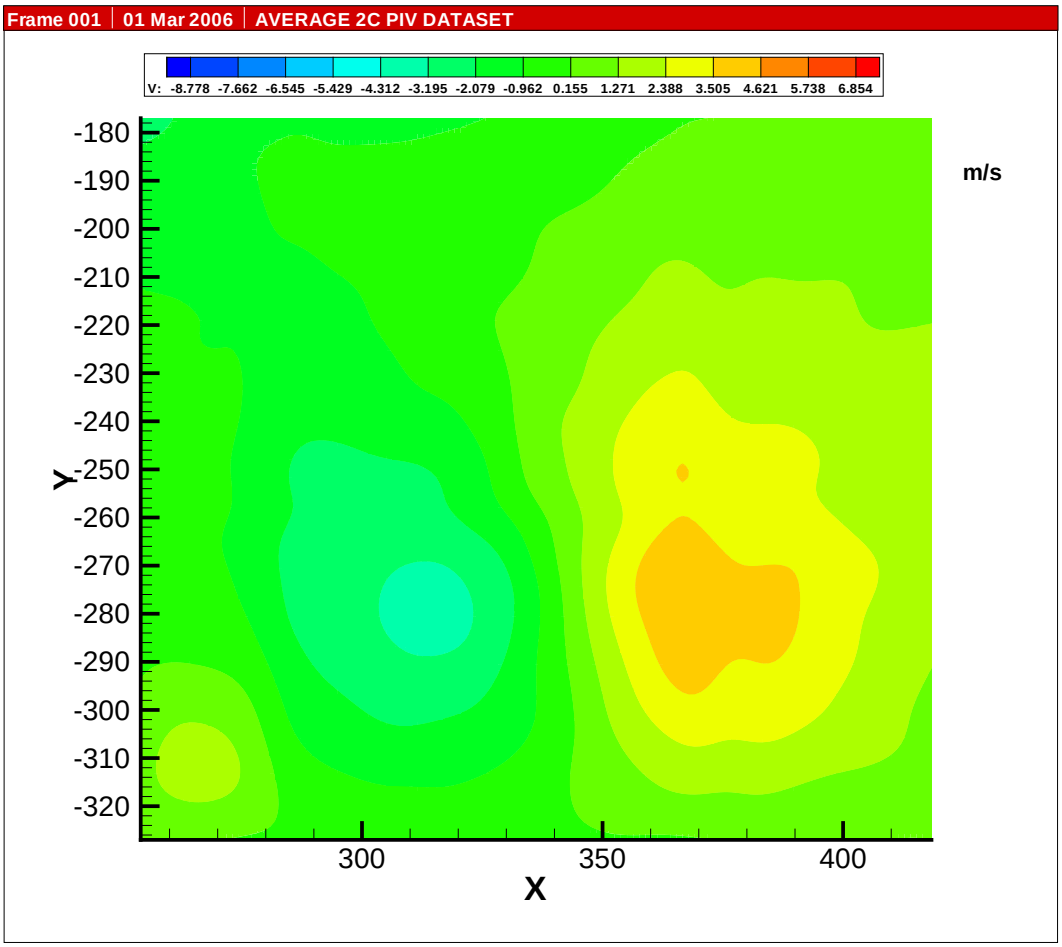

Figure 158: v Velocity at Advance Ratio 0.08- zone 6. Axes in mm.

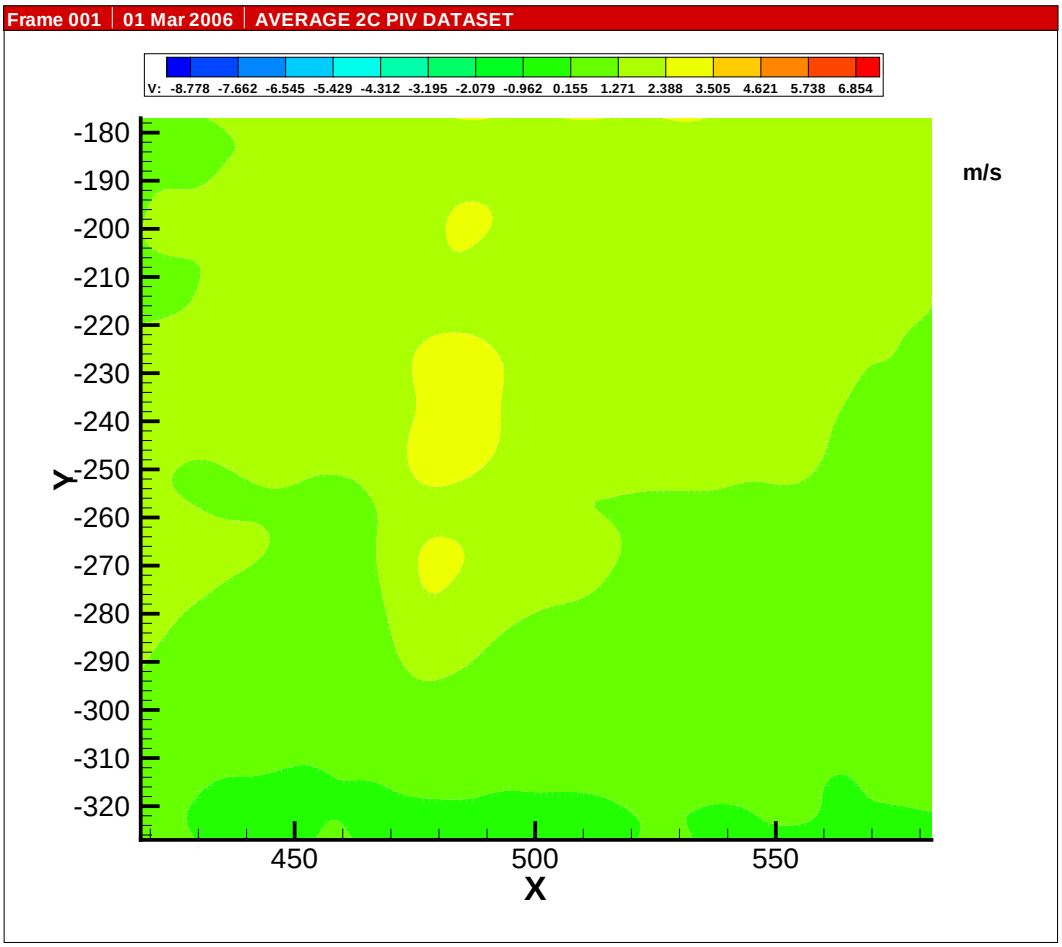

Figure 159: v Velocity at Advance Ratio 0.08- zone 7. Axes in mm.

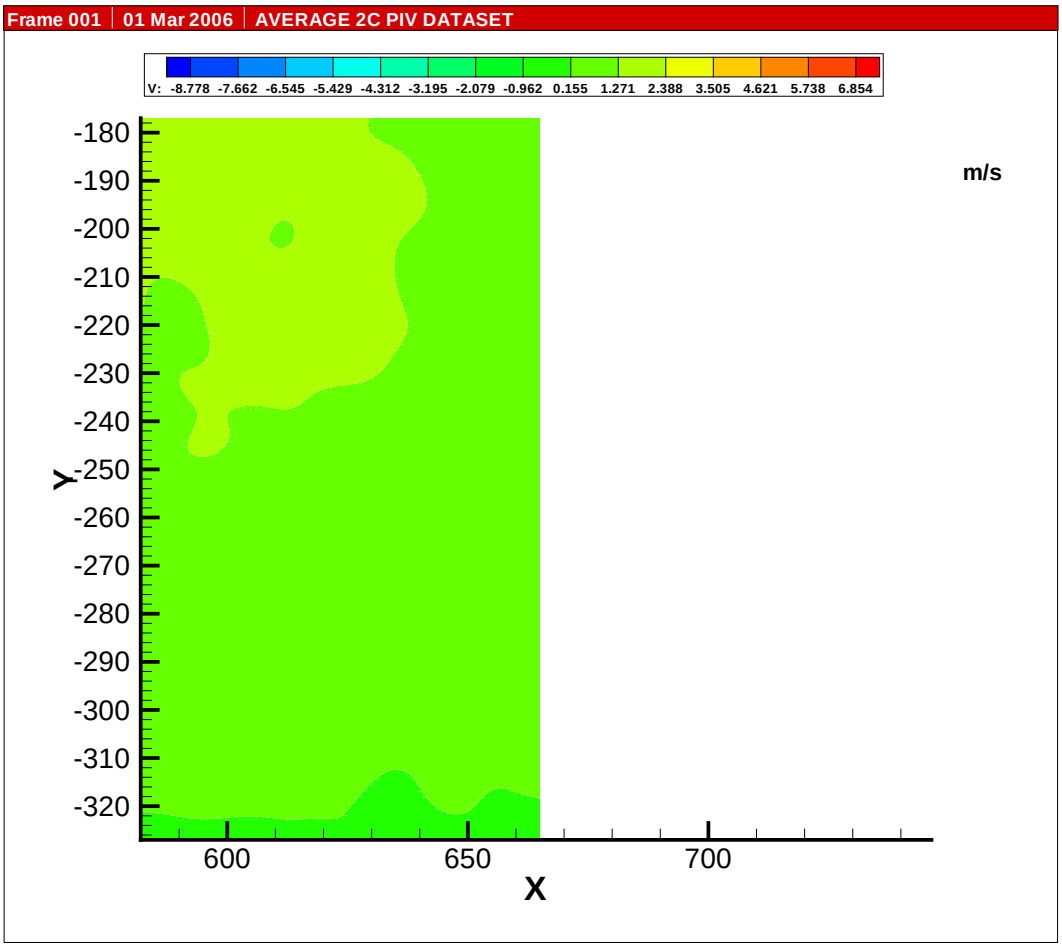

Figure 160: v Velocity at Advance Ratio 0.08- zone 8. Axes in mm.

REFERENCES

[1] Adrian, R. J., "Particle-imaging techniques for experimental fluid mechanics," *Annual Review of Fluid Mechanics*, vol. 23, pp. 261–304, 1991.

[2] Betz, A., "The ground effect on lifting propellors," *NACA TM 836*, 1938.

[3] Bolinder, J., "On the accuracy of a digital particle image velocimetry system," *Technical report, ISSN 0282 – 1990, ISRN LUTMDN/TMVK – 3186 – SE*, June 1999.

[4] Brand, A. G., "An experimental investigation of the interaction between a model rotor and airframe in forward flight," *PhD Thesis, Georgia Institute of Technology.*, p. 72, 1989.

[5] Brand, A. G., "An experimental investigation of the interaction between a rotor wake and airframe in forward flight," *PhD Thesis, Georgia Institute of Technology*, 1989.

[6] Cerde, T., Reichert, G., and Curtiss, H. C., "Influence of ground effect on helicopter take-off and landing performance," *Z. Flugweiss Weltraumforsch*, pp. 155–167, 1990.

[7] Chang, R. C. and Muirhead, V. U., "Effect of sink rate on ground effect of low-aspect-ratio wings," *Journal of Aircraft*, vol. 24, pp. 176–180, March 1986.

[8] Cheeseman, I. C. and Bennett, N. E., "The effect of ground on a helicopter rotor in forward flight," *NASA Ames Research Center Report 3021*, 1955.

[9] Chen, R. T. N., "Survey of non-uniform inflow models for rotorcraft flight dynamics and control applications," *15th European Rotorcraft Forum, Netherlands*, September 1989.

[10] Chen, Y. S. and Schweikhard, W. G., "Dynamic ground effects on a two-dimensional flat plate," *Journal of Aircraft*, vol. 22, pp. 638–630, July 1985.

[11] Christensen, K. T., Soloff, S. M., and Adrian, R. J., "Integrated particle image velocimetry (PIV) interrogation/validation software," *Technical Report 943, Department of Theoretical and Applied Mechanics, University of Illinois at Urbana-Champaign*, 2000.

[12] Cimbala, J. M., Gaublomme, D. P., and Oefelein, "Experiments on the unsteadiness associated with a ground vortex," *Journal of Aircraft*, 1991.

[13] Curry, E. C. and Owens, L. R., "Ground-effect characteristics of the Tu-144 supersonic transport airplane," *NASA/TM-2003-212035*, October 2003.

[14] Curtiss, H. C., Erdman, W., and Sun, M., "Ground effect aerodynamics," *International Conference on Rotorcraft Basic Research*, 1984.

[15] Curtiss, H. C., Sun, M., Putman, W. F., and Hanker, E. J., "Rotor aerodynamics in ground effect at low advance ratios," *Journal of the American Helicopter Society*, 1984.

[16] DuWalt, F. A., "Wakes of lifting propellors in ground effect," *CAL NO BB-1665-S-3, Cornell Aeronautical Laboratory*, 1966.

[17] Empey, W. E. and Ormiston, R. A., "Tail rotor thrust on a 5.5 foot helicopter model in ground effect," *National Forum of the American Helicopter Society*, vol. 30, 1974.

[18] Frandenburgh, E. A., "The helicopter and the ground effect machine," *Journal of the American Helicopter Society*, vol. 5, no. 4, pp. 26–28, 1960.

[19] Gao, Z. and He, C. J., "A study of the rotor wake in nape of the earth," *Journal of Nanjing Aeronautical Institute*, pp. 325–330, August 1986.

[20] Graber, A., Rose, A., and Seginer, A., "An investigation of a hovering rotor in ground effect," *Proceedings of the 16th European Rotorcraft Forum*, 1990.

[21] Gray, R. B., "An experimental smoke and magnetic analogy study of the induced flowfield about a model rotor in steady flight within ground effect," *NASA Contract NAW 6520*, 1959.

[22] Griffiths, D. A. and Leishman, J. G., "A study of dual rotor interference and ground effect using a free vortex wake model," *58th Annual Forum of AHS*, 2001.

[23] Hanker, E. J. and Smith, R. P., "Parameters affecting helicopter interactional aerodynamics in ground effect," *Journal of the American Helicopter Society*, 1985.

[24] Harris, F. D., Kasper, E. F., and Iseler, L. A., "U.S. civil rotorcraft accidents 1963 through 1997," *NASA TM 2000-209597*, 2000.

[25] Hayden, J. S., "The effect of the ground on helicopter hovering power required," *33rd Annual Forum of AHS*, 2001.

[26] He, C. J., "Development and application of a generalized dynamic wake theory for lifting rotors," *PhD Thesis, Georgia Institute of Technology*, July 1989.

[27] Heyson, H. H., "Ground effect for lifting rotors in forward flight," *NASA TN D-234*, 1960.

[28] Heyson, H. H., "Jet boundary corrections for lifting rotors centered in rectangular wind tunnels," *NASA TR R-71*, 1960.

[29] Heyson, H. H., "Linearized theory of wind tunnel jet boundary corrections and ground effect for vstol-stol aircraft," *NASA TR R-124*, 1962.

[30] Heyson, H. H., "Theoretical study of the effect of ground proximity on the induced efficiency of helicopter rotors," *NASA TMX-71951*, 1977.

[31] Heyson, H. H. and Grunwald, K. J., "Wind tunnel boundary interference for VSTOL-STOL aircraft," *NASA SP-116*, 1966.

[32] Heyson, H. H. and Katzoff, S., "Induced velocities near a lifting rotor with non-uniform disk loading," *NASA TN 3690*, 1957.

[33] Huston, R. J. and Morris, C. E. K., "A wind tunnel investigation of helicopter directional control in rearward flight in ground effect," *NASA TN D-6118*, 1971.

[34] Iboshi, N., Maeda, K., Hayata, Y., and Prasad, J. V. R., "Hovering performance of a rotor in dynamic ground effect," *Proceeding of 39th Aircraft Symposium*, 2001.

[35] Itoga, N., Nagashima, T., Iboshi, N., Kawakami, S., Prasad, J. V. R., and Peters, D. A., "Numerical analysis of ground effect for a lifting rotor hovering at close proximity to inclined flat surface," *Proceedings of the AHS International Meeting on Advanced Helicopter Technology*, 1998.

[36] Itoga, N., Nagashima, T., Iboshi, N., Kawakami, S., Prasad, J. V. R., and Peters, D. A., "A new numerical method for predicting aero-mechanical behaviors of a rotor hovering at close proximity to inclined flat surface," *Proceedings of the 55th AHS Annual Forum*, May 1999.

[37] Kang, N. and Sun, M., "Technical note: Predictions of the flowfield of a rotor in ground effect," *Journal of the American Helicopter Society*, vol. 42, April 1997.

[38] Kang, N. and Sun, M., "Simulated flowfields in near-ground operation of single and twin rotor configurations," *Journal of Aircraft*, vol. 37, No. 2, 2000.

[39] Keane, R. D. and Adrian, R. J., "Theory of cross-correlation analysis of PIV images," *Applied Science Research*, vol. 49, pp. 191–215, 1992.

[40] Kemmerly, G. T., Paulson, J. W., and Compton, M., "Exploratory evaluation of moving-model technique for measurement of dynamic ground effects," *Journal of Aircraft*, vol. 25, pp. 557–562, June 1988.

[41] Key, D. L., "Analysis of army helicopter pilot error mishap data and the implications for handling qualities," *European Rotorcraft Forum*, vol. 24, p. L4, 1999.

[42] Knight, M. and Hefner, R. A., "Analysis of ground effect on the lifting airscrew," *NACA Technical Note No. 835*, 1941.

[43] Koo, J. and Oka, T., "Experimental study on the ground effect of a model helicopter rotor in hovering," *NASA TT F-13938*, December 1971.

[44] Kusmarwanto, J., "Ground effect on a rotor wake," *Tech Report COLL Aeronautics-8510, Cranfield Institute of Technology, UK*, June 1985.

[45] Kussner, H. G., "Helicopter problems," *NACA TM 827*, 1937.

[46] Landgrebe, A. J., Taylor, R. B., Egolf, T. A., and Bennet, J. C., "Helicopter airflow and wake characteristics for low speed flight and hovering flight," *Journal of the American Helicopter Society*, 1982.

[47] Lee, C. S. and He, C. J., "A free wake/ ground vortex model for rotors at low speed in-ground effect flight," *51st American Helicopter Society Annual Forum*, vol. 1, 1995.

[48] Lee, P. H., Lan, C. E., and Muirhead, V. U., "Experimental investigation of dynamic ground effect," *NASA CR-180305*, 1986.

[49] Lee, P. H., Lan, C. E., and Muirhead, V. U., "Experimental investigation of dynamic ground effect," *NASA CR-180560*, 1987.

[50] Leishman, J. G., "Principles of helicopter aerodynamics," *Cambridge Aerospace Series*, p. 65, 2000.

[51] Lewis, R. B., "Army helicopter performance trends," *Journal of the American Helicopter Society*, vol. 17, no. 2, 1972.

[52] Light, J. S., "Tip vortex geometry of a hovering helicopter rotor in ground effect," *Journal of the American Helicopter Society*, 1993.

[53] Mahalingam, R., "Structure of the near wake of a rotor in forward flight and its effect on surface interactions," *PhD Thesis, Georgia Institute of Technology*, 1999.

[54] Mello, O. A. F., Prasad, J. V. R., and Sankar, L. N., "Analysis of helicopter-ship aerodynamic interaction," *AHS Aeromechanics Specialists Conference*, January 1994.

[55] Peters, D. A. and Gankar, G. H., "Review of dynamic inflow modeling for rotorcraft flight dynamics," *Vertica*, vol. 12, no. 3, pp. 213–242, 1988.

[56] Peters, D. A. and HaQuang, N., "Dynamic inflow modeling for practical applications," *Journal of AHS*, October 1988.

[57] Peters, D. A. and He, C. J., "A closed form unsteady aerodynamic theory for lifting rotors in hover and forward flight," *Proceedings of the 43rd AHS Annual Forum*, pp. 839–865, May 1987.

[58] Pitt, D. M. and Peters, D. A., "Theoretical prediction of dynamic inflow derivatives," *Vertica*, vol. 5, no. 1, pp. 21–34, 1981.

[59] Prasad, A. K., "Particle image velocimetry," *Current Science*, vol. 79, pp. 51–60, July 2000.

[60] Prasad, J. V. R. and Sankar, L. N., "Models for helicopter-ship dynamic interference study," *Project Final Report, Contract Number N62269-90-C-6246*, April 1996.

[61] Prouty, R. W., "Operations flight in turbulent air," *NASA Civil Helicopter Safety Web Site <http://safecopter.arc.nasa.gov>*, 2001.

[62] Quackenbush, T. R. and Wachspress, D. A., "Enhancements to a new free wake hover analysis," *NASA CR 177523*, 1989.

[63] Raffel1, M., Richard, H., Schneider, G., Klinge, F., Ehrenfried, K., Pengel, K., and Feenstra, G., "Recording and evaluation methods of PIV investigations on a helicopter rotor model," *11th International Symposium, Application of Laser Techniques to Fluid Mechanics*, July 2002.

[64] Reviewers' comments during 2003 Army Research Office Review Meeting at Georgia Tech.

[65] Saberi, H. A., "Analytical model of rotor wake aerodynamics in ground effect," *NASA CR-166533*, December 1983.

[66] Saberi, H. A., "Ground effect on helicopter aerodynamics and stability," *Technical Report, Stanford University*, January 1985.

[67] Saberi, H. A. and Maisel, M. D., "A free wake rotor analysis including ground effect," *Proceedings of the 43rd Annual AHS Forum*, May 1987.

[68] Serr, C., Hamm, J. Polz, G., Langer, J., Simoni, M., Russo, A., Young, C., Stevens, J., Desopper, A., and Papillier, D., "Improved methodology for take off and landing procedures," *The 25th European Rotorcraft Forum*, 1999.

[69] Sheridan, P. F. and Weisner, W., "Aerodynamics of helicopter flight near the ground," *33rd Annual American Helicopter Society*, 1977.

[70] Sheridan, P. F. and Weisner, W., "Mathematical modeling for helicopter simulation of low speed, low altitude and steeply descending flight," *NASA CR-166385*, 1982.

[71] Sun, M., "A study of helicopter rotor aerodynamics in ground effect at low speeds," *PhD Dissertation, Princeton University*, 1983.

[72] Wiesner, W. and Kohler, G., "Performace in presence of main rotor, ground and winds," *Journal of the American Helicopter Society*, vol. 19, no. 3, 1971.

[73] Wong, O. D., "Formation and evolution of tip vortices of an isolated rotor in forward flight," *PhD Thesis, Georgia Institute of Technology*, 2001.

[74] Zbrozek, J., "Ground effect on the lifting rotor," *ARC R and M 2347*, July 1947.

[75] Zhang, H., Prasad, J. V. R., and Sankar, L. N., "A simulation model of ship ground effect for helicopter-ship interaction study," *Proceedings of 51st AHS Annual Forum*, May 1998.

VITA

Balakrishnan Ganesh was born in Madras, India on June 09, 1971. He graduated from the National Defence Academy and the Air Force Academy, India.

He entered the graduate program at Georgia Tech in 1999 and earned his Master of Science degree in 2000.